

# Neuromorphic Computing with Halide Perovskites

Jeroen Johannes de Boer



university of  
 groningen

faculty of science  
 and engineering

zernike institute for  
 advanced materials



European Research Council

Ph.D. Thesis, University of Groningen, July 2025  
Jeroen Johannes de Boer

**Ph.D. Examining Committee**

Prof. W.R. Tress  
Prof. B. Noheda  
Prof. M.A Loi  
Dr. J.V. Milić  
Prof. E.C. Garnett

The work described in this thesis was performed between March 2021 and April 2025 at AMOLF, Science Park 104, 1098 XG Amsterdam, The Netherlands, and financed by the European Research Council (Grant Agreement No. 947221).

Copyright ©2025 by Jeroen J. de Boer

Printed by Ridderprint

ISBN: 978-94-92323-85-9

Thesis number: 2026-09, ISSN: 1570-1530

A digital version of this thesis can be downloaded at <https://ir.amolf.nl/>



university of  
 groningen

# Neuromorphic Computing with Halide Perovskites

**PhD thesis**

to obtain the degree of PhD of the  
University of Groningen  
on the authority of the  
Rector Magnificus Prof. J.M.A. Scherpen  
and in accordance with  
the decision by the College of Deans.

This thesis will be defended in public on

Monday 16 February 2026 at 11:00 hours

by

**Jeroen Johannes de Boer**

born on 02 September 1993

**Supervisor**  
Prof. B. Ehrler

**Co-supervisor**  
Dr. W. Albrecht

**Assessment Committee**  
Prof. W.R. Tress  
Prof. B. Noheda  
Prof. M.A Loi

# Contents

|          |  |            |
|----------|--|------------|
| <b>1</b> | <b>Introduction</b>  | <b>1</b>   |
| 1.1      | Neural Networks . . . . .  | 1          |
| 1.2      | Neuromorphic Computing . . . . .   | 2          |
| 1.3      | Halide Perovskites . . . . .   | 7          |
| 1.4      | Thesis Outline . . . . .   | 13         |
|          | References . . . . .   | 16         |
| <b>2</b> | <b>Microscale Artificial Synapses</b>  | <b>27</b>  |
| 2.1      | Introduction . . . . .   | 28         |
| 2.2      | Results and Discussion . . . . .   | 30         |
| 2.3      | Conclusion . . . . .   | 39         |
| 2.4      | Materials and Methods . . . . .  | 40         |
|          | Appendix 2.A Additional information . . . . .  | 42         |
|          | Appendix 2.B Considering crosstalk distance for high integration densities . . . . . | 48         |
|          | Appendix 2.C Compilation of Figure 2.5 . . . . .                                     | 49         |
|          | References . . . . .   | 51         |
| <b>3</b> | <b>Microscale Artificial Neurons</b>   | <b>57</b>  |
| 3.1      | Introduction . . . . .   | 58         |
| 3.2      | Results and Discussion . . . . .   | 59         |
| 3.3      | Conclusion . . . . .   | 67         |
| 3.4      | Materials and Methods . . . . .  | 68         |
|          | Appendix 3.A Additional information . . . . .  | 70         |
|          | Appendix 3.B Modeling of stochastic and deterministic neurons . . . . .              | 77         |
|          | Appendix 3.C Scaling of the spiking neuron . . . . .                                 | 79         |
|          | References . . . . .   | 80         |
| <b>4</b> | <b>Microscale Optoelectronic Synapses with Switchable Photocurrent</b>               | <b>85</b>  |
| 4.1      | Introduction . . . . .   | 86         |
| 4.2      | Results and Discussion . . . . .   | 87         |
| 4.3      | Conclusion . . . . .   | 98         |
| 4.4      | Materials and Methods . . . . .  | 99         |
|          | Appendix 4.A Additional information . . . . .  | 101        |
|          | References . . . . .   | 121        |
| <b>5</b> | <b>Microscale Optoelectronic Reservoir Networks for In-Sensor Computing</b>          | <b>127</b> |
| 5.1      | Introduction . . . . .   | 128        |
| 5.2      | Results and Discussion . . . . .   | 129        |
| 5.3      | Conclusion . . . . .   | 142        |
| 5.4      | Materials and Methods . . . . .  | 143        |
|          | Appendix 5.A Additional information . . . . .  | 147        |
|          | Appendix 5.B Impact of the $I_4$ currents on classification accuracy . . . . .       | 155        |

|   |     |
|---|-----|
| Appendix 5.C Additional transformations . . . . . | 159 |
| References . . . . .                              | 162 |
| Summary   | 165 |
| Nederlandse samenvatting                          | 169 |
| Publications                                      | 175 |
| Acknowledgements                                  | 179 |
| Curriculum Vitae                                  | 183 |

# 1

## Introduction

### 1.1 Neural Networks

**T**remendous progress has been made in the field of artificial intelligence (AI) over recent years. State-of-the-art large language models (LLMs), such as GPT-4, now approach the level of human experts on knowledge tests,[1] and recently, Google DeepMind’s AlphaFold allowed breakthrough protein folding discoveries,[2] granting the team a Nobel Prize.[3] A crucial factor in this progress is the upscaling of neural networks, which became possible when computation shifted from central processing units (CPUs) to graphics processing units (GPUs).[4, 5] This change resulted in significantly shorter training times for large neural networks. As a result, neural networks could be developed with increasing numbers of layers and training parameters. These “deep” neural networks, containing multiple hidden layers,[6] performed markedly better than previous “shallow” networks. AlexNet, one of the first deep neural networks, achieved a breakthrough accuracy of 84.7% in a computer vision competition, outperforming the runner-up by 10.8 percentage points.[7]

The size of neural networks has increased continuously since their conception. As a result, the number of arithmetic (floating point) operations (FLOPs) required for their training has grown exponentially each year, as shown in Figure 1.1. The shift of training to GPUs exacerbated this trend. Currently, the number of FLOPs required for training state-of-the-art models increases by approximately 4.6 times each year. Training the GPT-4 LLM required an estimated  $2.1 \times 10^{25}$  FLOPs, while an estimated  $3.0 \times 10^{21}$  FLOPs were performed for

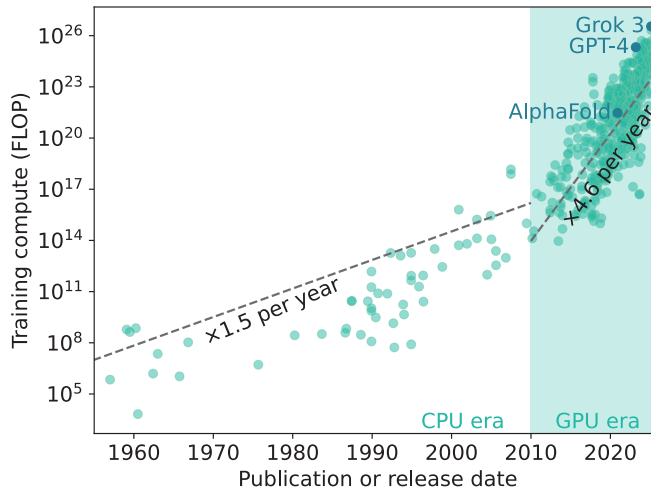


**Figure 1.1:** Evolution of required training compute to train neural networks (in FLOPs) over time. The required FLOPs increased approximately 1.5 times per year when models were trained on CPUs, and 4.6 times per year after training shifted to GPUs around 2010. Data taken from [8].

training of the AlphaFold model.[8] More recent models require even more FLOPs for training. For the training of Grok 3, for instance, an estimated  $3.5 \times 10^{26}$  FLOPs were executed. To accommodate this growth, both the GPU cluster size and training time increase annually as well. As a result, the peak power draw of GPU clusters is increasing 1.6 times each year.[8] Combined with the annual 1.2 fold increase in training time, the energy consumptions to train these frontier models is rapidly increasing.[8]

## 1.2 Neuromorphic Computing

A key goal of deep learning is to develop models with human or better-than-human level intelligence. While the models are approaching this level quickly, a striking feature of the human brain is that it performs all of its computational tasks while consuming only 20 W of power.[9] This is in stark contrast with the power consumption of contemporary frontier software neural networks.[8] The discrepancy in power consumption stems from the fundamentally different way in which the brain works.

Software neural networks are run on large clusters of GPUs that perform binary operations on large amounts of data, stored on separate memory units, shown schematically in Figure 1.2a. These GPUs and memory units perform many sequential multiplications of vectors, representing inputs, with matrices containing learned parameters (“weights”).[6] The vectors and matrices are copied from memory to the GPU for each computation, and

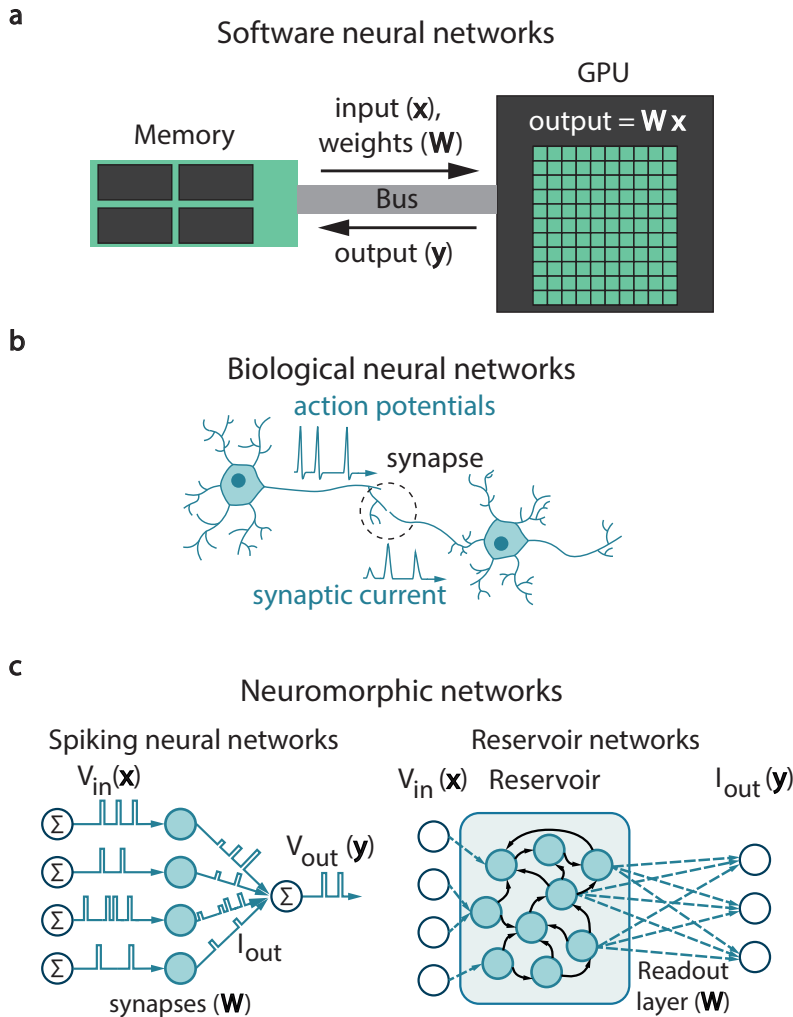


**Figure 1.2:** Neural network implementations. **(a)** Software neural networks run on conventional computers. Input vectors ( $\mathbf{x}$ ) and weight matrices ( $\mathbf{W}$ ) are transferred from memory to the GPU. The result of the vector-matrix multiplication ( $\mathbf{y}$ ) is written back to memory. Data transfer through the bus typically causes latency and high energy consumption. **(b)** Biological neural networks, which consist of many neurons connected by synapses. Neurons communicate through voltage pulses (action potentials), which are modulated by the synapses as a synaptic current. **(c)** Brain-inspired neuromorphic networks. Spiking neural networks (left) consist of electronic devices mimicking the biological networks with artificial neurons (providing  $V_{in}$  as input  $\mathbf{x}$ ), and artificial synapses (functioning as weight matrix  $\mathbf{W}$ , providing  $I_{out}$ ). Currents are integrated, and a voltage pulse is sent if a threshold is reached ( $V_{out}$ , representing the output  $\mathbf{y}$ ). Reservoir networks (right) consist of a fixed network (“Reservoir”) with short-term memory that nonlinearly transforms inputs  $\mathbf{x}$  ( $V_{in}$ ), to make them linearly separable. A readout layer with linear weights  $\mathbf{W}$  can perform classification or prediction based on the transformed input and yields the final output  $\mathbf{y}$  ( $I_{out}$ ). Memory and computation are combined in these neuromorphic networks, eliminating inefficient data transfer of conventional computers in **(a)**.

the results are written back to memory. The storage capacity of the GPU, as well as the data bandwidth between the GPU and memory, are limited. This places a constraint on the processing speed of software neural networks, commonly referred to as the “memory bottleneck”.[10] Data transfer not only introduces latency, but it is also typically the most energy-intensive process in digital computers.[10]

The biological neural network of the brain, on the other hand, consists of roughly  $10^{11}$  neurons[11] that are connected by up to  $10^{15}$  synapses.[12] Figure 1.2b schematically shows how the neurons fire voltage pulses, called action potentials, which are transferred by the synapses. The synapses determine how well action potentials are transmitted between neurons. They are highly dynamic and play an important role in learning and the processing of inputs.[13, 14] Because both processing and memory are combined in biological neural networks, they do not suffer from the memory bottleneck of classical computers. This feature not only reduces power consumption but also allows them to operate in parallel and process large amounts of data simultaneously.[12] Another important feature that helps save power is the event-driven way that inputs are processed. Each neuron only spikes if it receives inputs and remains idle otherwise.[15] Biological neural networks further enhance their efficiency by employing noise.[15] Interestingly, this inherent stochasticity does not hinder these networks but is an important feature that helps increase the robustness of signal encoding.[16]

The field of neuromorphic computing draws inspiration from biological neural networks to bridge the efficiency gap. Neuromorphic networks implement brain-inspired hardware and algorithms for information processing and learning.[17] Two examples are given in Figure 1.2c. The first example shows neuromorphic spiking neural networks (SNNs). These consist of artificial neurons and synapses to mimic the dynamics of biological networks.[18] The artificial neurons integrate incoming charge and fire voltage pulses after a threshold is reached. The artificial synapses determine the connection strength between neurons, commonly as a variable current output.[18] The synaptic connections in SNNs can be updated according to biology-inspired principles.[18–21] This way, SNNs aim to mimic the sparse, parallel, and event-driven dynamics of biological neural networks to match their efficiency.[21, 22] First implementations have shown drastically decreased energy consumption.[22] However, scaling these networks to sizes comparable to the human brain is still a major challenge.[23] This is in part because the electronic circuits necessary to mimic the functioning of neurons and synapses are complex and bulky.[18] A simpler implementation of a neuromorphic network is based on reservoir computing (RC), inspired by the recurrent connections in the brain. These networks consist of a “reservoir”, a fixed complex, dynamic system with short-term memory, and a linear

readout layer.[24, 25] In this approach, the reservoir performs a complex nonlinear transformation of input signals to increase the separability of inputs.[26] The simple readout layer can then perform classification or prediction based on the transformed input. Physical implementations of reservoir networks perform computation and memory within the same network and therefore also do not suffer from the memory bottleneck. Moreover, training them is simple because the nonlinear reservoir is fixed and only the linear readout layer contains learned parameters.[27]

### 1.2.1 Memristive Devices for Neuromorphic Computing

Implementing SNNs or physical RC requires hardware that mimics the dynamics of biological networks. Moreover, for efficient, real-time processing, the time constants of these dynamics should be well-matched with those of the inputs.[28, 29] This makes processing of inputs with time constants of milliseconds to seconds, such as gestures or speech, a major challenge for chips based on much faster conventional electronics.[29, 30]

The functionality of neuromorphic networks consisting of artificial synapses and neurons can be based on the resistance changes of memristive devices. These simple two or three-terminal devices can be implemented in higher densities than the bulkier neuromorphic devices based on conventional electronics.[31] Additionally, the timescale on which resistance changes occur can vary from hundreds of picoseconds[32, 33] to seconds,[34, 35] allowing easy matching of the time constant of the input by material choice.

Memristive devices show a resistance that can be varied by applying a voltage.[36] Various mechanisms can cause memristive properties in a broad range of materials. Formation and disruption of conductive filaments, for example, can cause large, abrupt resistance changes in metal oxides.[37, 38] Small, gradual resistance changes have been reported for these materials as well, caused by interfacial doping.[36, 39] Reversible doping can also cause resistance changes in three-terminal organic semiconductor devices.[34, 35, 40] Other mechanisms include reversible conductive-to-non-conductive phase changes[41] or ferroelectric effects.[42, 43]

#### Memristive devices for artificial synapses

Biological synapses modulate the connection strength between neurons, crucial to learning in biological neural networks.[13, 14] Artificial synapses of memristive devices mimic the modulation of the connection strength by their variable resistance. Research has mainly focused on stable (non-volatile) devices for this purpose.[44–47] Of the non-volatile responses, small, gradual resistance changes allow analog tuning of the resistance,

i.e. connection strength,[34, 35, 40] akin to biological synapses.[13, 14] Nonetheless, strategies exist to employ memristive devices showing large, binary resistance changes due to the formation of conductive filaments as well.[48] Non-volatile memristive devices have already been heavily downscaled to the square nanometer scale.[31, 41, 49] They can also be highly energy efficient, with an energy consumption in the femtojoule regime,[31, 34, 35] similar to biological synapses.[50] Even so, their implementation in neuromorphic circuits is still hindered by several factors. Square nanometer devices typically display high operating currents that are problematic for small interconnects of the chip.[44, 51] Moreover, the resistance changes are commonly stochastic.[52] While this is more faithful to biological synapses,[53, 54] algorithms implemented on contemporary memristive neuromorphic platforms usually require deterministic responses.[44, 55]

### Memristive devices for artificial neurons

Biological neurons receive input signals and transmit action potentials when combined inputs exceed a threshold, after which the neuron is reset to its initial state.[15] The inputs can be sensory stimuli, such as sight or touch,[12, 15] or action potentials from other neurons.[12, 15, 56] To mimic this behavior, memristive artificial neurons commonly connect a volatile memristive device that shows large, abrupt resistance changes in series with a resistor,[57, 58] possibly in combination with a parallel capacitor.[39, 59–62] When implemented with a series resistor only, the memristive device should initially have a higher resistance.[57, 58] An applied bias voltage then initially drops predominantly over the highly resistive memristive device. After some time, its resistance abruptly changes, which causes a voltage spike on the series resistor, reminiscent of an action potential. Importantly, the series resistor should now be more resistive than the memristive device. This causes the voltage to drop predominantly over the series resistor, allowing the volatile memristive device to reverse to its high-resistance state.[57, 58] For the parallel capacitor implementation, an initially applied voltage drops predominantly over the series resistor instead, due to the low impedance of the uncharged capacitor. As the capacitor is charged, the impedance of the parallel capacitor-memristive device increases. When the voltage drop reaches a threshold, the resistance of the memristive device rapidly drops, allowing a rapid discharge of the capacitor. This results in a current pulse similar to an action potential, while simultaneously resetting the memristive device to its high-resistance state.[39, 59–62] More complex circuits have been implemented as well.[63, 64] While these can approximate the functioning of biological neurons more closely,[64, 65] their increased number of devices makes high-density integration more challenging.

### 1.2.2 Neuromorphic Implementations with Memristive Devices

Despite their promising properties, neuromorphic chips made with memristive devices have so far been more limited compared to SNNs based on traditional electronic components. Memristive neuromorphic networks typically use memristive devices in crossbar arrays for efficient parallel vector-matrix multiplication.[44–47] In these systems, the memristive device acts as an analog, non-volatile memory element. When a voltage is applied, the readout current equals the product of the voltage and the device's conductance, according to Ohm's law. Connecting memristive devices in parallel and applying a bias voltage results in a total current that is the sum of the individual currents, following Kirchhoff's law. Combined, these two laws allow matrix-vector multiplication.[66] This hardware implementation mimics the underlying principle of parallel computation in biological neural networks and removes the memory bottleneck for more efficient computation.[45] Nonetheless, these implementations commonly suffer from device non-idealities. Reaching the same level of accuracy as software neural networks requires tuning of the resistances with high precision, which has so far not been possible in practice.[46, 47] Other common issues are unwanted resistance changes over time[67] and stochasticity in the resistance changes during programming.[44, 47]

Interestingly, biological neurons and synapses show similar “non-ideal” responses such as stochasticity[15, 53, 54] and volatile memory.[13, 14] Memristive devices could therefore be implemented in more biologically plausible networks that exploit these responses. Device volatility, for example, is important for neuromorphic networks with biology-inspired short-term memory,[68–70] as well as for reservoir networks.[71] Another example is a memristive neuron with stochastic spiking behavior due to stochastic resistance changes.[52] The stochasticity helps populations of these neurons to encode different inputs more accurately.[64, 72] While promising, these more biologically plausible memristive neuromorphic networks have been less explored so far.[73]

## 1.3 Halide Perovskites

Halide perovskites have recently been proposed as a novel material for memristive devices.[74, 75] They are a class of semiconductor materials with a chemical formula of  $ABX_3$ , where A is a monovalent cation (typically methyl ammonium or formamidinium), B is a divalent cation ( $Pb^{2+}$ ,  $Sn^{2+}$ ), and X is a halide or mixture of halides ( $Br^-$ ,  $I^-$ ). A schematic image of the crystal lattice is given in Figure 1.3a. The excellent optoelectronic properties of halide perovskites have enabled the development of efficient solar cells[76] and light-

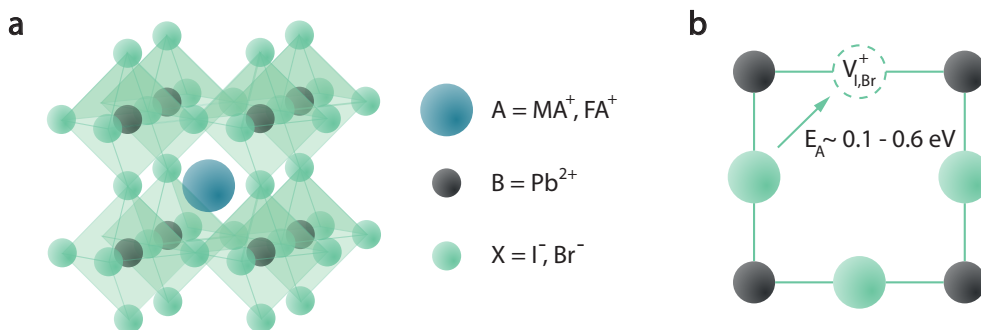


**Figure 1.3:** Mixed ionic-electronic conduction in halide perovskites. **(a)** Schematic illustration of the ABX<sub>3</sub> halide perovskite crystal lattice. A-site cations are usually organics (methyl ammonium (MA<sup>+</sup>) or formamidinium (FA<sup>+</sup>)), Pb<sup>2+</sup> is the most common B-site cation, and the X-sites are halides, such as I<sup>-</sup> or Br<sup>-</sup>. The B-site cation and halides form corner-sharing octahedra. The A-site cation sits in the center of these octahedra. **(b)** An A-site cation-halide plane of the crystal lattice with a halide vacancy at the top of the image. These vacancies are highly mobile, with reported activation energies between 0.1 and 0.6 eV.[83, 84]

emitting diodes.[77] Even so, these devices typically suffer from performance degradation due to facile movement of charged defects.[78]

### 1.3.1 Mixed Ionic-Electronic Conduction in Halide Perovskites

Bonds in the halide perovskite lattice are partially ionic, which break easily to form point defects in the form of ionic interstitials and vacancies, generally referred to as “mobile ions”.[79] The activation energy of defect formation is particularly low for halides, on the order of 0.1-0.2 eV.[80–82] As illustrated by Figure 1.3b, these vacancies are also highly mobile and migrate through the lattice by a hopping process, with activation energies in the range of 0.1-0.6 eV.[83, 84] However, migration of other ionic species, such as silver and gold electrode materials, has been reported as well.[85] Their charge causes these defects to drift along applied electric fields and accumulate at the perovskite-electrode interface. This re-distribution of ions affects the electronic device properties and leads to various forms of hysteresis.[86] The output current can be reduced as a voltage is applied due to the accumulation of ions, causing field screening at the interface.[78, 87] An increasing output current as a voltage is applied is also possible. This can, for example, be caused by a reduction of defects at the halide perovskite-electrode interface[88] or doping of the organic layers with halides.[89] Moreover, transient ionic displacement currents are commonly measured when the voltage bias is removed. These originate from the drift and diffusion as the accumulated ions redistribute.[90, 91] A striking property of halide perovskites is that ion migration in halide perovskites is exacerbated by illumination.[92]

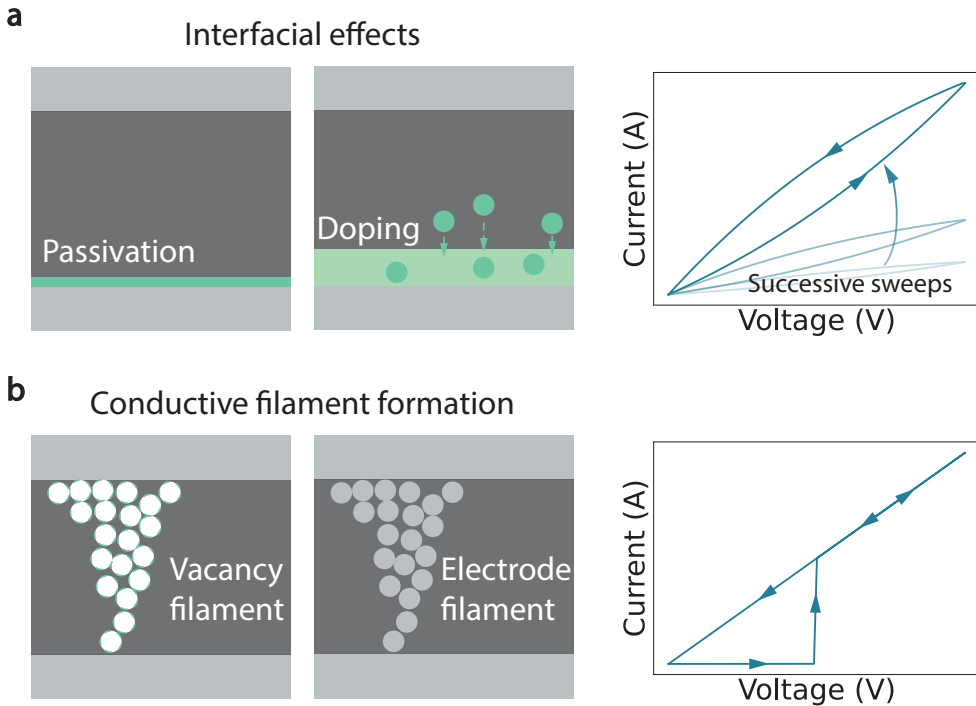


**Figure 1.4:** Commonly reported resistance change mechanisms in halide perovskite memristive devices. **(a)** Resistance changes due to interfacial effects, such as surface passivation (left) or doping of organic charge transport layers (right). These mechanisms typically cause gradual resistance changes with multiple accessible resistance states, as indicated in the I-V sweep. **(b)** Resistance changes caused by the reversible formation of conductive filaments of halide vacancies (left) or the electrode material (right). This mechanism commonly results in large, abrupt resistance changes illustrated by the I-V sweep. Arrows in the I-V plots indicate the voltage sweep direction.

### 1.3.2 Halide Perovskite Memristive Devices

Ion migration and the resulting hysteresis are unwanted in devices such as solar cells, where they cause performance degradation.[87] However, the various types of hysteresis are promising for neuromorphic applications. Moreover, ion migration typically occurs on the milliseconds to seconds timescale,[78, 87] well-matched with biologically relevant timescales. Halide perovskites can also be deposited with low-temperature, solution-based techniques, allowing novel implementations on flexible substrates.[93, 94] In light of these properties, several studies have investigated halide perovskite memristive devices for neuromorphic applications.

## Halide perovskite artificial synapses

Artificial synapses of halide perovskites can be highly energy-efficient due to the low activation energy for defect formation and migration.[74, 95, 96] Projections of the energy consumption per device area have predicted superior values for halide perovskite synapses compared to other materials showing memristive properties.[74] Energy consumptions as low as 14 fJ have been reported for changing the resistance of halide perovskite memristive devices,[95] similar to biological synapses.[50] The high energy efficiencies are promising for neuromorphic hardware, where the weight updates are a major contributor to the overall energy consumption.[21]

Halide perovskite memristive devices can show gradual, analog resistance changes,[74, 88, 89, 97] shown schematically in Figure 1.4a. These can be caused by a modulation of the charge injection or extraction energy barrier at the perovskite-electrode interface.[88, 95, 97] This response is also commonly demonstrated by halide perovskite synapses containing organic layers based on PEDOT:PSS.[74, 89, 97] These layers can be doped by mobile iodide ions of the halide perovskite layer, resulting in a lowering of the device resistance.[89] The gradual response is most similar to biological synapses,[13, 14] and closer to implementations of artificial synapses in contemporary neuromorphic networks.[21]

Abrupt, binary changes in resistance due to filament formation have been reported for halide perovskite memristive devices as well.[75, 98–100] These filaments can consist of halide vacancies,[96, 100] but also of electrode metals, such as silver.[75, 98–100] Reversible filament formation and the corresponding current response are illustrated in Figure 1.4b. The resistance changes of these devices are typically several orders of magnitude,[75, 101] up to  $10^9$ . [102] The filaments can be highly stable, with retention times of up to  $10^7$  seconds.[101] Interestingly, the stability of the filaments can also be reduced by lowering the operating current during the programming of the resistance.[103, 104] This more volatile behavior is commonly displayed by biological synapses.[13] The large, binary resistance changes are less similar to responses of biological synapses.[13, 14] Nevertheless, these devices can still reach intermediate resistances by controlling the operating current during the programming of the resistance through a compliance current.[101] Previous work on  $\text{HfO}_2$ -based memristive devices based on filament formation showed that this is also possible by adjusting the length of the programming voltage pulse.[105] This strategy might be applicable to halide perovskite memristive devices as well. Nonetheless, memristive devices showing only two stable states can still be implemented as artificial synapses by leveraging the inherent stochasticity of filament formation.[52] The synaptic weight can then be updated based on probabilistic algorithms, where an update pulse is applied to an array of parallel synapses.[55, 106]

Because of stochasticity, some devices will switch to the low resistance state, while others will retain their high resistance. The length of the update pulse controls the number of switched devices.[52] By summing the output currents of the binary synapses in the array, the array as a whole can output multiple analog currents.[55, 106]

The device response can further be altered by adjusting the perovskite composition. Addition of large A-site cations to the perovskite lattice, for example, can bring down operating currents, thereby reducing the energy consumption.[88, 96, 107] Their addition can also influence the retention time and switching speed by impeding halide migration through the perovskite.[107] By controlling the halide perovskite composition,[88, 96, 107] electrode material,[75, 108] and additional organic layers[99] as described above, halide perovskite artificial synapses can show resistance switching speeds on timescales ranging from hundreds of milliseconds[96, 107] down to hundreds of picoseconds.[109] Similarly, the retention time can be tuned from hundreds of milliseconds[74, 95, 107] up to the previously-mentioned  $10^7$  seconds[101] by adapting these device parameters.[101, 107] Moreover, analog, interfacial resistance change mechanisms can generally be obtained by incorporating organic layers such as those based on PEDOT:PSS,[74, 97, 107] using chemically inert electrodes, such as gold,[108] and increasing the distance between the electrodes.[95] Devices showing binary, filament-based resistance changes, on the other hand, can typically be fabricated by implementing reactive silver electrodes,[75, 98–100] and by having the perovskite layer in direct contact with the electrodes.[75, 100] Overall, the facile tunability of the resistance change dynamics of halide perovskite memristive devices makes them highly versatile. Ultimately, this might allow fabrication of all-halide perovskite neuromorphic networks by providing all required time constants with the same active material.[29, 110]

Besides these conventional all-electronic implementations, previous studies have combined optical and electrical inputs for programming and readout of the device as well.[111–114] In optoelectronic halide perovskite synapses, optical inputs can facilitate resistance changes induced by a bias voltage.[111, 114, 115] Another way these can be realized is in transistor architectures, where optical inputs are absorbed by the halide perovskite in the channel to increase channel conductivity.[112, 113, 116] These devices are promising for neuromorphic sensors that combine detection and processing of inputs.[117] Previously, the classification accuracy of such a neuromorphic sensor based on RC was enhanced by combining voltage and light inputs in a multimodal approach.[118] The same might be possible with these optoelectronic halide perovskite devices. While volatile halide perovskite devices have also been implemented in reservoir networks, these networks processed ei-

ther voltage[103, 104, 119] or light inputs.[120] Their use in multimodal reservoir networks capable of detecting both voltage and light inputs has not been studied.

### Halide perovskite artificial neurons

While several studies have looked into artificial synapse applications, halide perovskite artificial neurons have remained almost entirely unexplored. One study demonstrated how a volatile halide perovskite memristive device could implement signal integration.[121] However, this required external electronic circuits to produce an output spike and reset the device, and therefore did not significantly lower the device's complexity compared to conventional implementations.[18] Halide perovskite memristive devices can show the required abrupt, large, and volatile resistance changes necessary for artificial neuron implementations.[103, 104] Even so, simpler implementations with, e.g., parallel capacitors have not yet been reported. Artificial neurons are a key component of SNNs. Hence, the development of a less complex halide perovskite artificial neuron is a crucial step towards all-halide perovskite SNNs.

#### 1.3.3 Limitations of Halide Perovskite Memristive Devices

Despite their promising properties, several issues prevent the integration of halide perovskites for neuromorphic applications. On the material side, a common obstacle is their low stability. The soft, ionic bonds in the halide perovskite lattice break easily, resulting in rapid device breakdown during operation.[122] The device stability can be improved by proper encapsulation of the memristive device.[101, 109] Encapsulation can slow degradation by preventing outgassing of volatile decomposition reaction products,[123] while simultaneously limiting ingress of harmful atmospheric water and oxygen.[123–125] Furthermore, large organic A-site cations can also improve stability by forming a protective surface layer.[126] In addition, halide perovskites are highly soluble in solvents commonly used in lithography due to the ionic bonds, hindering microfabrication.[127] This forms a major bottleneck for high-density integration of halide perovskites in neuromorphic chips. A previously implemented strategy to circumvent this is to deposit the halide perovskite in a porous alumina membrane.[101, 109] A macroscale top electrode is then deposited on the substrate. While this can reduce the device area, it does not address the issue of patterning the top electrode and high-density integration. Another concern for upscaling is that halide perovskites contain toxic lead. This could be addressed by replacement with other metals, such as Cu,[128] or Sn.[129, 130] Other issues remain on the implementation side. The lack of experimentally demon-

strated halide perovskite artificial neurons is a major obstacle to the realization of halide perovskite neuromorphic networks. Moreover, studies have mostly focused on individual devices so far. Studies that did consider networks of halide perovskites are limited to RC approaches where the network processed either a voltage or light input. Networks that leverage the light-dependent ion migration of halide perovskites, a unique property that differentiates them from other memristive materials, have not yet been explored. These networks could emulate the efficient processing of sensory inputs by biological neural networks.

## 1.4 Thesis Outline

This thesis aims to demonstrate the versatility of halide perovskites for neuromorphic computing. It describes a microfabrication procedure for high-density integration of halide perovskite memristive devices. Efficient artificial synapses and neurons are fabricated with the procedure. Moreover, it shows how these components can be applied in brain-inspired networks for efficient learning and information processing.

**Chapter 2** addresses the issue of degradation of halide perovskites during microfabrication, a key issue that prevents their implementation in neuromorphic integrated circuits. We demonstrate a scalable method to fabricate halide perovskite artificial synapses on the microscale with a back-contacted architecture. The devices consist of two gold electrodes sandwiching an SiO<sub>2</sub> insulating spacer. The halide perovskite active layer is spin-coated over these electrodes in the final fabrication step, preventing degradation by exposure to solvents. Devices with a footprint of around 6 μm<sup>2</sup> are fabricated with this procedure. The devices show large resistance changes of up to five orders of magnitude, consistent with the formation of conductive filaments. Multiple resistance states are accessible with pulsed voltage measurements. The energy consumption of the resistance changes is as low as 640 fJ, owing to the small device size and, therefore, operating current. The retention time of the synapse is on the order of tens of seconds, similar to biological synapses. Compared to previous energy-efficient synapses based on other materials, the downscaled halide perovskite device excels in terms of the large dynamic range of the resistance change and its energy consumption. Furthermore, the switching speed of the halide perovskite synapse of tens of milliseconds is complementary to those of other synapses, with switching speeds of tens to hundreds of nanoseconds.

**Chapter 3** presents the first on-chip integrated halide perovskite artificial neuron. The neuron is based on a microscale halide perovskite memristive device fabricated in the back-contacted architecture. The memristive device contains a gold and silver electrode

and displays large, volatile resistance changes, with a retention time below 500 ms. The neuron is fabricated fully on-chip by connecting the volatile, microscale halide perovskite memristive device in series with a capacitor. Applying successive pulses to the device causes a large, abrupt lowering of the resistance, resulting in an output voltage spike accompanied by rapid charging of the capacitor. When the bias is removed, the capacitor discharges, aiding in the resetting of the volatile device. The spiking behavior is analyzed over several cycles, and we show that it follows Poisson behavior. We then simulate populations of neurons displaying spiking behavior by a Poisson process with the experimentally determined parameters. From the simulations, it follows that the stochastic spiking helps the population encode signals that would remain subthreshold for deterministic neurons. We calculate an energy consumption per spike between 20 and 60 pJ, lower than the 100 pJ of biological neurons. We estimate that further downscaling can decrease the energy consumption to 10 pJ without negatively impacting device performance.

**Chapter 4** introduces volatile optoelectronic synapses that are programmed electronically and read out optically. The synapses are fabricated on the microscale with the back-contacted layout, containing two gold electrodes and an insulating  $\text{Al}_2\text{O}_3$  layer over the bottom electrode. We show that this insulating layer prevents resistance changes by a bias voltage. Instead, the applied voltages cause accumulation of ions at the halide perovskite-electrode interface, resulting in a voltage buildup in the perovskite that persists after the bias voltage is removed. We demonstrate that illuminating the device yields an output photocurrent that is modulated by this voltage buildup. The sign and magnitude of the output photocurrent depend on the previously-applied bias voltage. Moreover, illuminating the device while applying the bias voltage results in larger photocurrent modulation. We implement an optoelectronic spike-timing-dependent plasticity (STDP) learning rule, inspired by biology, based on this enhancement of the photocurrent switching. We then simulate a neuromorphic camera of arrays of the optoelectronic synapse, based on the experimentally measured device response. We show that the optoelectronic STDP learning rule allows local, selective weight updates with a simple feedback-spike mechanism. The simulated camera shows attention-based learning, which can be leveraged to focus on features of interest. The camera could allow more efficient image classification by neuromorphic networks.

**Chapter 5** explores how volatile halide perovskite devices can be implemented in a multimodal in-sensor network. We use the same microscale optoelectronic devices with the  $\text{Al}_2\text{O}_3$  insulating layer as in **Chapter 4**. We show that applied voltage pulses cause a volatile ionic current that decays over hundreds of milliseconds. Applying light pulses as the voltage is applied results in a larger ionic current. We measure voltage, or combined light and

voltage 4-bit input sequences, where each bit represents a timestep where a pulse is (“1”) or is not (“0”) applied. We demonstrate that the ionic currents of different input sequences are separable, with some overlap when considering the measurement error. We use the ionic current measurements to simulate a reservoir network for in-sensor computing. The simulated network consists of arrays of the halide perovskite devices that transform the MNIST dataset. The transformed dataset is then classified with a linear readout layer. We obtain high classification accuracies of up to  $95.3 \pm 0.1\%$  for multimodal networks that transform the images based on both voltage and combined light and voltage inputs. When including experimentally measured noise, we find a minor accuracy penalty between 0.3 and 1.2 percentage points. We show with simulations of ionic current outputs that longer retention times with respect to the input frequency benefit MNIST classification. These simulations allow easy estimation of MNIST classification accuracies based on the output current of 4-bit input sequence measurements. Finally, we extend the handwritten digit classification to video inputs based on the N-MNIST dataset. We obtain the highest classification accuracy of  $89.0 \pm 0.1\%$  for the multimodal network, outperforming a reference network without volatile memory by 15.8 percentage points. These networks could be implemented fully in hardware for efficient combined sensing and processing.

# References

1. OpenAI *et al.* *GPT-4 Technical Report* 2024. arXiv: 2303.08774 [cs.CL].
2. Jumper, J. *et al.* Highly accurate protein structure prediction with AlphaFold. *Nature* **596**, 583–589 (2021).
3. *The Nobel Prize in Chemistry 2024* <https://www.nobelprize.org/prizes/chemistry/2024/summary/>. (accessed July 3, 2025)
4. Raina, R., Madhavan, A. & Ng, A. Y. *Large-scale deep unsupervised learning using graphics processors* in *Proceedings of the 26th Annual International Conference on Machine Learning* (ACM, Montreal Quebec Canada, 2009), 873–880.
5. Oh, K.-S. & Jung, K. GPU implementation of neural networks. *Pattern Recognition* **37**, 1311–1314 (2004).
6. Prince, S. J. *Deep neural networks* in *Understanding Deep Learning* 41–55 (The MIT Press, 2023).
7. Krizhevsky, A., Sutskever, I. & Hinton, G. E. ImageNet classification with deep convolutional neural networks. *Communications of the ACM* **60**, 84–90 (2017).
8. *Data on Notable AI Models* <https://epoch.ai/data/notable-ai-models>. (accessed July 11, 2025)
9. Kety, S. S. & Schmidt, C. F. The nitrous oxide method for the quantitative determination of cerebral blood flow in man: theory, procedure and normal values. *Journal of Clinical Investigation* **27**, 476–483 (1948).
10. Zidan, M. A., Strachan, J. P. & Lu, W. D. The future of electronics based on memristive systems. *Nature Electronics* **1**, 22–29 (2018).
11. Azevedo, F. A., Carvalho, L. R., Grinberg, L. T., Farfel, J. M., Ferretti, R. E., Leite, R. E., Filho, W. J., Lent, R. & Herculano-Houzel, S. Equal numbers of neuronal and nonneuronal cells make the human brain an isometrically scaled-up primate brain. *Journal of Comparative Neurology* **513**, 532–541 (2009).
12. Zhang, J. *Basic Neural Units of the Brain: Neurons, Synapses and Action Potential* 2019. arXiv: 1906.01703 [q-bio.NC].
13. Zucker, R. S. & Regehr, W. G. Short-Term Synaptic Plasticity. *Annual Review of Physiology* **64**, 355–405 (2002).

14. Bi, G.-q. & Poo, M.-m. Synaptic Modifications in Cultured Hippocampal Neurons: Dependence on Spike Timing, Synaptic Strength, and Postsynaptic Cell Type. *The Journal of Neuroscience* **18**, 10464–10472 (1998).
15. *Neural Encoding I: Firing Rates and Spike Statistics in Theoretical neuroscience: computational and mathematical modeling of neural systems* 3–44 (MIT Press, Cambridge, Mass., 2001).
16. Douglass, J. K., Wilkens, L., Pantazelou, E. & Moss, F. Noise enhancement of information transfer in crayfish mechanoreceptors by stochastic resonance. *Nature* **365**, 337–340 (1993).
17. Mead, C. Neuromorphic electronic systems. *Proceedings of the IEEE* **78**, 1629–1636 (1990).
18. Chicca, E., Stefanini, F., Bartolozzi, C. & Indiveri, G. Neuromorphic electronic circuits for building autonomous cognitive systems. *Proceedings of the IEEE* **102**, 1367–1388 (2014).
19. Serrano-Gotarredona, T., Masquelier, T., Prodromakis, T., Indiveri, G. & Linares-Barranco, B. STDP and sTDP variations with memristors for spiking neuromorphic learning systems. *Frontiers in Neuroscience* **7**, 2 (2013).
20. Pershin, Y. V. & Di Ventra, M. Experimental demonstration of associative memory with memristive neural networks. *Neural Networks* **23**, 881–886 (2010).
21. Davies, M. *et al.* Loihi: A Neuromorphic Manycore Processor with On-Chip Learning. *IEEE Micro* **38**, 82–99 (2018).
22. Merolla, P. A. *et al.* A million spiking-neuron integrated circuit with a scalable communication network and interface. *Science* **345**, 668–673 (2014).
23. Kudithipudi, D. *et al.* Neuromorphic computing at scale. *Nature* **637**, 801–812 (2025).
24. Jaeger, H. & Haas, H. Harnessing Nonlinearity: Predicting Chaotic Systems and Saving Energy in Wireless Communication. *Science* **304**, 78–80 (2004).
25. Appeltant, L., Soriano, M. C., Van Der Sande, G., Danckaert, J., Massar, S., Dambre, J., Schrauwen, B., Mirasso, C. R. & Fischer, I. Information processing using a single dynamical node as complex system. *Nature Communications* **2**, 468 (2011).
26. Cover, T. M. Geometrical and Statistical Properties of Systems of Linear Inequalities with Applications in Pattern Recognition. *IEEE Transactions on Electronic Computers* **EC-14**, 326–334 (1965).
27. Lukoševičius, M. & Jaeger, H. Reservoir computing approaches to recurrent neural network training. *Computer Science Review* **3**, 127–149 (2009).

28. Qiao, N., Mostafa, H., Corradi, F., Osswald, M., Stefanini, F., Sumislawska, D. & Indiveri, G. A reconfigurable on-line learning spiking neuromorphic processor comprising 256 neurons and 128K synapses. *Frontiers in Neuroscience* **9**, 141 (2015).
29. Chicca, E. & Indiveri, G. A recipe for creating ideal hybrid memristive-CMOS neuromorphic processing systems. *Applied Physics Letters* **116**, 120501 (2020).
30. Qiao, N., Bartolozzi, C. & Indiveri, G. An Ultralow Leakage Synaptic Scaling Homeostatic Plasticity Circuit With Configurable Time Scales up to 100 ks. *IEEE Transactions on Biomedical Circuits and Systems* **11**, 1271–1277 (2017).
31. Govoreanu, B. *et al.*  $10 \times 10 \text{ nm}^2$  Hf/HfOx crossbar resistive RAM with excellent performance, reliability and low-energy operation in 2011 International Electron Devices Meeting (2011), 31.6.1–31.6.4.
32. Torrezan, A. C., Strachan, J. P., Medeiros-Ribeiro, G. & Williams, R. S. Sub-nanosecond switching of a tantalum oxide memristor. *Nanotechnology* **22**, 485203 (2011).
33. Ma, C. *et al.* Sub-nanosecond memristor based on ferroelectric tunnel junction. *Nature Communications* **11**, 1439 (2020).
34. Xu, W., Min, S. Y., Hwang, H. & Lee, T. W. Organic core-sheath nanowire artificial synapses with femtojoule energy consumption. *Science Advances* **2**, e1501326 (2016).
35. Zhang, C., Wang, S., Zhao, X., Yang, Y., Tong, Y., Zhang, M., Tang, Q. & Liu, Y. Sub-Femtojoule-Energy-Consumption Conformable Synaptic Transistors Based on Organic Single-Crystalline Nanoribbons. *Advanced Functional Materials* **31**, 2007894 (2021).
36. Strukov, D. B., Snider, G. S., Stewart, D. R. & Williams, R. S. The missing memristor found. *Nature* **453**, 80–83 (2008).
37. Zhang, Y. *et al.* Evolution of the conductive filament system in HfO<sub>2</sub>-based memristors observed by direct atomic-scale imaging. *Nature Communications* **12**, 7232 (2021).
38. Wang, Z. *et al.* Memristors with diffusive dynamics as synaptic emulators for neuromorphic computing. *Nature Materials* **16**, 101–108 (2017).
39. Park, S.-O., Jeong, H., Park, J., Bae, J. & Choi, S. Experimental demonstration of highly reliable dynamic memristor for artificial neuron and neuromorphic computing. *Nature Communications* **13**, 2888 (2022).
40. Van de Burgt, Y., Lubberman, E., Fuller, E. J., Keene, S. T., Faria, G. C., Agarwal, S., Marinella, M. J., Alec Talin, A. & Salleo, A. A non-volatile organic electrochemical device as a low-voltage artificial synapse for neuromorphic computing. *Nature Materials* **16**, 414–418 (2017).

41. Kuzum, D., Jeyasingh, R. G. D., Lee, B. & Wong, H.-S. P. Nanoelectronic Programmable Synapses Based on Phase Change Materials for Brain-Inspired Computing. *Nano Letters* **12**, 2179–2186 (2012).
42. Chanthbouala, A. *et al.* A ferroelectric memristor. *Nature Materials* **11**, 860–864 (2012).
43. Kim, D. J., Lu, H., Ryu, S., Bark, C.-W., Eom, C.-B., Tsymbal, E. Y. & Gruverman, A. Ferroelectric Tunnel Memristor. *Nano Letters* **12**, 5697–5702 (2012).
44. Li, C. *et al.* Analogue signal and image processing with large memristor crossbars. *Nature Electronics* **1**, 52–59 (2018).
45. Yao, P. *et al.* Face classification using electronic synapses. *Nature communications* **8**, 15199 (2017).
46. Li, C. *et al.* Efficient and self-adaptive in-situ learning in multilayer memristor neural networks. *Nature Communications* **9**, 7–14 (2018).
47. Yao, P., Wu, H., Gao, B., Tang, J., Zhang, Q., Zhang, W., Yang, J. J. & Qian, H. Fully hardware-implemented memristor convolutional neural network. *Nature* **577**, 641–646 (2020).
48. Payvand, M., Nair, M. V., Müller, L. K. & Indiveri, G. A neuromorphic systems approach to in-memory computing with non-ideal memristive devices: from mitigation to exploitation. *Faraday Discussions* **213**, 487–510 (2019).
49. Ambrogio, S., Ciocchini, N., Laudato, M., Milo, V., Pirovano, A., Fantini, P. & Ielmini, D. Unsupervised Learning by Spike Timing Dependent Plasticity in Phase Change Memory (PCM) Synapses. *Frontiers in Neuroscience* **10**, 56 (2016).
50. Laughlin, S. B., De Ruyter Van Steveninck, R. R. & Anderson, J. C. The metabolic cost of neural information. *Nature Neuroscience* **1**, 36–41 (1998).
51. Agarwal, S., Plimpton, S. J., Hughart, D. R., Hsia, A. H., Richter, I., Cox, J. A., James, C. D. & Marinella, M. J. Resistive memory device requirements for a neural algorithm accelerator in 2016 International Joint Conference on Neural Networks (IJCNN) (2016), 929–938.
52. Jo, S. H., Kim, K.-H. & Lu, W. Programmable Resistance Switching in Nanoscale Two-Terminal Devices. *Nano Letters* **9**, 496–500 (2009).
53. Walmsley, B., Edwards, F. R. & Tracey, D. J. Nonuniform release probabilities underlie quantal synaptic transmission at a mammalian excitatory central synapse. *Journal of Neurophysiology* **60**, 889–908 (1988).
54. Del Castillo, J. & Katz, B. Quantal components of the end-plate potential. *The Journal of Physiology* **124**, 560–573 (1954).

55. Payvand, M., Muller, L. K. & Indiveri, G. *Event-based circuits for controlling stochastic learning with memristive devices in neuromorphic architectures in 2018 IEEE International Symposium on Circuits and Systems (ISCAS)* (IEEE, Florence, 2018), 1–5.
56. Averbeck, B. B., Latham, P. E. & Pouget, A. Neural correlations, population coding and computation. *Nature Reviews Neuroscience* **7**, 358–366 (2006).
57. Zhang, Y. *et al.* Highly Compact Artificial Memristive Neuron with Low Energy Consumption. *Small* **14**, 1802188 (2018).
58. Stoliar, P., Tranchant, J., Corraze, B., Janod, E., Besland, M.-P., Tesler, F., Rozenberg, M. & Cario, L. A Leaky-Integrate-and-Fire Neuron Analog Realized with a Mott Insulator. *Advanced Functional Materials* **27**, 1604740 (2017).
59. Zhang, X. *et al.* An Artificial Neuron Based on a Threshold Switching Memristor. *IEEE Electron Device Letters* **39**, 308–311 (2018).
60. Wu, Z., Lu, J., Shi, T., Zhao, X., Zhang, X., Yang, Y., Wu, F., Li, Y., Liu, Q. & Liu, M. A Habituation Sensory Nervous System with Memristors. *Advanced Materials* **32**, 2004398 (2020).
61. Al-Shedivat, M., Naous, R., Cauwenberghs, G. & Salama, K. N. Memristors Empower Spiking Neurons With Stochasticity. *IEEE Journal on Emerging and Selected Topics in Circuits and Systems* **5**, 242–253 (2015).
62. Lee, D. *et al.* Various Threshold Switching Devices for Integrate and Fire Neuron Applications. *Advanced Electronic Materials* **5**, 1800866 (2019).
63. Pickett, M. D., Medeiros-Ribeiro, G. & Williams, R. S. A scalable neuristor built with Mott memristors. *Nature Materials* **12**, 114–117 (2013).
64. Tuma, T., Pantazi, A., Le Gallo, M., Sebastian, A. & Eleftheriou, E. Stochastic phase-change neurons. *Nature Nanotechnology* **11**, 693–699 (2016).
65. Yi, W., Tsang, K. K., Lam, S. K., Bai, X., Crowell, J. A. & Flores, E. A. Biological plausibility and stochasticity in scalable VO<sub>2</sub> active memristor neurons. *Nature Communications* **9**, 4661 (2018).
66. Ielmini, D. & Wong, H. S. In-memory computing with resistive switching devices. *Nature Electronics* **1**, 333–343 (2018).
67. Fantini, A., Gorine, G., Degraeve, R., Goux, L., Chen, C. Y., Redolfi, A., Clima, S., Cabrini, A., Torelli, G. & Jurczak, M. *Intrinsic program instability in HfO<sub>2</sub> RRAM and consequences on program algorithms in 2015 IEEE International Electron Devices Meeting (IEDM)* (IEEE, Washington, DC, USA, 2015), 7.5.1–7.5.4.
68. Covi, E., Ielmini, D., Lin, Y.-H., Wang, W., Stecconi, T., Milo, V., Bricalli, A., Ambrosi, E., Pedretti, G. & Tseng, T.-Y. *A Volatile RRAM Synapse for Neuromorphic Computing in 2019 26th IEEE International Conference on Electronics, Circuits and Systems (ICECS)* (IEEE, Genoa, Italy, 2019), 903–906.

69. Ricci, S., Kappel, D., Tetzlaff, C., Ielmini, D. & Covi, E. Tunable synaptic working memory with volatile memristive devices. *Neuromorphic Computing and Engineering* **3**, 044004 (2023).
70. Wang, W., Covi, E., Milozzi, A., Farronato, M., Ricci, S., Sbandati, C., Pedretti, G. & Ielmini, D. Neuromorphic Motion Detection and Orientation Selectivity by Volatile Resistive Switching Memories. *Advanced Intelligent Systems* **3**, 2000224 (2021).
71. Du, C., Cai, F., Zidan, M. A., Ma, W., Lee, S. H. & Lu, W. D. Reservoir computing using dynamic memristors for temporal information processing. *Nature Communications* **8**, 2204 (2017).
72. Zendrikov, D., Solinas, S. & Indiveri, G. Brain-inspired methods for achieving robust computation in heterogeneous mixed-signal neuromorphic processing systems. *Neuromorphic Computing and Engineering* **3**, 034002 (2023).
73. Li, C., Zhang, X., Chen, P., Zhou, K., Yu, J., Wu, G., Xiang, D., Jiang, H., Wang, M. & Liu, Q. Short-term synaptic plasticity in emerging devices for neuromorphic computing. *iScience* **26**, 106315 (2023).
74. Xiao, Z. & Huang, J. Energy-efficient hybrid perovskite memristors and synaptic devices. *Advanced Electronic Materials* **2**, 1600100 (2016).
75. Yan, K., Peng, M., Yu, X., Cai, X., Chen, S., Hu, H., Chen, B., Gao, X., Dong, B. & Zou, D. High-performance perovskite memristor based on methyl ammonium lead halides. *Journal of Materials Chemistry C* **4**, 1375–1381 (2016).
76. Green, M. A., Dunlop, E. D., Yoshita, M., Kopidakis, N., Bothe, K., Siefert, G., Hinken, D., Rauer, M., Hohl-Ebinger, J. & Hao, X. Solar cell efficiency tables (Version 64). *Progress in Photovoltaics: Research and Applications* **32**, 425–441 (2024).
77. Hassan, Y. *et al.* Ligand-engineered bandgap stability in mixed-halide perovskite LEDs. *Nature* **591**, 72–77 (2021).
78. Tress, W., Marinova, N., Moehl, T., Zakeeruddin, S. M., Nazeeruddin, M. K. & Grätzel, M. Understanding the rate-dependent J–V hysteresis, slow time component, and aging in CH<sub>3</sub> NH<sub>3</sub> PbI<sub>3</sub> perovskite solar cells: the role of a compensated electric field. *Energy & Environmental Science* **8**, 995–1004 (2015).
79. Tress, W. Metal Halide Perovskites as Mixed Electronic-Ionic Conductors: Challenges and Opportunities - From Hysteresis to Memristivity. *Journal of Physical Chemistry Letters* **8**, 3106–3114 (2017).
80. Yin, W. J., Shi, T. & Yan, Y. Unusual defect physics in CH<sub>3</sub>NH<sub>3</sub>PbI<sub>3</sub> perovskite solar cell absorber. *Applied Physics Letters* **104**, 063903 (2014).
81. Kim, J., Lee, S. H., Lee, J. H. & Hong, K. H. The role of intrinsic defects in methylammonium lead iodide perovskite. *Journal of Physical Chemistry Letters* **5**, 1312–1317 (2014).

82. Walsh, A., Scanlon, D. O., Chen, S., Gong, X. G. & Wei, S.-H. Self-Regulation Mechanism for Charged Point Defects in Hybrid Halide Perovskites. *Angewandte Chemie International Edition* **54**, 1791–1794 (2015).
83. Eames, C., Frost, J. M., Barnes, P. R., O'regan, B. C., Walsh, A. & Islam, M. S. Ionic transport in hybrid lead iodide perovskite solar cells. *Nature communications* **6**, 7497 (2015).
84. Meloni, S. *et al.* Ionic polarization-induced current–voltage hysteresis in CH<sub>3</sub>NH<sub>3</sub>PbX<sub>3</sub> perovskite solar cells. *Nature Communications* **7**, 10334 (2016).
85. Kerner, R. A. *et al.* Electrochemical Doping of Halide Perovskites by Noble Metal Interstitial Cations. *Advanced Materials* **35**, 2302206 (2023).
86. Gonzales, C., Bou, A., Guerrero, A. & Bisquert, J. Capacitive and Inductive Characteristics of Volatile Perovskite Resistive Switching Devices with Analog Memory. *The Journal of Physical Chemistry Letters* **15**, 6496–6503 (2024).
87. Thiesbrummel, J. *et al.* Ion-induced field screening as a dominant factor in perovskite solar cell operational stability. **9**, 664–676 (2024).
88. Solanki, A., Guerrero, A., Zhang, Q., Bisquert, J. & Sum, T. C. Interfacial Mechanism for Efficient Resistive Switching in Ruddlesden–Popper Perovskites for Non-volatile Memories. *Journal of Physical Chemistry Letters* **11**, 463–470 (2020).
89. Xu, W., Cho, H., Kim, Y. H., Kim, Y. T., Wolf, C., Park, C. G. & Lee, T. W. Organometal Halide Perovskite Artificial Synapses. *Advanced Materials* **28**, 5916–5922 (2016).
90. Alvarez, A. O. *et al.* Ionic Field Screening in MAPbBr<sub>3</sub> Crystals Revealed from Remnant Sensitivity in X-ray Detection. *ACS Physical Chemistry Au* **3**, 386–393 (2023).
91. Diethelm, M., Lukas, T., Smith, J., Dasgupta, A., Caprioglio, P., Futscher, M., Hany, R. & Snaith, H. J. Probing ionic conductivity and electric field screening in perovskite solar cells: a novel exploration through ion drift currents. *Energy & Environmental Science* **18**, 1385–1397 (2025).
92. Zhao, Y.-C., Zhou, W.-K., Zhou, X., Liu, K.-H., Yu, D.-P. & Zhao, Q. Quantification of light-enhanced ionic transport in lead iodide perovskite thin films and its solar cell applications. *Light: Science & Applications* **6**, e16243–e16243 (2016).
93. Gu, C. & Lee, J. S. Flexible Hybrid Organic–Inorganic Perovskite Memory. *ACS Nano* **10**, 5413–5418 (2016).
94. Liu, D., Lin, Q., Zang, Z., Wang, M., Wangyang, P., Tang, X., Zhou, M. & Hu, W. Flexible All-Inorganic Perovskite CsPbBr<sub>3</sub> Nonvolatile Memory Device. *ACS Applied Materials and Interfaces* **9**, 6171–6176 (2017).
95. Gong, J., Yu, H., Zhou, X., Wei, H., Ma, M., Han, H., Zhang, S., Ni, Y., Li, Y. & Xu, W. Lateral Artificial Synapses on Hybrid Perovskite Platelets with Modulated Neuroplasticity. *Advanced Functional Materials* **30**, 2005413 (2020).

96. Tian, H., Zhao, L., Wang, X., Yeh, Y. W., Yao, N., Rand, B. P. & Ren, T. L. Extremely Low Operating Current Resistive Memory Based on Exfoliated 2D Perovskite Single Crystals for Neuromorphic Computing. *ACS Nano* **11**, 12247–12256 (2017).
97. John, R. A. *et al.* Ionotronic halide perovskite drift-diffusive synapses for low-power neuromorphic computation. *Advanced Materials* **30**, 1805454 (2018).
98. Luo, H. *et al.* In Situ Unveiling of the Resistive Switching Mechanism of Halide Perovskite-Based Memristors. *The Journal of Physical Chemistry Letters* **15**, 2453–2461 (2024).
99. Gonzales, C. & Guerrero, A. Mechanistic and Kinetic Analysis of Perovskite Memristors with Buffer Layers: The Case of a Two-Step Set Process. *The Journal of Physical Chemistry Letters* **14**, 1395–1402 (2023).
100. Zhu, X., Lee, J. & Lu, W. D. Iodine vacancy redistribution in organic–inorganic halide perovskite films and resistive switching effects. *Advanced Materials* **29**, 1700527 (2017).
101. Zhang, Y. *et al.* Three-dimensional perovskite nanowire array-based ultrafast resistive RAM with ultralong data retention. *Science advances* **7**, eabg3788 (2021).
102. Kim, H., Choi, M.-J., Suh, J. M., Han, J. S., Kim, S. G., Le, Q. V., Kim, S. Y. & Jang, H. W. Quasi-2D halide perovskites for resistive switching devices with ON/OFF ratios above 109. *NPG Asia Materials* **12**, 21 (2020).
103. John, R. A. *et al.* Reconfigurable halide perovskite nanocrystal memristors for neuromorphic computing. *Nature Communications* **13**, 2074 (2022).
104. Luo, Z., Wang, W., Wu, J., Ma, G., Hou, Y., Yang, C., Wang, X., Zheng, F., Zhao, Z., Zhao, Z., *et al.* Leveraging Dual Resistive Switching in Quasi-2D Perovskite Memristors for Integrated Non-volatile Memory, Synaptic Emulation, and Reservoir Computing. *ACS Applied Materials & Interfaces* **17**, 19879–19891 (2025).
105. Frascaroli, J., Brivio, S., Covi, E. & Spiga, S. Evidence of soft bound behaviour in analogue memristive devices for neuromorphic computing. *Scientific reports* **8**, 7178 (2018).
106. Gaba, S., Sheridan, P., Zhou, J., Choi, S. & Lu, W. Stochastic memristive devices for computing and neuromorphic applications. *Nanoscale* **5**, 5872 (2013).
107. Kim, S. I. *et al.* Dimensionality Dependent Plasticity in Halide Perovskite Artificial Synapses for Neuromorphic Computing. *Advanced Electronic Materials* **5**, 1900008 (2019).
108. Pérez-Martínez, J. C., Berruet, M., Gonzales, C., Salehpour, S., Bahari, A., Arredondo, B. & Guerrero, A. Role of Metal Contacts on Halide Perovskite Memristors. *Advanced Functional Materials* **33**, 2305211 (2023).

109. Poddar, S. *et al.* Down-Scalable and Ultra-fast Memristors with Ultra-high Density Three-Dimensional Arrays of Perovskite Quantum Wires. *Nano Letters* **21**, 5036–5044 (2021).
110. Zenke, F., Agnes, E. J. & Gerstner, W. Diverse synaptic plasticity mechanisms orchestrated to form and retrieve memories in spiking neural networks. *Nature Communications* **6**, 6922 (2015).
111. Ham, S., Choi, S., Cho, H., Na, S. I. & Wang, G. Photonic Organolead Halide Perovskite Artificial Synapse Capable of Accelerated Learning at Low Power Inspired by Dopamine-Facilitated Synaptic Activity. *Advanced Functional Materials* **29**, 1806646 (2019).
112. Liu, J., Yang, Z., Gong, Z., Shen, Z., Ye, Y., Yang, B., Qiu, Y., Ye, B., Xu, L., Guo, T., *et al.* Weak light-stimulated synaptic hybrid phototransistors based on islandlike perovskite films prepared by spin coating. *ACS Applied Materials & Interfaces* **13**, 13362–13371 (2021).
113. Ma, F. *et al.* Optoelectronic Perovskite Synapses for Neuromorphic Computing. *Advanced Functional Materials* **30**, 1908901 (2020).
114. Zhao, X., Wang, Z., Li, W., Sun, S., Xu, H., Zhou, P., Xu, J., Lin, Y. & Liu, Y. Photoassisted Electroforming Method for Reliable Low-Power Organic–Inorganic Perovskite Memristors. *Advanced Functional Materials* **30**, 1910151 (2020).
115. Zhou, F., Liu, Y., Shen, X., Wang, M., Yuan, F. & Chai, Y. Low-voltage, optoelectronic CH<sub>3</sub>NH<sub>3</sub>PbI<sub>3</sub>-xCl<sub>x</sub> memory with integrated sensing and logic operations. *Advanced Functional Materials* **28**, 1800080 (2018).
116. Subramanian Periyal, S., Jagadeeswararao, M., Ng, S. E., John, R. A. & Mathews, N. Halide Perovskite Quantum Dots Photosensitized-Amorphous Oxide Transistors for Multimodal Synapses. *Advanced Materials Technologies* **5**, 2000514 (2020).
117. Zhou, F. & Chai, Y. Near-sensor and in-sensor computing. *Nature Electronics* **3**, 664–671 (2020).
118. Liu, K., Zhang, T., Dang, B., Bao, L., Xu, L., Cheng, C., Yang, Z., Huang, R. & Yang, Y. An optoelectronic synapse based on  $\alpha$ -In<sub>2</sub>Se<sub>3</sub> with controllable temporal dynamics for multimode and multiscale reservoir computing. *Nature Electronics* **5**, 761–773 (2022).
119. Chen, L.-W., Wang, W.-C., Ko, S.-H., Chen, C.-Y., Hsu, C.-T., Chiao, F.-C., Chen, T.-W., Wu, K.-C. & Lin, H.-W. Highly Uniform All-Vacuum-Deposited Inorganic Perovskite Artificial Synapses for Reservoir Computing. *Advanced Intelligent Systems* **3**, 2000196 (2021).

120. Sharma, D., Luqman, A., Ng, S. E., Yantara, N., Xing, X., Tay, Y. B., Basu, A., Chattopadhyay, A. & Mathews, N. Halide perovskite photovoltaics for in-sensor reservoir computing. *Nano Energy* **129**, 109949 (2024).
121. Yang, J. Q., Wang, R., Wang, Z. P., Ma, Q. Y., Mao, J. Y., Ren, Y., Yang, X., Zhou, Y. & Han, S. T. Leaky integrate-and-fire neurons based on perovskite memristor for spiking neural networks. *Nano Energy* **74**, 104828 (2020).
122. Ren, Y., Ma, H., Wang, W., Wang, Z., Xu, H., Zhao, X., Liu, W., Ma, J. & Liu, Y. Cycling-Induced Degradation of Organic-Inorganic Perovskite-Based Resistive Switching Memory. *Advanced Materials Technologies* **4**, 1800238 (2019).
123. Shi, L. *et al.* Gas chromatography–mass spectrometry analyses of encapsulated stable perovskite solar cells. *Science* **368**, eaba2412 (2020).
124. Waleed, A., Tavakoli, M. M., Gu, L., Wang, Z., Zhang, D., Manikandan, A., Zhang, Q., Zhang, R., Chueh, Y.-L. & Fan, Z. Lead-free perovskite nanowire array photodetectors with drastically improved stability in nanoengineering templates. *Nano letters* **17**, 523–530 (2017).
125. McKenna, B., Troughton, J. R., Watson, T. M. & Evans, R. C. Enhancing the stability of organolead halide perovskite films through polymer encapsulation. *RSC Advances* **7**, 32942–32951 (2017).
126. Wang, Z., Lin, Q., Chmiel, F. P., Sakai, N., Herz, L. M. & Snaith, H. J. Efficient ambient-air-stable solar cells with 2D-3D heterostructured butylammonium-caesium-formamidinium lead halide perovskites. *Nature Energy* **2**, 1–10 (2017).
127. Lin, C. H., Cheng, B., Li, T. Y., Retamal, J. R. D., Wei, T. C., Fu, H. C., Fang, X. & He, J. H. Orthogonal Lithography for Halide Perovskite Optoelectronic Nanodevices. *ACS Nano* **13**, 1168–1176 (2019).
128. Zhang, L., Chen, Y., Mao, S., Li, Z., Jiang, C., Luo, C., Lin, H., Travas-Sejdic, J. & Peng, H. Lead-free halide perovskite-based optoelectronic synapse for reservoir computing. *Chemical Engineering Journal* **506**, 160106 (2025).
129. Chen, L., Xi, J., Tekelenburg, E. K., Tran, K., Portale, G., Brabec, C. J. & Loi, M. A. Quasi-2D Lead-Tin Perovskite Memory Devices Fabricated by Blade Coating. *Small Methods* **8**, 2300040 (2024).
130. Qian, W.-H., Cheng, X.-F., Zhou, J., He, J.-H., Li, H., Xu, Q.-F., Li, N.-J., Chen, D.-Y., Yao, Z.-G. & Lu, J.-M. Lead-free perovskite MASnBr<sub>3</sub>-based memristor for quaternary information storage. *InfoMat* **2**, 743–751 (2020).



# 2

## Microscale Artificial Synapses

### Abstract

The efficient conduction of mobile ions in halide perovskites is highly promising for artificial synapses (or memristive devices), devices with a conductivity that can be varied by applying a bias voltage. Here we address the challenge of downscaling halide perovskite-based artificial synapses to achieve low energy consumption and allow high-density integration. We fabricate halide perovskite artificial synapses in a back-contacted architecture to achieve microscale devices despite the high solubility of halide perovskites in polar solvents that are commonly used in lithography. The energy consumption of a conductance change of the device is as low as 640 fJ, among the lowest reported for two-terminal halide perovskite artificial synapses so far. Moreover, the high resistance of the device up to hundreds of megaohms, low operating voltage of 100 mV and simple two-terminal architecture enable implementation in highly dense crossbar arrays. These arrays could potentially show orders of magnitude lower energy consumption for computation compared to conventional digital computers.

---

This chapter is based on: De Boer, J. J. & Ehrler, B. Scalable Microscale Artificial Synapses of Lead Halide Perovskite with Femtojoule Energy Consumption. *ACS Energy Letters* **9**, 5787–5794 (2024)

## 2.1 Introduction

2

Recent years have seen the rapid development of ever more capable artificial intelligence (AI) models. These models now rival or even surpass human capabilities in a wide range of tasks, such as complex strategy games[1–3], image analysis[4, 5], predicting protein folding[6] or practicing law[7] and medicine.[8] While these feats are certainly impressive, the development comes with an exponential increase in computational demand and therefore power consumption.[9] As an example, at the time of writing the GPT models underlying ChatGPT are run on clusters ranging from eight up to thousands of GPUs each consuming up to 700 W of power.[10] This large computational demand and power consumption is especially problematic for AI applications where relatively small devices, such as smart sensors, are required to function autonomously and without connecting to large external servers and power sources. By contrast, the most complex neural network we know, the human brain, only consumes roughly 20 W of power.[11] One elegant solution to tackle this large discrepancy in power consumption is therefore to move to a novel way of computation that is inspired by the brain. In these so-called neuromorphic computing systems, electronic circuits are employed to mimic the functioning of biological neurons and synapses. Some well-known first implementations of this principle by Intel and IBM have demonstrated orders of magnitude reduction in power consumption for classification tasks already.[12, 13] The synapses in these neuromorphic systems were so far implemented by complementary metal-oxide semiconductor (CMOS) circuits.[14] However, these circuits are bulky and typically take up most of the available area on the chip.[14, 15] Moreover, the energy consumption of tens to hundreds of pJ per synaptic event in the aforementioned neuromorphic chips[12, 13] is still significantly higher than the 1-10 fJ consumed by their biological counterpart.[16] Memristive devices have recently gathered significant attention as an alternative building block of artificial synapses. These two-terminal devices have a resistance that can be varied by the application of a bias voltage and their working principle is typically based on formation of metallic filaments in metal oxides,[17, 18] a phase change from a non-conductive amorphous to a conductive crystalline material[19, 20] or polarization of a ferroelectric material.[21, 22] Their low energy consumption of operation down to the femtojoule range[17–22] and the possibility to implement memristive devices in dense crossbar arrays[23, 24] make them an attractive alternative to synapses that are solely based on CMOS circuits. There are several requirements for memristive devices before they can effectively replace or be incorporated into CMOS-based artificial synapses. Firstly, memristive devices with a range of switching speeds and state retention times

are required to construct neuromorphic systems capable of learning and remembering of information.[25, 26] In addition, the resistance of the device should be high to prevent parasitic voltage drops on the interconnecting wires and to prevent electromigration of wire material.[23, 24] Lastly, large conductivity changes are required to help reduce read errors in downscaled devices with low operating currents.[24]

Recently, halide perovskites have been proposed as a novel material for implementation in memristive devices.[27–30] Conductance changes in halide perovskite-based electronic devices are thought to originate from migration of ions or ion vacancies under the application of a bias voltage.[31] The low activation energy of ion-migration in this class of materials means that their projected energy consumption is among the lowest of all memristive materials reported in literature, in the femtojoule range for device areas at or below  $10 \mu\text{m}^2$ . [28, 32] In addition, large changes in the conductance [29, 33] and the large range of timescales for conductance changes ranging from hundreds of milliseconds down to hundreds of picoseconds [28, 33] make halide perovskites attractive candidate materials for artificial synapses. However, so far few studies have focused on downscaling of halide perovskite memristive devices, which is a major challenge due to the high solubility of halide perovskites in polar solvents that are commonly used in lithography procedures.[34] Downscaled halide perovskite devices with their promised femtojoule energy consumption have therefore not been demonstrated so far and there is currently no method to implement them in dense arrays on a chip. Moreover, downscaling of memristive devices based on other materials has previously been shown to result in higher operating voltages, [35–37] leading to higher energy consumptions than expected based on the macroscale device. The lack of downscaled memristive devices of halide perovskites therefore makes it difficult to assess whether these materials retain their favorable resistance change properties for smaller device areas and hence to verify their scalability.[38] In previous attempts, devices were downscaled by incorporation of halide perovskite in porous alumina membranes or in holes in a  $\text{SiO}_2$  layer with top contacts evaporated through a shadow mask. However, with these approaches, the energy consumption of conductance changes was still on the order of several picojoules and the device geometry is difficult to scale to large networks.[33, 39]

Here we report a method to downscale halide perovskite artificial synapses to the microscale to reach an energy consumption of conductance changes down to 640 fJ. The synapse is operated at low voltages of 100 to 200 mV with large conductance changes up to five orders of magnitude. Moreover, the synapse has a switching speed on the order of tens of milliseconds and a retention time of tens of seconds, similar to biological synapses. The timescales of conductance changes differ significantly from those of synapses based

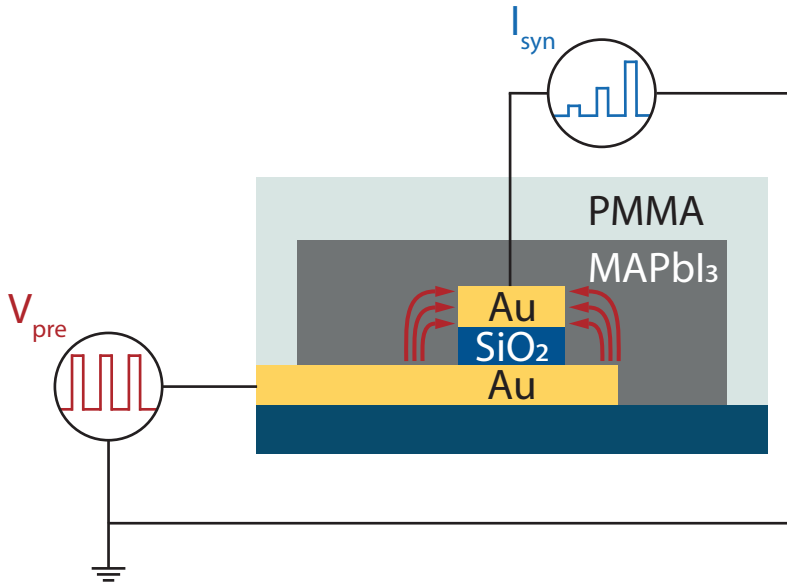


**Figure 2.1:** Schematic representation of the artificial synapse. The device consists of two gold electrodes that form a crosspoint and sandwich a  $\text{SiO}_2$  spacer layer. A  $\text{MAPbI}_3$  active layer is spin-coated over the electrodes. Bias-voltage induced hysteresis leads to a change in the postsynaptic current  $I_{syn}$  of the device with each successive presynaptic voltage pulse  $V_{pre}$  that is applied.

on metal oxides, phase change materials and ferroelectrics and therefore complements these existing memristive devices. The high resistance up to hundreds of megaohms and the two-terminal architecture make our devices ideal for integration in high density crossbar arrays.

## 2.2 Results and Discussion

The back-contacted, two terminal device architecture that was adopted for the downscaled synapses is shown schematically in Figure 2.1. The device consists of two gold electrodes that form a crosspoint with a  $\text{SiO}_2$  spacer that separates the electrodes. Methylammonium lead iodide ( $\text{MAPbI}_3$ ) perovskite is spin coated over the electrodes and forms the active layer of the device. By depositing both electrodes prior to perovskite deposition, our device avoids processing on top of the relatively sensitive perovskite layer. Depending on the bias voltage applied to the electrodes, current flows through the  $\text{MAPbI}_3$  layer from the top of the bottom electrode to the sides of the top electrode or vice versa. Bias voltages applied to the  $\text{MAPbI}_3$  layer induce hysteresis that modulates the resistance of the device, mimicking the plasticity of biological synapses.[40] Embedded in a network, one of the electrodes

would electronically connect to the presynaptic neuron that sends voltage pulses to the postsynaptic neuron via the other electrode of this synapse.

### 2.2.1 Fabrication Procedure

The device fabrication procedure is outlined in Figure 2.2a-e. First, the gold bottom electrodes were patterned on a Si/SiO<sub>2</sub> (100 nm) substrate by a UV-lithography procedure. A 60 nm SiO<sub>2</sub> layer was then deposited on the bottom electrode by inductively coupled plasma chemical vapor deposition (ICPCVD). Top electrodes were subsequently patterned on the SiO<sub>2</sub> layer by a second UV-lithography step, aligned perpendicular to the bottom electrode. The SiO<sub>2</sub> layer acts as an insulating layer that prevents a short-circuit between the top and bottom electrodes. The top electrodes were now used as a hard mask for reactive ion etching (RIE) of the SiO<sub>2</sub> layer. An optical microscopy and SEM image of the cross-point of the electrodes after the RIE of the SiO<sub>2</sub> layer are shown in Figure 2.2f. Finally, the MAPbI<sub>3</sub> active layer and a PMMA capping layer were spin-coated onto the substrate. An X-ray diffraction (XRD) pattern and scanning electron microscopy (SEM) image of a spin-coated MAPbI<sub>3</sub> film are given in Figure 2.A.1 of the Appendix. Spin coating the halide perovskite layer only in the final step prevents degradation of the perovskite layer due to exposure to polar solvents used in the lithography procedure. Moreover, the encapsulation with PMMA has been shown to significantly reduce the rate of degradation of the perovskite layer under ambient conditions and at elevated temperatures.[41]

A current-voltage characteristic (I-V curve) of the device before perovskite deposition was measured to ensure that the SiO<sub>2</sub> spacer does not form a shunt in the final device with the perovskite layer. As can be observed in Figure 2.A.2, the current that flows between the electrodes through the SiO<sub>2</sub> spacer falls below the detection limit of our measurement setup for all bias voltages used in this work. In addition, no resistance changes were measured up to 3 V without the perovskite. We can therefore exclude contributions of the SiO<sub>2</sub> layer to resistance changes of the final device.

The geometry of the current flow through the MAPbI<sub>3</sub> layer from the top of the bottom electrode to the sides of the top electrode makes the exact device area difficult to define. However, the device volume can still be minimized by decreasing the width of the electrodes. All devices discussed in the rest of this work contained gold top and bottom electrodes that were 2.5 μm wide. This electrode width was chosen as a compromise allowing for high fabrication yields and minimized device area. A clear advantage of our crossbar geometry is that the dimensions of the halide perovskite film do not limit the device dimensions and therefore the crosspoints can be implemented in dense arrays underneath a single, macroscopic film.

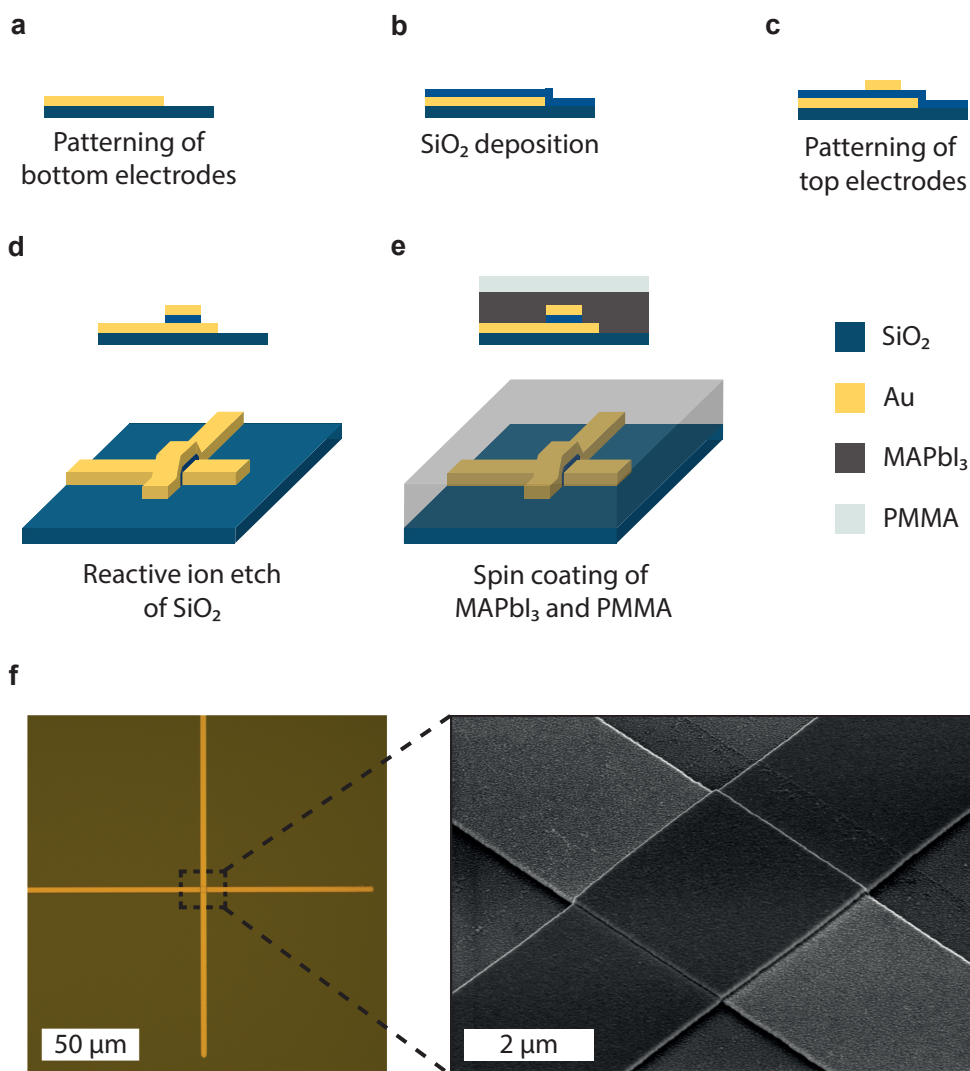


**Figure 2.2:** Fabrication procedure of the perovskite synapses. **(a)** 2.5 μm wide Au bottom electrodes are patterned on a thermally oxidized Si substrate by UV lithography. **(b)** A 60 nm insulating SiO<sub>2</sub> spacer is deposited by ICPCVD. **(c)** 2.5 μm Au top electrodes are patterned perpendicular to the bottom electrode in a second UV lithography step. **(d)** The top electrode is used as a hardmask during removal of SiO<sub>2</sub> from the bottom electrode with a reactive ion etch. **(e)** The perovskite active layer and a PMMA capping layer are spin-coated in the final fabrication step. **(f)** Optical microscopy and tilted SEM image of the crosspoint of two 2.5 μm electrodes.

### 2.2.2 Artificial synapse measurements

Thirty-five I-V curves demonstrating the typical conductance change behavior of the microscale device are shown in Figure 2.3a. The current rapidly increases by approximately

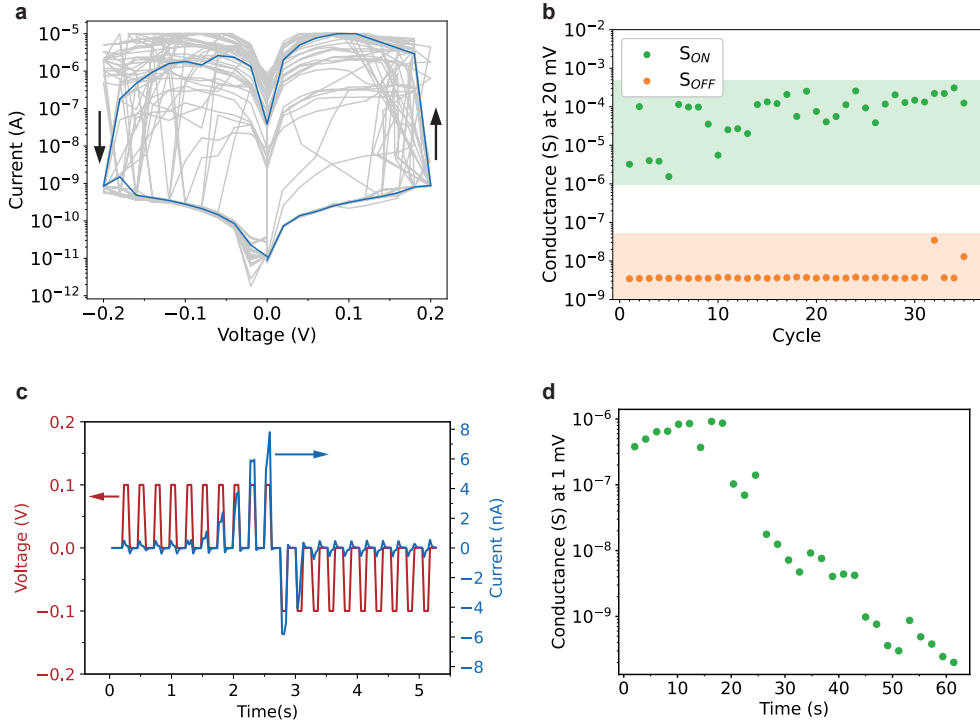


**Figure 2.3:** Conductance changes of the synapse. **(a)** The median (blue) of 35 I-V sweeps (grey) of the synapse, showing a rapid increase of the current between 100 and 200 mV. **(b)** The conductance in the forward ( $S_{OFF}$ ) and backward ( $S_{ON}$ ) sweep, calculated from the current measured at 0.02 V in the I-V sweeps in **(a)**. An increase in the conductance of three to five orders of magnitude is observed for each cycle. **(c)** Pulsed I-V measurements demonstrating the reversible conductance changes with ten 80 ms pulses of +100 mV, followed by ten pulses of -100 mV and of the same duration. **(d)** Retention time measured directly after switching the conductance of the synapse to  $S_{ON}$  with 10 pulses (200 mV, 80 ms). The retention time is measured with a 1 mV probe pulse. The conductive state is stable for tens of seconds.

three to five orders of magnitude when a potential of 0.1 to 0.2 V is reached in the forward sweep from 0 to 0.2 V. The device remains in this higher conductive state with conductance  $S_{ON}$  in the reverse sweep from 0.2 to -0.2 V and is reset to the lower conductive state with conductance  $S_{OFF}$  between 0 and -0.2 V. Similar rapid conductance changes of several orders of magnitude have been reported before in macroscopic perovskite memristive devices. Interestingly, for macroscale devices these changes typically occur at higher voltages than those reported here and are attributed to the formation of conductive filaments through the film.[42–44] One of the I-V sweeps is shown in Figure 2.A.3, plotted on the linear scale. From this measurement it follows that the synapse shows ohmic conduction after the conductance increase, which is expected after the formation of a conductive filament through the bulk of the film.[45] The I-V sweep therefore suggests that the

measured conductance changes in our device are due to the formation and rupture of a conductive filament as well. Formation of these conductive filaments in metal-halide perovskite-metal devices is well-established and has been demonstrated experimentally in previous reports.[43, 44, 46, 47] The lower voltages at which the conductance changes are observed can be explained by the shorter distance between the electrodes than those typically used in macroscale devices,[42–44] resulting in proportionally larger electric field strength. In the I-V sweep in Figure 2.A.3, the ohmic response of the device is not maintained for negative voltages, which we ascribe to the relative instability of the filament and the large electric field experienced by the filament, even at low applied voltages. Importantly, these measurements show that halide perovskite synapses maintain low operating voltages after downscaling. We note that conductance changes can also occur for negative applied voltages, as demonstrated in Figure 2.A.4. The device is symmetric, but switches preferentially in the direction of the initial voltage sweep. This behavior is consistent with the conductive filament mechanism.[45] Once the filament is formed in one direction, the field within the device is small. Only after the rupture of the filament can the voltage drop in the bulk of the device be large enough to grow a new filament in the reverse direction. The preference of switching in one sweeping direction that we show here is consistent with previous work on symmetric metal-halide perovskite-metal devices.[44]

The conductance values at 0.02 V for the forward and the backward sweeps were calculated by dividing the measured current by this voltage (Figure 2.3b). In each of the cycles the device shows a large  $S_{ON}$  to  $S_{OFF}$  ratio between 3 and 5 orders of magnitude and a low conductance down to the nS range, which is important for the scalability of the device.[23, 24] Although the conductance in the  $S_{OFF}$  state is consistent between cycles, there is some variation in the conductance in the  $S_{ON}$  state. There is no clear trend of decreasing or increasing  $S_{ON}$  with each successive cycle. Therefore, the variation is unlikely due to degradation of the device, but probably due to a stochastic nature of the resistance changes.[26]

The distribution of the voltages where conductance changes, the  $S_{OFF}$  and  $S_{ON}$  state conductance, and the  $S_{ON}$  to  $S_{OFF}$  ratio are given in Figure 2.A.5 of the Appendix. The voltages at which the conductance is switched on and off are  $0.16 \pm 0.03$  V and  $-0.12 \pm 0.06$  V, respectively. Despite these low switching voltages, the device shows a remarkably high  $S_{ON}$  to  $S_{OFF}$  ratio of  $2.7 \pm 2.2 \times 10^4$ .

To investigate the switching behavior, we applied a pulsed voltage. Voltage pulses produced more gradual conductance changes, as demonstrated in Figure 2.3c. Ten consecutive voltage pulses of 0.1 V and 80 ms in duration were applied to the device, followed

by ten consecutive pulses with the same duration, but of opposite polarity. The measured current during the application of the positive voltage pulses increased from 0.1 nA in the first pulse to 8 nA in the tenth pulse. During the subsequently applied negative voltage pulses, the current changed from -6 nA in the first negative pulse to -0.1 nA in the tenth pulse, indicating a decrease in the conductance of the device. The pulsed measurement demonstrates the change of the conductance of the device over orders of magnitude upon application of a bias voltage. In addition, the measurement shows that several conductive states are accessible between the  $S_{ON}$  and  $S_{OFF}$  states demonstrated in Figure 2.3b. This tunability of the conductive state of the synapse is analogous to the tunability of the connection strength of biological synapses, where several states are accessible depending on the degree of potentiation of the synapse.[48]

The retention time of the  $S_{ON}$  state was determined by applying periodic 1 mV probe pulses immediately after setting the device in the  $S_{ON}$  state. This voltage is too low to cause conductance changes of the device, as can be observed in Figure 2.A.6a. The evolution of the conductance over time is shown in Figure 2.3d, while the full measurement is given in Figure 2.A.6b. The conductive state does not decrease for the first 20 seconds of the measurement, after which the conductance starts to decay to the  $S_{OFF}$  state, which is reached 30 seconds after the start of the measurement. Similar time constants for changing and retention of the state of the synapse have been reported for biological synapses.[40]

I-V curves and the corresponding  $S_{ON}$  and  $S_{OFF}$  values at 20 mV of different devices are shown in Figure 2.A.7. From these IV curves it follows that devices from different batches all show similarly large conductance changes of several orders of magnitude with an onset between 200 and 400 mV, demonstrating the reproducibility of our fabrication procedure.

One of the promises of perovskite artificial synapses is that their energy consumption might be very low, approaching biological synapses. We reduced the voltage pulse duration to 55 ms to reduce the dissipated energy during a conductance change of the synapse. At such short time, and at the low current measured, the parasitic capacitance of our measurement setup introduced a significant measurement artifact, as is evident when comparing the measured data of the synapse in Figure 2.A.8a and b with data measured without contacting the sample in Figure 2.A.8c. We therefore corrected for this parasitic displacement current by subtracting the current measured without contacting the synapse from the measured data. The corrected pulsed measurement is shown in Figure 2.4a. The mean current determined at each of the ten pulses is plotted in Figure 2.4b. The current increased from 0.1 nA in the first pulse to 10 nA in the final pulse, similar to the

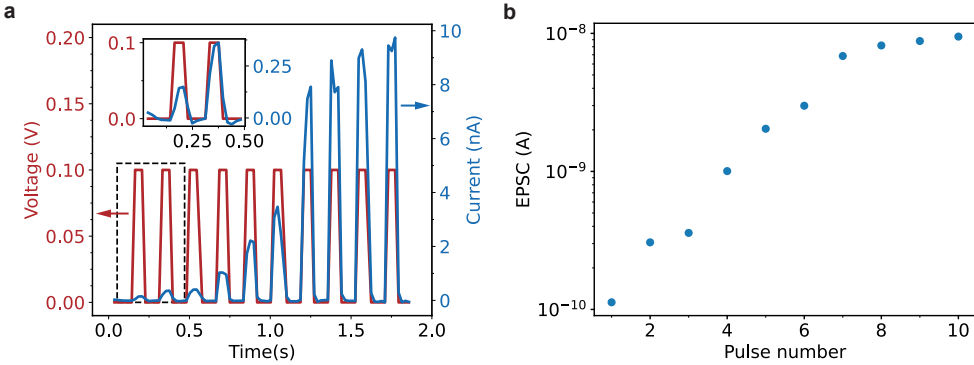


**Figure 2.4:** Performance characteristics of the artificial synapse. **(a)** Pulsed I-V measurements with 0.1 V, 55 ms pulses. An increase in the conductance of 2 orders of magnitude is measured between the first and tenth pulse. The inset highlights the first two pulses of the measurement in the dotted rectangle where approximately 640 fJ of energy is consumed to double the output current. **(b)** Average excitatory postsynaptic current (EPSC) at each of the spikes in **(a)**.

currents measured for the longer pulses (Figure 2.3c). Both the exponential increase of the current with each successive pulse,[45] and the fact that not each pulse brings about the same relative increase in the output current are expected for a memristive device where the inherently stochastic growth of a filament causes changes in the conductance.[49] Moreover, the figure again highlights that several conductive states can be accessed between the  $S_{OFF}$  and  $S_{ON}$  state by applying consecutive voltage pulses to the device. Although artificial synapses based on other materials have shown a larger number of accessible states,[20] our device still demonstrates the analog conductance changes that are reminiscent of biological synapses.[40, 48]

The inset of Figure 2.4a and the first two datapoints in Figure 2.4b show that the conductance of the synapse is approximately doubled in the second pulse. To calculate the energy consumption  $E$  of this doubling of the conductance change we take the product of the measured current  $I$ , applied voltage  $V$  and pulse duration  $t$ ,  $E = I \times V \times t$ , yielding an energy consumption of 640 fJ. Considering the large two-fold increase in the conductance, we expect that a further decrease of the energy consumption is possible by decreasing the pulse duration or magnitude of the voltage. The energy consumption is approaching values measured for biological synapses, which is especially promising in our scalable device architecture that could allow for the fabrication of entire microscopic artificial neural networks on a chip.

### 2.2.3 Performance Comparison

Femtojoule energy consumptions have been reported in previous work on macroscale halide perovskite artificial synapses,[43, 50, 51] but in those cases the energy consumption of the read pulses was considered and not of the conductance change itself, as we do here. In the final network the energy consumption of the conductance update will be a significantly larger contributor to the total energy consumption of the synapse compared to the read pulse.[12] In addition the energy consumption of a read pulse can be made arbitrarily small by applying a pulse with the shortest possible time and voltage amplitude. We therefore think it is more appropriate to consider the energy consumption of the conductance update when assessing the energy consumption of the synapse. We are aware of only one work where a lower energy consumption, of tens of femtojoules, was reported for a conductance change of a halide perovskite synapse.[52] However, in this work devices were fabricated with a lateral architecture, which is not suitable to achieve high device densities on the final chip.[38] Moreover, the distance between the electrodes in this work was 100  $\mu\text{m}$ . Downscaling of these devices for high device densities on a chip will require a smaller distance between the electrodes, which will likely increase the current and therefore energy consumption of the devices significantly.[53]

Energy consumptions of conductance changes in the femtojoule range have been reported for memristive devices based on filament growth in metal oxides,[17] phase change materials[19] and ferroelectrics[22] as well. However, device areas were significantly smaller in these earlier reports already. Assuming a linear decrease of the energy consumption with decreasing device area, we estimate that for similar device areas we can reach orders of magnitude lower energy consumptions with our device architecture, as illustrated by Figure 2.5a. Only three-terminal transistor versions of artificial synapses based on doping of an organic semiconductor have been reported to reach significantly lower energy consumptions for a given device area.[53, 54] Nevertheless, for these devices typically only the drain-source current is considered when calculating the energy consumption of the synapse, while the gate-source current due to leakage currents and capacitive charging is ignored. Taking into account this extra contribution to the energy consumption of the device would likely give significantly larger energy consumptions of these synapses. Apart from that, the three-terminal architecture is less scalable due to the incompatibility with high density crossbar arrays, unlike the simpler two-terminal architecture of the synapse presented here.[23, 24] Moreover, the organic artificial synapses only achieved  $S_{ON}$  to  $S_{OFF}$  ratios of up to 1 order of magnitude,[53, 54] while the synapse in our work reaches  $S_{ON}$  to  $S_{OFF}$  ratios of 3 to 5 orders of magnitude. In fact, the  $S_{ON}$  to  $S_{OFF}$  ratio we report here is among the highest of those reported for energy-efficient artificial

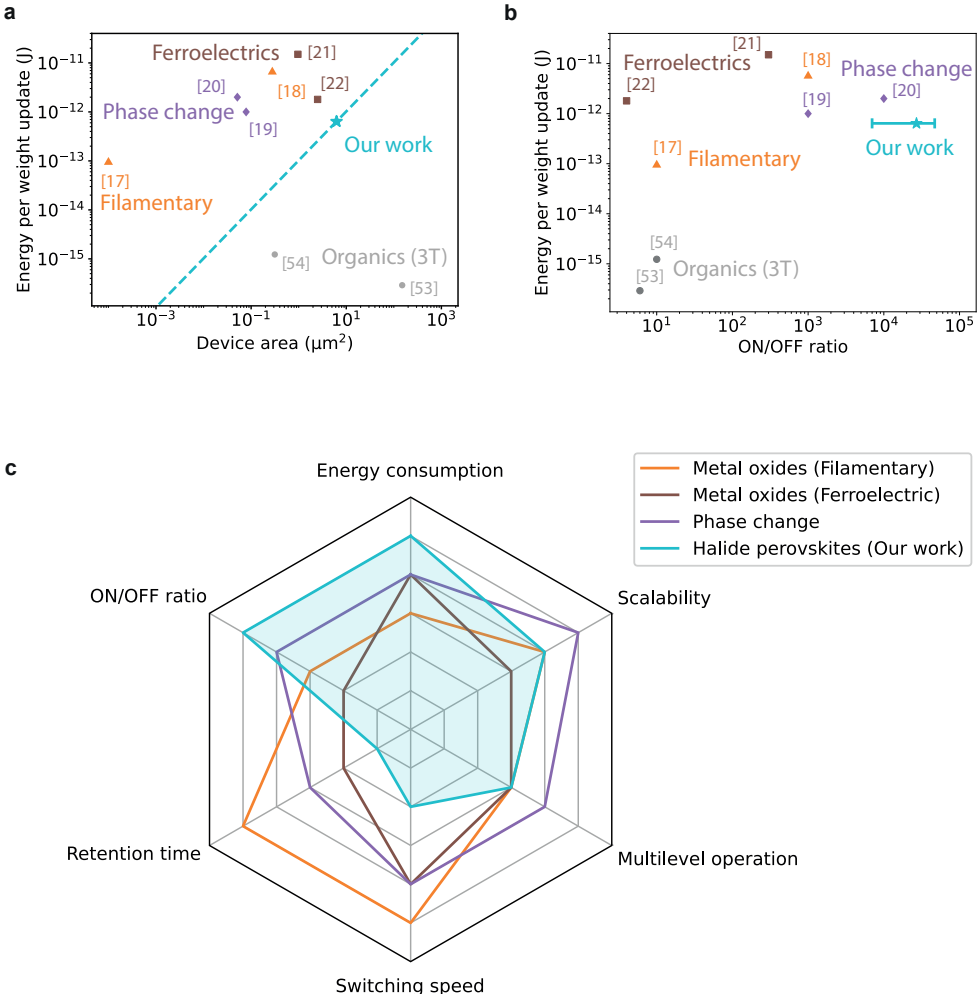


**Figure 2.5:** Comparison of the halide perovskite-based artificial synapse with low-energy consumption artificial synapses based on other materials. Energy efficiency with respect to (a) the device area and (b) ON/OFF ratio of the synapse compared to values reported in previous work. The error bar represents one standard deviation. (c) Comparison of the halide perovskite-based artificial synapse with two-terminal low-energy consumption artificial synapses based on other materials in terms of several key characteristics of artificial synapses. Section 2.C of the Appendix explains how the figure was compiled.

synapses, as can be seen in Figure 2.5b. This high  $S_{ON}$  to  $S_{OFF}$  ratio is important for the accuracy of computation, in particular for further downscaled devices with lower operating currents.[24]

It should be noted that crosstalk between devices could occur with our current device layout if devices are implemented in high density. However, we show in Section 2.B of the Appendix that lateral devices with a 90 nm distance between the electrodes do not show the same changes in the resistance over orders of magnitude. Hence, crosstalk should not be an issue for lateral distances of at least 90 nm between devices.

Figure 2.5c compares the performance characteristics of the artificial synapse presented in this work with two-terminal artificial synapses based on the other materials presented in Figure 2.5a and Figure 2.5b. Compared to the previously reported synapses, the artificial synapse presented in this work excels in terms of energy consumption and its simultaneously high ON/OFF ratio. The halide perovskite synapse has a switching speed on the order of tens of milliseconds and a retention time of tens of seconds. As efficient processing of data by neuromorphic hardware requires synapses with switching speeds and state retention times that are well-matched to those of the incoming data,[14, 55] these synapses are well suited for processing input signals such as speech or gestures that are received at a low rate.[56] Moreover, memristive elements with a large range of time constants for switching and state retention are required to design neuromorphic circuits that efficiently emulate the different forms of plasticity in the brain and to enable both learning and remembering of information by the same network.[12, 25, 26, 56] The synapse we present here therefore nicely complements metal oxide resistive switching,[17, 18] phase change[19, 20] and ferroelectric[21, 22] synapses for which faster switching speeds and longer retention times were reported.

## 2.3 Conclusion

In conclusion, we have described an artificial synapse with an energy consumption as low as 640 fJ, high ON/OFF ratio, with time constants for switching and state retention that are similar to those of biological synapses and that are complementary to existing downscaled artificial synapses based on other materials. Additionally, the synapse retained the low switching voltages and large conductance changes when scaled down, which proves that halide perovskite based artificial synapses can be scaled effectively at least to the microscale. This device is enabled by a UV-lithography procedure to fabricate back-contacted halide perovskite artificial synapses on the microscale. The back-contacted architecture allows deposition of the halide perovskite material in the

final step and thereby prevents degradation of the perovskite layer. Further downscaling of the device might reduce the energy consumption even further, potentially making the halide perovskite synapse the most energy efficient of all existing two-terminal devices. Moreover, the large conductance changes up to five orders of magnitude, large resistance up to hundreds of megaohms combined with the low 100 mV operating voltage and simple two-terminal architecture make the synapse promising for integration in dense crossbar arrays.

## 2.4 Materials and Methods

### 2.4.1 Materials

Si wafers were purchased from Siegert Wafer.  $\text{PbI}_2$  (99.99%) was purchased from TCI. Methylammonium iodide (MAI) was purchased from Solaronix. Anhydrous DMF and chlorobenzene were purchased from Sigma-Aldrich. 950 PMMA A8 was purchased from Kayaku Advanced Materials. All materials were used without further purification.

### 2.4.2 Fabrication of the back-contacted artificial synapse

Devices were fabricated on Si wafers with a 100 nm thermal oxide layer. Gold bottom electrodes were patterned on the wafer with a lift-off procedure with MA-N1410 photoresist. UV exposure with a Süss MA6/BA6 mask aligner was followed by development in MA-D533/s. A 5 nm Cr adhesion layer and an 80 nm Au electrode layer were deposited on the patterned resist by e-beam physical vapor deposition. Lift-off was then performed by soaking in acetone for one hour. A 60 nm  $\text{SiO}_2$  was deposited from a  $\text{O}_2$  and  $\text{SiH}_4$  gas mixture using ICPCVD in an Oxford PlasmaPro100 ICPCVD system. Gold top contacts were patterned using the same procedure as for the bottom electrodes. After patterning of the top electrodes, the  $\text{SiO}_2$  layer was etched in an Oxford Plasmalab 80 Plus system with an Ar and  $\text{CHF}_3$  gas mixture, using the top electrodes as a hardmask.

Inside a nitrogen filled glovebox ( $< 0.5$  ppm  $\text{O}_2$  and water), a stoichiometric mixture of  $\text{PbI}_2$  and MAI was dissolved in DMF to obtain a 40 wt%  $\text{MAPbI}_3$  precursor. The precursor was spin coated over the electrodes at 4000 rpm for 30 seconds in the same glovebox. Chlorobenzene was added as an antisolvent after 3 seconds of spinning. Directly after spin coating, the samples were annealed at 100 °C for 10 minutes. The 950 PMMA A8 solution was spin coated on top of the halide perovskite at 3000 rpm for 45 seconds, followed by a 5 minute bake at 100 °C.

### 2.4.3 Fabrication of lateral devices

Lateral devices were fabricated following the same procedure as for the back-contacted devices, but using an e-beam lithography procedure to pattern an ARP 6200 resist layer. A Raith Voyager lithography system was used to pattern the electrodes, wires and contact pads. The same subsequent metallization, lift-off and halide perovskite spin coating procedures were followed as for the back-contacted devices.

### 2.4.4 MAPbI<sub>3</sub> film characterization

X-ray diffraction measurements were performed on a Bruker D2 PHASER with a 1.54184 Å Cu K<sub>α</sub> source using a  $2\theta = 0.025^\circ$  step size and a 0.100 second exposure time per step. SEM images were taken on a FEI Verios 460 with a 5.00 kV acceleration voltage and a 100 pA beam current.

### 2.4.5 Electrical characterization

I-V curves between -0.2 and 0.2 V were measured with a Keithley 4200A-SCS Parameter Analyzer. Voltage pulses were applied with a Keysight B2902A Precision Source/Measure Unit. Pulses of 100 mV and a 80 to 55 ms pulse width were applied to change the conductivity of the device. For retention time measurements, 600 ms 1 mV pulses were applied after setting the conductivity of the device to read out the conductive state.

# Appendix

2

## 2.A Additional information

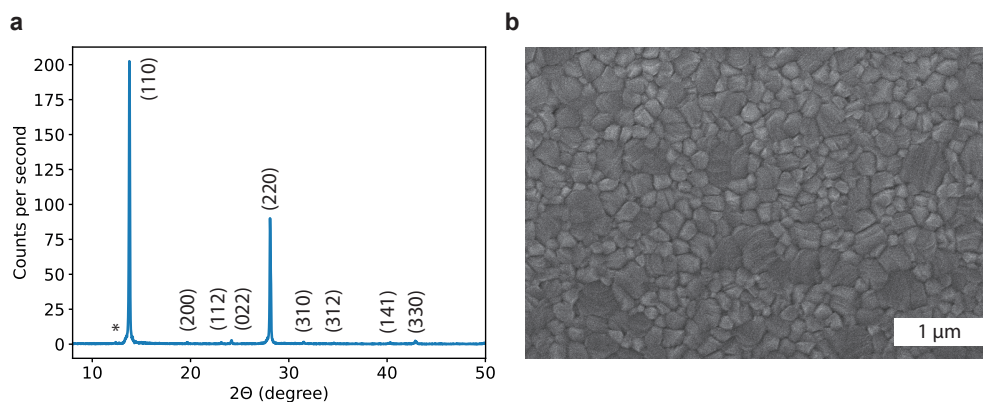


**Figure 2.A.1:** Characterization of the spin-coated MAPbI<sub>3</sub> film. **(a)** XRD pattern of the film. Each peak is annotated with the assigned crystal plane of the MAPbI<sub>3</sub> lattice. We attribute the peak indicated with the asterisk to the (001) plane of PbI<sub>2</sub>. **(b)** SEM image of the film, indicating that the crystallites in the film are between 100 and 500 nm in diameter.

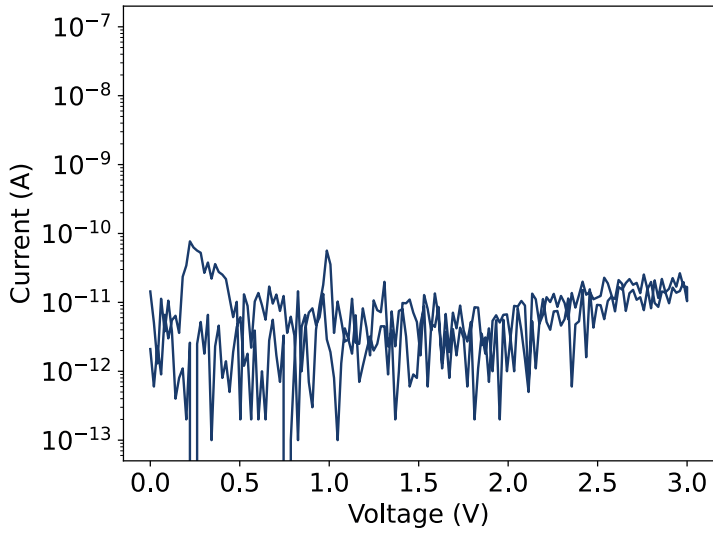


**Figure 2.A.2:** I-V sweep between 0 and 3 V of the device without a perovskite layer. The current remains at the resolution limit of the measurement setup over the whole voltage range.

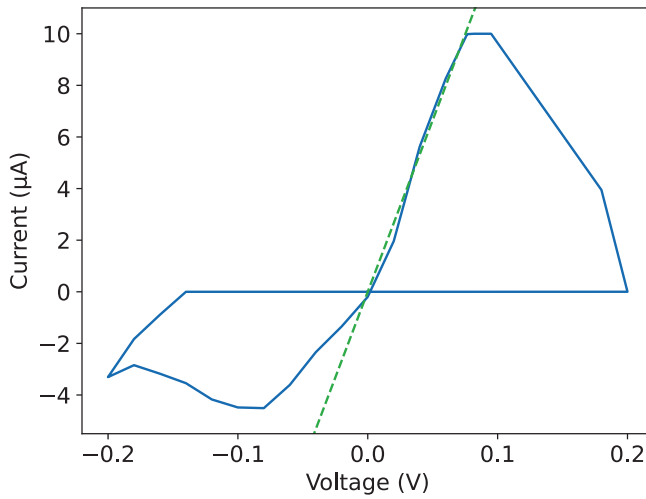


**Figure 2.A.3:** The I-V sweep of cycle 8 in Figure 2.3a, plotted on a linear scale. The region from the backwards sweep after the conductance change was fitted with Ohm's law. The obtained fit corresponded to a conductance of  $133 \mu\text{S}$  and is shown as the dashed green line. The fact that the region is described well by Ohm's law ( $R^2 = 0.99$ ) suggests that the conductance change is caused by the formation of a conductive filament in the perovskite film.

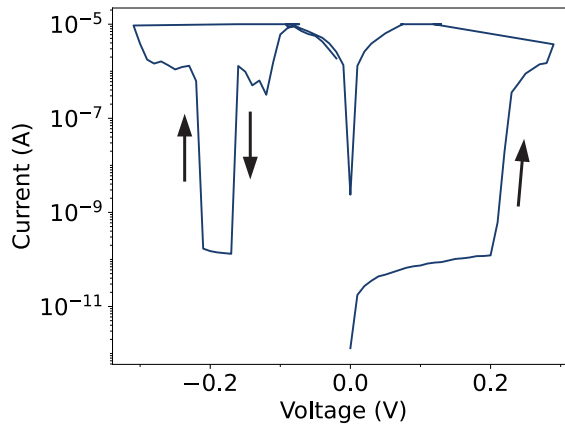


**Figure 2.A.4:** I-V sweep of the device with higher voltage amplitudes compared to Figure 2.3 of the main text. After setting and resetting the device at voltages similar to those in Figure 2.3, the conductance of the device increases rapidly for the negative sweeping direction as the voltage is further increased in the negative direction.

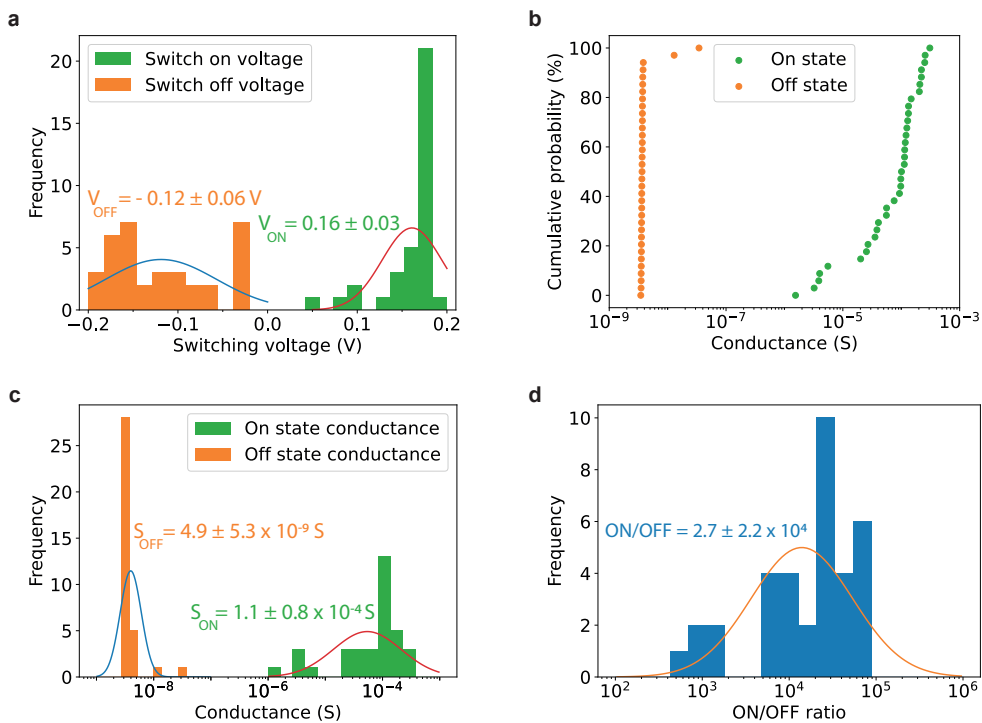


**Figure 2.A.5:** Statistical analysis of the conductance changes of the synapse, based on the 35 I-V curves in Figure 2.3a in the main text. **(a)** Histogram of the voltages at which the current switches to over ( $V_{ON}$ ) or below ( $V_{OFF}$ )  $10^{-8}$  A, with the corresponding fit to a normal distribution, mean and standard deviation. The cumulative probability **(b)** and the histogram, with fits to a log-normal distribution, the mean and standard deviation **(c)** of the different  $S_{OFF}$  and  $S_{ON}$  states. **(d)** A histogram of the  $S_{ON}/S_{OFF}$  ratio, with a fit to a log-normal distribution, the mean and standard deviation.

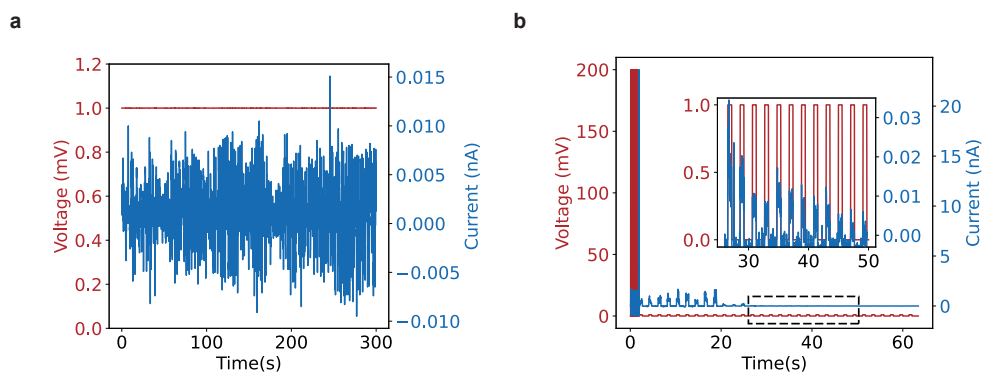


**Figure 2.A.6:** Retention time measurements of the synapse. **(a)** A constant potential of 1 mV is applied to the synapse for 300 seconds, which does not lead to any measurable change in the conductance. **(b)** Pulsed measurement where the conductance of the halide perovskite artificial synapse is tracked by applying periodic 1 mV pulses to the device, after an initial 200 mV pulse train to set the device in the  $S_{ON}$  state. The inset shows the pulsed measurement in the dotted rectangle after the initial 25 seconds.

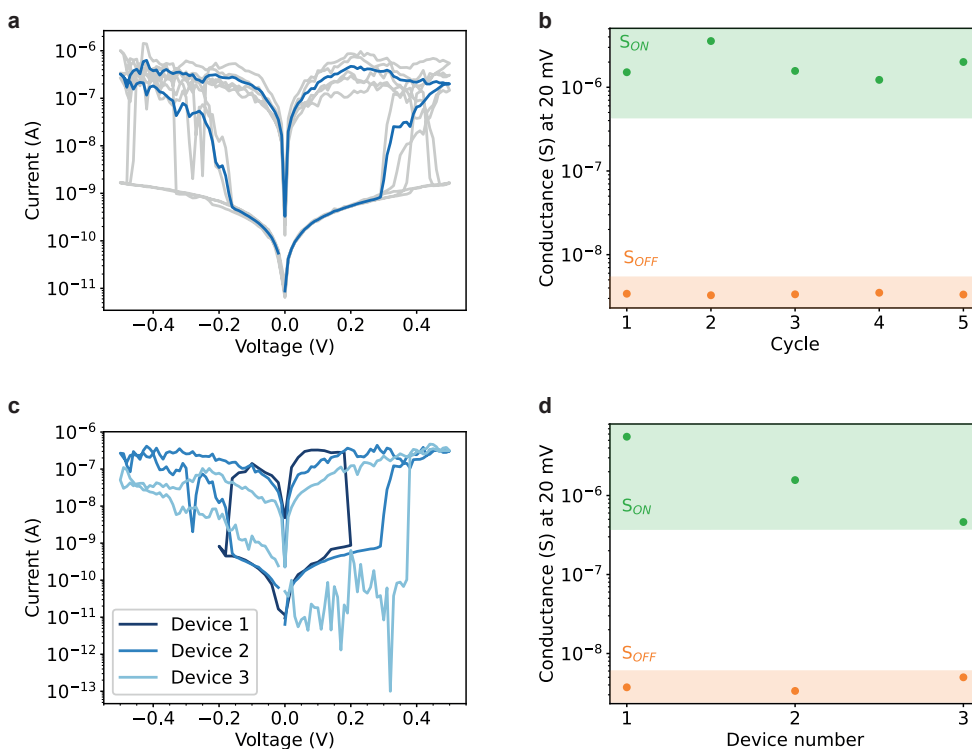


**Figure 2.A.7:** I-V curves of artificial synapses from different batches. **(a)** The average (blue) of five I-V curves (grey) measured from a device different to the one in the main text. The I-V curves demonstrate a similar rapid increase in the current at approximately 300 - 400 mV as shown in Figure 2.3a. **(b)** The conductance in the forward ( $S_{OFF}$ ) and backward ( $S_{ON}$ ) sweep, calculated from the current measured at 0.02 V in the I-V sweeps in **(a)**. **(c)** I-V curves of three devices from different batches and **(d)** the conductance in the forward ( $S_{OFF}$ ) and backward ( $S_{ON}$ ) sweep, calculated from the current measured at 0.02 V for each of the three devices. All curves show a similar rapid increase in the current, with an onset between approximately 200 and 350 mV, with a large conductance change of two to three orders of magnitude.

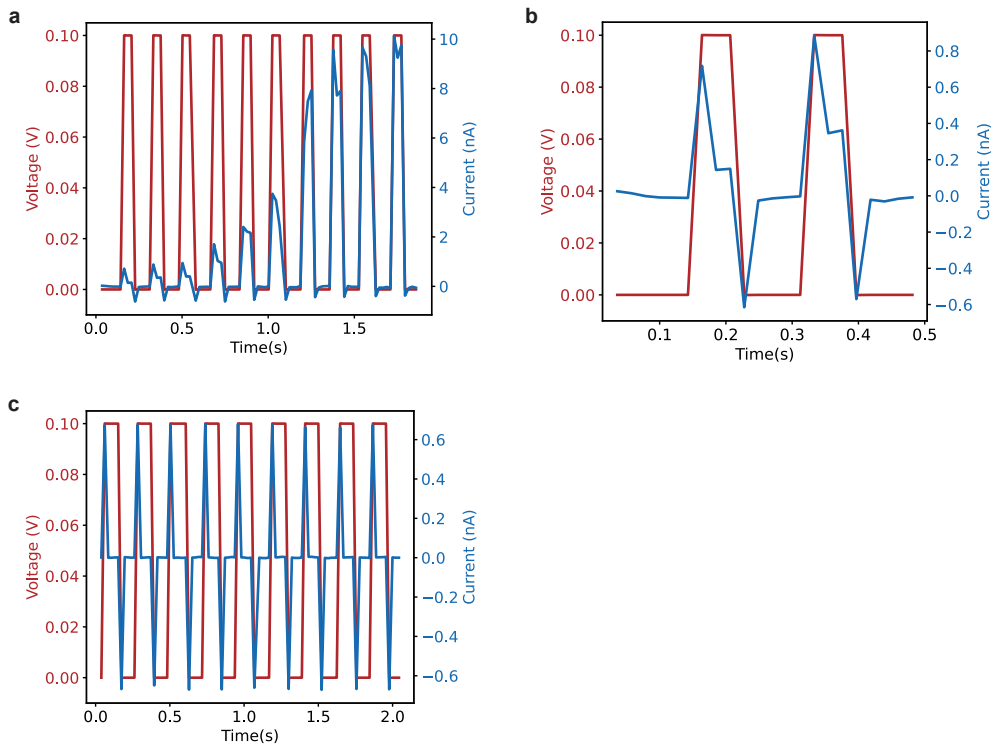


**Figure 2.A.8:** Uncorrected pulsed I-V data. **(a)** The full pulsed measurement, consisting of ten consecutive 0.1 V pulses of 55 ms in duration. **(b)** The first two pulses of **(a)**. **(c)** Pulsed measurement without contacting the sample.

## 2.B Considering crosstalk distance for high integration densities

2

At high integration density, crosstalk between neighboring devices might occur by formation of a conductive filament between top and bottom electrodes of two different, closely spaced devices. Taking into account that no switching occurs at 1 mV for a distance between the electrodes of 60 nm, it follows that there is no cross-talk of this type between devices so long as the electric field strength stays below approximately 17 kV/m. Assuming a uniform electric field between the electrodes so that  $E = \frac{V}{d}$ , where  $E$  is the electric field strength,  $V$  is the applied voltage and  $d$  is the distance between the electrodes, and assuming an operating voltage of 100 mV for each individual device, this implies that the distance between the devices would have to be 6  $\mu\text{m}$ , or 100 times the distance between the electrodes of an individual device to prevent crosstalk. However, this consideration is relevant for vertical integration, yet in practical devices the horizontal direction is more relevant for potential crosstalk.

To investigate horizontal crosstalk for densely integrated devices, we fabricated a lateral electrode device with 1  $\mu\text{m}$  wide electrodes with a gap size of 90 nm (Figure 2.B.1a), comparable to the distance between the electrodes of the device in the main text. Interestingly, hysteresis was observed for the device, as shown in Figure 2.B.1b, but this hysteresis was similar to the hysteresis that is typically reported for halide perovskite solar cells.[57] No abrupt changes in the current over orders of magnitude was observed, even when applying potentials up to 5 V. The difference in the response between horizontally and vertically oriented devices might be explained by the preferential migration of ions at grain boundaries,[58] and the consequential preferential formation of conductive filaments at these grain boundaries.[59] Although more measurements are required to confirm the limit of the lateral distance between devices to avoid crosstalk, this measurement shows that crosstalk over a distance of 90 nm would not be significant compared to the resistance changes of the device presented in the main text. At 90 nm distance, very high device densities can be reached.

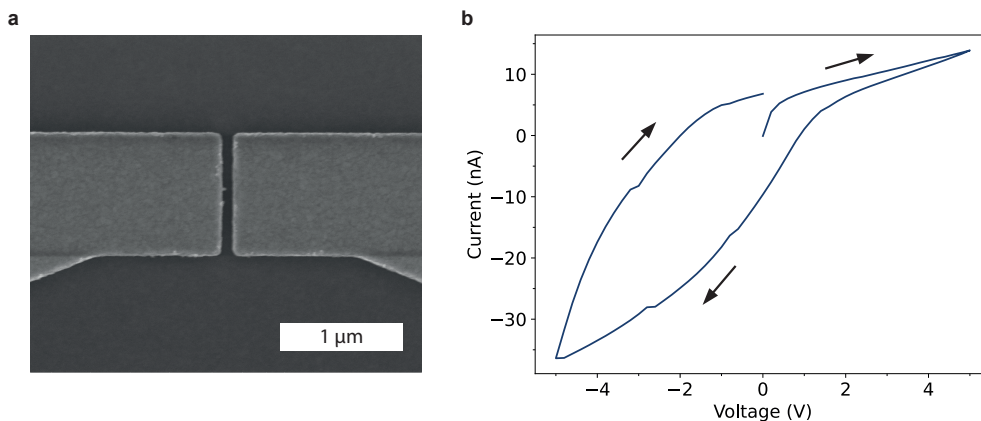


**Figure 2.B.1:** I-V sweep of a lateral device. (a) SEM image of the lateral electrodes with a width of 1 μm and a 90 nm gap. (b) I-V sweep of the lateral device after spin coating of MAPbI<sub>3</sub> and PMMA. No abrupt changes of the resistance over orders of magnitude is measured for the lateral device, even when applying up to 5 V.

## 2.C Compilation of Figure 2.5

To indicate the performance of our halide perovskite artificial synapse, we compared the energy consumption, ON/OFF ratio, retention time, switching speed and multilevel operation from the references in Figure 2.5a and b on energy-efficient artificial synapses with those of our synapse. The data we used to score the different devices is summarized in Table 2.C.1. For Figure 2.5a and b in the main text, we plot the energy consumptions listed in Table 2.C.1 with respect to the reported device area and ON/OFF ratio. The exact device area of our device is difficult to define due to the arc-shaped electric field drop indicated in Figure 2.1, which is why we take the  $2.5 \times 2.5 \mu\text{m}^2$  footprint of our device as an estimate. A linear decrease in energy consumption is expected as the device area is decreased further, due to the reduction in operating current. We indicate this linear decrease with the dashed line in Figure 2.5a. We note that taking a larger area for our device area to account for an electric field that extends further out from the electrodes would shift the data point for our device further to the right in the figure, without changing the trend in decreasing energy consumption with device area.

In Figure 2.5c we compare our device performance to that of the devices reported in the references in Figure 2.5a and b. Retention times were not listed in the case of the phase change and ferroelectric devices. We therefore estimated the retention time based on other works on the same materials. Ge<sub>2</sub>Sb<sub>2</sub>Te<sub>5</sub>-based phase change devices show similar retention times as the filamentary-type devices for the fully off and on states. However, there is typically considerable drift in the conductance of intermediate states

at much shorter timescales of tens to hundreds of seconds.[60] Their retention time was therefore scored lower than that of the filamentary type devices. For the ferroelectric devices, previous retention times on the order of  $10^4$  seconds at room temperature were reported.[61]

To assess the scalability of the different devices, we considered that the filamentary and phase change devices have already been implemented with sizes below a square micron. The filamentary-type devices were scored lower because of the relatively high ON-state conductance, which limits the maximum amount of devices that can be operated in parallel in crossbar arrays. The ferroelectric devices were scored lower because of concerns about the depolarization of oxide perovskite ferroelectric layers below a critical thickness,[62] as well as the non-uniform polarization on the nanoscale for  $\text{HfO}_2$ -based devices.[63] We scored our device based on the high resistance, ease of further down-scaling by further reducing the thickness of the electrodes and our initial data showing that the devices can be fabricated with a distance between devices below 100 nm without introducing significant crosstalk.

**Table 2.C.1:** Data on which the radar chart in Figure 2.5c in the main text is based.

| Device type    | Energy consumption | ON/OFF ratio | Retention time          | Switching speed | Number of accessible states | Reference |
|----------------|--------------------|--------------|-------------------------|-----------------|-----------------------------|-----------|
| Filamentary    | 100 fJ             | 10           | $\geq 10^5$ s at 250 °C | 10 – 100 ns     | 2                           | [17]      |
| Filamentary    | 6 pJ               | $10^3$       | $\geq 7200$ s at 100 °C | 10 – 30 ns      | 10                          | [18]      |
| Phase change   | 1 pJ               | $10^3$       | not listed              | 250 ns          | $\sim 100$                  | [19]      |
| Phase change   | 2 – 50 pJ          | $10^4$       | not listed              | 50 ns           | $\sim 100$                  | [20]      |
| Ferroelectrics | $\sim 15$ pJ       | 300          | not listed              | 10 – 200 ns     | $\sim 100$                  | [21]      |
| Ferroelectrics | 1.8 pJ             | 5            | not listed              | 100 ns          | $\sim 10$                   | [22]      |
| Our work       | 640 fJ             | $10^4$       | 30 s                    | 55 ms           | $\sim 10$                   | -         |

## References

1. Silver, D. *et al.* Mastering the game of Go without human knowledge. *Nature* **550**, 354–359 (2017).
2. Vinyals, O. *et al.* Grandmaster level in StarCraft II using multi-agent reinforcement learning. *Nature* **575**, 350–354 (2019).
3. OpenAI *et al.* *Dota 2 with Large Scale Deep Reinforcement Learning* 2019. arXiv: 1912.06680 [cs.LG].
4. McKinney, S. M. *et al.* International evaluation of an AI system for breast cancer screening. *Nature* **577**, 89–94 (2020).
5. He, K., Zhang, X., Ren, S. & Sun, J. *Delving Deep into Rectifiers: Surpassing Human-Level Performance on ImageNet Classification in 2015 IEEE International Conference on Computer Vision (ICCV)* (IEEE, Santiago, Chile, 2015), 1026–1034.
6. Jumper, J. *et al.* Highly accurate protein structure prediction with AlphaFold. *Nature* **596**, 583–589 (2021).
7. Katz, D. M., Bommarito, M. J., Gao, S. & Arredondo, P. GPT-4 Passes the Bar Exam. *Philosophical Transactions of the Royal Society A* **382**, 20230254 (2024).
8. Nori, H., King, N., McKinney, S. M., Carignan, D. & Horvitz, E. *Capabilities of GPT-4 on Medical Challenge Problems* 2023. arXiv: 2303.13375 [cs.CL].
9. Amodei, D. & Hernandez, D. *AI and compute* <https://openai.com/research/ai-and-compute>. (accessed Aug. 16, 2023)
10. Vegas, M. *Azure previews powerful and scalable virtual machine series to accelerate generative AI* <https://azure.microsoft.com/en-us/blog/azure-previews-powerful-and-scalable-virtual-machine-series-to-accelerate-generative-ai/>. (accessed Aug. 16, 2023)
11. Kety, S. S. & Schmidt, C. F. The nitrous oxide method for the quantitative determination of cerebral blood flow in man: theory, procedure and normal values. *Journal of Clinical Investigation* **27**, 476–483 (1948).
12. Davies, M. *et al.* Loihi: A Neuromorphic Manycore Processor with On-Chip Learning. *IEEE Micro* **38**, 82–99 (2018).
13. Merolla, P. A. *et al.* A million spiking-neuron integrated circuit with a scalable communication network and interface. *Science* **345**, 668–673 (2014).

14. Chicca, E., Stefanini, F., Bartolozzi, C. & Indiveri, G. Neuromorphic electronic circuits for building autonomous cognitive systems. *Proceedings of the IEEE* **102**, 1367–1388 (2014).
15. Qiao, N., Mostafa, H., Corradi, F., Osswald, M., Stefanini, F., Sumislawska, D. & Indiveri, G. A reconfigurable on-line learning spiking neuromorphic processor comprising 256 neurons and 128K synapses. *Frontiers in Neuroscience* **9**, 141 (2015).
16. Laughlin, S. B., De Ruyter Van Steveninck, R. R. & Anderson, J. C. The metabolic cost of neural information. *Nature Neuroscience* **1**, 36–41 (1998).
17. Govoreanu, B. *et al.*  $10 \times 10 \text{ nm}^2$  Hf/HfOx crossbar resistive RAM with excellent performance, reliability and low-energy operation in 2011 International Electron Devices Meeting (2011), 31.6.1–31.6.4.
18. Yu, S., Wu, Y., Jeyasingh, R., Kuzum, D. & Wong, H.-S. P. An Electronic Synapse Device Based on Metal Oxide Resistive Switching Memory for Neuromorphic Computation. *IEEE Transactions on Electron Devices* **58**, 2729–2737 (2011).
19. Ambrogio, S., Ciocchini, N., Laudato, M., Milo, V., Pirovano, A., Fantini, P. & Ielmini, D. Unsupervised Learning by Spike Timing Dependent Plasticity in Phase Change Memory (PCM) Synapses. *Frontiers in Neuroscience* **10**, 56 (2016).
20. Kuzum, D., Jeyasingh, R. G. D., Lee, B. & Wong, H.-S. P. Nanoelectronic Programmable Synapses Based on Phase Change Materials for Brain-Inspired Computing. *Nano Letters* **12**, 2179–2186 (2012).
21. Chanthbouala, A. *et al.* A ferroelectric memristor. *Nature Materials* **11**, 860–864 (2012).
22. Chen, L., Wang, T.-Y., Dai, Y.-W., Cha, M.-Y., Zhu, H., Sun, Q.-Q., Ding, S.-J., Zhou, P., Chua, L. & Zhang, D. W. Ultra-low power  $\text{Hf}_{0.5}\text{Zr}_{0.5}\text{O}_2$  based ferroelectric tunnel junction synapses for hardware neural network applications. *Nanoscale* **10**, 15826–15833 (2018).
23. Li, C. *et al.* Analogue signal and image processing with large memristor crossbars. *Nature Electronics* **1**, 52–59 (2018).
24. Agarwal, S., Plimpton, S. J., Hughart, D. R., Hsia, A. H., Richter, I., Cox, J. A., James, C. D. & Marinella, M. J. Resistive memory device requirements for a neural algorithm accelerator in 2016 International Joint Conference on Neural Networks (IJCNN) (2016), 929–938.
25. Zenke, F., Agnes, E. J. & Gerstner, W. Diverse synaptic plasticity mechanisms orchestrated to form and retrieve memories in spiking neural networks. *Nature Communications* **6**, 6922 (2015).

26. Payvand, M., Nair, M. V., Müller, L. K. & Indiveri, G. A neuromorphic systems approach to in-memory computing with non-ideal memristive devices: from mitigation to exploitation. *Faraday Discussions* **213**, 487–510 (2019).
27. Xiao, Z., Yuan, Y., Shao, Y., Wang, Q., Dong, Q., Bi, C., Sharma, P., Gruverman, A. & Huang, J. Giant switchable photovoltaic effect in organometal trihalide perovskite devices. *Nature Materials* **14**, 193–197 (2015).
28. Xiao, Z. & Huang, J. Energy-efficient hybrid perovskite memristors and synaptic devices. *Advanced Electronic Materials* **2**, 1600100 (2016).
29. Yan, K., Peng, M., Yu, X., Cai, X., Chen, S., Hu, H., Chen, B., Gao, X., Dong, B. & Zou, D. High-performance perovskite memristor based on methyl ammonium lead halides. *Journal of Materials Chemistry C* **4**, 1375–1381 (2016).
30. Sakhatskyi, K. *et al.* Assessing the Drawbacks and Benefits of Ion Migration in Lead Halide Perovskites. *ACS Energy Letters* **7**, 3401–3414 (2022).
31. Gonzales, C. & Guerrero, A. Mechanistic and Kinetic Analysis of Perovskite Memristors with Buffer Layers: The Case of a Two-Step Set Process. *The Journal of Physical Chemistry Letters* **14**, 1395–1402 (2023).
32. Xie, Z. *et al.* Unraveling Dual Operational Mechanisms in an Air-Stable All Inorganic Perovskite for Nonvolatile Memory and Neuromorphic Computing. *ACS Energy Letters* **9**, 948–958 (2024).
33. Zhang, Y. *et al.* Three-dimensional perovskite nanowire array-based ultrafast resistive RAM with ultralong data retention. *Science advances* **7**, eabg3788 (2021).
34. Lin, C. H., Cheng, B., Li, T. Y., Retamal, J. R. D., Wei, T. C., Fu, H. C., Fang, X. & He, J. H. Orthogonal Lithography for Halide Perovskite Optoelectronic Nanodevices. *ACS Nano* **13**, 1168–1176 (2019).
35. Shi, Y., Pan, C., Chen, V., Raghavan, N., Pey, K., Puglisi, F., Pop, E., Wong, H.-S. & Lanza, M. Coexistence of volatile and non-volatile resistive switching in 2D h-BN based electronic synapses in 2017 IEEE International Electron Devices Meeting (IEDM) (2017), 5–4.
36. Yi, W., Tsang, K. K., Lam, S. K., Bai, X., Crowell, J. A. & Flores, E. A. Biological plausibility and stochasticity in scalable VO<sub>2</sub> active memristor neurons. *Nature Communications* **9**, 4661 (2018).
37. Pi, S., Li, C., Jiang, H., Xia, W., Xin, H., Yang, J. J. & Xia, Q. Memristor crossbar arrays with 6-nm half-pitch and 2-nm critical dimension. *Nature Nanotechnology* **14**, 35–39 (2019).
38. Lanza, M. *et al.* Recommended Methods to Study Resistive Switching Devices. *Advanced Electronic Materials* **5**, 1–28 (2019).

39. Hwang, B. & Lee, J.-S. A Strategy to Design High-Density Nanoscale Devices utilizing Vapor Deposition of Metal Halide Perovskite Materials. *Advanced Materials* **29**, 1701048 (2017).
40. Lynch, G., Larson, J., Kelso, S., Barrionuevo, G. & Schottler, F. Intracellular injections of EGTA block induction of hippocampal long-term potentiation. *Nature* **305**, 719–721 (1983).
41. McKenna, B., Troughton, J. R., Watson, T. M. & Evans, R. C. Enhancing the stability of organolead halide perovskite films through polymer encapsulation. *RSC Advances* **7**, 32942–32951 (2017).
42. Sun, Y., Tai, M., Song, C., Wang, Z., Yin, J., Li, F., Wu, H., Zeng, F., Lin, H. & Pan, F. Competition between Metallic and Vacancy Defect Conductive Filaments in a CH<sub>3</sub>NH<sub>3</sub>PbI<sub>3</sub>-Based Memory Device. *Journal of Physical Chemistry C* **122**, 6431–6436 (2018).
43. Tian, H., Zhao, L., Wang, X., Yeh, Y. W., Yao, N., Rand, B. P. & Ren, T. L. Extremely Low Operating Current Resistive Memory Based on Exfoliated 2D Perovskite Single Crystals for Neuromorphic Computing. *ACS Nano* **11**, 12247–12256 (2017).
44. Zhu, X., Lee, J. & Lu, W. D. Iodine vacancy redistribution in organic–inorganic halide perovskite films and resistive switching effects. *Advanced Materials* **29**, 1700527 (2017).
45. Mazady, A. & Anwar, M. Memristor: Part I—The Underlying Physics and Conduction Mechanism. *IEEE Transactions on Electron Devices* **61**, 1054–1061 (2014).
46. Ren, Y., Ma, H., Wang, W., Wang, Z., Xu, H., Zhao, X., Liu, W., Ma, J. & Liu, Y. Cycling-Induced Degradation of Organic–Inorganic Perovskite-Based Resistive Switching Memory. *Advanced Materials Technologies* **4**, 1800238 (2019).
47. Luo, H. *et al.* In Situ Unveiling of the Resistive Switching Mechanism of Halide Perovskite-Based Memristors. *The Journal of Physical Chemistry Letters* **15**, 2453–2461 (2024).
48. Bi, G.-q. & Poo, M.-m. Synaptic Modifications in Cultured Hippocampal Neurons: Dependence on Spike Timing, Synaptic Strength, and Postsynaptic Cell Type. *The Journal of Neuroscience* **18**, 10464–10472 (1998).
49. Jo, S. H., Kim, K.-H. & Lu, W. Programmable Resistance Switching in Nanoscale Two-Terminal Devices. *Nano Letters* **9**, 496–500 (2009).
50. Xu, W., Cho, H., Kim, Y. H., Kim, Y. T., Wolf, C., Park, C. G. & Lee, T. W. Organometal Halide Perovskite Artificial Synapses. *Advanced Materials* **28**, 5916–5922 (2016).
51. Kim, S. I. *et al.* Dimensionality Dependent Plasticity in Halide Perovskite Artificial Synapses for Neuromorphic Computing. *Advanced Electronic Materials* **5**, 1900008 (2019).

52. Gong, J., Yu, H., Zhou, X., Wei, H., Ma, M., Han, H., Zhang, S., Ni, Y., Li, Y. & Xu, W. Lateral Artificial Synapses on Hybrid Perovskite Platelets with Modulated Neuroplasticity. *Advanced Functional Materials* **30**, 2005413 (2020).
53. Zhang, C., Wang, S., Zhao, X., Yang, Y., Tong, Y., Zhang, M., Tang, Q. & Liu, Y. Sub-Femtojoule-Energy-Consumption Conformable Synaptic Transistors Based on Organic Single-Crystalline Nanoribbons. *Advanced Functional Materials* **31**, 2007894 (2021).
54. Xu, W., Min, S. Y., Hwang, H. & Lee, T. W. Organic core-sheath nanowire artificial synapses with femtojoule energy consumption. *Science Advances* **2**, e1501326 (2016).
55. Moradi, S., Qiao, N., Stefanini, F. & Indiveri, G. A Scalable Multicore Architecture With Heterogeneous Memory Structures for Dynamic Neuromorphic Asynchronous Processors (DYNAPs). *IEEE Transactions on Biomedical Circuits and Systems* **12**, 106–122 (2018).
56. Chicca, E. & Indiveri, G. A recipe for creating ideal hybrid memristive-CMOS neuromorphic processing systems. *Applied Physics Letters* **116**, 120501 (2020).
57. Chen, B., Yang, M., Priya, S. & Zhu, K. Origin of J–V Hysteresis in Perovskite Solar Cells. *The Journal of Physical Chemistry Letters* **7**, 905–917 (2016).
58. Shao, Y. *et al.* Grain boundary dominated ion migration in polycrystalline organic-inorganic halide perovskite films. *Energy & Environmental Science* **9**, 1752–1759 (2016).
59. Lanza, M., Bersuker, G., Porti, M., Miranda, E., Nafria, M. & Aymerich, X. Resistive switching in hafnium dioxide layers: Local phenomenon at grain boundaries. *Applied Physics Letters* **101**, 193502 (2012).
60. Boniardi, M., Ielmini, D., Lavizzari, S., Lacaíta, A. L., Redael, A. & Pirovano, A. Statistics of Resistance Drift Due to Structural Relaxation in Phase-Change Memory Arrays. *IEEE Transactions on Electron Devices* **57**, 2690–2696 (2010).
61. Cheema, S. S., Shanker, N., Hsu, C.-H., Datar, A., Bae, J., Kwon, D. & Salahuddin, S. One Nanometer HfO<sub>2</sub>-Based Ferroelectric Tunnel Junctions on Silicon. *Advanced Electronic Materials* **8**, 2100499 (2022).
62. Junquera, J. & Ghosez, P. Critical thickness for ferroelectricity in perovskite ultrathin films. *Nature* **422**, 506–509 (2003).
63. Chouprik, A., Zakharchenko, S., Spiridonov, M., Zarubin, S., Chernikova, A., Kirtaev, R., Buragohain, P., Gruverman, A., Zenkevich, A. & Negrov, D. Ferroelectricity in Hf<sub>0.5</sub>Zr<sub>0.5</sub>O<sub>2</sub> Thin Films: A Microscopic Study of the Polarization Switching Phenomenon and Field-Induced Phase Transformations. *ACS Applied Materials & Interfaces* **10**, 8818–8826 (2018).



# 3

## Microscale Artificial Neurons

### Abstract

Hardware neural networks could perform certain computational tasks orders of magnitude more energy-efficiently than conventional computers. Artificial neurons are a key component of these networks and are currently implemented with electronic circuits based on capacitors and transistors. However, artificial neurons based on memristive devices are a promising alternative, owing to their potentially smaller size and inherent stochasticity. But despite their promise, demonstrations of memristive artificial neurons have so far been limited. Here we demonstrate a fully on-chip artificial neuron based on microscale electrodes and halide perovskite semiconductors as the active layer. By connecting a halide perovskite memristive device in series with a capacitor, the device demonstrates stochastic leaky integrate-and-fire behavior, with an energy consumption of 20 to 60 pJ per spike, lower than that of a biological neuron. We simulate populations of our neuron and show that the stochastic firing allows the detection of sub-threshold inputs. The neuron can easily be integrated with previously-demonstrated halide perovskite artificial synapses in energy-efficient neural networks.

---

This chapter is based on: De Boer, J. J. & Ehrler, B. Integrated artificial neurons from metal halide perovskites. *Materials Horizons* **12**, 2701–2708 (2025)

### 3.1 Introduction

Artificial intelligence-based systems have seen a rapid increase in their capabilities in a wide range of tasks, such as natural language processing,[1] image recognition,[2, 3] and strategizing.[4, 5] The increase in the performance of these systems is accompanied by an exponential increase in the computational power, and thus the energy consumption.[6] Neuromorphic computing addresses this issue by implementing neural networks in hardware, lowering the required energy by orders of magnitude compared to conventional computers.[7] Neuromorphic chips rely on two main components for computation: artificial neurons, which integrate incoming signals and fire a voltage pulse upon reaching a threshold, and artificial synapses, which determine the connection strength between neurons. Ideally, both components can be integrated into a single chip in a dense arrangement to enable large-scale artificial neural networks. Both the neurons and synapses are typically implemented with electronic circuits composed of transistors and capacitors.[8] On the other hand, implementations that use memristive elements, which change their resistance based on an applied voltage, can be more compact and highly energy efficient, making them an attractive alternative.[9] Much research has gone into developing artificial synapses that directly use the resistance change of a memristive element as a proxy for connection strength.[9–12] Memristive elements also show promise for use in artificial neurons, because of the inherent stochasticity in their resistance changes.[13] This inherent stochasticity of memristive neurons can be leveraged for better signal representation,[14, 15] or more efficient probabilistic computing than would be possible with deterministic neurons.[16] Nonetheless, applying memristive elements in artificial neurons is more complex and has been much less explored compared to their application in synapses.

Here, we demonstrate a simple memristive neuron based on a halide perovskite memristive element. Metal halide perovskites are semiconducting compounds that efficiently conduct both electronic and ionic charge carriers.[17] The efficient ion conduction in halide perovskites readily induces hysteresis, which was previously exploited to make energy-efficient artificial synapses.[18–20] While various halide perovskite artificial synapses have been reported, only one halide perovskite neuron has been experimentally demonstrated before.[21] However, this previous implementation used off-chip circuitry to implement signal integration and neuron-like spiking, making scaling difficult. We connect a microscale volatile halide perovskite memristive device in series with a capacitor. The series capacitor applies a reverse bias on the memristive element after spiking of the neuron, which aids in resetting the memristive element after each spike. This

makes our neuron design more robust against non-reversible resistance changes of the memristive component than designs with a series resistor,[22, 23] or capacitor connected in parallel.[16, 24, 25] Because our design consists of only two components, the neuron is also more easily scalable than implementations that require more complex circuitry besides the memristive element.[14, 26, 27] Moreover, the efficient ion conduction of halide perovskites allows an operating voltage of hundreds of millivolts, lower than in previous memristive neurons which is favorable for low energy consumptions. We fabricate our crosspoint neurons with a previously developed procedure that prevents degradation of the halide perovskite layer during lithography.[19] Our neuron is integrated fully on-chip without the need for external circuitry to emulate neuron functionality. In that way, the device architecture of our halide perovskite memristive device lends itself to further downscaling and the neuron could be easily integrated with halide perovskite artificial synapses that we have demonstrated before to form artificial neural networks with ultralow-energy consumption.[19]

## 3.2 Results and Discussion

### 3.2.1 A volatile resistive switch

Artificial neurons can be fabricated from a resistive switch that shows rapid, highly volatile switching connected in series with a capacitor.[28] Thereby, successive voltage pulses eventually switch the memristive element to the low resistance state, charging the capacitor (firing). Then, the charged capacitor reverse-biases the memristive element, switching it off again. We use a resistive switch that comprises of methylammonium lead triiodide ( $\text{MAPbI}_3$ ) as the active layer, and a gold and silver contact as the bottom and top contact respectively (Figure 3.1a and Methods Section 3.4). The  $2.5 \mu\text{m}$  wide contacts are arranged in an overlapping back-contact geometry, where the two contacts are orthogonally placed on top of each other with an insulating spacer layer of  $\text{SiO}_2$  in between. All lithographic processing steps are therefore performed before the perovskite deposition. The compact, dense structure lends itself to downscaling.[19] This resistive switch shows a unipolar behavior with a clear threshold voltage of about 0.3 V, where the resistance rapidly changes by four orders of magnitude from approximately  $1 \text{ G}\Omega$  to  $100 \text{ k}\Omega$  (Figure 3.1b). This resistance change is maintained for a short period only after switching off the voltage pulse, about 125 ms in the case of Figure 3.1c, a requirement for the fabrication of an artificial neuron. A histogram of retention times based on 40 measurements is given in Figure 3.A.2. In no case is the retention time more than 500 ms.

The resistance changes of the resistive switch are stochastic in nature, as is apparent from

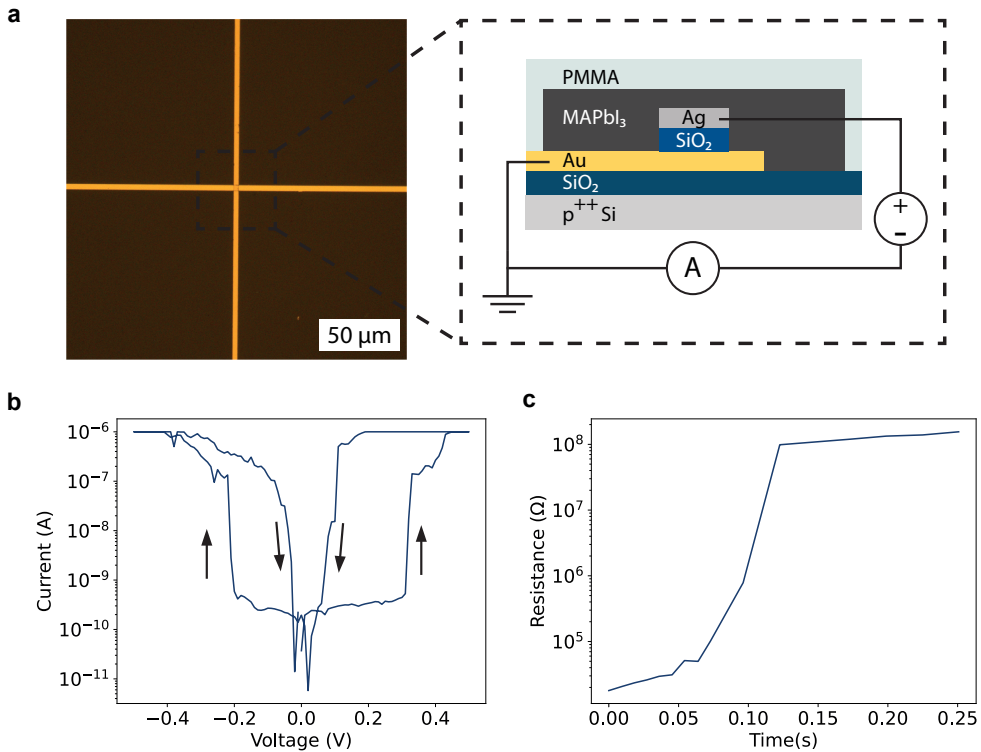


**Figure 3.1:** A volatile halide perovskite resistive switch. **(a)** Optical microscopy image of the cross-point formed by the gold and silver electrodes before deposition of the halide perovskite layer, with a schematic image of the full resistive switching device. A gold bottom electrode and silver top electrode sandwich an SiO<sub>2</sub> insulating layer. Halide perovskite is spin-coated over the electrodes and forms the active layer of the device. **(b)** I-V curve of the device, measured between  $-0.5$  and  $0.5$  V. The measured current increases by approximately 4 orders of magnitude at  $0.3$  V. The device returns to the initial high-resistive state as soon as the voltage is reduced to  $0$  V again and shows symmetric resistive switching properties in the negative poling direction. **(c)** Retention time measurement of the resistive switch. The resistance increases to that of the device in the high resistance state after approximately  $125$  ms. The full measurement is given in Figure 3.A.1.

the histograms of the time to switch after applying the voltage pulse in Figure 3.A.3a, b, and c and their corresponding fit with a Poisson distribution. Such a Poisson distribution for the switching time is expected for resistive switches that change their resistance due to stochastic formation and destruction of conductive filaments.[13] We note that resistance change can also occur for the same device but without the MAPbI<sub>3</sub> layer, as illustrated by Figure 3.A.4. The switching then happens at about 10× higher voltages. It has previously been shown that silver filaments can form in SiO<sub>2</sub> layers,[29] and the resistance changes therefore likely occur due to filament formation through the SiO<sub>2</sub> spacer between the Ag and Au electrodes. Thus, the role of the halide perovskite layer in the final device is to strongly facilitate the formation of these Ag filaments, enabling lower voltage operation and thereby reducing the energy consumption of the device.

### 3.2.2 A stochastic neuron

To turn this resistive switch into an artificial neuron, it needs to be connected to a capacitor. We implement this on-chip by connecting the resistive switch in series with a 300 pF capacitor that is formed by the Au bottom contact, the thermal SiO<sub>2</sub> layer and the highly-doped Si substrate, as shown in Figure 3.2a. With such a connection, the operation of the neuron follows three key steps, depicted in Figure 3.2b. In the first step, stimulation, the input voltage pulse experiences a resistive switch with high resistance. Therefore, every voltage pulse deposits only a small amount of charge on the capacitor, insufficient to build up significant voltage. After several pulses, the resistance of the resistive switch will promptly change to the low resistive state. At that point, the second step (firing) is initiated. The capacitor is quickly charged and the charge on the capacitor sets up a voltage that opposes the input voltage. The third step (resetting) is initiated when the applied voltage is removed. The capacitor discharges through the resistive switch, causing the resistive switch to return to the high resistive state, and the cycle can restart.

Figure 3.2c shows the experimental realization of the spiking of the artificial neuron. A 33 Hz, 750 mV pulse train is applied to the device and the voltage across the capacitor is measured. We observe firing pulses on the capacitor after one to three applied pulses. Fitting of the charging and discharging of the capacitor in Figure 3.A.5a and b reveals that the resistance of the resistive switch is reduced to 1 to 4 MΩ during most firing steps. The resistance obtained from the fit is higher than the 100 kΩ obtained in the voltage sweep in Figure 3.1b, indicating that the device has not fully switched to the low resistance state. The voltage drop over the resistive switch is gradually reduced as the filament is forming and the capacitor is charged, leading to only partial formation of the filament. This partial formation of the filament further aids the volatility and energy efficiency of the device.

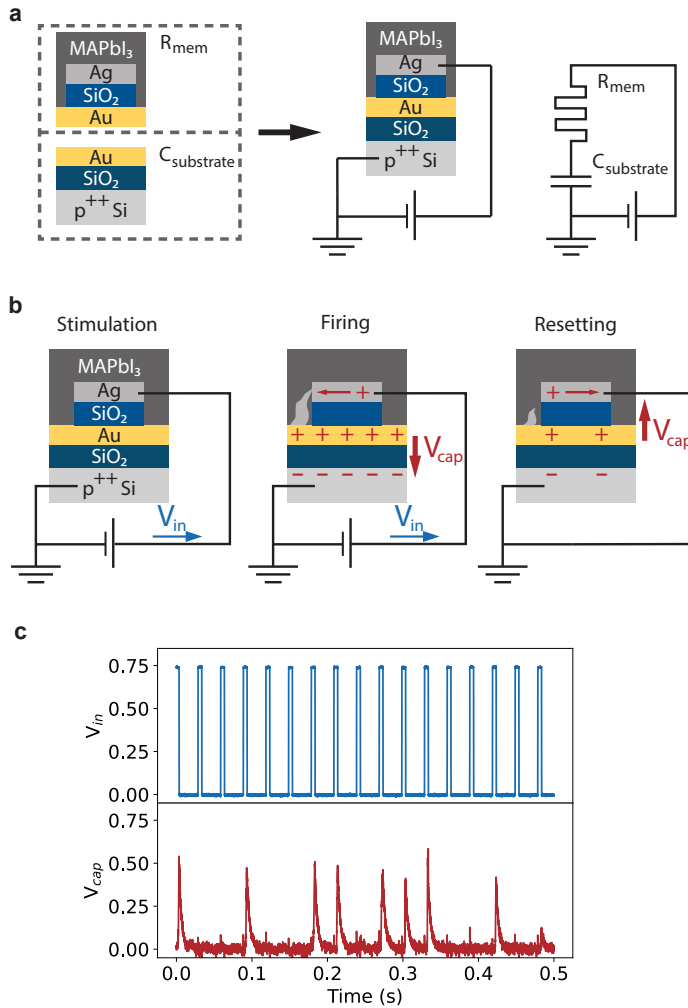


**Figure 3.2:** Operation of the artificial spiking neuron. (a) The neuron is constructed by connecting the memristive part of the device, consisting of the gold bottom electrode, silver top electrode and the MAPbI<sub>3</sub> layer, with the capacitor formed by the gold electrode and contact pad, the 100 nm thermal SiO<sub>2</sub> layer and the highly doped Si substrate in series. (b) Schematic representation of the three stages of the operation of the neuron. Upon application of a voltage, the device first undergoes a “stimulation” phase, where there is no significant voltage build-up on the capacitor due to the high resistance of the memristive part of the device. After enough voltage has been applied to the device, the memristive device switches to the low-resistance state and the capacitor is rapidly charged, causing a voltage buildup on the capacitor, i.e. “firing” of the neuron. When the applied voltage is removed, the capacitor discharges. This reverse-biases the resistive switch, aiding the disruption of the conductive filament, called the “resetting” process. (c) A pulsed measurement of the artificial neuron. A pulse train of 5 ms, 0.75 V pulses are applied with a 33 Hz frequency, resulting in firing spikes on the capacitor.

During discharging of the capacitor in the resetting step, a resistance of approximately  $10\text{ M}\Omega$  is extracted, which corresponds to the input impedance of the oscilloscope. Assuming that the resistive switch is brought back to its  $1\text{ G}\Omega$  high resistance state during the resetting step, the oscilloscope provides a lower resistance discharge path for the capacitor, which is a limitation of our current measurement setup (see Figure 3.A.5c).

The capacitive discharge fit immediately corresponds to the oscilloscope impedance (Figure 3.A.5a), from which we conclude that the resistive switch is reset as soon as the bias is removed, at least on the timescale of the measurement. No firing pulses were measured if the halide perovskite layer was omitted, as shown in Figure 3.A.6. The resistance changes that underlie the spiking behavior of the neuron, therefore, occur through the halide perovskite layer at these low applied voltages. Figure 3.A.7 shows that the stochastic spiking of the neuron was reproducible over multiple measurements.

### 3.2.3 Stochasticity for improved signal encoding

The firing pattern of the neuron is stochastic in nature, which is expected from the underlying stochastic switching mechanism of the resistive switch. Similar to the resistive switch itself, Figure 3.A.8a shows that the time under bias before spiking of the neuron follows a Poisson distribution, with a mean of  $6.9\text{ ms}$  for the  $0.75\text{ V}$  pulses. This stochastic switching is also observed in biological neurons and can have advantages compared to purely deterministic neurons.

To demonstrate this advantage we use the experimentally obtained mean switching time and resistances to model the behavior of the stochastic neuron. We compared the simulated stochastic neuron to a hypothetical deterministic neuron with a deterministic threshold of the same time constant ( $6.9\text{ ms}$ ) to determine the ability of stochastic and deterministic neurons to represent the input voltage pulse train. Modeling of the neuron is discussed in more detail in Section 3.B in the Appendix.

Figure 3.3a shows the simulated spiking behavior of a stochastic and a deterministic neuron. The spiking of the simulated stochastic neuron is similar to that in the measurement shown in Figure 3.2c. The simulated deterministic neuron, on the other hand, spikes at regular intervals.

To achieve more biologically plausible, robust, and accurate spiking neural networks, neurons are typically implemented in populations.[14, 15] In these networks, input signals are fed into the neurons in the populations and their collective output is collected as a population code. Figure 3.3b shows a simulation of populations of 100 stochastic or deterministic neurons. While the spikes of the stochastic neurons are distributed over

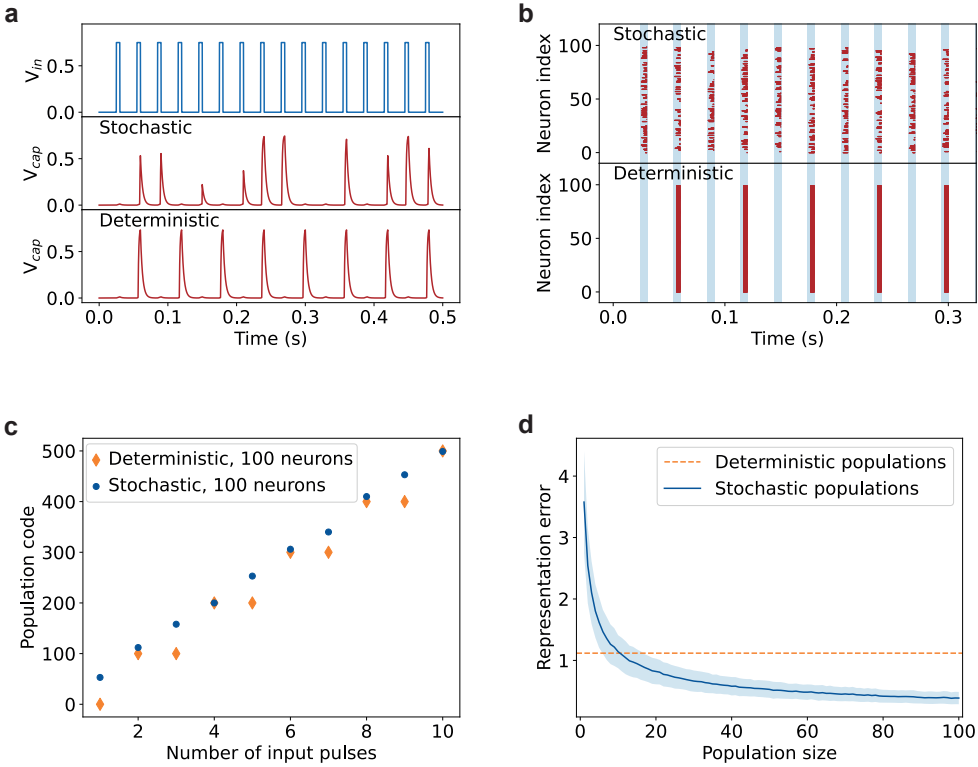


**Figure 3.3:** Simulations comparing the stochastic spiking of the neuron with a hypothetical deterministic version of the neuron. **(a)** Comparison of a simulated stochastic and deterministic spiking neuron, with the same input as in Figure 3.2c. Similar spiking behavior is obtained for the simulated and experimentally measured stochastic neurons. The deterministic neuron always spikes after a cumulative 6.9 ms of bias has been applied. **(b)** Simulated spiking behavior of populations of 100 stochastic and deterministic neurons. Ten voltage pulses are applied in the simulation with the same pulse duration, length, and magnitude as **(a)**. Blue-shaded regions indicate the application of the 750 mV pulses, while the red marks indicate spiking by the neuron. While the deterministic neurons all spike at the same time, spiking by the stochastic neurons is distributed more evenly throughout the applied pulses. **(c)** The population codes obtained for each applied pulse in **(b)**. We define the population code as the cumulative amount of spikes output by the population. For the deterministic population, the population code increases with each even number of applied pulses, while the stochastic population shows a more gradual increase with each applied pulse. **(d)** The representation error of deterministic and stochastic populations as a function of the population size, averaged over 1000 simulations. Deterministic populations have the same representation error regardless of their size. The representation error of the stochastic neurons decreases as the population size increases. The representation error of the stochastic populations is lower for population sizes of 11 or more neurons. The blue shaded region indicates one standard deviation.

all input voltage pulses, the deterministic neurons spike uniformly roughly each second input pulse.

From the simulations of the stochastic and deterministic neuron populations, we calculate the population code as the cumulative amount of spikes output by the total population after each successive input pulse, Figure 3.3c. The population code for the deterministic populations increases stepwise, showing that the stochastic neurons can better distinguish different numbers of applied pulses, i.e., they can better encode or represent the input. This process by which stochastic neurons can pick up on sub-threshold signals is called “stochastic resonance”. Biological neurons, which are also stochastic, rely on stochastic resonance to detect otherwise sub-threshold signals.[30]

To study the effect of population size on the reliability of signal detection, we simulated population codes for populations of 1 and up to 100 neurons and computed a signal representation error for each population size, see Figure 3.3d. Section 3.B in the Appendix explains how the representation error was determined. This representation error measures how well the population can encode and distinguish between different inputs. The representation error is initially larger for small populations of stochastic neurons compared to deterministic ones. However, the error rapidly decreases as the population size increases and drops below that of the deterministic neurons for relatively small population sizes of 11 or more stochastic neurons. These results are in line with previous work where the same benefit was found for stochasticity in artificial neuron populations.[14, 15]

### 3.2.4 Tunability of the neuron response

Experimentally, the neurons are stochastic, but the stochasticity is tunable. The spiking behavior of the neuron can be tuned by changing the parameters of the input voltage pulses. As shown in Figure 3.4a, the neuron outputs spikes with a higher probability for each input pulse if the frequency of the incoming pulses is increased. On the other hand, a lower input pulse frequency in Figure 3.4b leads to no spiking of the neuron, which is a clear demonstration of the leaky behavior of the neuron. Another demonstration of the leaky-integrate-and-fire behavior of the neuron is given in Figure 3.A.9. Increasing the pulse duration to 7.5 ms leads to firing with each applied voltage pulse, whereas 2 ms pulses applied with the same frequency do not lead to spiking of the neuron.

Changing the voltage also provides a way to change the firing pattern of the neuron. When the neuron is integrated in full networks, this would be equivalent to connecting the neuron through synapses with a low connection strength, i.e. a high resistance. The measurement in Figure 3.4c illustrates that a lower voltage drop over the neuron due to a

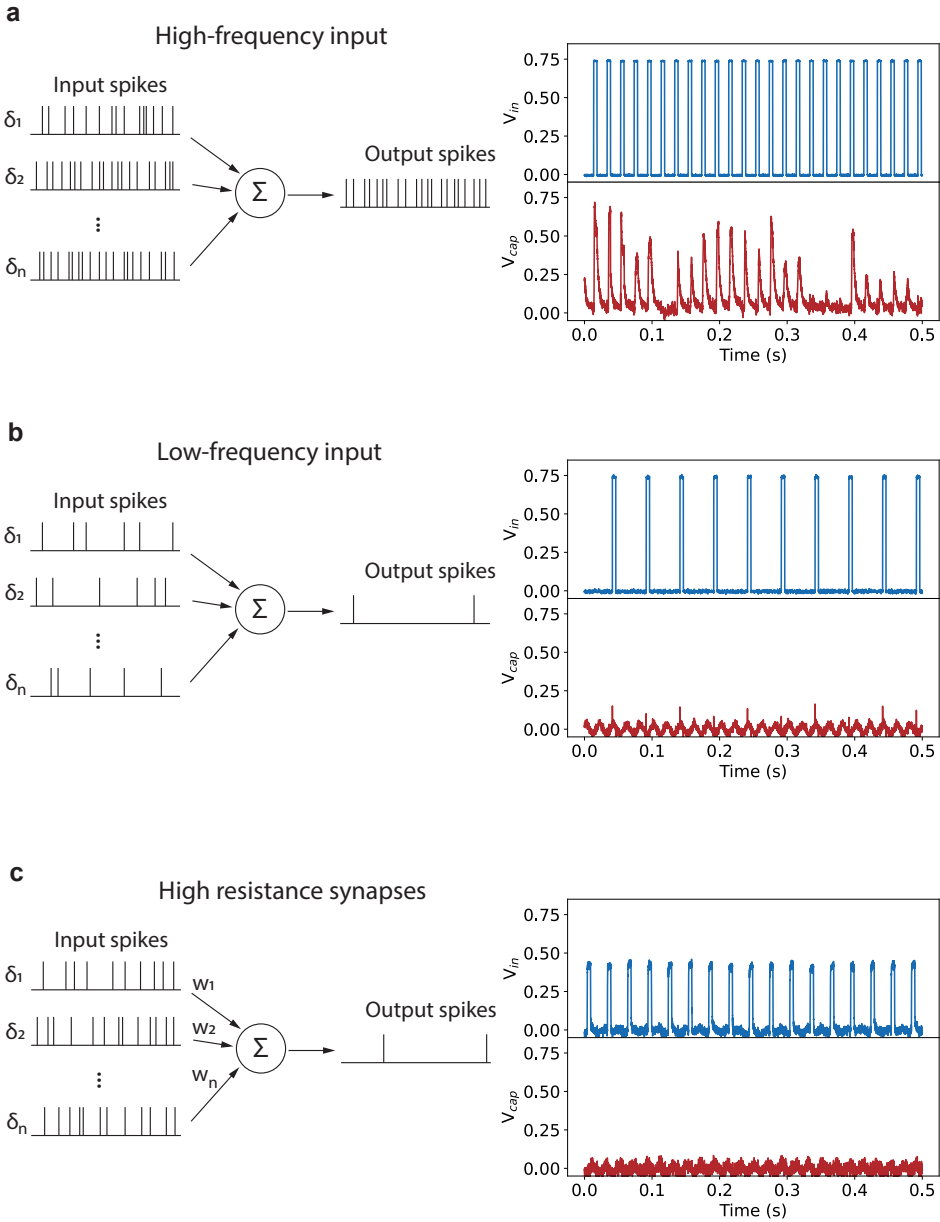


**Figure 3.4:** Tunability of the firing of the neuron. **(a)** Increasing the frequency of the incoming voltage pulses to 50 Hz leads to a higher firing probability with each input pulse. **(b)** At a lower frequency of incoming voltage pulses of 20 Hz the neuron does not fire. **(c)** A lower input voltage of 400 mV, corresponding to connection of the neuron through high resistance synapses, leads to no firing of the neuron.

resistive artificial synapse leads to no spiking of the neuron. Our spiking neuron therefore shows the leaky-integrate-and-fire behavior and synaptic strength-dependent spiking

properties required for constructing neuromorphic hardware with the synapse.

The energy consumption of the firing pulses can be calculated by  $E = \frac{1}{2} \times C \times V^2$ , with  $C$  the capacitance of the on-chip capacitor and  $V$  the voltage of the firing pulse, which yields an energy consumption per firing pulse between 20 to 60 pJ. This is already lower than the energy consumed by a biological neuron (on the order of 100 pJ), [31] and artificial neurons that have been implemented in hardware spiking neural networks before, [32] even in this early adaptation. More energy-efficient silicon artificial neurons that were demonstrated before have not yet been implemented in full networks. [33] In addition, neurons based on electronic circuits of traditional transistors and capacitors require a large number of these components, [8, 33] making the circuits bulky and therefore limiting the maximum density that can be reached on the final chip. In contrast, our design consists of only two components and could therefore be incorporated in higher densities more easily. Moreover, there is no detectable voltage build-up on the capacitor during the stimulation step before firing, meaning that the energy consumption per spike can be reduced by reducing the capacitance of the capacitor without negatively influencing the functioning of the neuron. We discuss further scaling effects in Section 3.C in the Appendix.

Biological neurons are sensitive to input signals of similar frequencies that we use in this work. [34] Although these frequencies are significantly lower than that of conventional computers, the different way that information is processed in neuromorphic networks still allows for efficient computation. In fact, neuromorphic networks require synapses and neurons that have time constants that are well-matched to their input for efficient computation. Thus, interfacing with the natural world, e.g. for learning from visual input, requires operating frequencies similar to those we use here. [7, 35] These time constants can be difficult to achieve with CMOS-based neuromorphic hardware. [36] Our neuron therefore provides a convenient alternative that is natively capable of operating at these frequencies. The ability to incorporate these neurons and the corresponding artificial synapses on flexible substrates could allow for novel application areas, including soft robots or even in combination with biological tissue. In addition, ion conductivity and corresponding resistance changes of halide perovskites can be tuned by light stimulation. [37] Perovskite neurons could therefore also open up new possibilities of hybrid electronic-photonic neuromorphic hardware, such as low-power smart sensors.

### 3.3 Conclusion

In conclusion, we have demonstrated the first fully on-chip halide perovskite artificial neuron. The neuron consists of only two components, which lends itself well to high-density

integration, and shows clear leaky-integrate-and-fire behavior, important for integration in neuromorphic hardware. The spiking of the neuron is stochastic, similar to biological neurons, yet with a lower energy consumption per spike between 20 to 60 pJ. The stochastic spiking of the neuron is beneficial for detecting sub-threshold input, similar to biological neurons. The energy consumption of the neuron could be further reduced by lowering the capacitance of the capacitor. The similarity in device architecture of this artificial neuron to the downscaled artificial synapses of MAPbI<sub>3</sub> that we have shown before,[19] allows easy implementation of energy-efficient all-halide perovskite neuromorphic hardware.

## 3.4 Materials and Methods

### 3.4.1 Materials

Heavily p-doped Si wafers (1-5  $\Omega$  cm resistivity) were purchased from Siegert Wafer. PbI<sub>2</sub> (99.99%) was purchased from TCI. Methylammonium iodide (MAI) was purchased from Solaronix. Anhydrous DMF and chlorobenzene were purchased from Sigma-Aldrich. 950 PMMA A8 was purchased from Kayaku Advanced Materials. All materials were used without further purification.

### 3.4.2 Fabrication of the on-chip artificial neuron

Devices were fabricated using a similar procedure as described before.[19] The artificial neurons were fabricated on heavily p-doped Si wafers with a 100 nm thermal oxide layer. Gold bottom electrodes were patterned on the wafer with a lift-off procedure using MA-N1410 photoresist. UV exposure with a Süss MA6/BA6 mask aligner was followed by development in MA-D533/s. A 5 nm Cr adhesion layer and an 80 nm Au electrode layer were deposited on the patterned resist by e-beam physical vapor deposition. Lift-off was then performed by soaking in acetone for one hour. A 60 nm SiO<sub>2</sub> layer was deposited from a O<sub>2</sub> and SiH<sub>4</sub> gas mixture using inductively-coupled plasma-enhanced chemical vapor deposition (ICPCVD) in an Oxford PlasmaPro100 ICPCVD system. Silver top contacts were patterned using the same procedure as for the bottom electrodes. After patterning of the top electrodes, the SiO<sub>2</sub> layer was etched in an Oxford Plasmalab 80 Plus system with an Ar and CHF<sub>3</sub> gas mixture, using the top electrodes as a hardmask.

Inside a nitrogen-filled glovebox (< 0.5 ppm O<sub>2</sub> and water), a stoichiometric mixture of PbI<sub>2</sub> and MAI was dissolved in DMF to obtain a 40 wt% MAPbI<sub>3</sub> precursor. The precursor was spin coated over the electrodes at 4000 rpm for 30 seconds in the same glovebox. Chlorobenzene was added as an antisolvent after 3 seconds of spinning. Directly after spin

coating the samples were annealed at 100 °C for 10 minutes. The 950 PMMA A8 solution was spin coated on top of the halide perovskite at 3000 rpm for 45 seconds, followed by a 5 minute bake at 100 °C.

### 3.4.3 Electrical characterization

I-V curves between  $-0.5$  and  $0.5$  V and the retention time of the low resistance state were measured with a Keysight B2902A Precision Source/Measure Unit.

Artificial neuron measurements were performed by applying voltage pulses between the heavily p-doped Si substrate and the silver top-electrode with a Rigol DG1062Z arbitrary waveform generator, while measuring the voltage between the gold bottom electrode and the Si substrate with a PicoScope 6402C oscilloscope. The data was smoothed using a moving average with a 5 point subset, corresponding to a  $20 \mu\text{s}$  time window. Afterward, 50 Hz noise from the AC power supply was removed using a fit to a sine wave with a 50 Hz frequency. Raw versions of the figures in the main text are given in Figure 3.A.10 and show that the measured signal is not affected significantly by the noise removal.

# Appendix

## 3.A Additional information

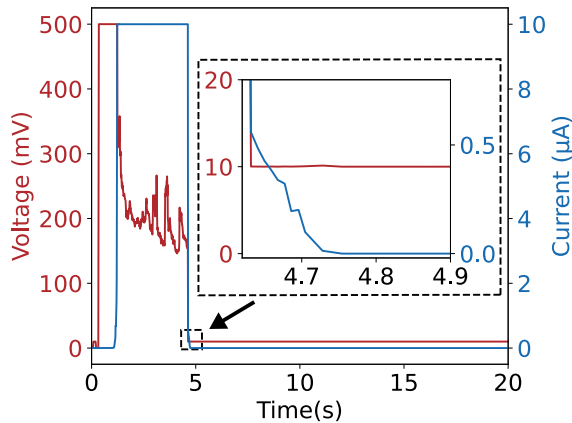


**Figure 3.A.1:** Retention time measurement of the resistive switch. A 500 mV pulse is applied to the device to bring the device to the low resistance state. After approximately one second, the resistance of the device rapidly drops. The measurement setup then reduces the applied voltage to ensure that the set compliance current of 10  $\mu\text{A}$  is not exceeded. After 4.5 seconds, the voltage is reduced to 10 mV to measure the evolution of the resistance over time. The inset shows a zoom-in on the region in the dotted rectangle, corresponding to the first hundreds of milliseconds after the potential is reduced to the 10 mV read-out voltage.

Figure 3.A.2a gives a histogram of retention times based on 40 measurements. The device is set to the high-conductive state by applying 500 mV, with the compliance current set to 10  $\mu\text{A}$ . The retention time was measured by applying 1 mV of constant bias. In several cases, the device reset to the low-conductance state within the integration time of the measurement setup (about 25 ms). An example of such a measurement is given in Figure 3.A.2b. These measurements were binned in the first bin (between 0 and 0.05 s) of the histogram in Figure 3.A.2a. The retention time was under 500 ms for all cases measured.

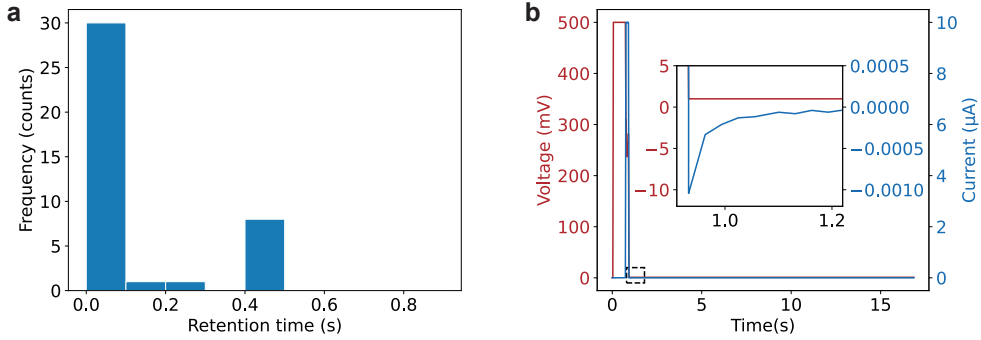


**Figure 3.A.2:** Analysis of retention times of the resistive switch. (a) Histogram of 40 retention time measurements. (b) Example of a measurement where the retention time was less than the integration time of the measurement setup, so only a discharge of the parasitic capacitance is measured. Although the exact retention time of these measurements could not be determined, they were added to the first bin of the histogram to still give an accurate representation.

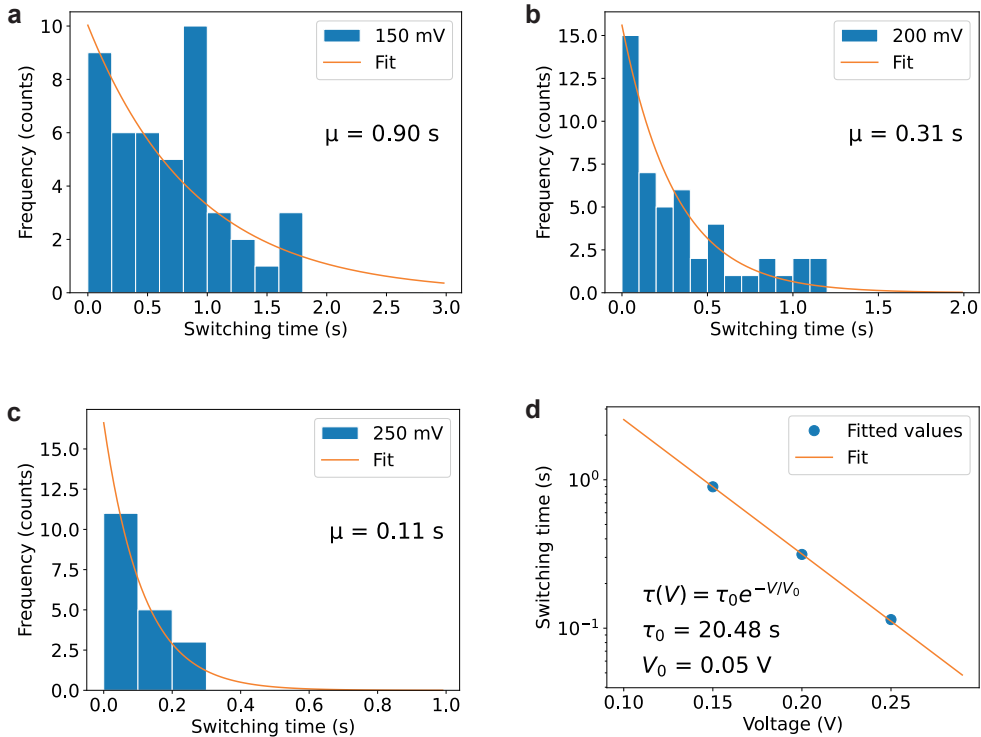


**Figure 3.A.3:** Histogram of the switching time for a switching event of the halide perovskite memristive device under an applied voltage of 150 (a), 200 (b), and 250 mV (c), with a fit based on a Poisson distribution. The means obtained from the fits are given in their respective figures. (d) A fit of the means obtained in the previous subfigures to the listed exponential function to extract the fitting parameters.

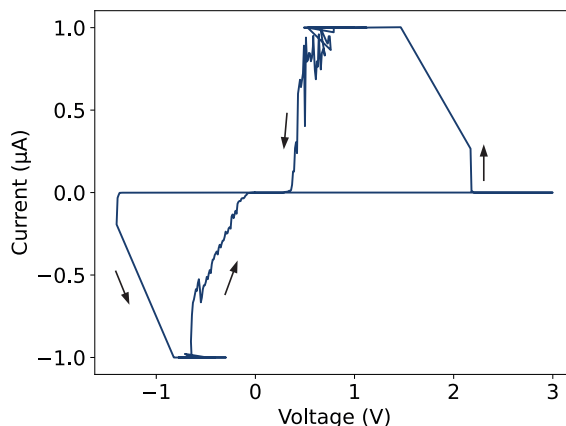


**Figure 3.A.4:** Resistive switching of a device without the halide perovskite layer. Resistive switching also occurs through the  $\text{SiO}_2$  spacer, albeit at higher voltages than for the device with a halide perovskite layer.

The probability of a resistance change of the memristive device upon the application of a voltage follows a Poisson distribution, as is evident from Figure 3.A.3a, b, and c. The formation of conductive filaments in memristive devices requires hopping of ions by a thermally activated process, which introduces this stochasticity. Random fluctuations are not averaged out according to the law of large numbers due to the small amount of ions needed to form the nanoscale filament. Previous work has described this Poisson behavior extensively and showed that the mean switching time depends exponentially on the applied bias according to  $\tau(V) = \tau_0 e^{-V/V_0}$ , where  $\tau$  is the mean switching time, and  $\tau_0$  and  $V_0$  are fitting parameters.[13] Figure 3.A.3d shows the same trend for our device, indicating that the same process of stochastic conductive filament formation underlies the operation of our device. Previous research on devices with similar electrodes and a halide perovskite active layer has shown that these conductive filaments consist of iodide vacancies[38] or silver.[39]

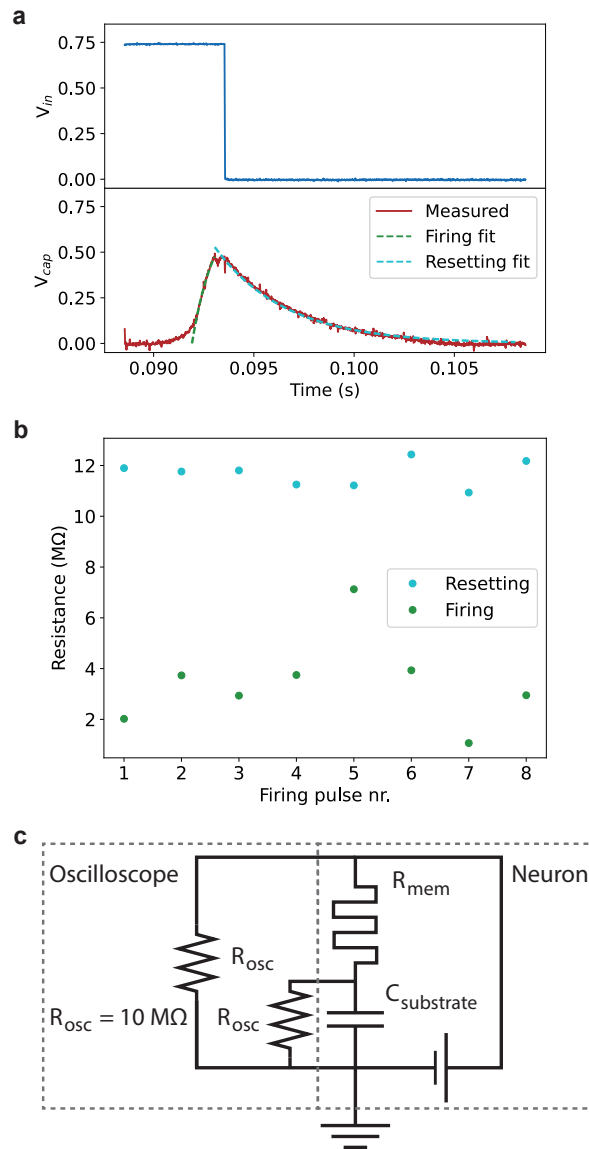


**Figure 3.A.5:** Fit of the firing pulses in Figure 3.2c with charging and discharging of a capacitor. **(a)** Fits of the charging (firing) and discharging (resetting) of the second firing pulse. **(b)** Extracted resistances of the charging and discharging of each of the firing pulses in Figure 3.2c. Error bars representing one standard deviation of the obtained resistance from the fit are included, but are smaller than the dots of the markers in the figure. **(c)** The circuit of the neuron with the 10  $M\Omega$  probes of the oscilloscope connected. The probes offer an alternative path for the capacitor to discharge.

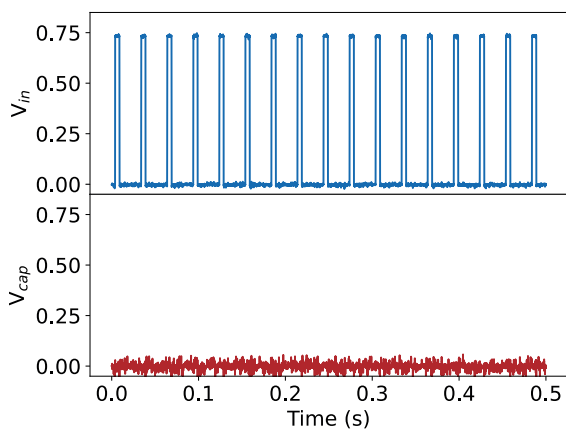


**Figure 3.A.6:** Spiking neuron measurements repeated on a substrate without the halide perovskite layer. No spiking is measured using the same parameters as for the spiking neuron in the main text.

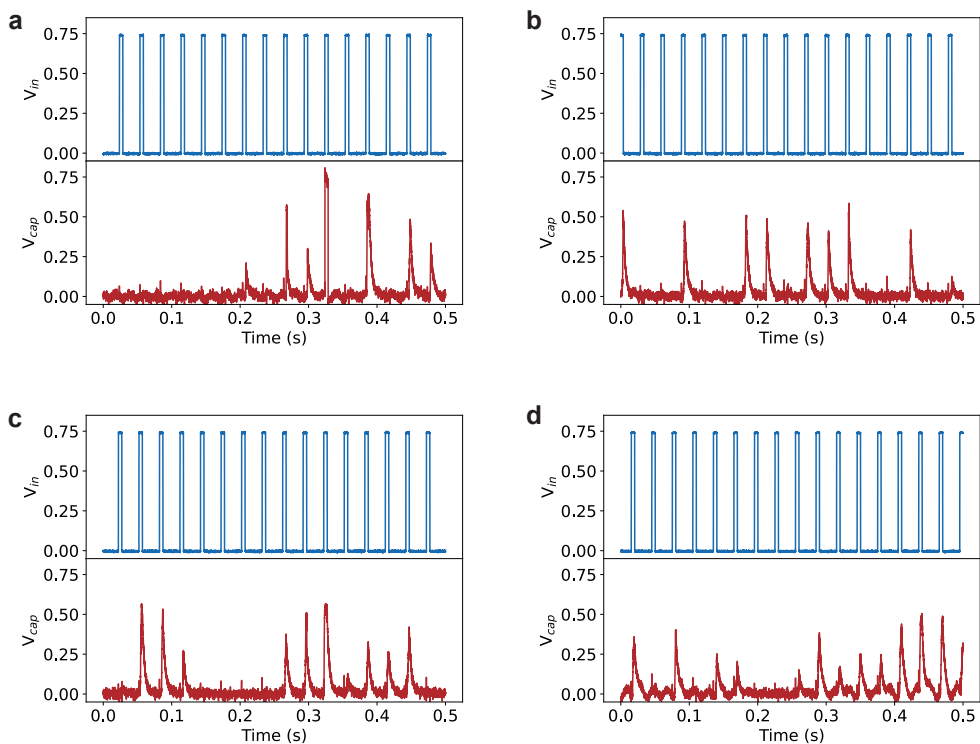


**Figure 3.A.7:** Four different measurements of the spiking neuron. In the measurements in (a), (b), (c), and (d) the same voltage profile, with 5 ms pulses of 750 mV, was applied to the neuron with a 33 Hz frequency. In all cases, this resulted in stochastic spiking by the neuron.

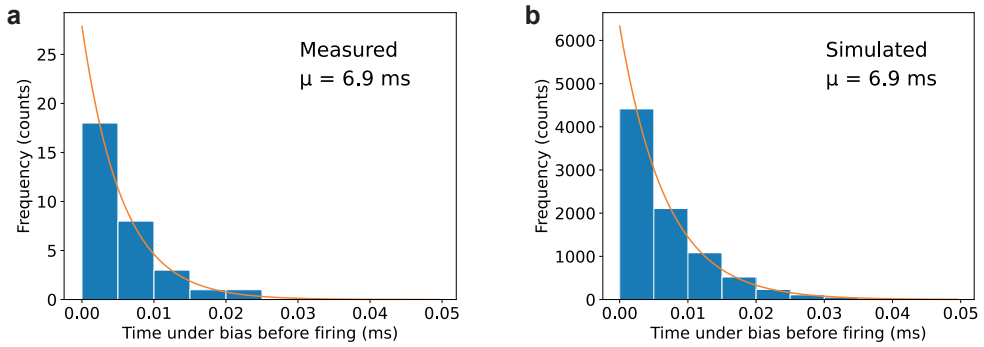


**Figure 3.A.8:** (a) Histogram of the time under bias before firing of the neuron based on the measurements in Figure 3.A.7. Spiking by the neuron was defined as the moment when the capacitor voltage exceeds 200 mV. The mean of the distribution is 6.9 ms. (b) The same histogram of spiking by the neuron compiled from simulated data to validate the model. We obtain the same mean of 6.9 ms of applied bias before spiking by the neuron.

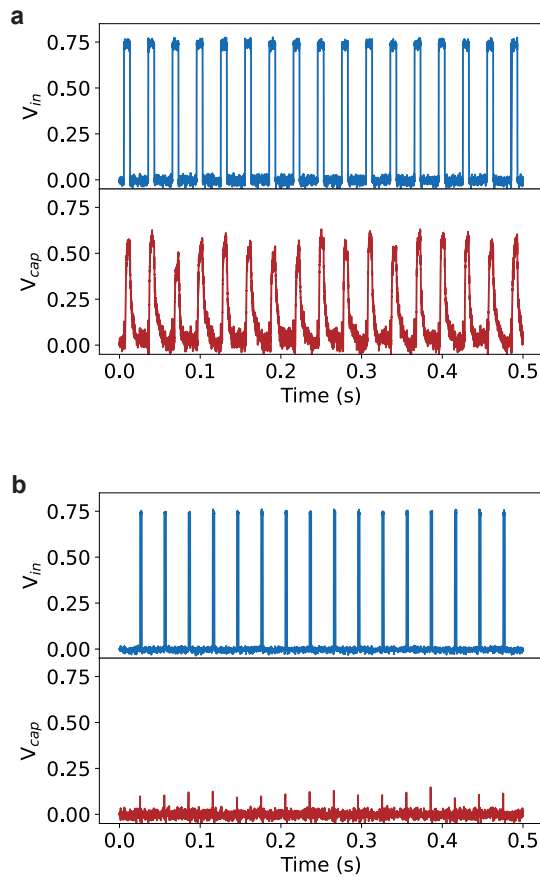


**Figure 3.A.9:** Stimulation of the neuron with 750 mV pulses with pulse durations of 7.5 ms in (a), which leads to firing with every applied pulse and with a duration of 2 ms in (b), which leads to no firing of the neuron.

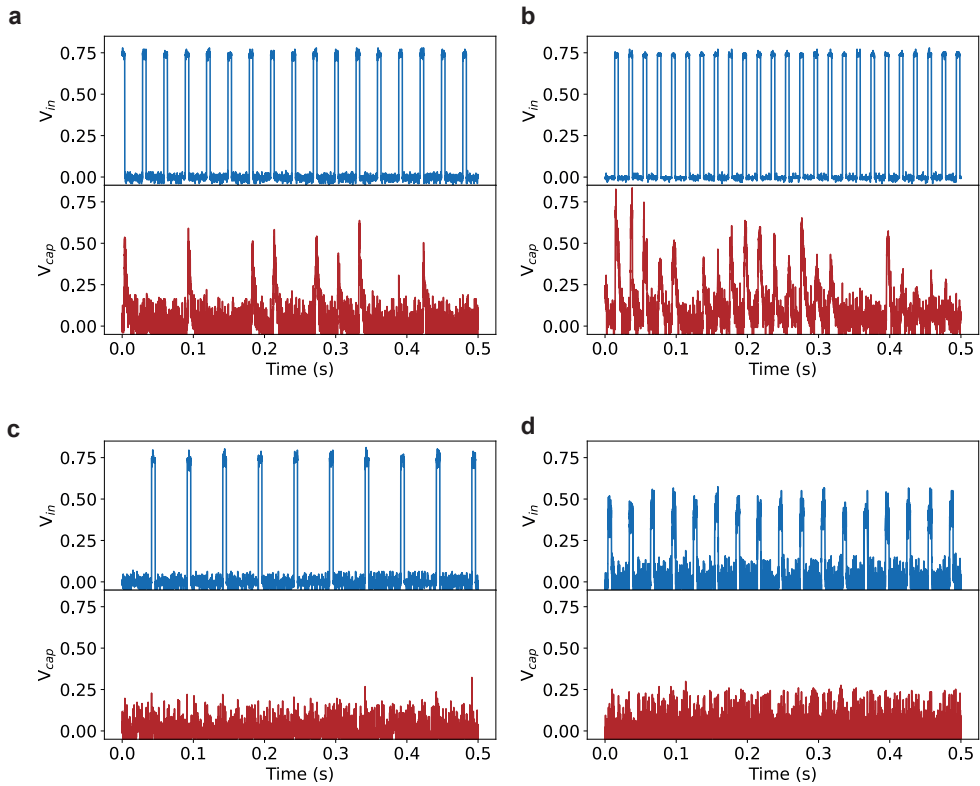


**Figure 3.A.10:** (a) Figure 3.2c, (b) Figure 3.3a, (c) Figure 3.3b and (d) Figure 3.3c before smoothing and removal of the 50 Hz signal of the AC mains. Comparing these figures with the figures in the main text shows that the noise is removed without distorting the measured signal.

### 3.B Modeling of stochastic and deterministic neurons

The simulated data in Figure 3.3 was obtained with experimentally determined resistances and capacitance. For the stochastic neurons, a switching time was drawn from a Poisson distribution with the experimentally determined mean of 6.9 ms from Figure 3.A.8, using a random number generator. Voltage pulses are applied in the simulation, which causes a voltage buildup on the capacitor with an RC constant of  $300 \text{ pF} \times 1 \text{ G}\Omega = 0.3 \text{ s}$ . The time under bias is then tracked until the switching time is reached. At this point, the RC constant decreases significantly to  $300 \text{ pF} \times 3 \text{ M}\Omega = 0.9 \text{ ms}$  due to the resistance change of the resistive switch. After the voltage is removed, the capacitor discharges through a  $10 \text{ M}\Omega$  resistor and a new switching time is drawn from the Poisson distribution. The same procedure is followed for deterministic neurons, but with a switching time always set to 6.9 ms. For validation of the model, we simulated the spiking of a neuron using the same input voltage profile as for the measurements in Figure 3.A.7, but over a longer period of 500 seconds, constituting 16,666 applied voltage pulses. A histogram of the time under bias before spiking by the neuron based on the simulation is given in Figure 3.A.8b. The mean obtained from the simulation of 6.9 ms agrees with the experimentally obtained mean.

To determine the representation error of the neuron populations in Figure 3.3d, the population code of the neuron populations, i.e., the cumulative sum of spikes for each applied pulse, is compared to the ideal population code. For stochastic neurons, the chance of the neurons outputting a spike is  $P(5 \text{ ms}) = 1 - e^{-\frac{5 \text{ ms}}{6.9 \text{ ms}}} \approx 0.52$  for each 5 ms input voltage pulse. In the ideal case, the mean number of spikes per neuron in a population is, therefore, equal to 0.52 multiplied by the number of applied pulses. Figure 3.B.1a compares the ideal mean number of spikes with that of a simulation of stochastic neuron populations of different sizes. Because of the non-zero chance of spiking by the stochastic neuron for each applied pulse, the population can capture all applied voltage pulses. For larger population sizes, the mean of the pulses approaches that of the ideal case. The deterministic neurons always spike after 6.9 ms of bias, or every second pulse. Because of the deterministic nature of the neuron, additional spikes are never output by deterministic populations for uneven numbers of applied pulses, as illustrated by Figure 3.B.1b.

To obtain the representation error from the simulations, we take the Euclidian norm of the difference between the ideal and the simulated mean numbers of spikes for each population,

$E = \sqrt{\sum_{i=1}^{10} (\mu_{i,simulated} - \mu_{i,ideal})^2}$ , where  $i$  refers to the applied pulse number and  $\mu$  is the mean number of spikes per neuron. To obtain the results shown in Figure 3.3d, we repeated the simulations 1000 times for neuron populations of 1 and up to 100 neurons.

The average representation error is shown in the figure.

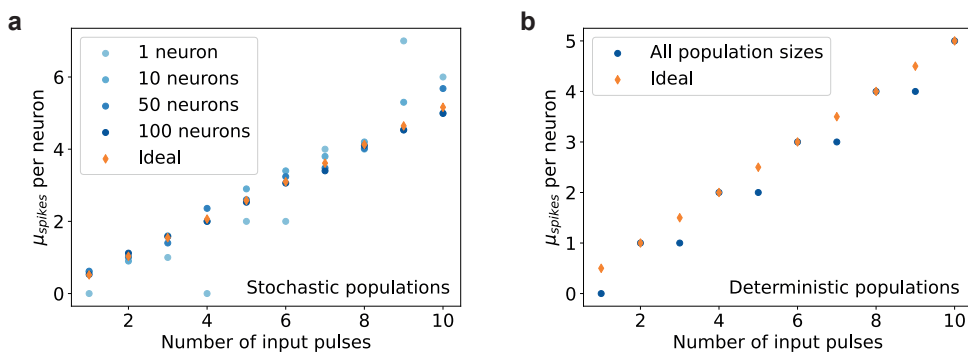


**Figure 3.B.1:** The mean number of spikes per neuron of the stochastic and deterministic neuron populations, compared to their respective ideal mean number of spikes. **(a)** The mean number of spikes per number of stochastic populations of different sizes. Owing to the stochastic nature of the spiking, the average number of spikes converges to the ideal case for all applied pulses as the population size increases. **(b)** The mean number of spikes of deterministic populations. By definition, the mean does not change for different population sizes. The mean does not increase for uneven number pulses but matches perfectly with the ideal mean for even numbers of applied pulses.

### 3.C Scaling of the spiking neuron

There are two main limitations of further scaling of the neuron. First, the RC constant should remain high enough to prevent excessive charge buildup on the capacitor during the stimulation phase. To estimate scaling limitations, we set a limit of 100 mV of voltage buildup during stimulation of the neuron, while the resistive switch is still in the OFF-state. A voltage buildup of 100 mV is still easy to distinguish from a firing event where the voltage rises to several hundreds of millivolts, as in the measurements in Figure 3.A.7. Assuming the same input pulses of 750 mV and 5 ms in length as in Figure 3.2c, the RC constant should then be at least  $RC = -\frac{t}{\ln\left(1 - \frac{V(t)}{V_{supply}}\right)} = -\frac{5 \times 10^{-3} \text{ s}}{\ln\left(1 - \frac{100 \text{ mV}}{750 \text{ mV}}\right)} \approx 35 \text{ ms}$ . Further downscaling of the resistive switch should linearly increase its low-conductance state resistance. Balancing this resistance with the series capacitance to satisfy the constraint on the RC constant allows for easy scaling of the neuron.

Even if the low-conductance state resistance is not reduced further as the resistive switch is scaled, due to a parasitic resistance in the circuit, for example, the capacitance can still be reduced by approximately an order of magnitude, to  $C = \frac{0.035 \text{ s}}{10^9 \Omega} = 35 \text{ pF}$ , assuming an OFF-state resistance of 1 G $\Omega$  extracted from the I-V curve in Figure 3.1b. Assuming that the reduction in the capacitance means that the capacitor is now always fully charged with a firing event, this would reduce the energy consumption of the neuron to  $E = \frac{1}{2} \times C \times V^2 = \frac{1}{2} \times 35 \times 10^{-12} \text{ F} \times (0.75 \text{ V})^2 \approx 9.8 \text{ pJ}$ . Even in this upper limit, the energy consumption of the neuron would be close to that of the most energy-efficient silicon neurons.[33]

A second limitation is that the amount of charge on the capacitor should be large enough to aid the resetting of the resistive switch after firing. From Figure 3.A.5a we see that the device is in the high resistive state right after the voltage is turned off. Thus, the switching time is <1 ms. The neuron would work in a similar way with a switching time 2-3 orders of magnitude slower, which means that a capacitance 2-3 orders of magnitude smaller would suffice, in the hundreds of femtofarad regime. Common CMOS technology utilizes architectures that can fabricate capacitors on this scale with very small device footprint.[40]

# References

1. Brown, T. *et al.* *Language Models are Few-Shot Learners in Advances in Neural Information Processing Systems* **33** (Curran Associates, Inc., 2020), 1877–1901.
2. McKinney, S. M. *et al.* International evaluation of an AI system for breast cancer screening. *Nature* **577**, 89–94 (2020).
3. He, K., Zhang, X., Ren, S. & Sun, J. *Delving Deep into Rectifiers: Surpassing Human-Level Performance on ImageNet Classification in 2015 IEEE International Conference on Computer Vision (ICCV)* (IEEE, Santiago, Chile, 2015), 1026–1034.
4. Vinyals, O. *et al.* Grandmaster level in StarCraft II using multi-agent reinforcement learning. *Nature* **575**, 350–354 (2019).
5. Silver, D. *et al.* Mastering the game of Go without human knowledge. *Nature* **550**, 354–359 (2017).
6. Mehonic, A. & Kenyon, A. J. Brain-inspired computing needs a master plan. *Nature* **604**, 255–260 (2022).
7. Merolla, P. A. *et al.* A million spiking-neuron integrated circuit with a scalable communication network and interface. *Science* **345**, 668–673 (2014).
8. Chicca, E., Stefanini, F., Bartolozzi, C. & Indiveri, G. Neuromorphic electronic circuits for building autonomous cognitive systems. *Proceedings of the IEEE* **102**, 1367–1388 (2014).
9. Govoreanu, B. *et al.* *10×10nm<sup>2</sup> Hf/HfOx crossbar resistive RAM with excellent performance, reliability and low-energy operation in 2011 International Electron Devices Meeting* (2011), 31.6.1–31.6.4.
10. Xu, W., Min, S. Y., Hwang, H. & Lee, T. W. Organic core-sheath nanowire artificial synapses with femtojoule energy consumption. *Science Advances* **2**, e1501326 (2016).
11. Chanthbouala, A. *et al.* A ferroelectric memristor. *Nature Materials* **11**, 860–864 (2012).
12. Kuzum, D., Jeyasingh, R. G. D., Lee, B. & Wong, H.-S. P. Nanoelectronic Programmable Synapses Based on Phase Change Materials for Brain-Inspired Computing. *Nano Letters* **12**, 2179–2186 (2012).
13. Jo, S. H., Kim, K.-H. & Lu, W. Programmable Resistance Switching in Nanoscale Two-Terminal Devices. *Nano Letters* **9**, 496–500 (2009).

14. Tuma, T., Pantazi, A., Le Gallo, M., Sebastian, A. & Eleftheriou, E. Stochastic phase-change neurons. *Nature Nanotechnology* **11**, 693–699 (2016).
15. Zendrikov, D., Solinas, S. & Indiveri, G. Brain-inspired methods for achieving robust computation in heterogeneous mixed-signal neuromorphic processing systems. *Neuromorphic Computing and Engineering* **3**, 034002 (2023).
16. Al-Shedivat, M., Naous, R., Cauwenberghs, G. & Salama, K. N. Memristors Empower Spiking Neurons With Stochasticity. *IEEE Journal on Emerging and Selected Topics in Circuits and Systems* **5**, 242–253 (2015).
17. Eames, C., Frost, J. M., Barnes, P. R., O'regan, B. C., Walsh, A. & Islam, M. S. Ionic transport in hybrid lead iodide perovskite solar cells. *Nature communications* **6**, 7497 (2015).
18. Xiao, Z. & Huang, J. Energy-efficient hybrid perovskite memristors and synaptic devices. *Advanced Electronic Materials* **2**, 1600100 (2016).
19. De Boer, J. J. & Ehrler, B. Scalable Microscale Artificial Synapses of Lead Halide Perovskite with Femtojoule Energy Consumption. *ACS Energy Letters* **9**, 5787–5794 (2024).
20. Kim, S. I. *et al.* Dimensionality Dependent Plasticity in Halide Perovskite Artificial Synapses for Neuromorphic Computing. *Advanced Electronic Materials* **5**, 1900008 (2019).
21. Yang, J. Q., Wang, R., Wang, Z. P., Ma, Q. Y., Mao, J. Y., Ren, Y., Yang, X., Zhou, Y. & Han, S. T. Leaky integrate-and-fire neurons based on perovskite memristor for spiking neural networks. *Nano Energy* **74**, 104828 (2020).
22. Stoliar, P., Tranchant, J., Corraze, B., Janod, E., Besland, M.-P., Tesler, F., Rozenberg, M. & Cario, L. A Leaky-Integrate-and-Fire Neuron Analog Realized with a Mott Insulator. *Advanced Functional Materials* **27**, 1604740 (2017).
23. Zhang, Y. *et al.* Highly Compact Artificial Memristive Neuron with Low Energy Consumption. *Small* **14**, 1802188 (2018).
24. Kalita, H., Krishnaprasad, A., Choudhary, N., Das, S., Dev, D., Ding, Y., Tetard, L., Chung, H.-S., Jung, Y. & Roy, T. Artificial Neuron using Vertical MoS<sub>2</sub>/Graphene Threshold Switching Memristors. *Scientific Reports* **9**, 53 (2019).
25. Zhang, X. *et al.* An Artificial Neuron Based on a Threshold Switching Memristor. *IEEE Electron Device Letters* **39**, 308–311 (2018).
26. Pickett, M. D., Medeiros-Ribeiro, G. & Williams, R. S. A scalable neuristor built with Mott memristors. *Nature Materials* **12**, 114–117 (2013).
27. Yi, W., Tsang, K. K., Lam, S. K., Bai, X., Crowell, J. A. & Flores, E. A. Biological plausibility and stochasticity in scalable VO<sub>2</sub> active memristor neurons. *Nature Communications* **9**, 4661 (2018).

28. Wang, Z. *et al.* Capacitive neural network with neuro-transistors. *Nature Communications* **9**, 1–10 (2018).
29. Wang, Z. *et al.* Memristors with diffusive dynamics as synaptic emulators for neuromorphic computing. *Nature Materials* **16**, 101–108 (2017).
30. Douglass, J. K., Wilkens, L., Pantazelou, E. & Moss, F. Noise enhancement of information transfer in crayfish mechanoreceptors by stochastic resonance. *Nature* **365**, 337–340 (1993).
31. Lennie, P. The Cost of Cortical Computation. *Current Biology* **13**, 493–497 (2003).
32. Moradi, S., Qiao, N., Stefanini, F. & Indiveri, G. A Scalable Multicore Architecture With Heterogeneous Memory Structures for Dynamic Neuromorphic Asynchronous Processors (DYNAPs). *IEEE Transactions on Biomedical Circuits and Systems* **12**, 106–122 (2018).
33. Rubino, A., Payvand, M. & Indiveri, G. *Ultra-Low Power Silicon Neuron Circuit for Extreme-Edge Neuromorphic Intelligence* in *2019 26th IEEE International Conference on Electronics, Circuits and Systems (ICECS)* (IEEE, Genoa, Italy, 2019), 458–461.
34. Fourcaud-Trocmé, N., Hansel, D., van Vreeswijk, C. & Brunel, N. How Spike Generation Mechanisms Determine the Neuronal Response to Fluctuating Inputs. *The Journal of Neuroscience* **23**, 11628–11640 (2003).
35. Qiao, N., Mostafa, H., Corradi, F., Osswald, M., Stefanini, F., Sumislawska, D. & Indiveri, G. A reconfigurable on-line learning spiking neuromorphic processor comprising 256 neurons and 128K synapses. *Frontiers in Neuroscience* **9**, 141 (2015).
36. Qiao, N., Bartolozzi, C. & Indiveri, G. An Ultralow Leakage Synaptic Scaling Homeostatic Plasticity Circuit With Configurable Time Scales up to 100 ks. *IEEE Transactions on Biomedical Circuits and Systems* **11**, 1271–1277 (2017).
37. Ham, S., Choi, S., Cho, H., Na, S. I. & Wang, G. Photonic Organolead Halide Perovskite Artificial Synapse Capable of Accelerated Learning at Low Power Inspired by Dopamine-Facilitated Synaptic Activity. *Advanced Functional Materials* **29**, 1806646 (2019).
38. Zhu, X., Lee, J. & Lu, W. D. Iodine vacancy redistribution in organic–inorganic halide perovskite films and resistive switching effects. *Advanced Materials* **29**, 1700527 (2017).
39. Luo, H. *et al.* In Situ Unveiling of the Resistive Switching Mechanism of Halide Perovskite-Based Memristors. *The Journal of Physical Chemistry Letters* **15**, 2453–2461 (2024).

40. Brunet, M. & Kleimann, P. High-Density 3-D Capacitors for Power Systems On-Chip: Evaluation of a Technology Based on Silicon Submicrometer Pore Arrays Formed by Electrochemical Etching. *IEEE Transactions on Power Electronics* **28**, 4440–4448 (2013).



# 4

## Microscale Optoelectronic Synapses with Switchable Photocurrent

### Abstract

Efficient visual data processing by neuromorphic networks requires volatile artificial synapses that detect and process light inputs, ideally in the same device. Here we demonstrate microscale back-contacted optoelectronic halide perovskite artificial synapses that leverage ion migration induced by a bias voltage to modulate their photocurrent. The photocurrent changes are due to the accumulation of mobile ions, which induces a transient electric field in the perovskite. The photocurrent changes are volatile, decaying on the order of seconds. The photocurrent changes can be controlled by both the applied voltage and illumination. The symmetric device supports changing of the photocurrent polarity, switching between inhibitory and excitatory functioning. The photocurrent can be updated by spike-timing-dependent plasticity (STDP)-learning rules inspired by biology. We show with simulations how this could be exploited as an attention mechanism in a neuromorphic detector. Our fabrication procedure is compatible with high-density integration with CMOS and memristive neuromorphic networks for energy-efficient visual data processing inspired by the brain.

---

This chapter is based on: de Boer, J.J., Alvarez, A.O., Schmidt, M.C., Sitaridis, D. & Ehrler, B. Microscale optoelectronic synapses with switchable photocurrent from halide perovskite, *in preparation*

## 4.1 Introduction

Rapid developments in the field of artificial intelligence (AI) have led to impressive performance of neural networks over a broad range of tasks, such as natural language processing,[1, 2] image recognition,[3, 4] and protein folding prediction.[5] However, the increase in the capabilities of neural networks has come at the price of exponentially increasing energy consumption.[6] Neuromorphic computing offers a more energy-efficient alternative to neural networks run on classical computers.[7] In neuromorphic computing, electronic analogs to biological neurons and synapses mimic highly energy-efficient biological neural networks. Similar to their biological counterpart, neuromorphic artificial synapses process and store information within the network by changing the synaptic connection strength between neurons, typically through a variable resistance. This can be implemented with memristive devices, which have a resistance that can be varied by applying a bias voltage.[8] Volatile memristive devices, of which the resistance change decays to a steady-state high-resistive state over time, are particularly well-suited to mimic brain-like filtering and processing of sensory information.[9, 10] For this application, the volatility of the devices ensures that signals that occur at different points in time can be distinguished. When applied as a filter, the output intensity of volatile devices changes depending on recent input, for example allowing them to function as bandpass filters.[9] Volatile devices can also be implemented for short-term working memory. Information relevant to a task, such as speech recognition or recalling a recently detected object, is stored for a short time and automatically forgotten after the task is completed.[11, 12] Here, the volatility of the memristive devices prevents the storage of information that is no longer relevant to the network.

Halide perovskites are an emerging class of semiconducting materials for neuromorphic devices. Highly mobile ionic defects in these materials readily cause hysteresis, which has been leveraged to fabricate energy-efficient artificial synapses,[13–15] and, more recently, neurons.[16] Hysteresis typically occurs on the hundreds of milliseconds to seconds time-scales,[17, 18] ideal for volatile synapses. Moreover, their easy solution-processability allows facile deposition, even on flexible substrates.[19, 20] Halide perovskites are also excellent light absorbers, with a band gap that can be tuned by incorporating different halides.[21] A notable property of halide perovskites is that the ionic mobility is coupled to light absorption, with higher ionic mobilities under more intense illumination conditions.[22] This interplay of ionic mobility and the photogenerated charge carriers might therefore enable the use of halide perovskites for simultaneous detection and processing of visual input. This application would further enhance the energy efficiency

and scalability of neuromorphic networks.[23]

Although first macroscale implementations of optoelectronic halide perovskite synapses that can process light pulses have shown impressive energy,[14, 24] and light-detection efficiencies,[25] their scalability remains challenging. This is due to complex device architectures requiring multiple active layers,[26, 27] sometimes with a third gate electrode,[25, 28, 29] and the high solubility of halide perovskites in polar solvents,[30] which makes microfabrication with lithography difficult.

Here, we adapt the lithographic procedure we recently developed for all-electronic halide perovskite synapses and neurons[13, 16] to fabricate volatile halide perovskite optoelectronic synapses on the microscale. Applying a voltage pulse to the synapse causes subsequent volatile photocurrent enhancement that decays over approximately 5 seconds. From transient photocurrent measurements and drift-diffusion simulations we deduce that the mechanism is the accumulation of mobile ions by the bias voltage, which induces an electric field in the perovskite. We postulate that this improves the extraction of photogenerated charge carriers under illumination, resulting in a volatile photocurrent enhancement. We demonstrate that the photocurrent enhancement is more significant for higher applied bias voltages and light intensities during the voltage. We attribute this dependence to the higher ionic mobility under illumination and therefore more significant ionic accumulation for higher applied voltages. We show that the photocurrent polarity can be both positive and negative depending on the applied voltage, a unique feature of our device that enables facile switching from excitatory to inhibitory functioning. We fabricate devices that are sensitive to different parts of the visible spectrum by incorporating MAPbI<sub>3</sub>, FAPbBr<sub>3</sub>, and FAPb(I<sub>0.5</sub>Br<sub>0.5</sub>)<sub>3</sub> perovskites, and show that the photocurrent changes generalize over all of these perovskite layers. Finally, we show STDP learning by the synapse and simulate how this could be used for a neuromorphic detector employing an attention mechanism. The easily scalable device structure and mild conditions during the fabrication process allow the implementation of this detector with existing neuromorphic chips.

## 4.2 Results and Discussion

### 4.2.1 Device architecture

Figure 4.1a shows a schematic and optical microscopy image of our microscale halide perovskite volatile optoelectronic synapse (MPOS). Two 2.5 μm wide gold electrodes form a cross-point device that sandwiches an approximately 15 nm ALD-deposited Al<sub>2</sub>O<sub>3</sub> layer. We spin-coat the MAPbI<sub>3</sub> active layer over the electrodes in the final step to prevent degra-

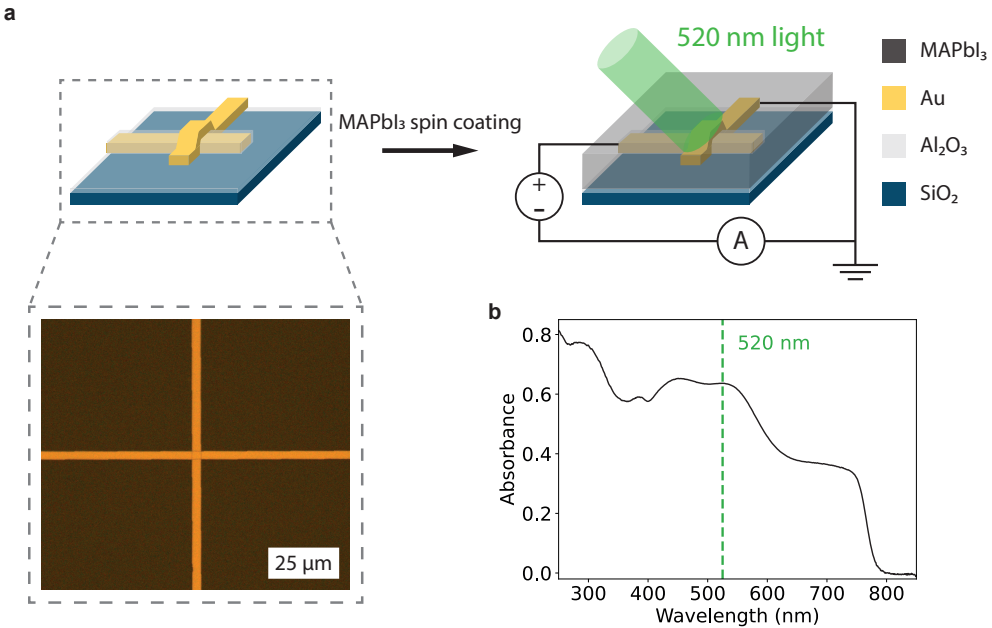


**Figure 4.1:** The volatile halide perovskite optoelectronic synapse. **(a)** Schematic drawing of the halide perovskite optoelectronic synapse. After microfabrication of the 2.5 μm wide gold electrodes, the MAPbI<sub>3</sub> layer is spin-coated on the substrate. The device is connected to an SMU to apply voltages and measure current, and light is supplied as an additional input. **(b)** UV-Vis absorption spectrum of the MAPbI<sub>3</sub> film on a quartz substrate. The halide perovskite layer absorbs light over a broad range of wavelengths.

dation during lithography. Voltages and currents can be applied and measured between the top and bottom electrodes of the device. Importantly, the back-contact architecture also allows for the illumination of the MAPbI<sub>3</sub> layer without unwanted reflections off the gold electrodes. Figure 4.1b shows that the MAPbI<sub>3</sub> layer we employ efficiently absorbs light with wavelengths below 780 nm. The absorption for 520 nm light, used in later measurements, is highlighted with a green dotted line. The broad absorption range enables the MPOS to process input light signals all over the visible range and into the UV. This makes it more versatile than optoelectronic synapses based on materials that can only process UV-light inputs due to their limited absorption in the visible spectrum.[31, 32]

#### 4.2.2 Photocurrent switching

Figure 4.2a shows an example measurement of the synapse. Initially, pulsing a 520 nm LED gives a small photocurrent of tens of picoamps. After applying a -1 V pulse to the device under illumination, an initial increase of the current is measured in the dark. This current decreases exponentially. When a light pulse is applied during this decay process,

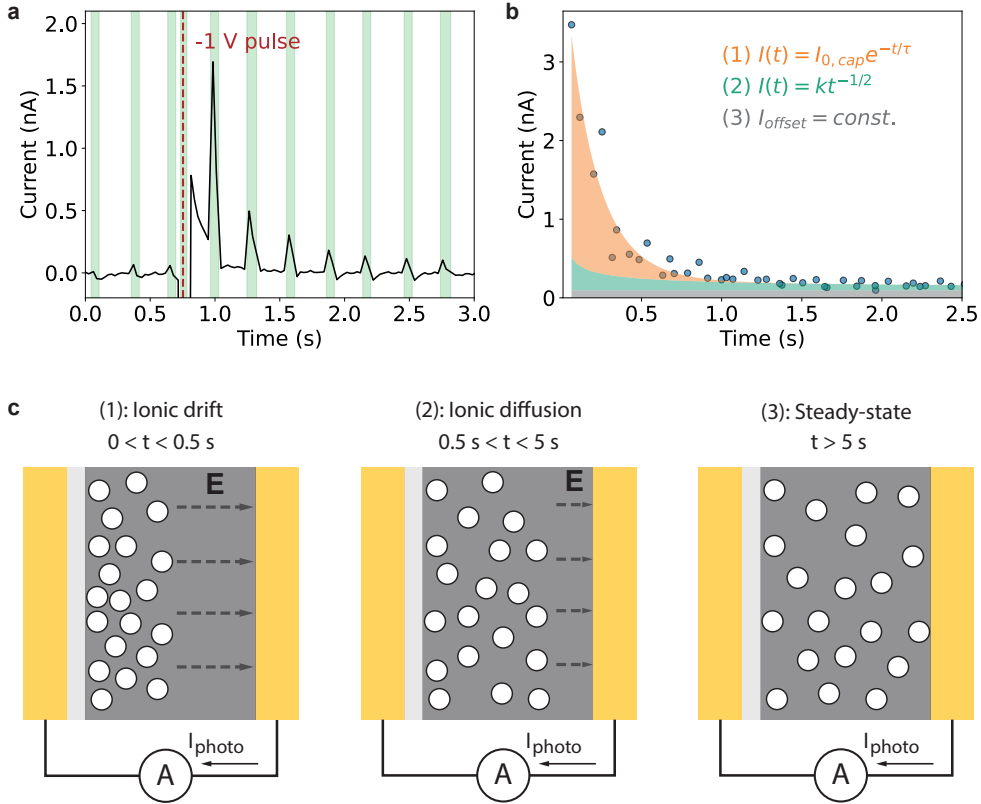


**Figure 4.2:** Setting and reading out of the state of the optoelectronic synapse. A small initial photocurrent is read out when the device is illuminated with a green LED, indicated by the green regions in (a). The photocurrent is increased after applying a  $-1$  V pulse, indicated with the red dotted line, and then decays over several seconds. (b) Photocurrent after applying the  $-1$  V pulse, data from five measurements. Data fitted with drift, diffusion, and a constant offset current:  $I(t) = I_{0,cap}e^{-t/\tau} + kt^{-1/2} + I_{offset}$ . (c) Schematic of the proposed mechanism of the transient photocurrent response. The applied voltage pulse accumulates halide vacancies (white circles) at the cathode, resulting in an electric field inside the perovskite. At  $0 < t < 0.5$  seconds, the vacancies redistribute by a drift process, resulting in an exponential decrease of the induced electric field and hence the measured photocurrent, as captured by equation (1) in (b). For later times,  $0.5 < t < 5$  seconds, the vacancies redistribute predominantly due to diffusion, resulting in a transient current response according to (2). After approximately 5 seconds, further decay becomes negligible and only the constant offset current (3) is measured.

a strongly increased photocurrent of 1.7 nA is measured. The enhanced photocurrent then decays over time as measured with each successive light pulse.

We analyze the photocurrent by repeating the measurement in Figure 4.2a five times. The measured photocurrents are plotted over time in Figure 4.2b, where  $t = 0$  indicates the time where the voltage pulse is removed. To fit the photocurrent decay over time, we assume a decay due to a combined drift and diffusion process, with a constant offset current:  $I(t) = I_{0,cap}e^{-t/\tau} + kt^{-1/2} + I_{offset}$ . This time-dependence of the current follows from the linear regions in plots of the transient photocurrent on the  $t^{-1/2}$  and semi-log scale in Figure 4.A.1a and b, respectively. The obtained fitting parameters are given in Table 4.1. The stacked plot in Figure 4.2b of both contributions demonstrates an initial decay predominantly due to the exponential  $I_{0,cap}e^{-t/\tau}$  term (drift). After approximately 0.5 seconds, the photocurrent decays predominantly according to the  $kt^{-1/2}$  contribution (diffusion).

I-V sweeps of the device in the dark and under constant illumination are given in Figure 4.A.2. Both sweeps show a combined capacitive and resistive response without obvious signs of resistance changes within each scan, as can be seen in perovskite memristive devices.[14] We, therefore, exclude resistance changes as the origin of the photocurrent enhancement. Instead, we propose the model presented schematically in Figure 4.2c. During the applied voltage pulse, the mobile iodide vacancies in the perovskite layer accumulate at the interface between the perovskite and the cathode.[33] The resulting electric field screens the applied voltage inside the perovskite layer. After the voltage is removed, accumulated iodide vacancies induce an electric field inside the perovskite, as indicated in the left panel of Figure 4.2c. This field causes extraction of photogenerated charge carriers.[34] On a timescale of hundreds of milliseconds, the electric field induces the drift of the positively charged halide vacancies away from the cathode. The resulting exponential decrease in the magnitude of the electric field then results in a proportional decay of the photocurrent. After approximately 0.5 seconds, the halide vacancies have partially redistributed in the perovskite layer, as indicated by the middle panel in Figure 4.2c. Now the electric field inside the perovskite is smaller and the ions further re-distribute by a diffusion-limited process, which follows a  $t^{-1/2}$  time dependence.[35] This competition between ionic drift and diffusion currents in memristive devices is well-known for other materials.[36] After the redistribution of the halide vacancies, the device reaches a steady state where only the original small offset current is measured, as shown in the right panel in Figure 4.2c. The origin of this offset current is likely a small electronic asymmetry in the device, e.g. because one electrode is covered with the  $\text{Al}_2\text{O}_3$  layer, or it could be due to a defective perovskite-electrode interface. The decay over hundreds of milliseconds to seconds we measure here is in agreement with previous work on ion migration in halide

**Table 4.1:** Fitting parameters obtained for the data in Figure 4.2b. The offset current  $I_{offset}$  was determined by taking the mean of the photocurrents measured before application of the  $-1$  V pulse. Errors indicate one standard deviation.

| Fitting parameter | Value                         |
|-------------------|-------------------------------|
| $I_{0,cap}$       | $3.9 \pm 0.2$ nA              |
| $\tau$            | $0.19 \pm 0.01$ s             |
| $k$               | $0.11 \pm 0.02$ nA $\sqrt{s}$ |
| $I_{offset}$      | $0.095 \pm 0.014$ nA          |

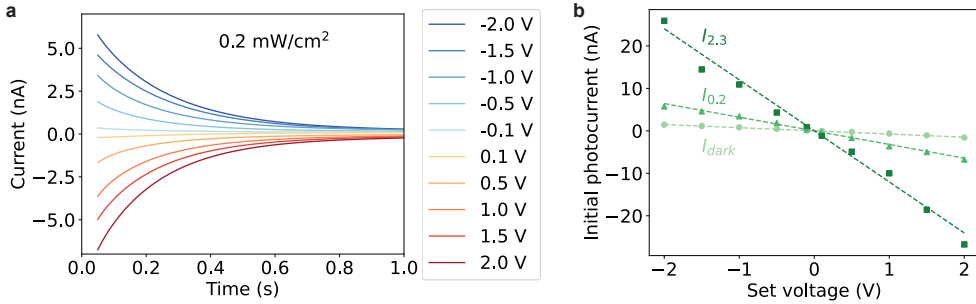
perovskites.[17, 18] Our proposed mechanism is supported by drift-diffusion simulations, given in Figure 4.A.3, which show the accumulation of halide vacancies and resulting build-up of an electric field in the device by a  $-1$  V pulse. The simulations show a redistribution of the vacancies and consequential decay of the electric field over similar timescales as in Figure 4.2b. Figure 4.A.4 demonstrates that there is also an ionic current contribution to the total current measured when a light pulse is applied. However, this contribution is only minor, in line with previous work on similar halide perovskite devices.[17]

Figure 4.A.5 demonstrates that applying a voltage pulse of opposite polarity results in a photocurrent enhancement with a similar magnitude but opposite polarity, following the same combined exponential and power-law decay. This further supports our proposed model, which predicts that the iodide vacancies accumulate at opposite electrodes for positive and negative voltages. The resulting electric fields and photocurrents are, therefore, also of opposite polarity. The ability to tune the polarity of the photocurrent, i.e. the synaptic weight, is a notable feature of the MPOS. Typically, the output current polarity of an artificial synapse is bound to that of a read voltage.[37] Excitatory and inhibitory functioning of a synaptic device in a neuromorphic network are therefore set by the circuitry and applied read voltage. By contrast, the weights of the MPOS can be switched to either positive or negative values for the same input optical pulse. This allows facile switching between inhibitory and excitatory functioning by the same synapse.

### 4.2.3 Modulation of the photocurrent switching

Figure 4.3a demonstrates that the magnitude of the synaptic weight can be tuned by varying the magnitude of the applied voltage. Larger voltage amplitudes, which are expected to cause the accumulation of a larger number of iodide vacancies, cause a larger photocurrent enhancement. In all cases, the photocurrent decays according to the combined drift and diffusion process.

The initial photocurrents at 0.05 seconds in Figure 4.3a are plotted in Figure 4.3b. From this figure, it follows that the magnitude of the photocurrent depends linearly on the applied



**Figure 4.3:** Modulation of the photocurrent change with different voltages and light intensities. **(a)** Fits to transient photocurrent measurements with applied voltage pulses ranging from  $-2.0$  to  $+2.0$  V. All with the same light intensity of  $0.2 \text{ mW/cm}^2$  during the voltage pulse. Larger photocurrent changes are measured for larger voltage amplitudes. **(b)** Comparison of the initial photocurrents, i.e. the photocurrents at 0.05 seconds from the transient current fits, for different applied voltages and light intensities of  $2.3 \text{ mW/cm}^2$  ( $I_{2.3}$ , squares),  $0.2 \text{ mW/cm}^2$  ( $I_{0.2}$ , triangles), and no light ( $I_{dark}$ , circles) during the voltage pulse. Linear fits to the initial photocurrents yield steeper slopes of  $-12.0$  and  $-3.2 \text{ nA/V}$  for  $I_{2.3}$  and  $I_{0.2}$ , respectively, compared to the slope of  $-0.7 \text{ nA/V}$  for  $I_{dark}$ .

voltage. The linear dependence can be explained by ion drift to the electrodes when applying the bias voltage. When the voltage is applied, an electric field is built up in the device according to  $V(t) = V_{sup}(1 - e^{-t/\tau})$ . [38, 39] Assuming the same characteristic time  $\tau$  and using the same duration for each applied voltage pulse  $t$ , the voltage in the device increases linearly with the input voltage  $V_{sup}$ . The linearity of the photocurrent change with respect to the input voltage makes weight changes of the MPOS with different voltages easily predictable. This predictability is important for reliable training of neuromorphic networks. [40]

Figure 4.3b shows that the magnitude of the photocurrent is also altered by the illumination intensity during the voltage pulse. A higher irradiance of  $2.3 \text{ mW/cm}^2$  ( $I_{2.3}$ ) causes a larger photocurrent change compared to a lower irradiance of  $0.2 \text{ mW/cm}^2$  ( $I_{0.2}$ ). The photocurrent change is the smallest when the device is not illuminated during the voltage pulse ( $I_{dark}$ ). The transient photocurrents over the whole voltage range for  $I_{2.3}$  and  $I_{dark}$  are given in Figure 4.A.6. These measurements show a similar photocurrent decay initially dominated by a drift process, which transitions to a diffusion-limited current decay at later times. The greater magnitude of the photocurrent changes at higher illumination intensities can be explained by the higher ionic mobility in halide perovskites under illumination. [22] A higher ionic conductivity during the applied voltage pulse causes a more rapid build-up of the electric field, i.e. accumulation of halide vacancies. The larger electric field in the device leads to a larger photocurrent when light pulses are applied.

The trends we observe for the photocurrent enhancement are not limited to 520 nm light

excitation. Figure 4.A.7 shows the same measurement as in Figure 4.3, repeated with 450 and 620 nm light. These light sources, matched by photon flux to the 520 nm source, give similar photocurrent changes that are linear with the input voltage, demonstrating that the synapse can be operated with wavelengths ranging over the visible spectrum.

The photocurrent enhancement is also generalizable over different perovskites. As an example, we fabricated the same optoelectronic synapses with  $\text{FAPbBr}_3$  and  $\text{FAPb}(\text{I}_{0.5}\text{Br}_{0.5})_3$  active layers. 4.A.8a and b show the absorption spectra of  $\text{FAPbBr}_3$  and  $\text{FAPb}(\text{I}_{0.5}\text{Br}_{0.5})_3$ , respectively. The absorption onset of the perovskite layer shifts to shorter wavelengths for higher bromide contents. The  $-1$  V measurements in 4.A.8c and d (520 nm illumination) and Figure 4.A.9a and b (450 nm illumination), as well as the corresponding input voltage and illumination intensity sweeps in 4.A.8e and f and Figure 4.A.9c and d show the same trends for these perovskite compositions as for the  $\text{MAPbI}_3$  films. These results show that we can exploit the easily tunable band gap of halide perovskites to fabricate optoelectronic synapses that are only sensitive to specific wavelengths of light.

An important feature of the MPOS is that the synaptic weight of the device is changed with electronic pulses while it is read out with light pulses. Typically, both occur with the same type of input, i.e., all electronically or all optically, which can result in accidental weight changes during read-out.[12, 41] Three-terminal synaptic transistors prevent this issue by using two lateral electrodes for read-out and a third gate electrode for weight updates.[42, 43] However, this comes at the cost of higher device complexity and size and, therefore, scalability. Using optical signals for read-out and electronic signals for weight updates prevents accidental weight changes while maintaining the scalability of two-terminal devices.

#### 4.2.4 Optoelectronic STDP measurements

To demonstrate learning by the MPOS, we perform STDP measurements. A classic example of STDP-like learning in neuromorphic networks is inspired by Pavlovian conditioning, typically demonstrated in simple two-input, one-output networks. The first input (“sight of food”) and the output neuron (“salivation”) are initially correlated, meaning they are connected by a synapse with a high weight. In all-electronic neuromorphic networks, this is implemented as a high conductance of the synapse. The second input (“ringing of a bell”), on the other hand, is initially not correlated to the same output, which is implemented as a low synaptic weight, or low conductance of the second synapse. Due to the difference in the synaptic weights, initially inputs through the high-conductance synapse cause spiking by the output neuron, while inputs through the low-conductance synapse do not. However, by presenting both inputs simultaneously, this simple network can learn to associate the two inputs through STDP. In STDP, back-propagating pulses are generated by the neuron

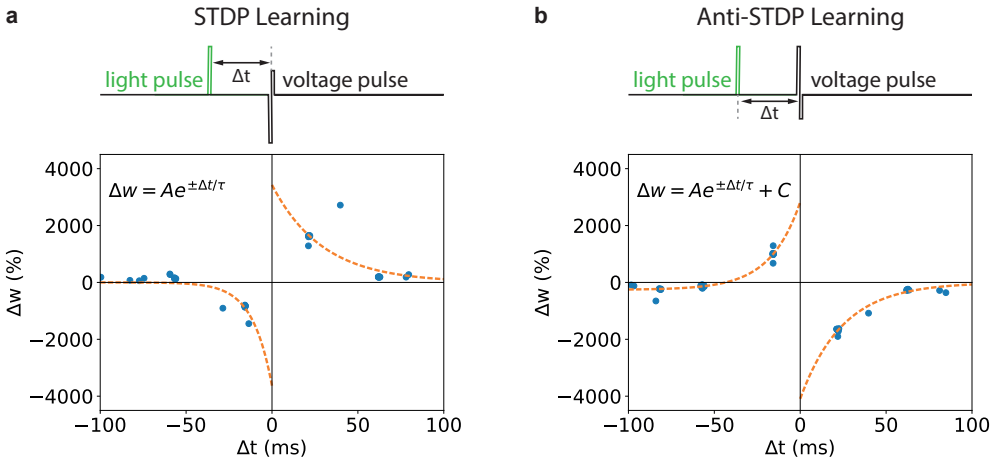


**Figure 4.4:** STDP learning rules applied to the synapse. Applying a  $-1$  to  $+0.5$  V pulse results in STDP learning in (a), while a  $+1$  V to  $-0.5$  V pulse leads to anti-STDP learning in (b). The weight updates were fit to exponential decay or growth, with the addition of an offset in (b) to prevent overestimation of the exponential growth for  $-\Delta t$  due to the negative data points at  $\Delta t < -50$  ms. Highly symmetric weight changes are obtained for STDP and anti-STDP learning, as well as for  $+\Delta t$  and  $-\Delta t$  within both learning rules.

as it spikes due to inputs through the high-conductance synapse. Overlap with simultaneous inputs through the low-conductance synapse results in a voltage drop that is large enough to increase its weight. After learning, presenting only the second input is enough to cause spiking of the output neuron, i.e. ringing the bell causes salivation by the dog.[44–46] STDP learning is commonly employed in large neuromorphic networks,[47] for example for the recognition of complex patterns, such as handwritten digits.[48]

Figure 4.4 shows optoelectronic STDP measurements of the MPOS. Contrary to the simpler voltage pulse application shown in Figure 4.3, here we apply an initial  $-1$  or  $+1$  V pulse, which is followed immediately by a  $0.5$  V pulse with the opposite polarity. At the same time, a light pulse is introduced with different time delays with respect to the applied voltage profile, shown schematically in the top parts of Figure 4.4a and b. The weight update is now dominated by the initial  $\pm 1$  V or the following  $\pm 0.5$  V pulse, depending on which part of the voltage profile overlaps with the light pulse. In a neuromorphic network employing STDP-learning, this voltage profile would be applied by a firing artificial neuron. If the input precedes the firing of the neuron (positive  $\Delta t$ ), there is a causal relationship between the input and the firing, and the synaptic weight will increase. In our implementation, this is due to the overlap between the light pulse and the  $-1$  V pulse. The resulting increase in photocurrent corresponds to the increase in synaptic weight. Conversely, if the input follows after the firing of the neuron (negative  $\Delta t$ ), signifying an anti-causal relationship, the weight will be decreased. Here, this is brought about by the overlap of the light pulse with

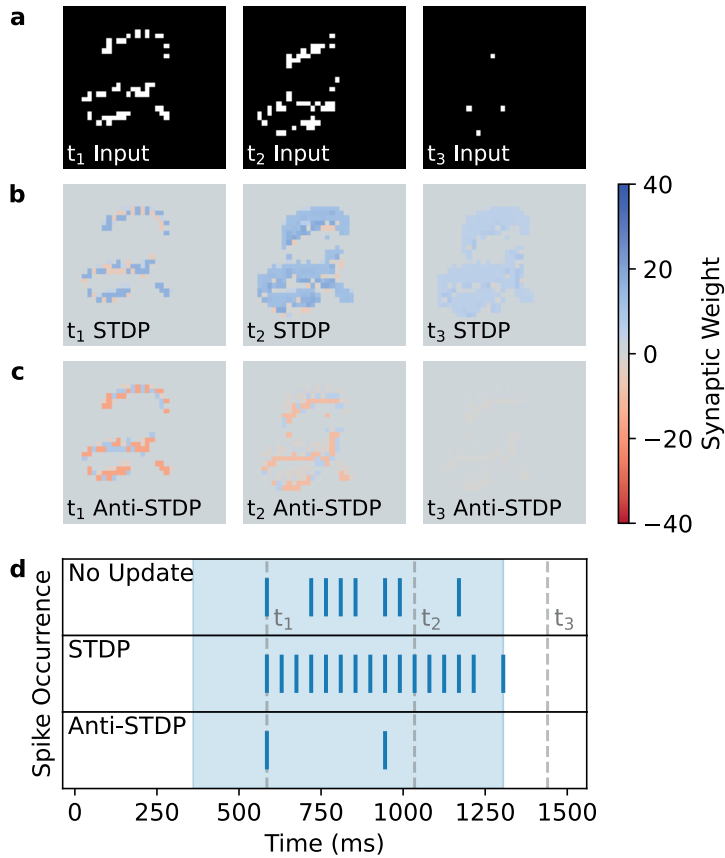
the +0.5 V pulse, resulting in a lower photocurrent. In this way, STDP allows associative learning in a neuromorphic network.

Figure 4.4a demonstrates that the MPOS shows STDP learning for a  $-1$  to  $+0.5$  V pulse and light pulse inputs with different time delays. Similar to the photocurrent changes in Figure 4.3, we can obtain the inverse weight changes by applying a  $+1$  to  $-0.5$  V pulse in Figure 4.4b, resulting in anti-STDP learning. The high symmetry of the (anti-)STDP responses of the synapse allows predictable updates of the synaptic weights, which is important for reliable learning in neuromorphic networks.[40] In both cases, large weight updates of up to 2000% are obtained. This large dynamic range allows for easy distinction of different states of the MPOS. Both positive and negative photocurrents can be achieved within each STDP learning rule, depending on the sign of the time delay. Importantly, this shows that the simple STDP learning rule is sufficient to support the unique advantage of switching between inhibitory and excitatory functioning of the synapse.

#### 4.2.5 A neuromorphic camera with attention-based learning

We envision that these results could be particularly interesting for the development of neuromorphic detectors that process visual information. Modern state-of-the-art software neural networks based on transformer models achieve high classification accuracies by employing an attention mechanism to focus only on the relevant regions of an image.[3, 4] A detector consisting of dense cross-bar arrays of the MPOS could employ a similar mechanism through STDP. To showcase this application, we simulated two-dimensional arrays of the synapses connected to a leaky integrate-and-fire neuron. The arrays are illuminated with a moving hand-written digit sample from the N-MNIST dataset,[49] and the resulting photocurrent is integrated by the neuron. Neuron spikes are used as a feedback signal to update the synaptic weights depending on the simultaneous illumination condition of each synapse. Feedback neuron spikes were simulated as simple  $-1$  V pulses, as in Figure 4.2b, or the (anti-)STDP pulses from Figure 4.4, to represent all experimentally demonstrated update rules in this work (see Section 4.A.1 in the Appendix for more details).

Figure 4.5 shows three points in time of the simulations of arrays implementing STDP and anti-STDP learning. Figure 4.5a shows the three input frames of the N-MNIST sample at these times. The first neuron spike occurs at time  $t_1$ , as the left image is presented. The left frame in Figure 4.5b shows the synaptic weights after an STDP weight update by this spike. The weights of the synapses that were illuminated right before the neuron spiked have increased, in accordance with the measurements in Figure 4.4a. As is evident from Figure 4.5d, the increased weights, i.e. higher photocurrents, of the synapses in the array



**Figure 4.5:** Simulations of an attention mechanism for arrays of the optoelectronic synapses connected to a simple leaky integrate-and-fire neuron. Frames of an N-MNIST sample number 2 are projected on the arrays over time. (a) Frames of the sample at different times of interest. (b), (c) The synaptic weights of optoelectronic synapse arrays implementing STDP and anti-STDP learning, respectively, taken after projecting the frames in (a) on the arrays. (d) Event-plot of the neuron spikes over time for arrays implementing either no synaptic weight updates (“No Update”), or the STDP and anti-STDP weight updates from (b) and (c). After each neuron spike, all synaptic weights in the arrays are updated according to their respective update rule. The blue-shaded region indicates the simulation times between 360 ms to 1305 ms where the input number 2 is visible in the N-MNIST frames, which should cause spiking by the neuron. The first neuron spike occurs at time  $t_1$  (585 ms), after input of the left panel in (a). The spike causes positive synaptic weight changes for the STDP array (left panel in (b)), and negative weights changes for the anti-STDP array (left panel in (c)). At time  $t_2$  (1035 ms) the frame in the middle panel in (a) is projected on the arrays. The resulting photocurrent is not high enough to cause spiking for the array that does not implement weight updates. The higher photocurrents output by the STDP array (middle panel in (b)) are large enough to cause spiking, while the negative photocurrents output by the anti-STDP array (middle panel in (c)) suppress spiking. After 1305 ms, only noise is projected on the arrays and no further spiking is recorded, resulting in decay of the synaptic weights. The noise projected on the arrays at time  $t_3$  (1440 ms) is shown in the right panel in (a). The decaying synaptic weights are shown in the right panels of (b) and (c).

cause a higher spiking frequency of the neuron with subsequent inputs. On the other hand, the left frame of Figure 4.5c shows the synaptic weights for an array implementing anti-STDP learning. Synapses that were illuminated right before the spike have their weights decreased, as in Figure 4.4b. Figure 4.5d shows that this change reduces the neuron spike frequency for later inputs.

The synaptic weights are updated according to the STDP and anti-STDP learning rules from Figure 4.4 as the handwritten digit moves downwards between  $t_1$  and  $t_2$ , shown in the middle panel in Figure 4.5a. STDP learning causes the weights to increase dynamically based on the movement of the digit, as shown in the middle panel of Figure 4.5b, while they are decreased for anti-STDP learning, illustrated by the middle panel of Figure 4.5c. After the digit is no longer visible and only noise is presented to the array at time  $t_3$  in the right panel in Figure 4.5a, the volatility of the synapses causes the weights to decay, as demonstrated by the right panels in Figure 4.5b and c. Importantly, this prevents spiking of the neuron due to noise and resets the weights in the arrays for new input features of interest.

The simulations show that, even though voltage pulses are applied to all synapses in the array, the optoelectronic STDP learning rule we implement in Figure 4.4a only increases the weights of the synapses detecting the feature of interest. This attention mechanism causes the array to adaptively focus on the digit, allowing the neuron to respond more quickly to the input. Anti-STDP learning, on the other hand, can be implemented to reduce attention, forcing the neuron to ignore specific features. This way, the synapse array combines the filtering and working memory applications of volatile synapses. The transient photocurrent enhancement can be seen as a working memory that keeps track of the location of features of interest to filter visual data and focus only on relevant stimuli. The device design allows for flexible tuning of the response parameters.  $\text{FAPbBr}_3$  and  $\text{FAPb}(\text{I}_{0.5}\text{Br}_{0.5})_3$  layers could be incorporated into the arrays, as demonstrated by 4.A.8 and Figure 4.A.9, for finer control over attention by not only considering the light intensity, but also its wavelength. This is especially relevant for more complex input images that contain different colors.[32] Apart from that, Figure 4.A.14 shows a more top-down attention mechanism that can be realized by applying voltage pulses to only a subset of synapses in the array. A similar algorithm has been proposed before, and could be implemented for more complex inputs, for example in image processing for autonomous vehicles.[50]

Recently, similar detectors of volatile memristive devices employing an attention mechanism have been proposed, based on synaptic transistors of two-dimensional materials,[50, 51] or a metal oxide active layer.[32] On the device level, the two-terminal architecture and the easier deposition of the halide perovskite layer over large areas make our MPOS easier

to scale compared to these implementations. Moreover, light absorption by the halide perovskite layer can be tuned into the visible spectrum by altering its composition, giving more control over the attention mechanism. On the algorithm side, the optoelectronic (anti-)STDP updates we present here remove the need to determine which synapses to update by a top-down approach and instead allow a more easily implemented bottom-up attention mechanism. This way the synapses leverage the unique combination of light-dependent mixed ionic-electronic conductivity, tunability of the bandgap, and facile deposition of halide perovskites to enable neuromorphic detectors with more biologically plausible learning.

### 4.3 Conclusion

In summary, we have demonstrated microscale volatile optoelectronic synapses made from  $\text{MAPbI}_3$ ,  $\text{FAPbBr}_3$ , and  $\text{FAPb}(\text{I}_{0.5}\text{Br}_{0.5})_3$  halide perovskites. The MPOS leverage mobile ions to form a transient electric field after applying a bias voltage, resulting in volatile photocurrent changes upon illumination of the device. We have shown that the magnitude and polarity of the photocurrent are tunable with the applied voltage and light intensity due to the higher iodide-vacancy mobility under illumination and the larger electric field build-up for higher applied voltages. Important features of the MPOS are the separation of electronic writing and photonic read-out, preventing accidental changes in the synaptic weight, and the accessibility of both positive and negative synaptic weights, which allows easy switching between excitatory and inhibitory functioning. The MPOS showed learning based on STDP weight updates, and we simulated how this learning rule could be implemented for a bottom-up attention mechanism in neuromorphic sensors to focus on regions of interest in visual data. Sensors that are only sensitive to parts of the visible spectrum could be fabricated by changing the halide perovskite in the synapse, giving further control over the attention mechanism. The easy scalability of our two-terminal microscale devices and the broad absorption range make the MPOS particularly well-suited for this application. Moreover, the mild fabrication conditions allow easy implementation of the MPOS with existing memristive or CMOS-based neuromorphic networks, extending even to novel implementations on flexible substrates.

## 4.4 Materials and Methods

### 4.4.1 Materials

Si wafers with a 100 nm dry thermal oxide layer were purchased from Siegert Wafer.  $\text{PbI}_2$  (99.99%),  $\text{PbBr}_2$  (99.99%), and formamidinium iodide (FAI, 99.99%) were purchased from TCI. Methylammonium iodide (MAI) was purchased from Solaronix.  $\text{Al}(\text{CH}_3)_3$  (97%), formamidinium bromide (FABr, >98.0%) and anhydrous DMF, DMSO, and chlorobenzene were purchased from Sigma-Aldrich. MA-N1410 resist and its corresponding MA-D533/s developer were purchased from Micro Resist. All materials were used without further purification.

### 4.4.2 Fabrication of the optoelectronic synapse

Gold bottom electrodes were patterned on the silicon wafer with the thermal oxide layer using a lift-off process with MA-N1410 photoresist. The resist was exposed to UV light in a Süss MA6/BA6 mask aligner. The exposed resist was developed in MA-D533/s. A chrome adhesion layer (5 nm) and the gold electrode layer (80 nm) were deposited on the patterned resist by e-beam physical vapor deposition. Lift-off was performed by soaking in acetone for one hour. A 15 nm  $\text{Al}_2\text{O}_3$  layer was deposited in a home-built atomic-layer deposition setup at 250 °C, using  $\text{Al}(\text{CH}_3)_3$  and  $\text{H}_2\text{O}$  as the precursor gasses. The gold top electrodes were patterned perpendicular to the bottom electrodes using the same UV lithography procedure.

Inside a  $\text{N}_2$ -filled glovebox,  $\text{MAPbI}_3$ ,  $\text{FAPbBr}_3$ , and  $\text{FAPb}(\text{I}_{0.5}\text{Br}_{0.5})_3$  precursors were mixed by dissolving stoichiometric 1.1 mmolar mixtures of the respective solids in 1 mL DMF and 0.1 mL DMSO. The precursors were filtered with 0.2  $\mu\text{m}$  PTFE filters and spin coated over the gold electrodes at 4000 rpm for 30 seconds with a SCIPRIOS SpinCoating Robot. Chlorobenzene (250  $\mu\text{L}$  per substrate) was added after 5 seconds of spinning as an anti-solvent to induce crystallization. The substrates were annealed at 100 °C for 10 minutes directly after spin coating. The devices were then encapsulated by adding a drop of Blu-fixx epoxy on the active area. A glass coverslip was dropped on the epoxy, which was cured with a UV torch for 1 minute afterward. The same spin coating procedure was followed to deposit the three perovskite layers on quartz substrates for absorption measurements.

### 4.4.3 UV/Vis absorption measurements

Absorption measurements were performed from 250 to 900 nm with a Perkin Elmer Lambda 750 UV/Vis/NIR spectrophotometer inside an integrating sphere. Deuterium

and tungsten-halogen lamp light sources and an InGaAs detector were used for the measurements.

#### 4.4.4 Photocurrent measurements

All electronic measurements were performed with a Keysight B2902A Precision Source/Measure Unit. One channel of the SMU was used to apply voltage pulses to and measure the current of the synapse, while a second channel was used to drive the 450, 520, or 620 nm high power Cree XLamp XP-E LEDs. Irradiances were measured with a Thorlabs PM100D optical power meter with a S120VC sensor.

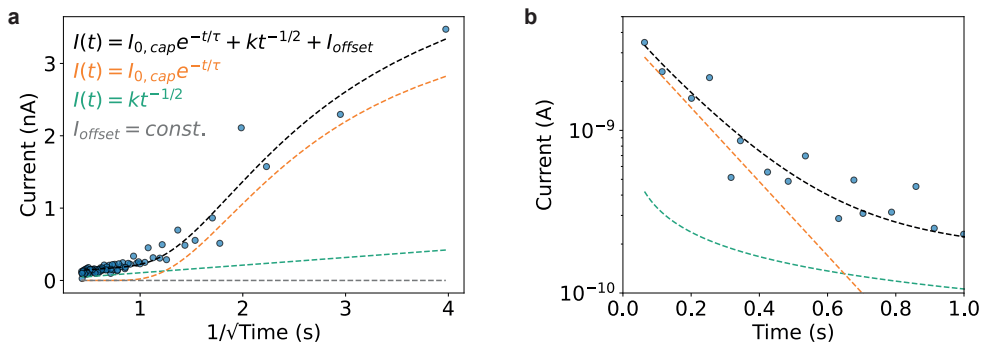
#### 4.4.5 Drift-diffusion measurements

Drift-diffusion simulations were carried out with the software package Setfos by Fluxim. The device parameters are listed in Table 4.2. We simulated the relaxation of the potential and mobile ion density at 0 V after removing the initially applied voltage of 1 V.

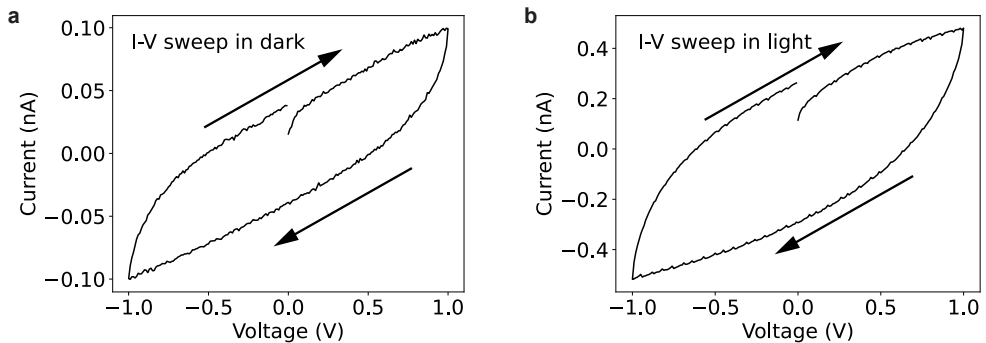
**Table 4.2:** Simulation parameters used for the drift-diffusion simulations.

| Parameter  | Value              | Reference |
|--|--------------------|-----------|
| Thickness insulator (nm)   | 15                 |           |
| Relative permittivity insulator  | 9                  |           |
| Electron affinity insulator (eV)   | 2.5                |           |
| Band gap insulator (eV)  | 5                  |           |
| Thickness perovskite (nm)  | 50                 |           |
| Relative permittivity perovskite   | 24.1               | [52]      |
| Electron affinity perovskite (eV)  | 3.9                | [53]      |
| Band gap perovskite (eV)   | 1.6                | [53]      |
| Effective density of states perovskite conduction band ( $1/\text{cm}^3$ ) | $8 \times 10^{18}$ |           |
| Effective density of states perovskite valence band ( $1/\text{cm}^3$ )    | $8 \times 10^{18}$ |           |
| Mobile positive ion density ( $1/\text{cm}^3$ )                            | $3 \times 10^{17}$ |           |
| Immobile negative ion density ( $1/\text{cm}^3$ )                          | $3 \times 10^{17}$ |           |
| Work function electrodes (eV)  | 5.1                |           |

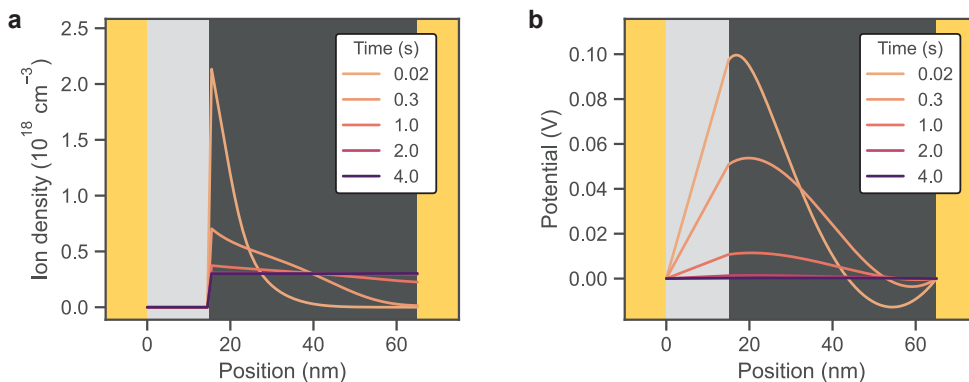
#### 4.A Additional information



**Figure 4.A.1:** Plots of the measured photocurrents from Figure 4.2b on different scales for fitting of the data. (a) Plot on the  $t^{-\frac{1}{2}}$  scale. The linear increase of the photocurrent until approximately  $1.5 \text{ sec}^{-\frac{1}{2}}$  indicates a current decay with  $t^{-\frac{1}{2}}$  proportionality for  $t > \frac{1}{1.5^2} \approx 0.44$  seconds, in line with a diffusion-limited process. (b) Plot on the semi-log scale. The plot shows a linear decrease in the current for the times before approximately 0.5 seconds, which can be explained by a capacitive drift current.

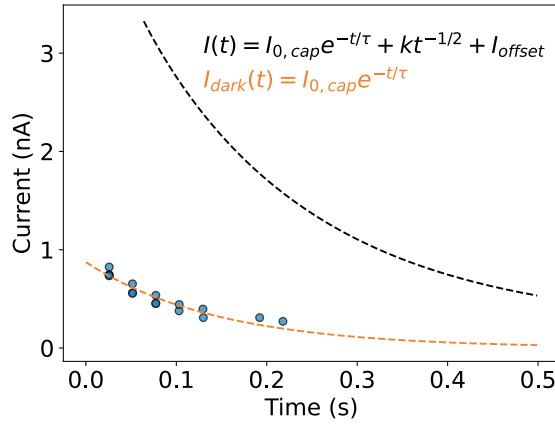


**Figure 4.A.2:** I-V sweeps of the device under different illumination conditions. (a) An I-V sweep in the dark. (b) An I-V sweep on the same device under illumination with a 520 nm LED, at an irradiance of  $0.2 \text{ mW/cm}^2$ . For both plots, the arrows indicate the current measured at each voltage sweep direction. The plots were obtained by averaging the current over three consecutive measurements to reduce noise. The current responses are typical for a capacitive displacement, combined with a resistive current. A larger current is measured for the device as it is illuminated, indicating a lower resistance. No significant changes in the resistance of the device were measured within either scan.

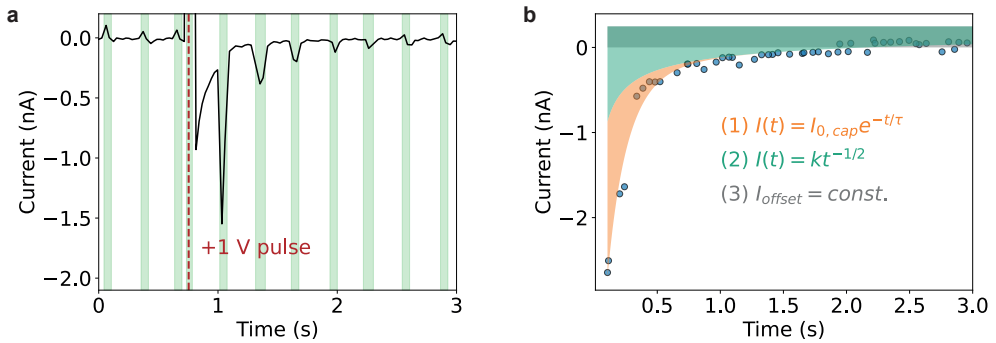


**Figure 4.A.3:** Drift-diffusion simulation of the device after removal of a  $-1$  V pulse at time = 0 s. **(a)** The halide vacancy distribution after the pulse. **(b)** The resulting potential in the device after the pulse. The initial accumulation of halide vacancies at the  $\text{Al}_2\text{O}_3$ -covered cathode results in a potential in the device. The vacancies redistribute over approximately 4.0 seconds, causing a decay of the potential.

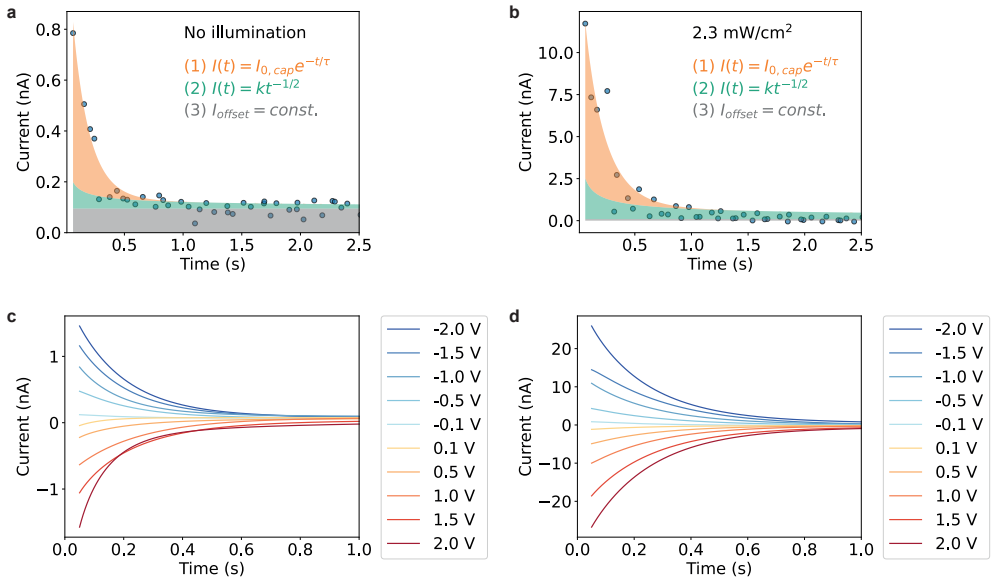
Figure 4.A.4 shows a fit to the current in dark after a  $-1$  V pulse is applied and before application of a light pulse. The data is taken from the same measurements as Figure 4.2b in the main text. The data is fit with an exponential decay (fitting parameters were  $I_{0,cap} = 0.87 \pm 0.04$  nA, and  $\tau = 0.15 \pm 0.01$  s). Fitting with an additional diffusion term was not successful, which is likely due to the relatively low contribution of this term for these short timescales. The decay time on the hundreds of milliseconds timescale implies that this is the ionic drift current in the dark. The black curve represents the fit to the photocurrent from Figure 4.2b. From the fits it follows that the ionic current contributes 17% to the total current at 0.06 seconds, when the first light pulse is applied. For later times, the fits suggest that the relative contribution of the ionic current decreases due to the lack of a diffusion and constant offset term for the current in dark.



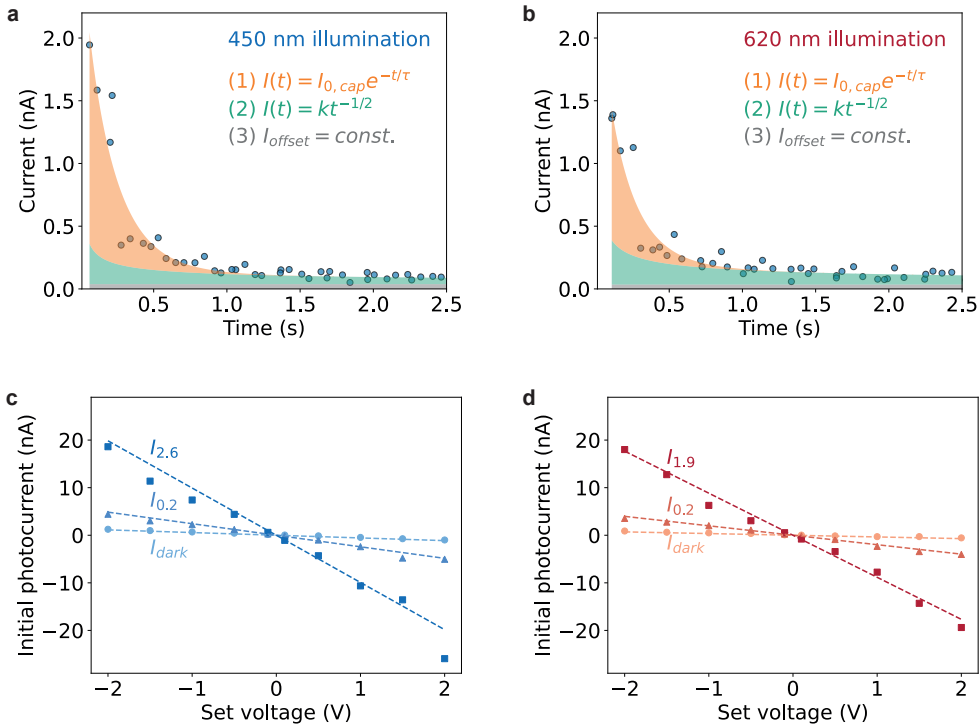
**Figure 4.A.4:** Fit of the current in dark measured after the  $-1$  V pulse and before the first light pulse in Figure 4.2a and b in the main text. Data taken from the same 5 measurements as in Figure 4.2b in the main text. The dark current is fit to an exponential decay and compared to the fit to the measured photocurrents from Figure 4.2b.



**Figure 4.A.5:** Setting and reading out of the state of the optoelectronic synapse with a  $+1$  V applied pulse. **(a)** Measured photocurrents over time. Similar to the measurement in Figure 4.2a, a small initial photocurrent is read out when the device is illuminated with a green LED, indicated by the green regions. After applying the  $+1$  V pulse, indicated by the red dotted line, a negative photocurrent is read out with consecutive light pulses, which decays to the initial photocurrent from before the voltage pulse over time. **(b)** Fitting of the photocurrents in **(a)** over time, after applying a  $+1$  V at time  $= 0$  s. The blue markers indicate the measured photocurrents over five measurements. The same fitting equation that considers a combined ionic drift and diffusion process for the current decay, combined with a constant offset current was used to fit the transient photocurrent:  $I(t) = I_{0,cap}e^{-t/\tau} + kt^{-1/2} + I_{offset}$ .



**Figure 4.A.6:** Fitting of the photocurrents over time for different illumination intensity conditions. **(a)** Shows the photocurrents over time after a  $-1$  V pulse without illumination, while **(b)** shows the data for simultaneous illumination with a  $2.3 \text{ mW/cm}^2$  irradiance. The blue markers indicate the measured photocurrents over five measurements. The transient photocurrent was fit using the same equation as in Figure 4.2b:  $I(t) = I_{0, cap} e^{-t/\tau} + kt^{-1/2} + I_{offset}$ . A similar initial drift followed by a diffusion-limited photocurrent decay is obtained for both conditions. Fitting parameters are given in Table 4.A.1. **(c)** and **(d)** show fits of transient photocurrent measurements with applied voltage pulses ranging from  $-2.0$  to  $+0.5$  V for no illumination or illumination with a  $2.3 \text{ mW/cm}^2$  irradiance during the voltage pulse, respectively. Larger photocurrent changes are measured for larger voltage amplitudes and for higher irradiance during the voltage pulse.



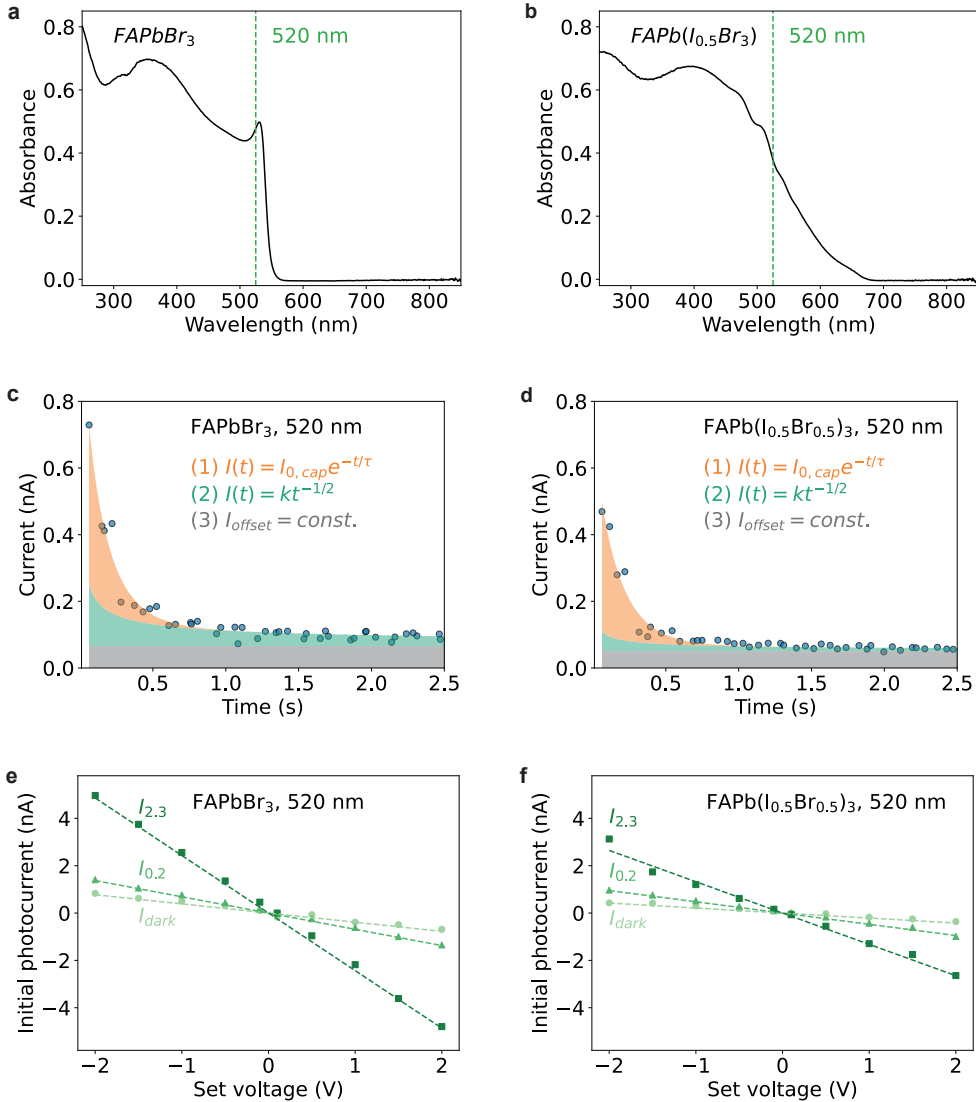
**Figure 4.A.7:** Fitting of the photocurrents over time for different wavelengths of light. **(a)** Fits of the measured photocurrent after applying a  $-1$  V pulse at time  $= 0$  s with simultaneous illumination with 450 nm light, with a  $0.24$   $\text{mW}/\text{cm}^2$  irradiance. **(b)** The same experiment as in **(a)**, repeated with 620 nm light, with a  $0.18$   $\text{mW}/\text{cm}^2$  irradiance. The power densities were adjusted to ensure equal photon flux for each of the three wavelengths of light. The blue markers indicate the measured photocurrents over five measurements. Similar to before, the transient photocurrent was fit with:  $I(t) = I_{0, cap} e^{-t/\tau} + kt^{-1/2} + I_{offset}$ . A similar initial drift followed by a diffusion-limited photocurrent decay is obtained for both wavelengths. Fitting parameters are given in Table 4.A.1. **(c)** Comparison of the photocurrents at 0.05 seconds, obtained from the transient current fits, for different applied voltages, and 450 nm light intensities of  $2.6$   $\text{mW}/\text{cm}^2$  ( $I_{2.6}$ , squares),  $0.2$   $\text{mW}/\text{cm}^2$  ( $I_{0.2}$ , triangles), and no light ( $I_{dark}$ , circles) during the voltage pulse. Slopes of the linear fits of the initial photocurrents are  $-9.9$ ,  $-2.4$ , and  $-0.6$   $\text{nA}/\text{V}$  for  $I_{2.6}$ ,  $I_{0.2}$ , and  $I_{dark}$ , respectively. **(d)** The same measurements repeated for 620 nm light excitation, with irradiances of  $1.9$   $\text{mW}/\text{cm}^2$  ( $I_{1.9}$ , squares),  $0.2$   $\text{mW}/\text{cm}^2$  ( $I_{0.2}$ , triangles), and no light ( $I_{dark}$ , circles) during the voltage pulse. The obtained slopes of  $I_{1.9}$ ,  $I_{0.2}$ , and  $I_{dark}$  are respectively  $-8.8$ ,  $-2.0$ , and  $-0.4$   $\text{nA}/\text{V}$ .

Figure 4.A.7 shows similar photocurrent changes observed in Figure 4.2b and 4.3b for 450 and 620 nm light. For both light sources, the photocurrent is enhanced after applying a  $-1$  V pulse, as shown in Figure 4.A.7a and b. After initial drift-dominated decay, the photocurrent then decays further by a diffusion-limited process. Fitting parameters of the measurements are given in Table 4.A.1.

Similar to the 520 nm experiments in Figure 4.3b, the photocurrent changes for the 450 and 620 nm light sources are linear with respect to the input voltage and more significant under higher irradiances, as follows from Figure 4.A.7c and d and the fitting parameters. The larger photocurrent changes for the 450 nm light can be explained by the higher absorption by the MAPbI<sub>3</sub> layer for this wavelength of light (see the UV/Vis absorption spectrum in Figure 4.1c).

**Table 4.A.1:** Fitting parameters for the measurements performed with different irradiance (Figure 4.A.6a and b) or wavelength (Figure 4.A.7a and b) during the  $-1$  V pulse. Errors indicate one standard deviation.

| Illumination conditions         | $I_{0,cap}$ (nA) | $\tau$ (s)      | $k$ (nA $\sqrt{s}$ ) | $I_{offset}$ (nA) |
|---------------------------------|------------------|-----------------|----------------------|-------------------|
| No illumination                 | $0.97 \pm 0.09$  | $0.14 \pm 0.01$ | $0.026 \pm 0.016$    | $0.074 \pm 0.011$ |
| 520 nm, 2.3 mW/cm <sup>2</sup>  | $13.0 \pm 1.4$   | $0.19 \pm 0.02$ | $0.61 \pm 0.33$      | $-0.33 \pm 0.22$  |
| 450 nm, 0.24 mW/cm <sup>2</sup> | $2.3 \pm 0.2$    | $0.20 \pm 0.02$ | $0.080 \pm 0.054$    | $0.038 \pm 0.035$ |
| 620 nm, 0.18 mW/cm <sup>2</sup> | $1.9 \pm 0.2$    | $0.18 \pm 0.02$ | $0.12 \pm 0.04$      | $0.035 \pm 0.028$ |



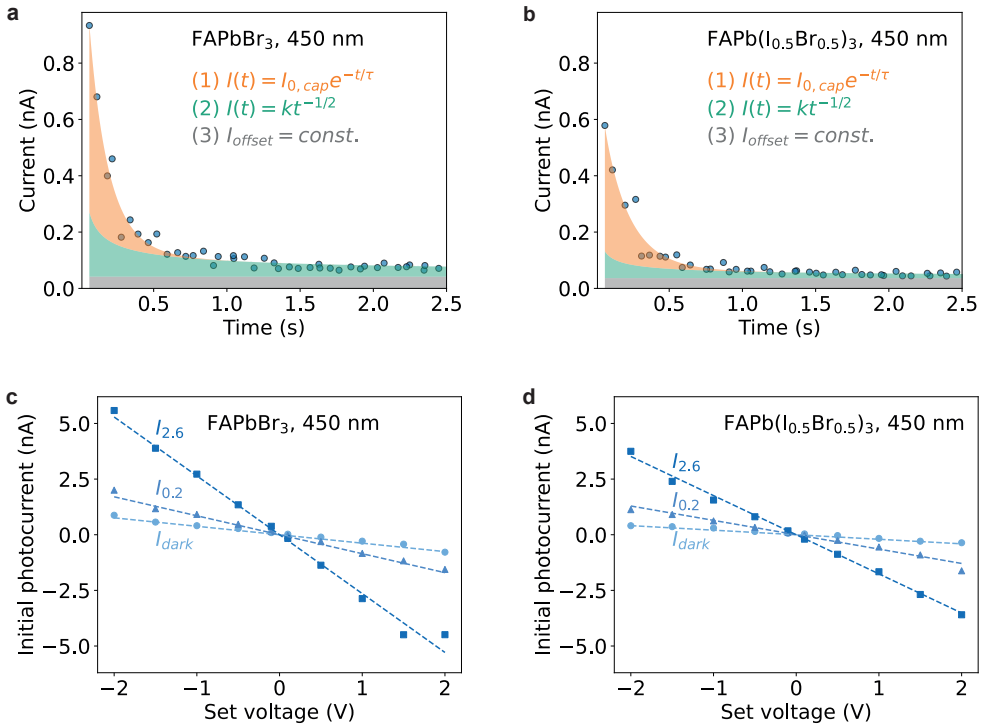
**Figure 4.A.8:** Optoelectronic synapse measurements on devices with FAPbBr<sub>3</sub> and FAPb(I<sub>0.5</sub>Br<sub>0.5</sub>)<sub>3</sub> halide perovskite active layers with 520 nm light. (a), (b) Absorption spectra of, respectively, FAPbBr<sub>3</sub> and FAPb(I<sub>0.5</sub>Br<sub>0.5</sub>)<sub>3</sub> on quartz substrates. The absorption onsets shift to lower wavelengths for perovskite layers with a larger bromide content. (c), (d) Fits to transient photocurrent measurements with a  $-1$  V pulse at  $t = 0$  seconds and 520 nm light illumination with a  $0.2$  mW/cm<sup>2</sup> irradiance. Both devices show similar decays, with a larger photocurrent measured for the FAPbBr<sub>3</sub>-device. (e), (f) Linear fits to initial photocurrents obtained for different set voltages and illumination intensities of  $2.3$  mW/cm<sup>2</sup> ( $I_{2.3}$ , squares),  $0.2$  mW/cm<sup>2</sup> ( $I_{0.2}$ , triangles), or no illumination ( $I_{dark}$ , circles). For the FAPbBr<sub>3</sub> device, the slopes of  $I_{2.3}$ ,  $I_{0.2}$ , and  $I_{dark}$  were  $-2.4$ ,  $-0.7$ , and  $-0.4$  nA/V, respectively. The slopes of  $I_{2.3}$ ,  $I_{0.2}$ , and  $I_{dark}$  for the FAPb(I<sub>0.5</sub>Br<sub>0.5</sub>)<sub>3</sub> device were respectively  $-1.3$ ,  $-0.5$ , and  $-0.2$  nA/V.

Figure 4.A.8 shows that optoelectronic synapses can be fabricated with  $\text{FAPbBr}_3$  and  $\text{FAPb}(\text{I}_{0.5}\text{Br}_{0.5})_3$  active layers as well. The absorption spectra of  $\text{FAPbBr}_3$  and  $\text{FAPb}(\text{I}_{0.5}\text{Br}_{0.5})_3$  in Figure 4.A.8a and b, respectively, show that the absorption onset of these perovskites shift to shorter wavelengths for more bromide-containing perovskites. Figure 4.A.8c and d show measurements of photocurrent modulation with a  $-1$  V pulse. Both perovskites show similar photocurrent enhancements and decays, again first dominated by drift, followed by diffusion at later times. Figure 4.A.8e and f show the expected higher photocurrent enhancement for larger voltage amplitudes and illumination intensities. The slightly larger photocurrent enhancement of the  $\text{FAPbBr}_3$  device can be explained by the higher 520 nm light absorption of this film.

Figure 4.A.9a and b show similar photocurrent decays for measurements with 450 nm illumination. Both devices show slightly higher photocurrents compared to the 520 nm illumination conditions in Figure 4.A.8c and d. The fits to the initial photocurrents with respect to the set voltage in Figure 4.A.9c and d are also slightly steeper compared to those in Figure 4.A.8e and f. Both discrepancies can be explained by the higher absorbance for shorter wavelengths of both perovskites, as follows from the absorption spectra in Figure 4.A.8a and b. Fitting parameters for the measurements in Figure 4.A.8c and d and Figure 4.A.9a and b are given in Table 4.A.2. For both wavelengths, the photocurrent enhancement is much less significant compared to the measurements on the  $\text{MAPbI}_3$  device in Figure 4.2b and Figure 4.3b. This can be explained by the higher mobility of iodide vacancies in  $\text{MAPbI}_3$  perovskites.[54, 55]

**Table 4.A.2:** Fitting parameters for the measurements on the  $\text{FAPbBr}_3$  and  $\text{FAPb}(\text{I}_{0.5}\text{Br}_{0.5})_3$  devices in Figure 4.A.8c and d and Figure 4.A.9a and b. Errors indicate one standard deviation.

| Illumination conditions                                 | $I_{0, \text{cap}}$ (nA) | $\tau$ (s)      | $k$ (nA $\sqrt{\text{s}}$ ) | $I_{\text{offset}}$ (nA) |
|---|--------------------------|-----------------|-----------------------------|--------------------------|
| $\text{FAPbBr}_3$ (520 nm)                              | $0.71 \pm 0.05$          | $0.16 \pm 0.01$ | $0.046 \pm 0.010$           | $0.066 \pm 0.006$        |
| $\text{FAPbBr}_3$ (450 nm)                              | $1.0 \pm 0.1$            | $0.14 \pm 0.01$ | $0.056 \pm 0.01$            | $0.042 \pm 0.07$         |
| $\text{FAPb}(\text{I}_{0.5}\text{Br}_{0.5})_3$ (520 nm) | $0.56 \pm 0.04$          | $0.17 \pm 0.01$ | $0.015 \pm 0.008$           | $0.050 \pm 0.005$        |
| $\text{FAPb}(\text{I}_{0.5}\text{Br}_{0.5})_3$ (450 nm) | $0.63 \pm 0.04$          | $0.18 \pm 0.01$ | $0.023 \pm 0.009$           | $0.037 \pm 0.006$        |



**Figure 4.A.9:** Optoelectronic synapse measurements on devices with FAPbBr<sub>3</sub> and FAPb(I<sub>0.5</sub>Br<sub>0.5</sub>)<sub>3</sub> halide perovskite active layers with 450 nm light. **(a), (b)** Fits to transient photocurrent measurements with a  $-1$  V pulse at  $t = 0$  seconds and 450 nm light illumination with a  $0.2$  mW/cm<sup>2</sup> irradiance. As in Figure 4.A.8, photocurrent decays are similar for both devices, with a larger initial photocurrent measured for the FAPbBr<sub>3</sub> device. **(c), (d)** Linear fits to initial photocurrents obtained for different set voltages and illumination intensities. Irradiances were  $2.6$  mW/cm<sup>2</sup> ( $I_{2.6}$ , squares),  $0.2$  mW/cm<sup>2</sup> ( $I_{0.2}$ , triangles), or the devices were kept in dark during the voltage pulse ( $I_{dark}$ , circles). For the FAPbBr<sub>3</sub> device, slopes of  $-2.6$ ,  $-0.9$ , and  $-0.4$  nA/V were found for  $I_{2.6}$ ,  $I_{0.2}$ , and  $I_{dark}$ , respectively. For the FAPb(I<sub>0.5</sub>Br<sub>0.5</sub>)<sub>3</sub> device, the slopes of  $I_{2.6}$ ,  $I_{0.2}$ , and  $I_{dark}$  were  $-1.8$ ,  $-0.6$ , and  $-0.2$  nA/V, respectively.

### 4.A.1 Simulating optoelectronic synapse arrays implementing different learning rules

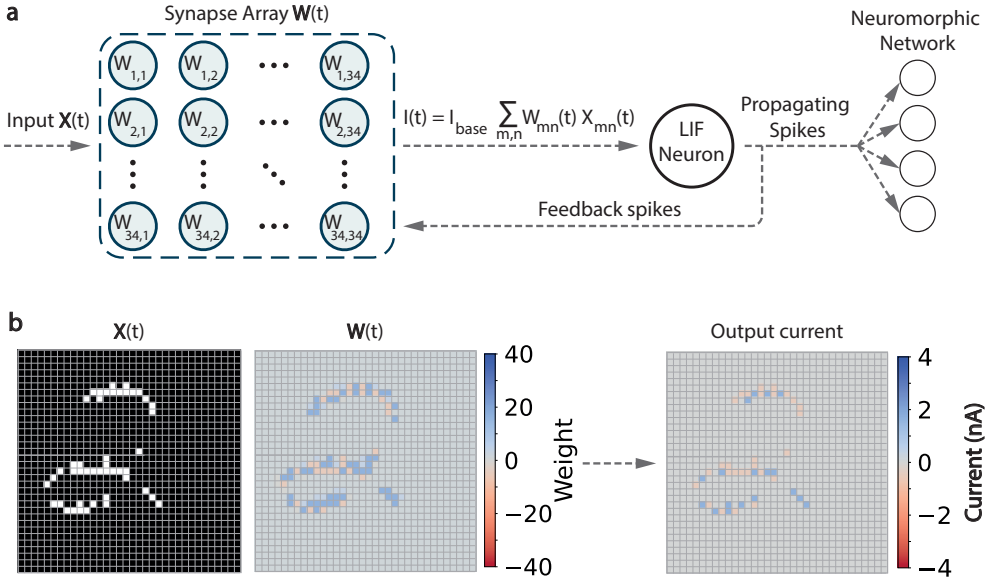


**Figure 4.A.10:** Schematic representation of the simulations. (a) Input frames  $\mathbf{X}(t)$  are projected on an array of synapses  $\mathbf{W}(t)$ . Each synapse outputs a weight-dependent current if it is illuminated. All currents are summed and integrated by a leaky integrate-and-fire neuron. Spike outputs by the neuron are used as feedback to update the synaptic weights. The spikes can also be propagated to a neuromorphic network for further processing of the input. (b) Example calculation of the current for the input frame  $\mathbf{X}(t)$  and synapse array  $\mathbf{W}(t)$  after the STDP weight update at  $t_1$  in Figure 4.5b. The currents of all pixels are summed to obtain  $I(t)$ .

The simulations in Figure 4.5 and Figure 4.A.14 were performed with a custom Python module. The module used NumPy (version 1.26.4) for numerical operations, run in Python version 3.11. The simulations are illustrated schematically in Figure 4.A.10a and b. A 34-by-34-pixel sample of the N-MNIST test set was binarized and binned into 2.5 ms frames. Binarized input frames are represented by the two-dimensional matrix  $\mathbf{X}(t)$ , where each element is either 1 (illuminated pixels), or 0 (dark pixels), so that  $\mathbf{X}(t) \in \{0, 1\}^{34 \times 34}$ . Illumination was modeled based on the 520 nm, 0.2 mW/cm<sup>2</sup> data in the main text. Each frame is sequentially projected onto the 34-by-34 volatile synapse array  $\mathbf{W}(t)$ , where each pixel  $X_{mn}(t)$  is used as input for its corresponding synapse  $W_{mn}(t)$ . The timestep between frames is increased from 2.5 to 45 ms to match the timesteps in the experimental measurements. This leads to an artificial “slowing” of the video data. The 45 ms timestep is a limitation of our experimental setup, and could be overcome with a faster electrical characterization of the MPOS.

For each timestep, first the total photocurrent output of the synapse array is calculated based on  $\mathbf{X}(t)$  and  $\mathbf{W}(t)$ , as shown in Figure 4.A.10a. Figure 4.A.10b shows an example calculation of the output current. This current is then used to update the membrane potential of a leaky integrate-and-fire (LIF) neuron, which fires a spike if the membrane potential reaches a threshold. The spike is applied to the synapses in the array as a feedback signal. In actual implementations, the spikes can also be propagated to following layers of a more complex network. The adaptive focusing on features of interest could help these networks with, for example, classification tasks.[7] Finally, the synaptic weights in the array are updated. If a feedback spike is provided, the synaptic weights are updated based on the voltage profile of the spike and the simultaneous illumination conditions. If no feedback spike is provided, the synaptic weights decay to a steady-state value. This Section first briefly explains calculations of the photocurrent output by the synapse array and the LIF neuron membrane potential updates. Next, it describes how the synaptic weights are obtained for different feedback spikes.

The photocurrent generated by each synapse is determined by multiplying its binary input,  $X_{mn}(t)$  a base current  $I_{base}$  of 95 pA (the constant offset photocurrent  $I_{offset}$  in Figure 4.2b of the main text), and a scale factor (synaptic weight),  $W_{mn}(t)$ . All currents are summed, giving a total current output of the synapse array of:

$$I(t) = I_{base} \cdot \langle \mathbf{W}(t), \mathbf{X}(t) \rangle = I_{base} \cdot \sum_{m=1}^M \sum_{n=1}^N W_{mn}(t) X_{mn}(t) \quad (4.1)$$

The membrane potential of the LIF neuron is updated after each frame based on this current. We set the threshold (1 V), characteristic time (50 ms), and the resistance ( $2.3 \times 10^8 \Omega$ ) of the neuron to obtain appropriate spike rates for the given inputs. After the threshold voltage is reached, the neuron outputs a spike and the membrane potential of the neuron is reset to 0 V.

The spike applied to the synapse array causes an update of the synaptic weights. The volatility of the synapses is modeled as a weight decay to a steady-state value of 1.0 in timesteps where no feedback spike is applied. All weight decays are modeled based on an exponential  $I_{0,cap}e^{-t/\tau}$  drift term. From the fit in Figure 4.2b in the main text, it follows that the photocurrent decays predominantly by this term. The decay by the  $kt^{-1/2}$  diffusion term is only minor and is therefore ignored in the simulations for simplicity. This approximation allows us to describe the synaptic weight changes based on the charging and discharging of a capacitor, where the capacitor voltage is due to ion accumulation at the cathode (per the left panel in Figure 4.2c).[39] The photocurrent response is determined by this voltage, which is therefore used as a measure for the synaptic weight. With the capacitor approx-

imation, the change in voltage in the device for simple voltage pulses as in Figure 4.3 can be described as an RC step response:

$$V(t) = V_{sup} + (V_{init} - V_{sup})e^{-t/\tau} \quad (4.2)$$

where  $V(t)$  is the time-dependent voltage in the synapse induced by ion accumulation,  $V_{sup}$  the spike voltage applied to the device,  $V_{init}$  the voltage in the device before the update pulse,  $t$  is the duration of the pulse, and  $\tau$  is the characteristic time. As the timestep in the simulations is constant, equation 4.2 can be rewritten as a first-order linear recurrence relation:

$$V_{i+1} = V_{sup} + (V_i - V_{sup})e^{-\frac{t_1}{\tau}} = V_i e^{-\frac{t_1}{\tau}} + a \quad (4.3)$$

where  $a = V_{sup}(1 - e^{-\frac{t_1}{\tau}})$ ,  $V_i$  and  $V_{i+1}$  are the voltage in the device at timestep  $i$  and  $i + 1$ , respectively. In our simulations,  $t_1$  is the 45 ms timestep. In the absence of a feedback spike ( $V_{sup} = 0$ ),  $a = 0$  and the voltage decays exponentially. The photocurrent is assumed to be directly proportional to this voltage, which follows from the linear increases in photocurrent with applied voltage magnitude in Figure 4.3b. This assumption is further supported by the constant resistance observed in the I-V sweeps in light and dark in Figure 4.A.2.

From the measurements in Figure 4.2b and Figure 4.A.6a, it follows that a higher photocurrent is extracted after a  $-1$  V pulse is applied while the device is illuminated compared to if the device is kept in dark during the  $-1$  V pulse. This can be captured by equation 4.3 as a difference in the characteristic time  $\tau$  during the application of the feedback spike voltage. Mechanistically, the difference in  $\tau$  can be explained by a higher ionic conductivity under illumination.[22] The characteristic time if the device is in dark can be approximated as  $\tau_{dark} = 190$  ms based on the fit in Figure 4.2b, where the device is kept in dark the majority of the time. Assuming a linear relation between the photocurrent and the built-in voltage,  $\tau_{light}$  can be found by setting:

$$\frac{I_{0,light}}{I_{0,dark}} = \frac{V_{i+1,light}}{V_{i+1,dark}} \quad (4.4)$$

Where  $I_{0,light}$  and  $I_{0,dark}$  are obtained from the drift-term fit in Figure 4.2b and Figure 4.A.6a, respectively, and  $V_{i+1,light}$  and  $V_{i+1,dark}$  are obtained from equation 3, setting  $\tau = \tau_{dark}$  for  $V_{i+1,dark}$ , and  $V_i = 0$  V for both voltages, per the experimental conditions. From equation 4.4 we obtain  $\tau_{light} = 24$  ms.

Changes to the induced electric field in the device  $V_i$  for different illumination conditions and feedback pulse voltages can now be described using  $\tau_{dark}$  and  $\tau_{light}$  and equation

4.3. The synaptic weight  $W_i$  is a scale factor of the base current that relates this  $V_i$  to the output photocurrent  $I_i$ :

$$I_i = I_{base} \cdot W_i(V_i) \quad (4.5)$$

Before any voltage is applied to the device, the device is in steady-state conditions. Consequently, the device outputs only the base current upon illumination, for which we define the synaptic weight as 1.0:

$$W_i(V_i = 0) \equiv 1.0 \quad (4.6)$$

From the linear dependence of the photocurrent  $I_i$  on the induced electric field,  $V_i$ , and of the photocurrent on the synaptic weight in equation 4.5, it follows that the synaptic weight should also depend linearly on  $V_i$ . Also considering equation 4.6, the synaptic weight can be calculated as:

$$W_i(V_i) = 1 + \alpha V_i \quad (4.7)$$

where  $\alpha$  is a constant scale factor. To determine  $\alpha$ , we calculate  $W_{i+1}(V_{i+1})$  and  $V_{i+1}$  for the measurement in Figure 4.2b using equations 4.5 and 4.3, respectively. From the obtained values ( $W_{i+1}(V_{i+1}) = 31.6$  and  $V_{i+1} = -0.85$  V), we calculate  $\alpha = -\frac{30.6}{0.85 \text{ V}}$ . Substituting into equation 4.7 yields:

$$W_i(V_i) = 1 - \frac{V_i}{0.85 \text{ V}} \cdot 30.6 \quad (4.8)$$

Finally, a first-order linear recurrence relation of  $W_{i+1}$  in terms of  $W_i$  can be found by substituting equation 4.3 into equation 4.8:

$$W_{i+1} = e^{-\frac{t_1}{\tau}} W_i + b \quad (4.9)$$

with  $b = 1 - e^{-\frac{t_1}{\tau}} - \frac{a}{0.85 \text{ V}} \cdot 30.6$ , and  $a$  the term of equation 4.3.

To validate the derived expressions for the synaptic weights and corresponding photocurrents, we used equation 4.5 and 4.9 to reproduce experimental results in the main text. Figure 4.A.11a compares the calculated weight and photocurrent for different applied voltages  $V_{sup}$  to the experimental results from Figure 4.3b. Figure 4.A.11b compares the weight and photocurrent decay obtained from the simulations with the results from Figure 4.2b. Both are described well by the simulations. The simulated weight changes slightly underestimate the values obtained from experiment because of the lack of the diffusion component. As an illustration, Figure 4.A.11c shows a simple simulation of weight updates of a synapse

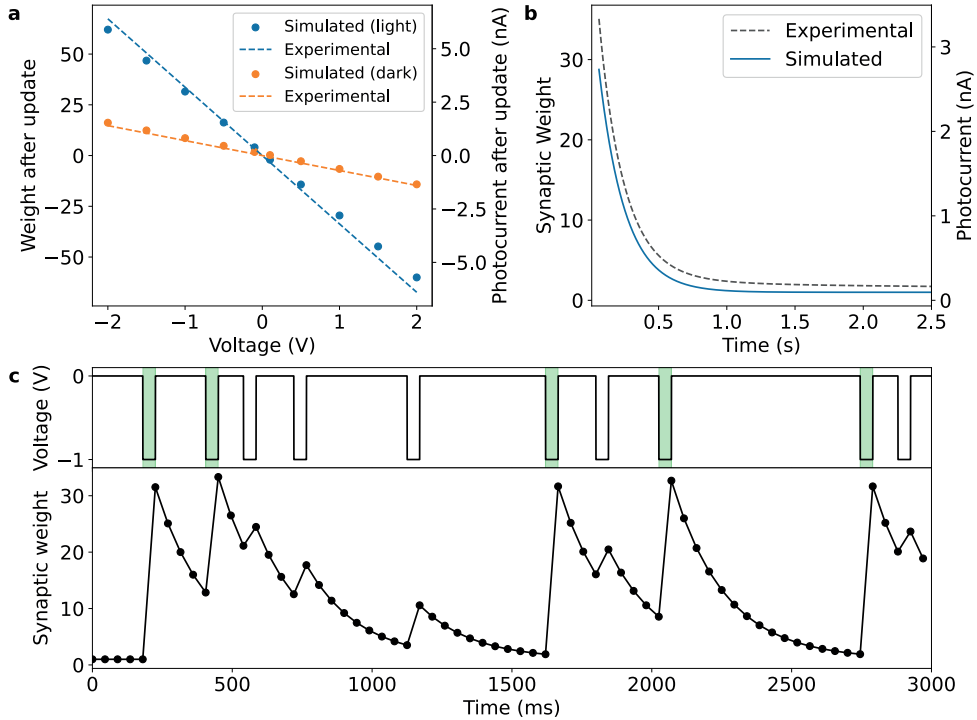


**Figure 4.A.11:** Comparison of simulations of weight updates of a single synapse to experiments to validate the simulation results. (a) Comparison of weight changes with respect to voltage with experimental results. (b) Comparison of the simulated weight decay over time with experimental results. In both (a) and (b), the simulated weights slightly underestimate the synaptic weights. (c) Simulation of synaptic weight updates based on a random voltage and light profile. The random voltage profile is shown in the top panel. Green shaded regions indicate simultaneous illumination of the device. The synaptic weight in the bottom panel increases when a voltage is applied. Every marker represents the synaptic weight at a 45 ms timestep. Increases are more significant if the device is illuminated during a  $-1$  V pulse.

when a random voltage and light profile is applied. Similar to the plot in Figure 4.A.11a, larger weight updates are found for voltage pulses that overlap with light pulses. This simple simulation shows how the weight increases logarithmically with successive applied pulses, and decays exponentially when no voltage is applied, as expected from the approximation of the weight changes as charging and discharging of a capacitor.

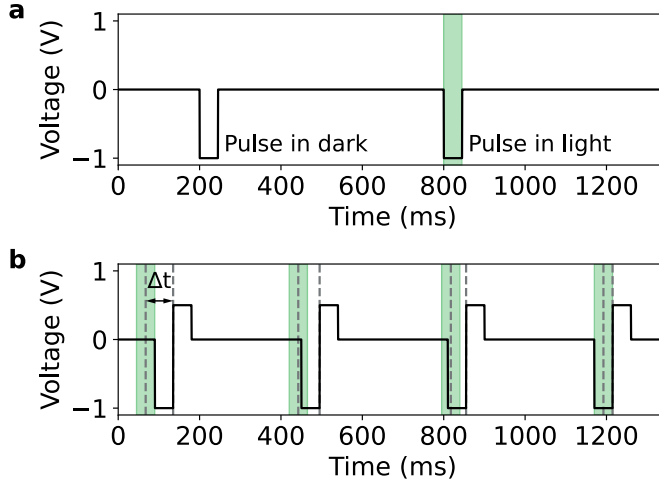


**Figure 4.A.12:** Schematic of different illumination conditions during applied voltages that are considered by the simulations. (a) Simple voltage pulses ( $-1$  V in this plot) are either applied in the dark, or with simultaneous illumination, shown by the green shaded area. (b)  $-1$  V to  $+0.5$  V STDP pulses overlap partially with the light pulses. The overlap is expressed as the time difference of the center of the STDP voltage profile and the center of the  $45$  ms light pulse,  $\Delta t$ . The schematic shows examples where  $\Delta t$  is positive and decreasing with each pulse.

Simulations implementing (anti-)STDP feedback spikes from Figure 4.4 follow a similar procedure. First the total photocurrent is determined using equation 4.1, after which the membrane potential of the same LIF neuron is updated and compared to its threshold. Finally, the synaptic weights are updated. Weight decay was simulated based on equation 4.3. However, determining  $V_i$  for the more complex  $\mp 1$  V to  $\pm 0.5$  V feedback pulses requires a modification of this equation to:

$$V_{i+1} = V_i e^{-\frac{t_1}{\tau_{\mp 1V}}} e^{-\frac{t_1}{\tau_{\pm 0.5V}}} \pm c \quad (4.10)$$

where  $c = e^{-\frac{t_1}{\tau_{\mp 1V}}} e^{-\frac{t_1}{\tau_{\pm 0.5V}}} - 1.5e^{-\frac{t_1}{\tau_{\pm 0.5V}}} + 0.5$ , and  $\tau_{\mp 1V}$  and  $\tau_{\pm 0.5V}$  are the characteristic times during the  $\mp 1$  V and  $\pm 0.5$  V pulses, respectively.

In addition to this, the weight updates described before assume illumination of the synapse for the entire duration of the feedback pulse, or no illumination at all, shown by Figure 4.A.12a. By contrast, the (anti-)STDP updates depend on the time difference between the feedback spike and the illumination of the synapse ( $\Delta t$ ), and allow varying degrees of overlap with the feedback spike, illustrated by Figure 4.A.12b. Figure 4.4 in the main text shows that the sign and magnitude of the weight changes depend on this delay time. Modifications to the previously derived equations to calculate weight updates as a

function of  $\Delta t$  are described below.

First, equation 4.8 is redefined to correct for any differences compared to the simple feedback pulse case. For the STDP measurement in Figure 4.4a in the main text,  $W_{i+1}(V_{i+1}) = 17$  for  $\Delta t = 22.5$  ms. This time delay corresponds to full overlap of the light pulse with the  $-1$  V pulse, followed by a  $+0.5$  V pulse in dark, as in the right-most condition in Figure 4.A.12b. The corresponding  $V_{i+1}$  can therefore be calculated from equation 4.10, by setting  $\tau_{-1V} = \tau_{light}$  and  $\tau_{+0.5V} = \tau_{dark}$ , yielding  $V_{i+1} = -0.57$  V. Substitution of  $W_{i+1}(V_{i+1})$  and the obtained value for  $V_{i+1}$  into equation 4.7 gives:

$$W_i(V_i) = 1 - \frac{V_i}{0.57 \text{ V}} \cdot 16 \quad (4.11)$$

We note that equation 4.8 gives a slightly different weight of  $W_{i+1}(V_{i+1} = -0.57 \text{ V}) = 21.5$ . A possible explanation could be an imperfect overlap of the light pulse with the  $-1$  V pulse, causing some overlap with the following  $+0.5$  V pulse as well. Substitution of equation 4.10 into equation 4.11 to express the weight changes as a first-order linear recurrence relation gives:

$$W_{i+1} = e^{-\frac{t_1}{\tau_{\mp 1V}}} e^{-\frac{t_1}{\tau_{\pm 0.5V}}} W_i + d \quad (4.12)$$

where  $d = 1 - e^{-\frac{t_1}{\tau_{\mp 1V}}} e^{-\frac{t_1}{\tau_{\pm 0.5V}}} \mp \frac{c}{0.57} \cdot 16$ , and  $c$  the term of equation 4.10.

In the derivation of equation 4.11, the  $-1$  V pulse fully overlapped with the light pulse and the  $+0.5$  V pulse was fully in dark, so  $\tau_{-1V} = \tau_{light}$  and  $\tau_{+0.5V} = \tau_{dark}$ . However, other values of  $\Delta t$  would give partial overlap with the voltage pulses. Figure 4.4 shows that this results in smaller modulation of the synaptic weight, which can be explained by a value for  $\tau$  between  $\tau_{light}$  and  $\tau_{dark}$ . Hence, instead of  $\tau \in \{\tau_{light}, \tau_{dark}\}$ ,  $\tau$  is a continuous function of delay  $\Delta t$  for the (anti-)STDP updates. An expression for  $\tau(\Delta t)$  can be found by setting equation 4.12 equal to the fitting equation of Figure 4.4:

$$e^{-\frac{t_1}{\tau_{\mp 1V}}} e^{-\frac{t_1}{\tau_{\pm 0.5V}}} W_1 + d = A e^{\pm \Delta t / \tau_{fit}} \quad (4.13)$$

where  $A$  and  $\tau_{fit}$  are obtained from the empirical fits in Figure 4.4 and  $W_1 = 1.0$  per the experimental conditions. To obtain  $\tau(\Delta t)$ , it is assumed that either the  $\mp 1$  V or the  $\pm 0.5$  V pulse is fully in dark, so  $\tau_{\mp 1V} = \tau_{dark}$  or  $\tau_{\pm 0.5V} = \tau_{dark}$ . Based on this assumption, (partial) overlap of the light pulse with the  $-1$  V part of the STDP pulse gives:

$$\tau_{-1V} = - \frac{t_1}{\ln \left[ 1.5 - \frac{0.5}{e^{-\frac{t_1}{\tau_{dark}}}} + \frac{0.57}{16 e^{-\frac{t_1}{\tau_{dark}}}} (1 - 34.3 e^{-\frac{\Delta t}{29.4 \text{ ms}}}) \right]} \quad (4.14)$$

While overlap of the light pulse with the +0.5 V part of the STDP pulse gives:

$$\tau_{+0.5V} = - \frac{t_1}{\ln \left[ \frac{1}{e^{-\frac{t_1}{\tau_{dark}} - 1.5}} \left( \frac{0.57}{16} (36.3e^{\frac{\Delta t}{11.3 \text{ ms}}} + 1) - 0.5 \right) \right]} \quad (4.15)$$

Similarly, for the anti-STDP pulses, ignoring the offset in the fitting equation, overlap of the light pulse with the +1 V pulse gives:

$$\tau_{+1V} = - \frac{t_1}{\ln \left[ 1.5 - \frac{0.5}{e^{-\frac{t_1}{\tau_{dark}}}} + \frac{0.57}{16e^{-\frac{t_1}{\tau_{dark}}}} (1 + 40.9e^{-\frac{\Delta t}{24.7 \text{ ms}}}) \right]} \quad (4.16)$$

and overlap with the -0.5 V pulse yields:

$$\tau_{-0.5V} = - \frac{t_1}{\ln \left[ \frac{1}{e^{-\frac{t_1}{\tau_{dark}} - 1.5}} \left( \frac{0.57}{16} (30.8e^{\frac{\Delta t}{17.5 \text{ ms}}} - 1) - 0.5 \right) \right]} \quad (4.17)$$

The equations derived above were validated by comparing weights obtained from simulations to the experimentally obtained weight changes in Figure 4.4. Figure 4.A.13a and b show a perfect match. Figure 4.A.13c shows a simple simulation of STDP weight updates of a single synapse. A random STDP voltage profile is applied to the synapse, which updates its weight depending on the overlap with the light pulse. Similar to the simulation in Figure 4.A.11c, this simple simulation shows the expected logarithmic weight increases, and exponential decays with each update. However, the STDP pulses allow both positive and negative weights for the same feedback pulse voltage profile depending on the overlap with the light pulse.

When the (anti-)STDP pulses are used to update the synapse array,  $\Delta t$  is determined by searching  $\mathbf{X}(t)$  for a light pulse from  $t = t_{spike} - 100 \text{ ms}$  to  $t = t_{spike} + 100 \text{ ms}$ . If multiple light pulses are found,  $\Delta t$  is determined from the light pulse that is closest in time to the feedback spike. If no light pulse is found, the synaptic weight does not change, in accordance with the experimental results in Figure 4.4. Currently, the timestep in the simulation and the light and voltage pulse durations are all 45 ms, per the experimental conditions in the main text. Consequently, the light pulses overlap fully with either the -1 V or the +0.5 V part of the STDP pulse, or not at all. This is a limitation of our current simulations that stems from the minimum step size of 45 ms in the measurements. Nevertheless, the (anti-)STDP updates can be extended easily to also allow the partial overlaps shown in Figure 4.A.12b. Smaller step sizes could be implemented with the currently derived equations, extrapolating our experimental results. In future work, the measurements could be repeated on a setup that allows smaller timesteps to validate that the equations and as-

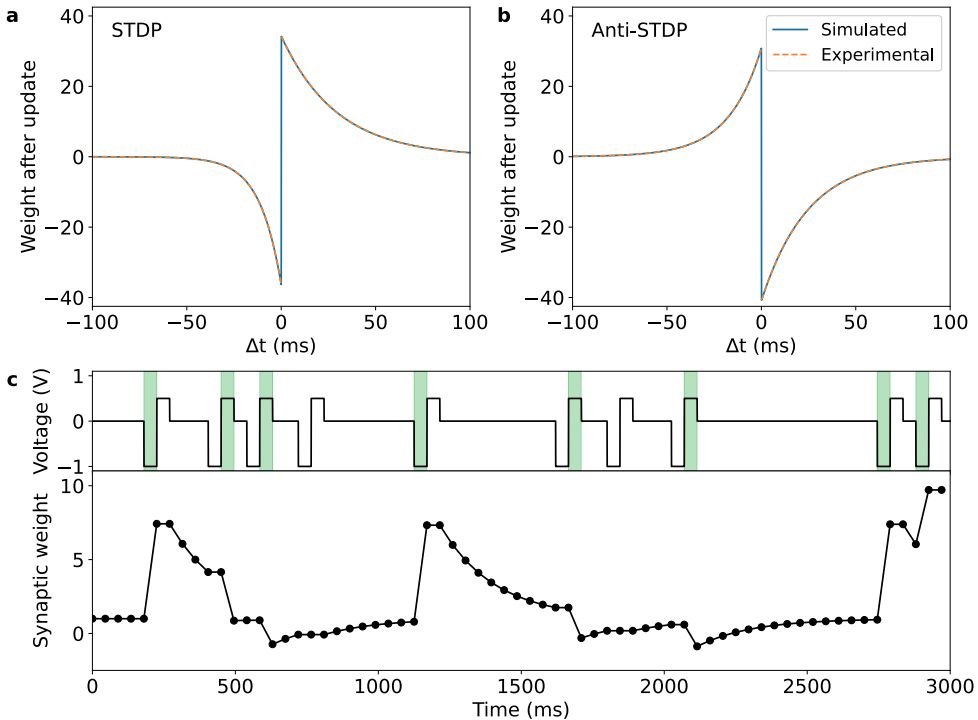


**Figure 4.A.13:** STDP weight updates simulated for a single synapse to validate the simulation results. (a) Comparison of simulated  $\Delta t$  dependent weight updates for STDP with the experimental fit in Figure 4.4a. (b) Comparison of the simulated  $\Delta t$  dependent weight updates for anti-STDP with the experimental fit in Figure 4.4b. Simulated and experimentally obtained weight updates match perfectly for both update rules. (c) Simulation of STDP synaptic weight updates based on a random STDP voltage and light profile. The random STDP voltage profile is shown in the top panel. Green shaded regions indicate simultaneous illumination of the device. The synaptic weight in the bottom panel increases or decreases depending on what part of the voltage profile overlaps with the light pulse. Every marker represents the synaptic weight at a 45 ms timestep.

assumptions hold for shorter timescales as well. Equations 4.14 - 4.17 could then be updated accordingly if necessary.

#### 4.A.2 Attention-based learning with simple $-1$ V pulses

Figure 4.A.14c demonstrates how a more top-down attention mechanism can be implemented by applying  $-1$  V pulses only to illuminated synapses after each neuron spike. Positive weights are obtained only in the regions illuminated with the number 2, similar to the STDP-learning array in Figure 4.5b. However, applying the  $-1$  V pulses to all pixels, as with the STDP-learning algorithm, causes all synaptic weights to converge to the same high value over time and does not lead to attention, as demonstrated by Figure 4.A.14b. These results illustrate that this top-down approach requires a more elaborate feedback mechanism compared to the (anti-)STDP updates in Figure 4.5 in the main text. This makes the top-down approach more difficult to scale. Nevertheless, this approach could be worthwhile for more complex inputs where the (anti-)STDP updates cannot sufficiently separate features of interest.

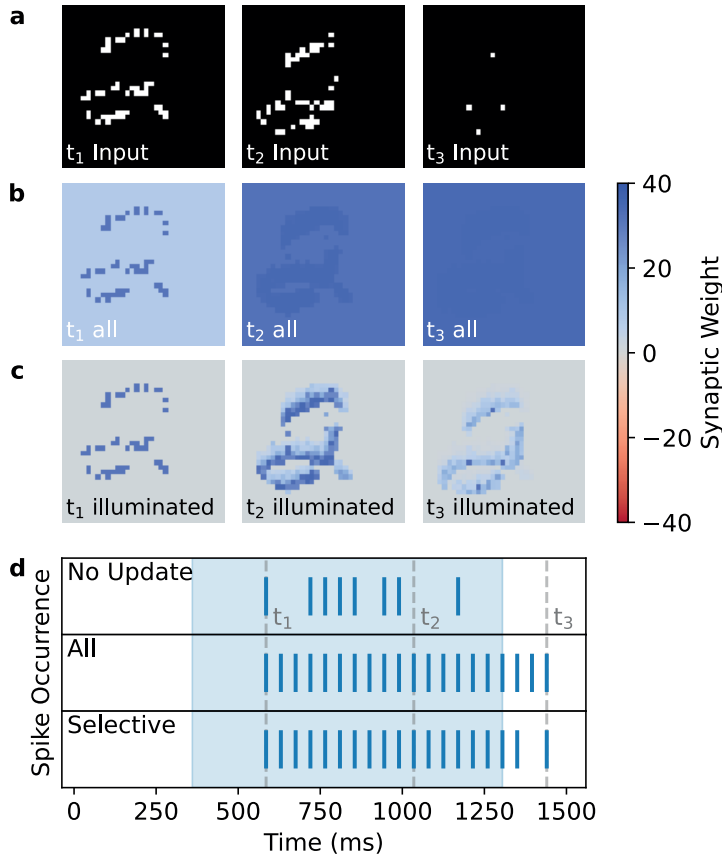


**Figure 4.A.14:** The attention mechanism implemented with  $-1$  V pulses. (a) The same input frames of the N-MNIST sample number 2 as in Figure 4.5 in the main text. The frames are taken at the same simulation times  $t_1$  (585 ms),  $t_2$  (1035 ms), and  $t_3$  (1440 ms). (b) The synaptic weights of an optoelectronic synapse array to which  $-1$  V pulses are applied to all synapses after each neuron spike. The three panels show the weights of the array after being presented the frames in (a). The synaptic weights of illuminated synapses are increased to a larger degree, but cumulative spiking causes all synapses to have the same weights after  $t_3$ . (c) The synaptic weights of an optoelectronic synapse array to which  $-1$  V pulses are applied selectively only to illuminated synapses after each neuron spike. Larger synaptic weights are found only in regions that were illuminated with the number 2. (d) Event-plot of the neuron spikes over time. Higher spiking frequencies are found for the arrays implementing the weight changes in (b) (“All”) and (c) (“Selective”) compared to an array that does not implement any weight changes (“No Update”). The blue shaded region indicates the times during which the number 2 is visible in the N-MNIST frames, i.e. when the neuron should output spikes.

# References

1. Brown, T. *et al.* *Language Models are Few-Shot Learners* in *Advances in Neural Information Processing Systems* **33** (Curran Associates, Inc., 2020), 1877–1901.
2. Vaswani, A., Shazeer, N., Parmar, N., Uszkoreit, J., Jones, L., Gomez, A. N., Kaiser, Ł. u. & Polosukhin, I. *Attention is All you Need* in *Advances in Neural Information Processing Systems* **30** (Curran Associates, Inc., 2017).
3. Dosovitskiy, A. *et al.* *An Image is Worth 16x16 Words: Transformers for Image Recognition at Scale* 2021. arXiv: 2010.11929 [cs.CV].
4. Liu, Z., Lin, Y., Cao, Y., Hu, H., Wei, Y., Zhang, Z., Lin, S. & Guo, B. *Swin Transformer: Hierarchical Vision Transformer using Shifted Windows* in *2021 IEEE/CVF International Conference on Computer Vision (ICCV)* (IEEE, Montreal, QC, Canada, 2021), 9992–10002.
5. Jumper, J. *et al.* Highly accurate protein structure prediction with AlphaFold. *Nature* **596**, 583–589 (2021).
6. Mehonic, A. & Kenyon, A. J. Brain-inspired computing needs a master plan. *Nature* **604**, 255–260 (2022).
7. Merolla, P. A. *et al.* A million spiking-neuron integrated circuit with a scalable communication network and interface. *Science* **345**, 668–673 (2014).
8. Strukov, D. B., Snider, G. S., Stewart, D. R. & Williams, R. S. The missing memristor found. *Nature* **453**, 80–83 (2008).
9. Wan, X., He, Y., Nie, S., Shi, Y. & Wan, Q. Biological Band-Pass Filtering Emulated by Oxide-Based Neuromorphic Transistors. *IEEE Electron Device Letters* **39**, 1764–1767 (2018).
10. Wang, W., Covi, E., Milozzi, A., Farronato, M., Ricci, S., Sbandati, C., Pedretti, G. & Ielmini, D. Neuromorphic Motion Detection and Orientation Selectivity by Volatile Resistive Switching Memories. *Advanced Intelligent Systems* **3**, 2000224 (2021).
11. Covi, E., Ielmini, D., Lin, Y.-H., Wang, W., Stecconi, T., Milo, V., Bricalli, A., Ambrosi, E., Pedretti, G. & Tseng, T.-Y. *A Volatile RRAM Synapse for Neuromorphic Computing* in *2019 26th IEEE International Conference on Electronics, Circuits and Systems (ICECS)* (IEEE, Genoa, Italy, 2019), 903–906.
12. Ricci, S., Kappel, D., Tetzlaff, C., Ielmini, D. & Covi, E. Tunable synaptic working memory with volatile memristive devices. *Neuromorphic Computing and Engineering* **3**, 044004 (2023).

13. De Boer, J. J. & Ehrler, B. Scalable Microscale Artificial Synapses of Lead Halide Perovskite with Femtojoule Energy Consumption. *ACS Energy Letters* **9**, 5787–5794 (2024).
14. Xiao, Z. & Huang, J. Energy-efficient hybrid perovskite memristors and synaptic devices. *Advanced Electronic Materials* **2**, 1600100 (2016).
15. Gong, J., Yu, H., Zhou, X., Wei, H., Ma, M., Han, H., Zhang, S., Ni, Y., Li, Y. & Xu, W. Lateral Artificial Synapses on Hybrid Perovskite Platelets with Modulated Neuroplasticity. *Advanced Functional Materials* **30**, 2005413 (2020).
16. De Boer, J. J. & Ehrler, B. Integrated artificial neurons from metal halide perovskites. *Materials Horizons* **12**, 2701–2708 (2025).
17. Schmidt, M. C., Alvarez, A. O., de Boer, J. J., van de Ven, L. J. & Ehrler, B. Consistent Interpretation of Time- and Frequency-Domain Traces of Ion Migration in Perovskite Semiconductors. *ACS Energy Letters* **9**, 5850–5858 (2024).
18. Tress, W., Marinova, N., Moehl, T., Zakeeruddin, S. M., Nazeeruddin, M. K. & Grätzel, M. Understanding the rate-dependent J–V hysteresis, slow time component, and aging in CH<sub>3</sub> NH<sub>3</sub> PbI<sub>3</sub> perovskite solar cells: the role of a compensated electric field. *Energy & Environmental Science* **8**, 995–1004 (2015).
19. Gu, C. & Lee, J. S. Flexible Hybrid Organic-Inorganic Perovskite Memory. *ACS Nano* **10**, 5413–5418 (2016).
20. Liu, D., Lin, Q., Zang, Z., Wang, M., Wangyang, P., Tang, X., Zhou, M. & Hu, W. Flexible All-Inorganic Perovskite CsPbBr<sub>3</sub> Nonvolatile Memory Device. *ACS Applied Materials and Interfaces* **9**, 6171–6176 (2017).
21. Hoke, E. T., Slotcavage, D. J., Dohner, E. R., Bowring, A. R., Karunadasa, H. I. & McGehee, M. D. Reversible photo-induced trap formation in mixed-halide hybrid perovskites for photovoltaics. *Chemical Science* **6**, 613–617 (2015).
22. Zhao, Y.-C., Zhou, W.-K., Zhou, X., Liu, K.-H., Yu, D.-P. & Zhao, Q. Quantification of light-enhanced ionic transport in lead iodide perovskite thin films and its solar cell applications. *Light: Science & Applications* **6**, e16243–e16243 (2016).
23. Zhou, F. & Chai, Y. Near-sensor and in-sensor computing. *Nature Electronics* **3**, 664–671 (2020).
24. Ham, S., Choi, S., Cho, H., Na, S. I. & Wang, G. Photonic Organolead Halide Perovskite Artificial Synapse Capable of Accelerated Learning at Low Power Inspired by Dopamine-Facilitated Synaptic Activity. *Advanced Functional Materials* **29**, 1806646 (2019).

25. Liu, J., Yang, Z., Gong, Z., Shen, Z., Ye, Y., Yang, B., Qiu, Y., Ye, B., Xu, L., Guo, T., *et al.* Weak light-stimulated synaptic hybrid phototransistors based on islandlike perovskite films prepared by spin coating. *ACS Applied Materials & Interfaces* **13**, 13362–13371 (2021).
26. Rogdakis, K., Loizos, M., Viskadourous, G. & Kymakis, E. Memristive perovskite solar cells towards parallel solar energy harvesting and processing-in-memory computing. *Materials Advances* **3**, 7002–7014 (2022).
27. Sharma, D., Luqman, A., Ng, S. E., Yantara, N., Xing, X., Tay, Y. B., Basu, A., Chattopadhyay, A. & Mathews, N. Halide perovskite photovoltaics for in-sensor reservoir computing. *Nano Energy* **129**, 109949 (2024).
28. Subramanian Periyal, S., Jagadeeswararao, M., Ng, S. E., John, R. A. & Mathews, N. Halide Perovskite Quantum Dots Photosensitized-Amorphous Oxide Transistors for Multimodal Synapses. *Advanced Materials Technologies* **5**, 2000514 (2020).
29. Ma, F. *et al.* Optoelectronic Perovskite Synapses for Neuromorphic Computing. *Advanced Functional Materials* **30**, 1908901 (2020).
30. Lin, C. H., Cheng, B., Li, T. Y., Retamal, J. R. D., Wei, T. C., Fu, H. C., Fang, X. & He, J. H. Orthogonal Lithography for Halide Perovskite Optoelectronic Nanodevices. *ACS Nano* **13**, 1168–1176 (2019).
31. Zhang, Z., Zhao, X., Zhang, X., Hou, X., Ma, X., Tang, S., Zhang, Y., Xu, G., Liu, Q. & Long, S. In-sensor reservoir computing system for latent fingerprint recognition with deep ultraviolet photo-synapses and memristor array. *Nature Communications* **13**, 6590 (2022).
32. Xu, K. *et al.* Ga<sub>2</sub>O<sub>3</sub> Bipolar Heterojunction-Based Optoelectronic Synapse Array with Visual Attention. *The Journal of Physical Chemistry Letters* **15**, 556–564 (2024).
33. Eames, C., Frost, J. M., Barnes, P. R., O'regan, B. C., Walsh, A. & Islam, M. S. Ionic transport in hybrid lead iodide perovskite solar cells. *Nature communications* **6**, 7497 (2015).
34. Alvarez, A. O. *et al.* Ionic Field Screening in MAPbBr<sub>3</sub> Crystals Revealed from Remnant Sensitivity in X-ray Detection. *ACS Physical Chemistry Au* **3**, 386–393 (2023).
35. Bard, A. J. & Faulkner, L. R. en. *Basic Potential Step Methods in Electrochemical methods: fundamentals and applications* 2. edition, 156–225 (Wiley, New York Weinheim, 2001).
36. Messerschmitt, F., Kubicek, M., Schweiger, S. & Rupp, J. L. Memristor kinetics and diffusion characteristics for mixed anionic-electronic SrTiO<sub>3-δ</sub> bits: the memristor-based Cottrell analysis connecting material to device performance. *Advanced Functional Materials* **24**, 7448–7460 (2014).

37. Ielmini, D. & Wong, H. S. In-memory computing with resistive switching devices. *Nature Electronics* **1**, 333–343 (2018).
38. Almora, O., Guerrero, A. & Garcia-Belmonte, G. Ionic charging by local imbalance at interfaces in hybrid lead halide perovskites. *Applied Physics Letters* **108**, 043903 (2016).
39. Bard, A. J. & Faulkner, L. R. en. *Introduction and Overview of Electrode Processes in Electrochemical methods: fundamentals and applications* 2. edition, 1–43 (Wiley, New York Weinheim, 2001).
40. Agarwal, S., Plimpton, S. J., Hughart, D. R., Hsia, A. H., Richter, I., Cox, J. A., James, C. D. & Marinella, M. J. Resistive memory device requirements for a neural algorithm accelerator in 2016 International Joint Conference on Neural Networks (IJCNN) (2016), 929–938.
41. Jo, S. H., Chang, T., Ebong, I., Bhadviya, B. B., Mazumder, P. & Lu, W. Nanoscale memristor device as synapse in neuromorphic systems. *Nano Letters* **10**, 1297–1301 (2010).
42. Kim, M.-K. & Lee, J.-S. Ferroelectric Analog Synaptic Transistors. *Nano Letters* **19**, 2044–2050 (2019).
43. Van de Burgt, Y., Lubberman, E., Fuller, E. J., Keene, S. T., Faria, G. C., Agarwal, S., Marinella, M. J., Alec Talin, A. & Salleo, A. A non-volatile organic electrochemical device as a low-voltage artificial synapse for neuromorphic computing. *Nature Materials* **16**, 414–418 (2017).
44. Pershin, Y. V. & Di Ventra, M. Experimental demonstration of associative memory with memristive neural networks. *Neural Networks* **23**, 881–886 (2010).
45. Wang, Z. *et al.* Capacitive neural network with neuro-transistors. *Nature Communications* **9**, 1–10 (2018).
46. Yu, F., Zhu, L. Q., Xiao, H., Gao, W. T. & Guo, Y. B. Restickable Oxide Neuromorphic Transistors with Spike-Timing-Dependent Plasticity and Pavlovian Associative Learning Activities. *Advanced Functional Materials* **28**, 1804025 (2018).
47. Davies, M. *et al.* Loihi: A Neuromorphic Manycore Processor with On-Chip Learning. *IEEE Micro* **38**, 82–99 (2018).
48. Ambrogio, S., Ciocchini, N., Laudato, M., Milo, V., Pirovano, A., Fantini, P. & Ielmini, D. Unsupervised Learning by Spike Timing Dependent Plasticity in Phase Change Memory (PCM) Synapses. *Frontiers in Neuroscience* **10**, 56 (2016).
49. Orchard, G., Jayawant, A., Cohen, G. K. & Thakor, N. Converting static image datasets to spiking neuromorphic datasets using saccades. *Frontiers in neuroscience* **9**, 437 (2015).

50. Liu, C., Wang, Y., Zhang, T., Yuan, R. & Yang, Y. An Attention Mechanism-Based Adaptive Feedback Computing Component by Neuromorphic Ion Gated MoS<sub>2</sub> Transistors. *Advanced Electronic Materials* **9**, 2201060 (2023).
51. Chen, Y., Kang, Y., Hao, H., Xie, X., Zeng, J., Xu, T., Li, C., Tan, Y. & Fang, L. All Two-dimensional Integration-Type Optoelectronic Synapse Mimicking Visual Attention Mechanism for Multi-Target Recognition. *Advanced Functional Materials* **33**, 2209781 (2023).
52. Brivio, F., Butler, K. T., Walsh, A. & van Schilfgaarde, M. Relativistic quasiparticle self-consistent electronic structure of hybrid halide perovskite photovoltaic absorbers. *Physical Review B* **89**, 155204 (2014).
53. Caputo, M. *et al.* Electronic structure of MAPbI<sub>3</sub> and MAPbCl<sub>3</sub>: importance of band alignment. *Scientific Reports* **9**, 15159 (2019).
54. Haruyama, J., Sodeyama, K., Han, L. & Tateyama, Y. First-Principles Study of Ion Diffusion in Perovskite Solar Cell Sensitizers. *Journal of the American Chemical Society* **137**, 10048–10051 (2015).
55. Oranskaia, A., Yin, J., Bakr, O. M., Brédas, J.-L. & Mohammed, O. F. Halogen Migration in Hybrid Perovskites: The Organic Cation Matters. *The Journal of Physical Chemistry Letters* **9**, 5474–5480 (2018).



# 5

## Microscale Optoelectronic Reservoir Networks for In-Sensor Computing

### Abstract

Physical reservoir computing is a promising framework for efficient neuromorphic in and near-sensor computing applications. Here we demonstrate a multimodal optoelectronic reservoir network based on halide perovskite semiconductor devices, capable of processing both voltage and light inputs. The devices consist of micrometer-sized, asymmetric crossbars covered with a  $\text{MAPbI}_3$  perovskite film. In a network, we simulate the performance by transforming MNIST images and videos based on the N-MNIST dataset using 4-bit inputs and training linear readout layers for classification. We demonstrate multimodal networks capable of processing both voltage and light inputs, reaching mean accuracies up to  $95.3 \pm 0.1\%$  and  $89.0 \pm 0.1\%$  for image and video classification, respectively. We observed only minor deterioration by measurement noise. The networks significantly outperformed linear classifier references, by 3.1% for images and 15.8% for video. We show that longer retention times benefit classification accuracy for single-mode networks, and give guidelines for choosing optimal experimental parameters. Moreover, the microscale device architecture lends itself well to further downscaling in high-density sensor arrays, making the devices ideal for efficient in-sensor computing.

---

This chapter is based on: de Boer, J.J., Alvarez, A.O., Schmidt, M.C., & Ehrler, B. In-sensor computing with halide perovskite-based optoelectronic reservoir networks. *Device* (2025), *in press*

## 5.1 Introduction

While upscaling of neural networks has resulted in impressive increases in their capabilities, it has also led to an exponential rise in energy consumption.[1] Novel neuromorphic hardware neural networks inspired by the brain are an appealing, more energy-efficient alternative.[2, 3] Brain-inspired networks that process inputs close to the sensor are particularly interesting for reducing inefficient data transfer and power consumption.[4] Physical reservoir computing is a compelling approach for this purpose, as it leverages inherent device dynamics to preprocess inputs. In reservoir computing, a fixed dynamical system nonlinearly transforms inputs to increase linear separability,[5] after which a simple linear readout layer is used for classification.[6, 7] As only the simple linear readout layer is trained, these networks are significantly easier to implement in hardware than neuromorphic networks with many complex trained layers.[2, 8]

Physical reservoirs for in-sensor computing commonly apply the “single dynamical node” approach,[7] shown schematically in Figure 5.1a. A time-dependent input is fed into the device (“reservoir node”), which changes its state. The reservoir node has a volatile memory, so that its state depends on both the presented input and its history. The reservoir node states are collected over time, and a linear weighted sum is taken to yield the final output. For in-sensor computing, this approach is typically extended to arrays of reservoir nodes,[9] as illustrated schematically in Figure 5.1b. After the input is transformed, the final output is obtained by taking a weighted sum of the reservoir states. This can be implemented by running the readout reservoir states through a resistive or memristive device array.[9] Optionally, the output can be collected for further processing on digital platforms. These networks do not require external memory if only the final device states are considered, strongly reducing inefficient data transport.[3]

A broad range of platforms is suitable for physical reservoir computing because the reservoir only requires a fixed nonlinear transformation of an input. Implementations include memristive devices,[9, 10] photonic circuits,[11, 12] and spintronic devices.[13] The ability of optoelectronic devices to process a broad range of inputs makes them particularly attractive for in-sensor reservoir computing.[14] These devices can process various multimodal optical and electronic inputs and combine them to increase classification accuracy.[15] Halide perovskites have excellent optoelectronic properties and are hence well-suited for reservoir computing. Next to strong light absorption, they feature complex and tunable transient behavior due to ion migration induced by a light or voltage bias.[16] Several reports have explored the use of halide perovskites for reservoir computing.[17–20] However, in these implementations, the reservoir was limited to detecting either a voltage

or a light-based input, and multimodal sensing was not explored. Moreover, these reports did not address the difficulty of microfabrication of halide perovskite devices,[21] which is necessary for high-density integration.

Here, we address these gaps by implementing the microscale halide perovskite devices we developed as optoelectronic artificial synapses in Chapter 4 for reservoir computing. After applying a voltage pulse, the devices output an ionic displacement current that decays on the seconds to hundreds of milliseconds timescale. Illuminating the device when a voltage is applied increases the current modulation. We investigate the linear separability of four-bit light and voltage inputs based on this volatile current. Based on the results, we construct in-sensor reservoir computing networks that transform and classify handwritten digits from images (MNIST) and video (modified N-MNIST), while accounting for experimentally measured noise. We obtain classification accuracies up to  $95.3 \pm 0.1\%$  for image and  $89.0 \pm 0.1\%$  for video datasets when combining both inputs in the same multimodal network, surpassing linear classifier references. When considering only one type of input, light-input networks outperformed networks based on voltage inputs. We show with simulations that this is due to the shorter retention time relative to the input frequency for voltage inputs. The simulations allow facile estimation of network accuracies based on the 4-bit input measurements, valuable when fine-tuning experimental parameters. They also show complementary transformations by the light and voltage networks, leading to the high accuracy of the multimodal networks. Our results demonstrate the potential of halide perovskite volatile devices for efficient, multimodal in-sensor computing.

## 5.2 Results and Discussion

### 5.2.1 Reservoir computing with a volatile halide perovskite device

A schematic image of the microscale halide perovskite device is shown in Figure 5.1c. The device consists of  $2.5 \mu\text{m}$ -wide, back-contacted crosspoint electrodes of gold that sandwich an insulating  $\text{Al}_2\text{O}_3$  layer. A  $\text{MAPbI}_3$  layer is spin-coated over the crosspoint electrodes. We have developed this device architecture in Chapter 3 and 4 to prevent degradation of the perovskite layer during microfabrication.

The example of a pulsed voltage and light measurement in Figure 5.1d shows how the device could be used as a reservoir node. Four  $-1 \text{ V}$  pulses, corresponding to the four inputs at different times in Figure 5.1a, are applied to the device. The current, resembling the read-out states  $\mathbf{x}(t)$ , is measured continuously. Each combination of a  $-1 \text{ V}$  pulse and the subsequent dwell time, during which the current is measured, represents one  $\Delta t$  timestep from Figure 5.1a. We use  $\Delta t$  to refer to the timesteps instead of the more conventional “ $\tau$ ” to

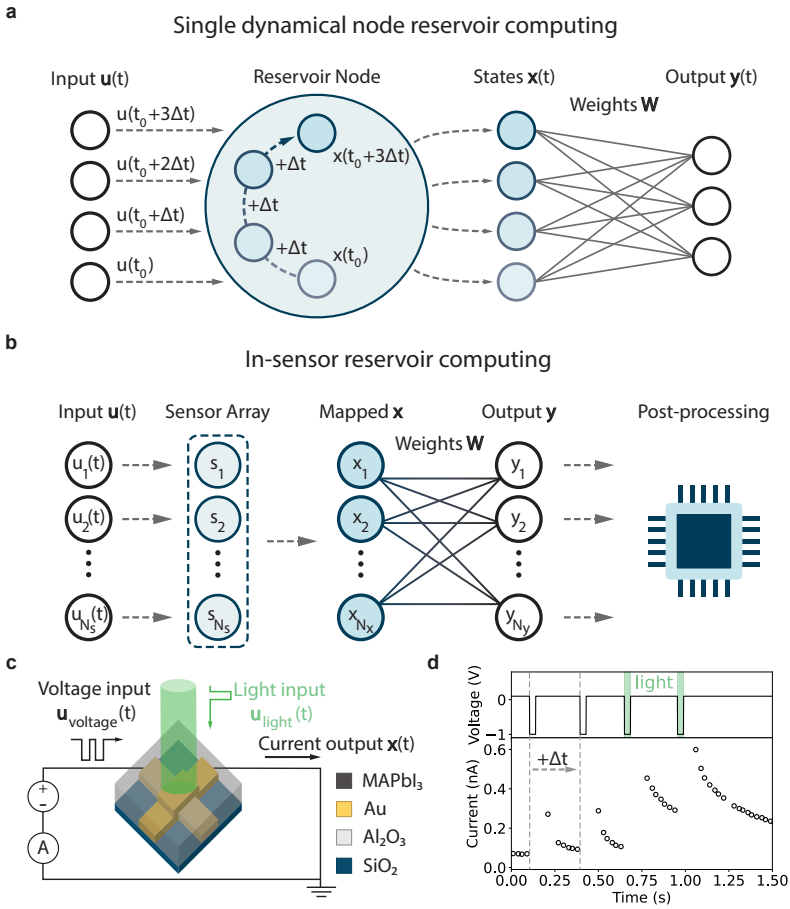


**Figure 5.1:** Reservoir computing with volatile artificial synapses. **(a)** Schematic representation of reservoir computing with a single dynamical node. This node can be implemented with a volatile device (“reservoir node”) processing a time-encoded input, represented by input vector  $u(t)$ . Each element of  $u(t)$  is an input at time  $t$ . The input changes some internal state of the node, resulting in a nonlinear transformation of the input. The output of the reservoir node at each point in time, represented by  $x(t)$ , depends on the input at that time and the previous state of the node. The states collected in  $x(t)$  are read out by taking a weighted sum with the weight matrix  $W$ , giving the final output of the network,  $y(t)$ . **(b)** Schematic of in-sensor reservoir computing with an array of volatile devices. Each device  $s_n$  receives a time-varying input  $u_n(t)$  and transforms it to one or multiple states. The states of all nodes are collected in  $x$ . Similar to reservoir computing with a single dynamical node, the final output  $y$  is obtained by taking a weighted sum with the weight matrix  $W$ . Afterwards, the output can be collected for further processing. In both **(a)** and **(b)**, only the weights in  $W$  are adapted during training. **(c)** Schematic drawing of the volatile optoelectronic halide perovskite artificial synapse. The microscale device can process both voltage and light inputs ( $u(t)$ ) and gives a current as an output ( $x(t)$ ). **(d)** An example pulsed voltage measurement showing a slow current decay over hundreds of milliseconds after an applied pulse. A second pulse applied during the decay gives a higher current compared to the first pulse. Simultaneously illuminating the device when two more voltage pulses are applied increases the change in current. The currents measured during the pulses are omitted for clarity. The pulse and its following dwell time correspond to one timestep ( $\Delta t$ ) in **(a)**.

avoid confusion with the characteristic decay time of the current.[22] Applying  $-1$  V pulses results in a current that decays slowly over hundreds of milliseconds after each pulse. The current recorded after the second pulse (0.29 nA) is slightly larger than after the first pulse (0.27 nA). Higher current changes are obtained after the third (0.40 nA) and fourth (0.60 nA)  $-1$  V pulses, during which the device was simultaneously illuminated. This difference demonstrates that the device's response to a new input, i.e. its read-out state, depends on both the input itself and the history of previous inputs, a requirement of reservoir computing. Crucially, both the voltage and light pulses affect the current in distinct ways.

In Chapter 4, we have shown that the current decay of this device after a voltage pulse is governed by a combined ionic drift and diffusion process. Here, the decay follows the same ionic drift and diffusion processes, as follows from the fit in Figure 5.A.1. Drift-diffusion simulations in Figure 5.A.2 further corroborate that the transient current response is due to an ionic displacement current. The increase in current after each pulse is due to further accumulation of ions. Illumination during the  $-1$  V pulse likely enhances the accumulation due to the higher ionic conductivity in light,[23] in line with the results in Chapter 4. Using this volatile current for reservoir computing requires a linearly separable output for different inputs. We first investigate this linearity for voltage inputs without illumination. Next, we explore it for inputs combining voltage pulses with light inputs.

### 5.2.2 Voltage inputs

The voltage input measurements are shown schematically in Figure 5.2a. Input sequences were provided in four timesteps with a 150 ms duration ( $\Delta t$  in Figure 5.1d). A  $-1$  V pulse can be applied during the first 50 ms of each timestep. Next, the current is measured for 100 ms, always without applied voltage. The four timesteps allow sixteen different voltage input sequences. These inputs can be represented as binary numbers, where a timestep with an applied  $-1$  V pulse is denoted as a binary "1", and a timestep without applied voltage as a binary "0".

An example measurement with a 1011 input sequence (input  $\mathbf{u}(t)$  in Figure 5.1a and b) is shown in Figure 5.2b. Three  $-1$  V pulses are applied to the device, with a missing  $-1$  V pulse at the second timestep, shown as a dotted line. The currents collected in each timestep, corresponding to the readout states  $\mathbf{x}$  in Figure 5.1a and b, are referred to as  $I_1$ ,  $I_2$ ,  $I_3$ , and  $I_4$  in the plot. The current is increased after each pulse and decays in the absence of an applied voltage, consistent with an ionic displacement current. Each of the sixteen possible four-bit sequences was measured 100 times. The separability of the sixteen inputs was investigated by comparing the means and standard deviations of the  $I_1$ ,  $I_2$ ,  $I_3$ , and  $I_4$  currents.

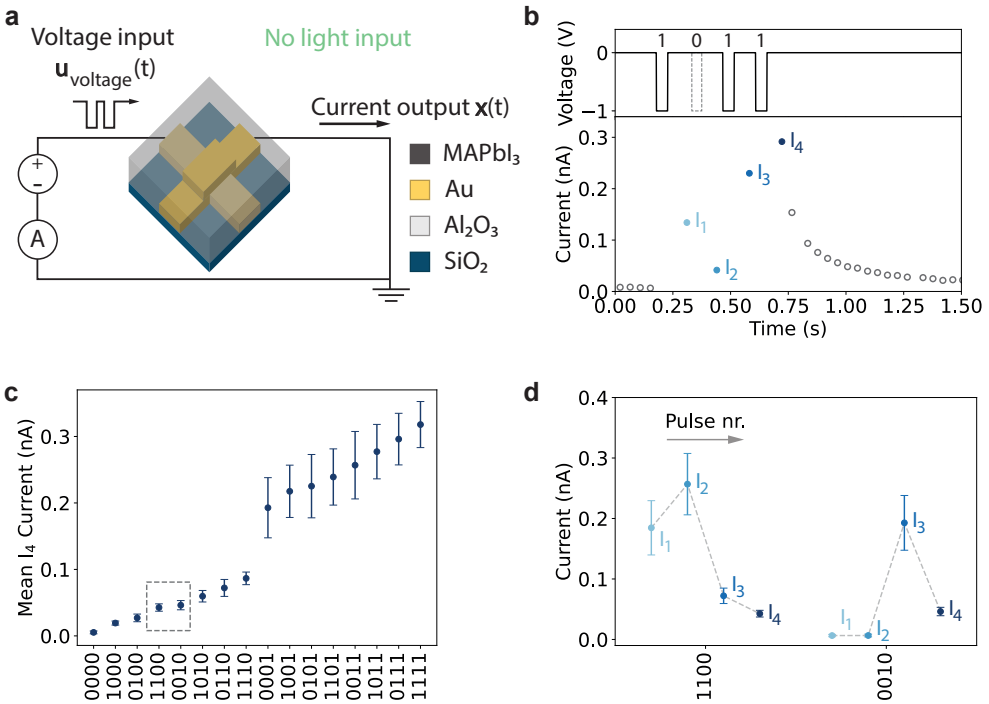


**Figure 5.2:** Electronic measurements of four-bit voltage profiles. **(a)** Schematic of the measurements. A four-bit,  $-1$  V pulsed input is applied, and the resulting current is measured. **(b)** An example measurement of three  $-1$  V pulses, shown in the top panel. The dotted line after the first pulse indicates a missing  $-1$  V pulse for that  $\Delta t$  timestep. Hence, this voltage profile corresponds to a 1011 input. The bottom panel shows the measured currents. Currents after each of the four pulses used for further analysis ( $I_1, I_2, I_3,$  and  $I_4$ ) are shown in blue. **(c)** Mean  $I_4$  currents for each four-bit input. Output currents are higher for inputs with more  $-1$  V pulses, and for inputs with pulses applied later in the 4-bit input. Some means are close to overlapping, such as those of the 1100 and 0010 inputs highlighted by the dashed gray box. **(d)** Mean  $I_1, I_2, I_3,$  and  $I_4$  currents of the highlighted 1100 and 0010 input. While the  $I_4$  currents are similar, the  $I_1, I_2,$  and  $I_3$  currents are easily separable.

Figure 5.2c shows the obtained mean and standard deviation of the  $I_4$  currents. The figure shows that the measured current increases as a larger number of voltage pulses is applied and when pulses are applied for later bits, as expected for an ionic displacement current. Some input sequences lead to similar currents, such as the highlighted 1100 and 0010 sequences. Even so, Figure 5.2d shows that the mean  $I_1$ ,  $I_2$ , and  $I_3$  currents are easily separable. The mean currents after each bit of all inputs are given in Figure 5.A.3. Even though the standard deviations of several means overlap, the standard errors of the means are small, as demonstrated by Figure 5.A.4. This implies that the means are well-defined.

For in-sensor reservoir computing applications, it is important that values from each distribution are meaningfully different. This difference can be determined from the overlap of the probability mass of the distributions, i.e. their overlap coefficient.[24] The overlap coefficients represent the fraction of common random samples of two distributions. Large overlap coefficients indicate that it is likely that similar currents will be obtained for different inputs. The overlap coefficients of the  $I_4$  current distributions are given in Figure 5.A.5a. While 68 of the 120 overlap coefficients are negligible, below 1%, 39 inputs have significant overlap coefficients of 10% or higher. These inputs could be confused if only one sample is provided to the network, potentially reducing its accuracy. The overlap of the distributions can be reduced significantly by mapping the inputs to both the  $I_2$  and the  $I_4$  currents, as demonstrated by Figure 5.A.5b. In this case, 106 overlap coefficients are below 1%, and only 9 overlap coefficients above 10% are found. Figure 5.A.5c shows that mapping to all four currents results in negligible overlap coefficients for all inputs. Nonetheless, an important caveat is that mapping to multiple currents requires additional memory elements in the in-sensor computing array, increasing device complexity and reducing energy efficiency.

### 5.2.3 Light inputs

Next, we investigate the separability of the input sequences using light in addition to voltage pulses. A schematic of the light input measurement is given in Figure 5.3a. Each timestep ( $\Delta t$  in Figure 5.1d) for the light inputs was 270 ms. At the start of each timestep, a  $-1$  V pulse is applied for approximately 40 ms. Afterwards, the voltage is changed to a constant  $+100$  mV, and the current is measured. The voltage pulses set the input frequency ( $\Delta t$ ) of the device. Light pulses can be applied simultaneously with the  $-1$  V pulses. Applying a light pulse during the  $-1$  V pulse is considered a binary “1”, while no applied light during the  $-1$  V pulse is represented by a binary “0”. The device was not illuminated at any other part of the timestep. In our current implementation, it was not possible to induce a volatile current by applying light pulses without a bias voltage. This suggests that

5

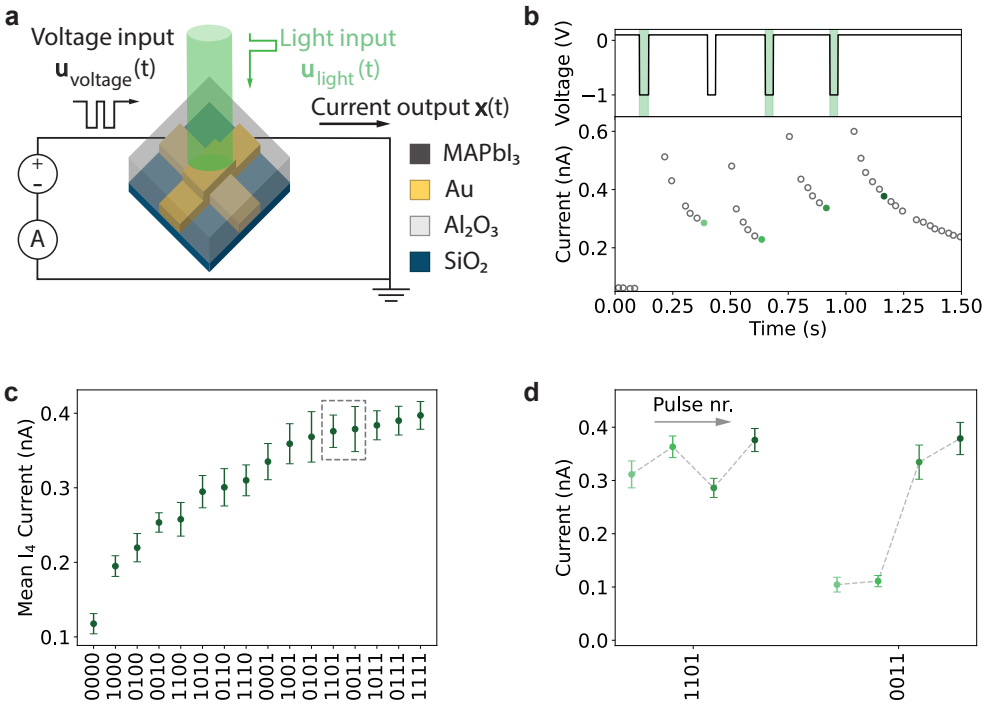


**Figure 5.3:** Optoelectronic measurements of four-bit light pulse inputs. **(a)** Schematic of the measurements. Periodic  $-1$  V pulses are applied to the device. Four-bit light input sequences are applied simultaneously with the  $-1$  V pulses. **(b)** An example measurement of the 1011 sequence is shown as green shaded regions in the top panel. Measured currents are shown in the bottom panel. The  $I_1$ ,  $I_2$ ,  $I_3$ , and  $I_4$  currents used for further analysis are shown in green. **(c)** Mean  $I_4$  currents for each four-bit input. The mean currents are higher for inputs where more light pulses are applied, and where these pulses are applied for later bits. The gray dotted box highlights the 1101 and 0011 inputs as an example of inputs with similar means. **(d)** The  $I_1$ ,  $I_2$ ,  $I_3$ , and  $I_4$  currents of the 1101 and 0011 inputs highlighted in (c). While the  $I_4$  currents are similar, the  $I_1$ ,  $I_2$ , and  $I_3$  currents are noticeably different.

illumination does not generate a photovoltage that can drive ion migration. Fabricating devices with electronically asymmetric electrodes could remedy this limitation.[19]

An example measurement of a 1011 input sequence ( $\mathbf{u}(t)$  in Figure 5.1a and b) is shown in Figure 5.3b. Similar to the example voltage input measurement in Figure 5.2b, the current is increased after each  $-1$  V pulse. When the device is illuminated during the voltage pulse, the current increase is enhanced, in accordance with Chapter 4. This enhancement can be explained by the higher ion mobility in the perovskite layer under illumination. Interestingly, the current also seems to decay more slowly for the light inputs compared to the voltage input in Figure 5.2b. Fits to the current decay after the 0000 and 0001 input sequences in Figure 5.A.6 show that this is due to a shift from a faster drift to a slower diffusion decay. This trend indicates that accumulated ions experience a weaker electric field after applying light pulses. A possible explanation might be a flattening of the electronic bands as the perovskite layer is illuminated, due to the increase in electronic charge carrier density.[25] Analogous to the voltage sequences, the separability of each of the sixteen possible inputs was investigated based on the means and standard deviations of the  $I_1$ ,  $I_2$ ,  $I_3$ , and  $I_4$  currents ( $\mathbf{x}$  in Figure 5.1b).

The means and standard deviations of the  $I_4$  currents for each input sequence are given in Figure 5.3c. Higher currents are obtained when a larger number of light pulses are applied, and when the pulses are applied in later timesteps. Similarly to the voltage inputs, some sequences for the light inputs show comparable  $I_4$  current. The constant 100 mV offset we use reduces the overlap somewhat. Figure 5.A.7 shows the mean  $I_4$  currents if no offset was applied, resulting in more similar values. Nonetheless, several means are closely spaced, such as those of the highlighted 1101 and 0011 input sequences. Despite these similar mean  $I_4$  currents, the  $I_1$ ,  $I_2$ , and  $I_3$  currents are more easily separable, as demonstrated by Figure 5.3d. The mean  $I_1$ ,  $I_2$ ,  $I_3$ , and  $I_4$  currents and standard deviations of each 4-bit light sequence are given in Figure 5.A.8. Similar to the 4-bit voltage sequences measurements, standard errors of the means are small, as illustrated by Figure 5.A.9. Overlap coefficients are given in Figure 5.A.10. Of the 120 coefficients, 55 are 10% or larger when mapping to only the  $I_4$  current. High overlap coefficients are found particularly for inputs containing three or four light pulses. Similar to the voltage inputs, overlap is reduced significantly by mapping to both  $I_2$  and  $I_4$ , with only 18 significant overlap coefficients. Again, mapping to all four currents yields no significant overlap for any combination of inputs.

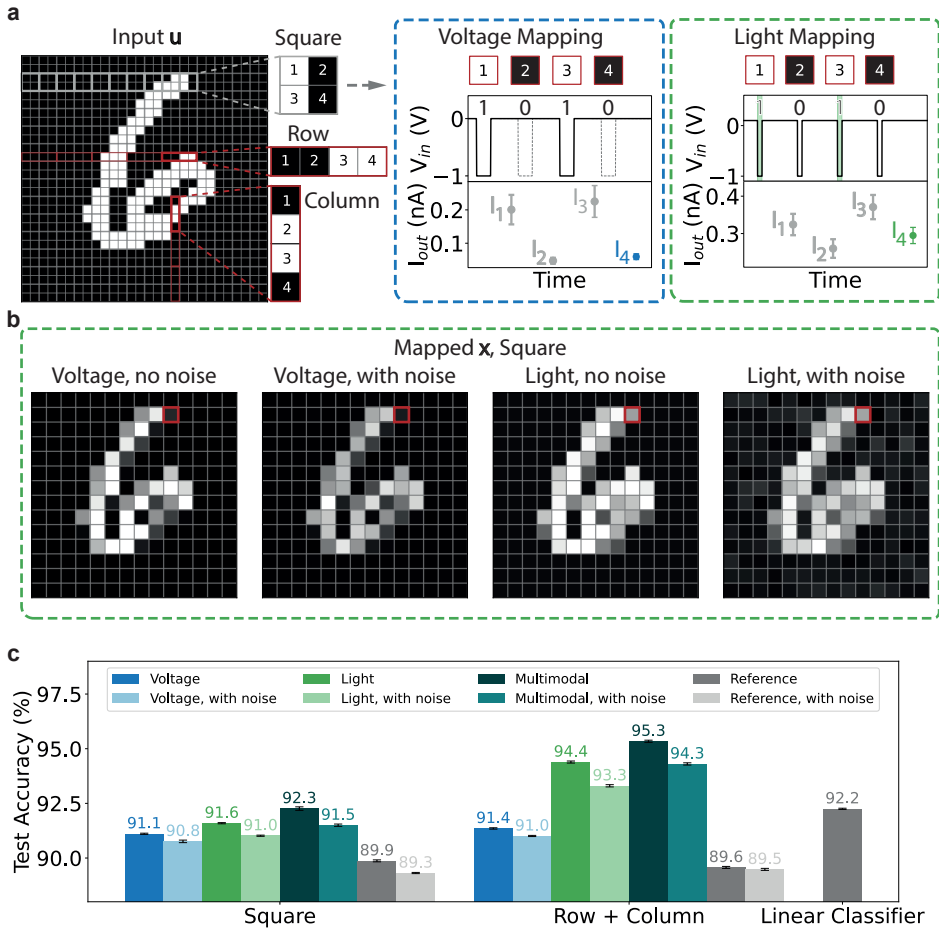


**Figure 5.4:** MNIST classification with images transformed based on light and voltage inputs. **(a)** Example transformation of a binarized MNIST image of a number 6. The image is divided into 2x2 pixel squares (“Square”), 4 pixel rows (“Rows”), or 4 pixel columns (“Columns”). Pixels are laid out in a row from the pixels labeled “1” to “4”. White pixels are interpreted as a “1” (voltage or light pulse input), and black pixels as a “0” (no input). The obtained 4-bit binary sequence is matched to experimental voltage or light inputs, shown for the 1010 sequence of the square example. The square, row, or column is converted (mapped) to the  $I_4$  current of that sequence. **(b)** Example transformation based on square mapping to the voltage and light-input data. In the “no noise” transformations, the 2-by-2 pixel squares were mapped to the mean  $I_4$  current of the sequences. Noise was included in the “with noise” case as described in the Methods section. The pixel highlighted in red corresponds to the red patch in **(a)**. **(c)** Mean classification accuracies of datasets transformed by mapping the images with the Square, or combined Row and Column approach to the  $I_4$  currents of the voltage, light, or a combination of both (multimodal) measurements. Accuracies are compared to references for which each square, row, or column was mapped to the binary value of pixel 4 in **(a)**, without considering the values of pixels 1, 2, and 3. From this, we can determine the benefit of the volatile memory (see Methods for details). The accuracies are compared to a linear classifier reference trained on the binarized MNIST dataset without any transformations. Each test accuracy was determined from 10 independent runs with different random seeds. Error bars indicate one standard deviation.

### 5.2.4 MNIST classification

In the next step, we demonstrate the use of our optoelectronic artificial synapse in a reservoir network. Reservoir networks were implemented based on either the voltage or light sequences. MNIST handwritten digit classification was used to benchmark network performance. Each sample of the binarized MNIST dataset was divided into 2x2 pixel patches (“Square”), 4 pixel rows (“Row”), or 4 pixel columns (“Column”). These 4-pixel arrays were then converted to 4-bit binary sequences. White pixels are interpreted as a “1” (an input voltage or light pulse) and black pixels as a “0” (no input pulse). The sequence is constructed by combining the obtained binary values in the order denoted in Figure 5.4a. Next, we define a mapping  $f : A \rightarrow B$ , where A is any of the 16 possible 4-bit sequences, obtained from the image, and B the corresponding  $I_4$  current from Figure 5.2c (voltage input) or Figure 5.3c (light input). An example mapping of a 2x2 pixel square is shown in Figure 5.4a. The square is converted to the 1010 pixel sequence which is mapped to the  $I_4$  current of the 1010 voltage (Figure 5.2c) or light input (Figure 5.3c). In a physical implementation, each square, row, or column would contain the input to one device in the sensor array. The 4-bit sequences would then be applied as in Figure 5.2c or Figure 5.3c, and afterwards the  $I_4$  current of each device in the array would be collected for readout. This method of temporally encoding segments of an image is commonly used in reservoir computing.[26] The purpose of the reservoir in this application is to correlate the pixel values to extract features in the images important for their classification. The square, row, and column approach to transforming the images will therefore lead to the extraction of features in one (column and row) or two dimensions (square).

Figure 5.4b shows the MNIST sample after mapping all squares to the corresponding  $I_4$  currents of the 4-bit voltage and light inputs. The transformed images correspond to the mapped vector  $\mathbf{x}$  in Figure 5.1b, where the  $I_4$  currents represent the states collected from each node. We account for experimental noise in the transformation by mapping each square to a random number taken from a normal distribution with the experimentally determined  $I_4$  current mean and standard deviation for that sequence. Brighter pixels, corresponding to higher  $I_4$  currents, are obtained for the light-transformed images compared to voltage-inputs. Thus, compared to the voltage-input based transformations, pixel values (currents) from earlier inputs are retained to a greater extent for the light-transformed images, in line with the example 1010 mapping in Figure 5.4a. The longer retention can be explained by the shift to slower current decay by ionic diffusion after light inputs (Figure 5.A.6), resulting in a longer memory window.

Each image in the MNIST dataset was transformed by the Square, Row, or Column mapping approach. Linear readout layers were then trained on the transformed datasets.

Figure 5.4c shows the obtained classification accuracies over ten independent runs for different transformations. The networks are compared to reference networks trained on the binarized MNIST dataset for which each square, row, or column was mapped to the binary value of pixel 4 in Figure 5.4a. These reference networks are equivalent to using a regular, memory-less sensor array ( $\mathbf{s}$ ), such as a camera, in combination with a resistor array weight matrix ( $\mathbf{W}$ ). Comparing the reservoir network accuracies with the reference therefore allows an accurate assessment of the contribution of the reservoir. The accuracies are also compared to a linear classifier trained directly on the binarized MNIST dataset. Reservoir transformations successfully increase the linear separability of the dataset if reservoir network accuracies exceed that of this reference.

For the Square mapping approach, the light-based networks outperformed those based on voltage inputs (0.5%,  $p < 0.001$ ). We show in Section 5.B with simulations that this is due to the longer memory window of light inputs, which results in higher contrast for patches at the edges of the digits after the transformation. The ratio of the retention time to the input frequency of the light inputs is close to the optimum in the simulations. Conversely, the shorter relative memory window of the voltage-based networks provides higher contrast at patches containing many white pixels, which are typically found in the centers of the digits. This is also visualized in Figure 5.4b. Previously, better performance of reservoir networks was found when combining two sensing modes into a single, multimodal network.[15, 27] These multimodal networks combine two nonlinear transformations to increase linear separability. We construct multimodal networks by combining the  $I_4$  currents of the voltage and light networks into a single mapped state vector  $\mathbf{x}$ . The weight matrix is trained on the combined states.

The multimodal network outperforms all other networks implementing the square mapping, with a mean accuracy of  $92.3 \pm 0.1\%$  (all differences  $p < 0.001$ ). The improved performance likely stems from the complementary combination of enhanced contrast at the edge of the digit by the light-mapping and at the centers of the digits by the voltage-mapping. The addition of noise comparable to the experimental noise only slightly decreases the accuracy of the networks. Adding noise decreased the light-input and multimodal network accuracy more strongly, likely due to the higher overlap coefficients of the light input  $I_4$  currents (Figure 5.A.10) than those of the voltage inputs (Figure 5.A.5). In all cases, the reservoir networks outperform the square reference, also when considering the noise. This result shows that the transformations encode information relevant for classification, also when considering experimental noise. Nevertheless, even without considering experimental noise, the multimodal network with the Square transformation does not significantly outperform the linear classifier ( $p = 0.681$ ).

In previous implementations of in-sensor reservoir networks, the MNIST dataset is typically transformed in a four-pixel line-by-line fashion (“Row”, or “Column” in Figure 5.4a).[15, 28–30] We implement the same transformations in Figure 5.C.1a, b, and c. The Figure shows that these transformations distort the image more strongly than the square mapping method we follow in Figure 5.4. The classification accuracies are given in Figure 5.C.1d. The accuracies for both the voltage ( $89.0 \pm 0.1\%$ ,  $88.6 \pm 0.1\%$  with noise) and light inputs ( $90.8 \pm 0.1\%$ ,  $90.0 \pm 0.1\%$  with noise) were slightly higher for the row than the column mapping, but are lower than those we obtained for the square mapping in Figure 5.4c. This is likely due to a stronger loss of relevant features as the images are compressed in only one dimension. Interestingly, the mean accuracy of the multimodal network was  $92.6 \pm 0.1\%$  ( $91.5 \pm 0.1\%$  with noise), slightly higher than for the square mapping ( $p < 0.001$ ). This accuracy exceeds that of the linear classifier ( $p < 0.001$ ), although only if experimental noise is not considered. Similar to the square mapping, this could be explained by the complementary combination of the light and voltage  $I_4$  current mapping. Furthermore, the four-pixel rows extend over a larger distance in the image. This might allow the network to better extract relevant features for classification. Notably, the accuracies of the light input and the multimodal networks are higher than those reported in previous work.[15, 28–30] For the light-based network, this could be due to a more favorable current output for the input sequences, as explained in Section 5.B. Another explanation might be a more thorough hyperparameter search before training the readout layers. For the multimodal network, the accuracy is likely increased further by the complementary combination of the light and voltage mapping, in line with previous work.[15, 27] Importantly, some previously reported accuracies are comparable or even lower than the reference we report here.[15] This finding highlights the importance of thoroughly evaluating the reservoir performance in comparison to reference linear classifiers to prevent overestimating the contribution of the reservoir transformations.

A proven way to increase the accuracy of a reservoir computing network is to present the images to the network at different rotations.[26] We implement this here by mapping each digit with both the row and column approaches and concatenating the obtained mapped image vectors to obtain a single combined vector  $\mathbf{x}$  for each image. The readout layers are then trained on the combined row and column transformed dataset. Network accuracies are shown in Figure 5.4c as “Row + Column”. As expected, mean accuracies increased compared to those of the square and separate row and column mapping. The highest obtained mean accuracy was  $95.3 \pm 0.1\%$  for the multimodal network. By combining the row and column mappings, the separability of features is increased in both dimensions. Compared to the square mapping, features are extracted over larger distances in the images (4

instead of 2 pixels in either direction), which can explain the better performance. Both the light-input and multimodal networks implementing this mapping approach exceed the linear classifier. These networks also further improve on previously reported in-sensor reservoir implementations.[15, 28–30] Increasing the number of pixels mapped by each device could further enhance the network accuracy.[26] The light inputs in particular appear to have a sufficiently long retention time for mapping more than the currently implemented 4 pixels at a time. Previously, applying additional rotations to the MNIST dataset resulted in higher accuracies for software reservoir networks.[26] The same approach might increase the accuracy of our networks as well. Another method to increase the accuracy is to add hidden layers that perform further nonlinear transformations of the data.[19] However, such are difficult to implement in hardware and are therefore less interesting for in-sensor computing.

### 5.2.5 MNIST classification from video

Next, we investigated the reservoir network performance for natively temporal inputs relevant to in-sensor computing. Handwritten digit classification from video, based on the N-MNIST dataset,[31] is taken as an example. While the light input lends itself well to detecting and transforming visual data, the voltage implementation could be useful for processing data from a separate sensor detecting, for example, tactile signals.[15] We followed a similar approach as before. First, 34-by-34 pixel binned and binarized N-MNIST frames are mapped to the experimental voltage and light data, as shown schematically in Figure 5.5a. However, instead of squares, rows, or columns, individual pixels of four consecutive frames are mapped to the  $I_1$ ,  $I_2$ ,  $I_3$ , and  $I_4$  currents.

Figure 5.5b shows the frames after each pixel is mapped to the corresponding mean currents of the 4-bit light sequence. The number six of the previous frames remains visible with lower brightness in each consecutive frame, visualizing that information from previous frames is retained. Figure 5.5c shows the transformed sample accounting for the experimental noise, and the sample transformed based on voltage inputs. In all cases, the number six remains recognizable after the transformation. However, the features of previous frames remain brighter for the sample mapped to the light input. This is again a result of the longer retention of information compared to the voltage input, similar to Figure 5.4.

The dataset was transformed based on voltage and light input experimental currents. As in Figure 5.4, multimodal networks were implemented by combining the voltage and light-input transformed frames. Next, linear readout layers were trained on the transformed datasets. A reference network was trained on a dataset that was not transformed.

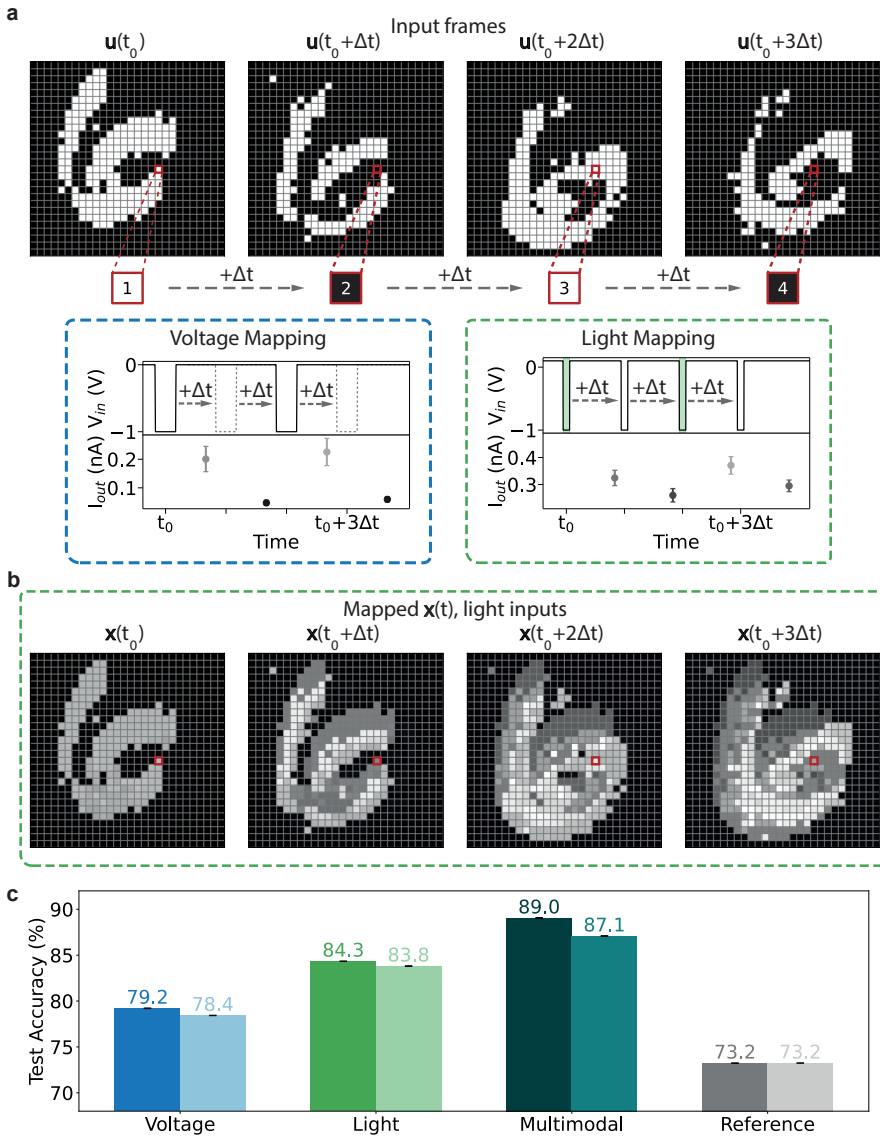


**Figure 5.5:** Handwritten digit classification from video with frames transformed based on light and voltage inputs. **(a)** Four consecutive frames of a number 6. Pixels underneath each frame show the pixel highlighted in red at each timestep. For each pixel in the four frames, its four consecutive values are converted to a four-bit light or voltage pulse input sequence. The sequence is then applied (in silico) to the experimentally measured artificial synapse. **(b)** Transformations of the frames in **(a)** after each timestep, based on the means of the four-bit light inputs. Each pixel is mapped following the procedure outlined in **(a)**. The red boxes highlight the same pixel as in the frames in **(a)**. **(c)** Classification accuracies obtained for the reservoir networks based on voltage (blue), light (green), and multimodal (teal) inputs. The accuracies are compared to a reference (gray) trained on the dataset without transformations. Accuracies for networks also considering experimental noise are given in lighter colors. Accuracies were obtained by taking the mean of 10 independent training runs.

In our implementation, the frames ( $\mathbf{u}(t)$ ) are projected on the sensor array ( $\mathbf{s}$ ), and the output currents of each device ( $\mathbf{x}(t)$ ) are collected continuously. Weighted sums of the currents are taken with the weight matrix ( $\mathbf{W}$ ) after each input frame (for each timestep  $\Delta t$ ), to classify each frame consecutively. Analogous to the MNIST classification in Figure 5.4, the reference network is equivalent to an in-sensor network with a conventional, memory-less sensor array such as a camera. The benefit of the transformations can be evaluated by comparison with the reference. Network accuracies are given in Figure 5.5c. Compared to the MNIST dataset, the video data is significantly less linearly separable, as follows from the lower reference classification accuracy of  $73.2 \pm 0.1\%$ . Interestingly, markedly higher classification accuracies were found for the reservoir networks ( $79.2 \pm 0.1\%$ ,  $84.3 \pm 0.1\%$ , and  $89.0 \pm 0.1\%$  for voltage, light, and multimodal sequences, respectively, all  $p < 0.001$ ). This implies that the transformations substantially increased the linear separability of the dataset. The better performance of the light compared to the voltage input networks we find here is again likely due to the longer retention time of the light inputs (see Section 5.B). The higher accuracy of the multimodal network again likely follows from the complementary transformations by the light and voltage networks. Also, similar to the MNIST classification results, adding experimental noise resulted in only a slight decrease in accuracy (0.8%, 0.5%, and 1.9% for the voltage, light, and multimodal networks, respectively, all  $p < 0.001$ ).

The considerable increases in classification accuracy of the MNIST handwritten digits from both images and video show that the volatile optoelectronic devices are promising for in-sensor computing applications. Particularly when implementing them in multimodal networks. Moreover, the back-contacted microscale device architecture lends itself well to high-density integration in in-sensor computing arrays. Currently, we have only implemented binary inputs. The capabilities of these arrays could be further extended by considering different light intensities and voltage magnitudes. This extension would allow processing real-time, analog signals. Analog inputs could simultaneously increase the range of accessible reservoir states, potentially resulting in even more capable nonlinear transformations.

### 5.3 Conclusion

In summary, we have demonstrated physical reservoir networks based on back-contacted, microscale halide perovskite devices. The networks encoded MNIST images and N-MNIST-based videos based on experimentally measured currents of the device using 4-bit voltage and light input sequences. We have shown with drift-diffusion simulations that the mea-

sured current transients are due to ion migration in the device. When employed in a network in silico, multimodal networks based on the devices that processed both light and voltage inputs gave notably higher classification accuracies compared to a linear classifier reference. The mean accuracy of the multimodal network was  $95.3 \pm 0.1\%$ . We explain with simulations that the high accuracy is due to light-based transformations complementing those based on voltage due to their difference in retention time, emphasizing different features in the images. As a result, the accuracies we report here for the light-based and multimodal networks are higher than those in previous work that followed a similar approach.[15, 28–30] Notable accuracy increases with respect to the reference were found for MNIST classification from video as well. The mean accuracy of the networks increased by up to 15.8% to  $89.0 \pm 0.1\%$  for the multimodal mapping. Hence, the ability of the halide perovskite devices to process both voltage and light inputs allows multimodal processing in the same chip, significantly improving accuracy. These accuracy gains, combined with the microscale device architecture that lends itself well to high-density integration, are promising for efficient in-sensor computing applications.

## 5.4 Materials and Methods

### 5.4.1 Materials

Silicon wafers with a 100 nm dry thermal oxide layer were purchased from Siegert Wafer.  $\text{PbI}_2$  (99.99%) was purchased from TCI. Methylammonium iodide (MAI, purity not listed) was purchased from Solaronix.  $\text{Al}(\text{CH}_3)_3$  (97%), anhydrous DMF, DMSO, and chlorobenzene were purchased from Sigma-Aldrich. MA-N1410 resist and MA-D533/s developer were purchased from Micro Resist. All materials were used without further purification.

### 5.4.2 Halide perovskite device fabrication

Halide perovskite devices were fabricated as reported in Chapter 4. In short, 2.5  $\mu\text{m}$  wide gold bottom electrodes with a thickness of 80 nm were patterned on the silicon wafer using a lift-off process with the MA-N1410 resist. A 15 nm  $\text{Al}_2\text{O}_3$  insulating layer was deposited over the bottom electrode by atomic-layer deposition from  $\text{Al}(\text{CH}_3)_3$  and  $\text{H}_2\text{O}$  precursor gases in a home-built atomic-layer deposition setup at 250 °C. The lift-off process was repeated to pattern 2.5  $\mu\text{m}$  wide, 80 nm thick gold top contacts perpendicular to the bottom electrodes.

Inside a  $\text{N}_2$ -filled glovebox, the  $\text{MAPbI}_3$  precursor was prepared by dissolving 1.1 mmol  $\text{PbI}_2$  and MAI in 1 mL DMF and 0.1 mL DMSO. The precursor was filtered through a 0.2  $\mu\text{m}$  PTFE

filter and spin-coated on a die cut from the patterned wafer at 4000 rpm for 30 seconds. After 5 seconds, 250  $\mu\text{L}$  of chlorobenzene was added to the spinning sample. The sample was annealed at 100  $^{\circ}\text{C}$  for 10 minutes. The sample was then encapsulated with Blufixx epoxy and a glass coverslip, cured for 1 minute with a UV torch.

### 5.4.3 4-bit input measurements

The 4-bit input sequence measurements were performed with a Keysight B2902A Precision Source/Measure Unit. One channel of the SMU was used to apply voltage pulses to the device and measure the output current. For the light inputs, a second channel was used to drive a 520 nm high-power Cree XLamp XP-E LED. The irradiance was 2.8  $\text{mW}/\text{cm}^2$ , measured with a Thorlabs PM100D optical power meter with an S120VC sensor. Measurements of each input sequence were repeated 100 times. The  $I_1$ ,  $I_2$ ,  $I_3$ , and  $I_4$  currents in the main text were determined by taking the mean and standard deviation over all measurements.

### 5.4.4 Drift-diffusion simulations

The drift-diffusion simulations were carried out using Setfos by Fluxim with the device parameters listed in Table 5.1. We simulated the current due to mobile ions after applying a voltage pulse train of 1 to 4 voltage pulses of  $-1$  V.

**Table 5.1:** Simulation parameters used for the drift-diffusion simulations. A schematic of the simulated device stack is given in Figure 5.A.2c and d.

| Parameter  | Value               | Reference |
|--|---------------------|-----------|
| $\text{Al}_2\text{O}_3$ Thickness (nm)                                     | 15                  |           |
| Relative permittivity $\text{Al}_2\text{O}_3$                              | 9                   |           |
| Electron affinity $\text{Al}_2\text{O}_3$ (eV)                             | 2.5                 |           |
| Band gap $\text{Al}_2\text{O}_3$ (eV)                                      | 5                   |           |
| Thickness perovskite (nm)  | 50                  |           |
| Relative permittivity perovskite   | 24.1                | [32]      |
| Electron affinity perovskite (eV)  | 3.9                 | [33]      |
| Band gap perovskite (eV)   | 1.6                 | [33]      |
| Effective density of states perovskite conduction band ( $1/\text{cm}^3$ ) | $8 \times 10^{18}$  |           |
| Effective density of states perovskite valence band ( $1/\text{cm}^3$ )    | $8 \times 10^{18}$  |           |
| Mobile positive ion density ( $1/\text{cm}^3$ )                            | $3 \times 10^{17}$  |           |
| Immobile negative ion density ( $1/\text{cm}^3$ )                          | $3 \times 10^{17}$  |           |
| Mobility mobile ions ( $\text{cm}^2/\text{Vs}$ )                           | $1 \times 10^{-10}$ |           |
| Work function electrodes (eV)  | 5.1                 |           |
| Voltage pulse duration (s)   | 0.05                |           |
| Time between voltage pulses (s)  | 0.1                 |           |

### 5.4.5 Transformations of the MNIST and N-MNIST datasets

Lookup tables were constructed from the experimentally measured mean currents of each 4-bit input. Means were taken over 100 measurements for each input. The 28-by-28-pixel MNIST images were binarized with a threshold of 0.5. The binarized images were then divided into square 2-by-2-pixel patches, 4-pixel rows, or 4-pixel columns. The pixels of each patch were converted to a 4-bit sequence, as shown in Figure 5.4a. The sequences were then mapped by matching them to a 4-bit input sequence in the lookup table. The corresponding currents were added to a new array representing the transformed image. To account for the experimental noise, a random number was taken from a normal distribution with the mean and standard deviation determined from the 100 measurements of the corresponding  $I_4$  current, instead of mapping to the  $I_4$  current mean. The mean and standard deviation of each sequence are displayed in Figure 5.2c (for voltage inputs) and Figure 5.3c (for light inputs). For the references, a Gaussian blur was applied with a variance determined from the original MNIST dataset, see Figure 5.C.3a. This is the noise that would be expected if the binarized MNIST images are projected on a conventional camera. Figure 5.C.3b shows that the blurring (kernel size = 5,  $\sigma = 0.522$ ) approximates the observed noise well.

The N-MNIST dataset was imported with Tonic (version 1.6.0). The original spiking, event-based dataset was filtered, binned, and thresholded to reconstruct videos of the original moving MNIST images. This modified dataset is more relevant for real-time video recognition using the in-sensor networks for simultaneous detection and processing. A denoise filter with a 10 ms filter time was applied to the dataset, and the samples were binned into 50 ms frames. Next, the pixel values in the first four 34-by-34-pixel frames of each sample were normalized, and the frames were binarized with a threshold of 0.2. This threshold yielded the most recognizable digits in the frames. A similar approach was followed to map the frames to the voltage and light-input data as for the MNIST mapping. However, instead of squares, rows, or columns, each individual pixel was mapped based on its four consecutive values in the four frames. After mapping each pixel, the four frames were added to the dataset separately. This extended the training and test datasets from 60,000 to 240,000 and from 10,000 to 40,000 samples, respectively. Noise was introduced as Gaussian blurring with the same parameters as for the MNIST dataset.

### 5.4.6 Network training

Readout layers were trained on the input vectors with PyTorch (version 2.6.0), using the Adam optimizer. Hyperparameters (learning rate, weight decay, and  $\beta_1$  and  $\beta_2$  of the

Adam optimizer) were tuned over 100 runs with Optuna (version 4.2.1), using the Tree-structured Parzen Estimator algorithm. A large, fixed batch size of 256 was chosen for faster training.[34] The MNIST dataset was randomly split into a training set containing 50,000 samples and a validation set of 10,000 samples during hyperparameter tuning. Readout layers with 1960 ( $14 \times 14 \times 10$ , square, or  $7 \times 28 \times 10$ , row, and column mapping), 3920 ( $7 \times 28 \times 10 \times 2$ , combined row and column mapping, or  $14 \times 14 \times 10 \times 2$ , multimodal square mapping), or 7840 ( $7 \times 28 \times 10 \times 2 \times 2$ , multimodal combined row and column mapping) weights were trained on the mapped images. The N-MNIST dataset was randomly split into a 200,000-sample train and a 40,000-sample validation set. The readout layers, consisting of 11560 ( $34 \times 34 \times 10$ ), or 23120 ( $34 \times 34 \times 10 \times 2$ , multimodal mapping) weights, were trained on the transformed frames.

After hyperparameter tuning, training was repeated on the full training dataset with the optimal hyperparameters. Mean network accuracies and standard deviations were recorded from a seed sweep over the same 10 seeds for all networks. All mean accuracies and their standard deviations are rounded to the first decimal place. Standard deviations that would be rounded to 0.0% (e.g. 0.03%) were rounded up to 0.1% instead to account for experimental error. All standard deviations were  $\leq 0.10\%$ .

Paired t-tests were performed to check the significance of differences in accuracy. All mean accuracies within each plot were significantly different ( $p < 0.001$ ), with the exception of the accuracies of the multimodal, square mapping network and the reference in Figure 5.4c ( $p = 0.681$ ), and the reference networks with and without noise for the row mapping in Figure 5.C.1d ( $p = 0.275$ ), and the video dataset in Figure 5.5c ( $p = 0.546$ ).

## 5.A Additional information

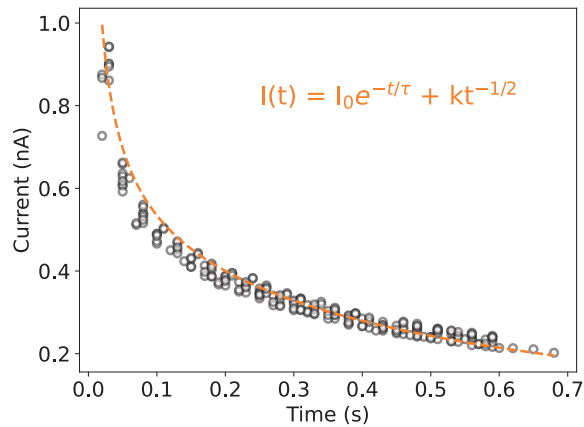


**Figure 5.A.1:** Fit to the combined data of the ten transient current measurements as in Figure 5.11d. The current is measured after the final  $-1$  V pulse, and fit with equation  $I(t) = I_0 e^{-t/\tau} + kt^{-1/2}$ . Fitting parameters are given in Table 5.A.1.

**Table 5.A.1:** Fitting parameters for the fit in Figure 5.A.1. Errors represent the fitting error.

| Fitting parameter | Value                           |
|-------------------|---------------------------------|
| $I_0$             | $0.22 \pm 0.02$ nA              |
| $\tau$            | $0.53 \pm 0.04$ s               |
| $k$               | $0.110 \pm 0.005$ nA $\sqrt{s}$ |

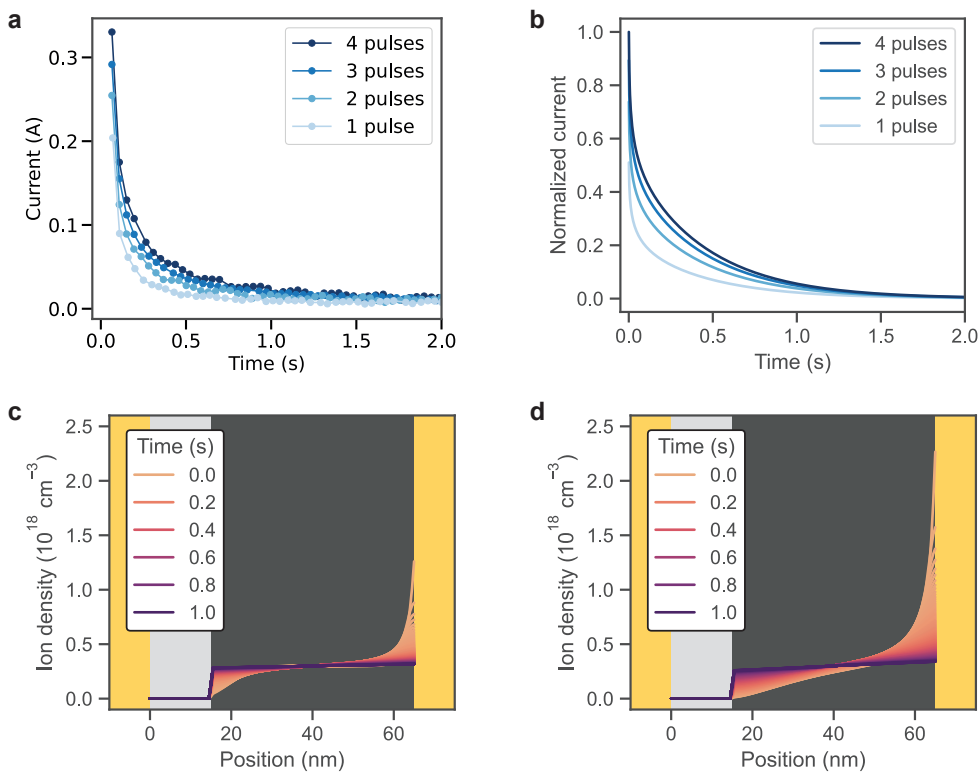


**Figure 5.A.2:** Comparison of measured transient currents with drift-diffusion simulations. **(a)** Measured currents after applying a series of  $-1$  V pulses. The final pulse is removed at  $t = 0$  sec. **(b)** Drift-diffusion simulations of the measurements. **(c)** Ion densities after applying a single  $-1$  V pulse. Ions are initially accumulated at the cathode and redistribute throughout the perovskite layer within seconds. **(d)** The same simulation as in **(c)**, but after applying four  $-1$  V pulses. The same effect is observed, but with a larger magnitude.

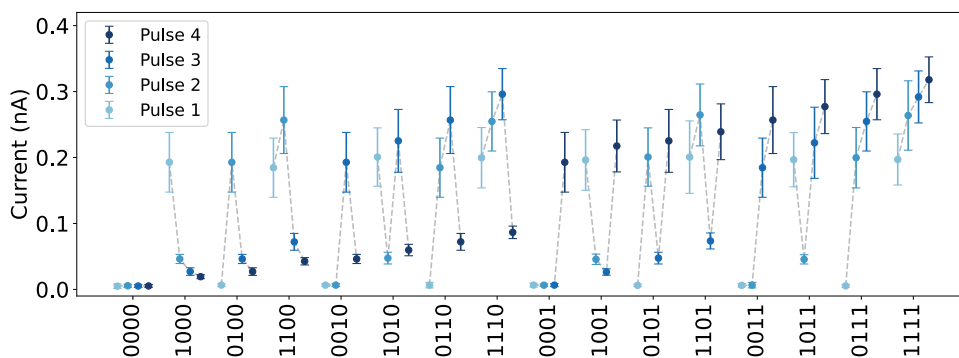


**Figure 5.A.3:** Mean currents after each of the four pulses of the 4-bit voltage inputs. Means taken over 100 measurements, with error bars representing one standard deviation. Gray dotted lines are added for each input to guide the eye. Inputs with similar mean final currents are more easily separable by considering intermediate currents.

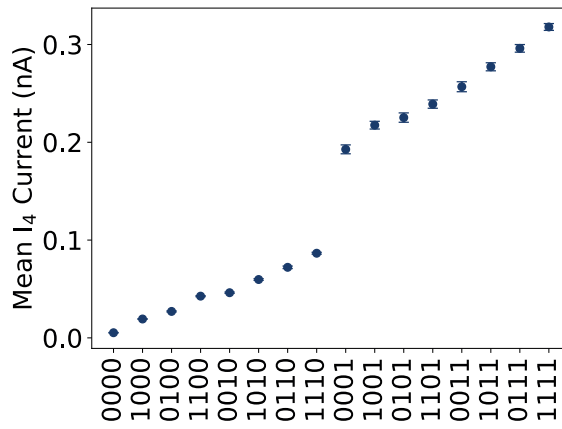


**Figure 5.A.4:** Mean currents with error on the mean of the 4-bit voltage inputs. The low errors on the means indicate that the obtained means are well-defined.

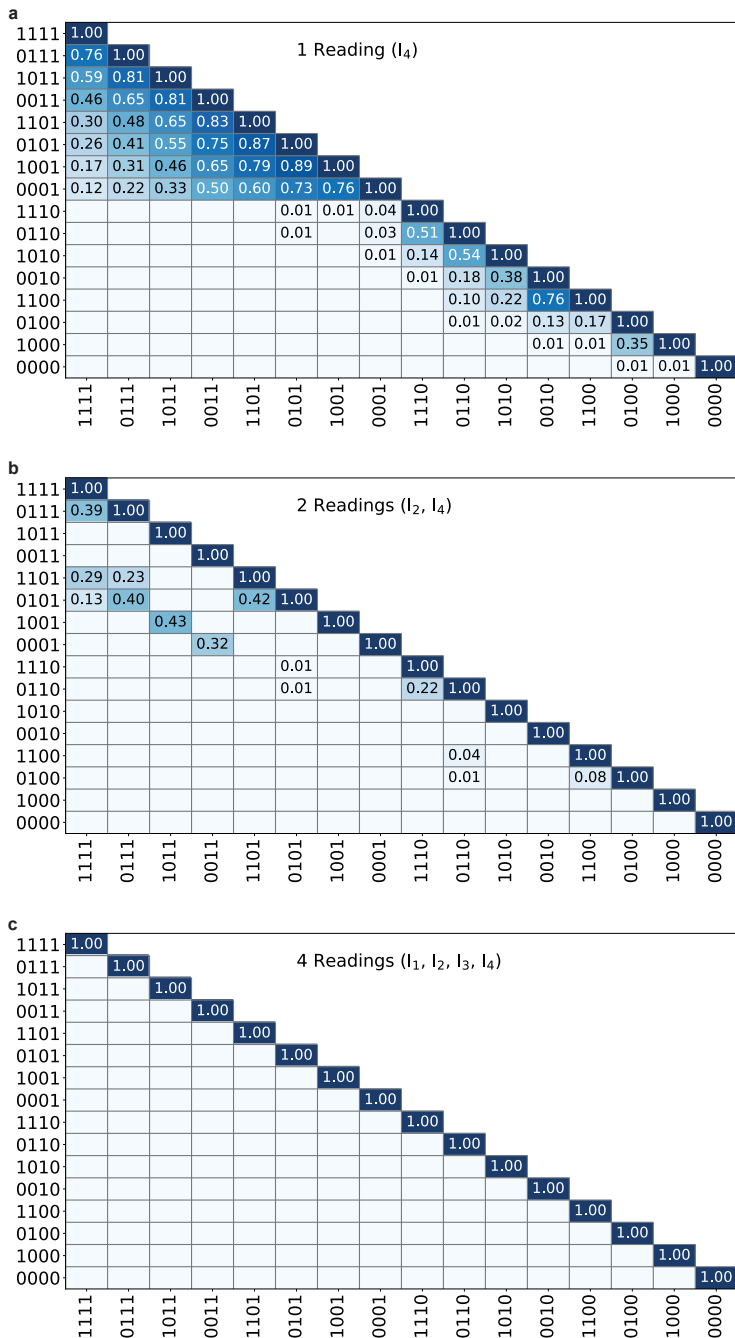


**Figure 5.A.5:** Overlap matrices of the four-bit voltage input mappings to (a) the current after the fourth bit, (b) the current after the second and the fourth bit, and (c) the currents after all four bits. Overlap coefficients below 0.01 are not plotted for clarity. Significant overlap coefficients are found for similar inputs when mapping to fewer currents.

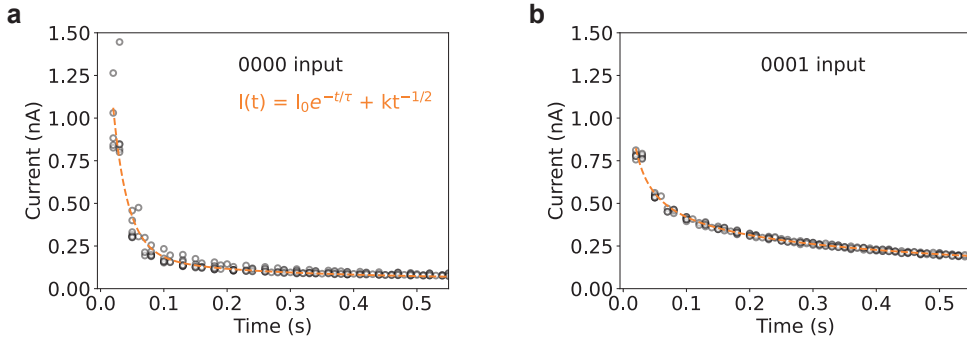


**Figure 5.A.6:** Fits to the combined data of ten 0000 (a) and 0001 (b) light input sequence transient current measurements. The current is measured after the final  $-1$  V pulse and fit with equation  $I(t) = I_0 e^{-t/\tau} + kt^{-1/2}$ . Fitting parameters are given in Table 5.A.2.

**Table 5.A.2:** Fitting parameters of the current decays in Figure 5.A.6a and b. Errors represent the fitting error.

| Input | $I_0$ (nA)      | $\tau$ (s)        | $k$ (nA $\sqrt{s}$ ) |
|-------|-----------------|-------------------|----------------------|
| 0000  | $1.64 \pm 0.14$ | $0.023 \pm 0.002$ | $0.052 \pm 0.003$    |
| 0001  | $0.12 \pm 0.01$ | $0.737 \pm 0.066$ | $0.100 \pm 0.002$    |

5

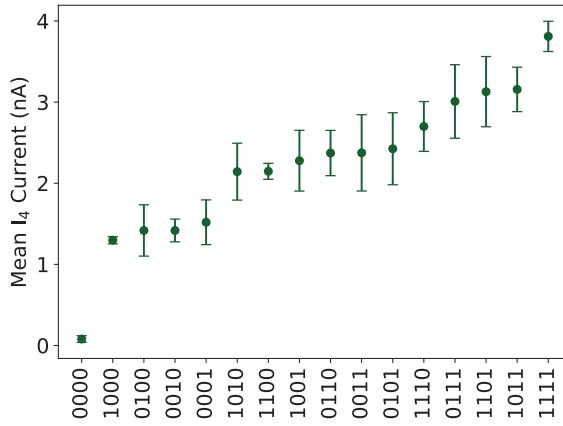


**Figure 5.A.7:** Mean  $I_4$  current for each of the 4-bit inputs if no 100 mV offset bias is applied between the  $-1$  V pulses. More overlap between  $I_4$  currents is found compared to the measurement with the offset in Figure 5.3c of the main text.

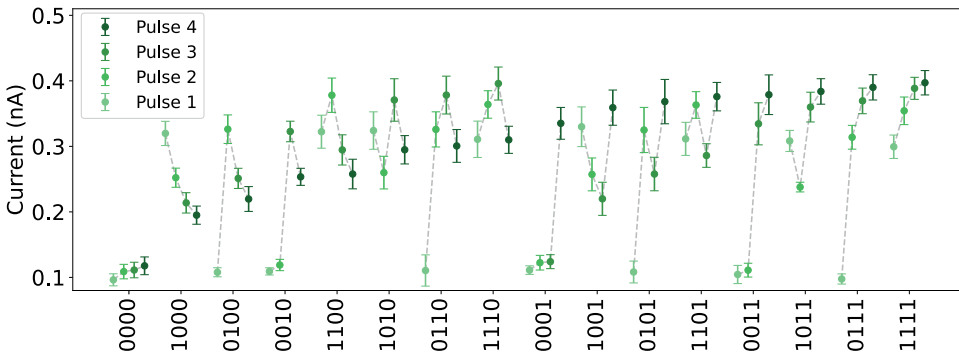


**Figure 5.A.8:** Mean currents after each of the four pulses of the 4-bit light inputs. Means taken over 100 measurements, with error bars representing one standard deviation. Gray dotted lines are added for each input to guide the eye. Inputs with similar mean final currents are more easily separable by considering intermediate currents.

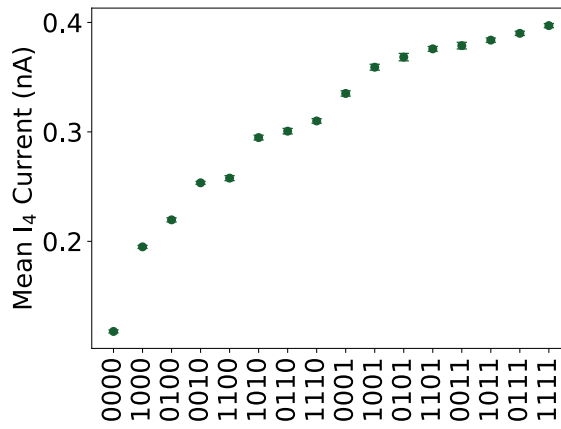


**Figure 5.A.9:** Mean currents with error of the mean of the 4-bit light inputs. The low errors of the means indicate that the obtained means are well-defined.

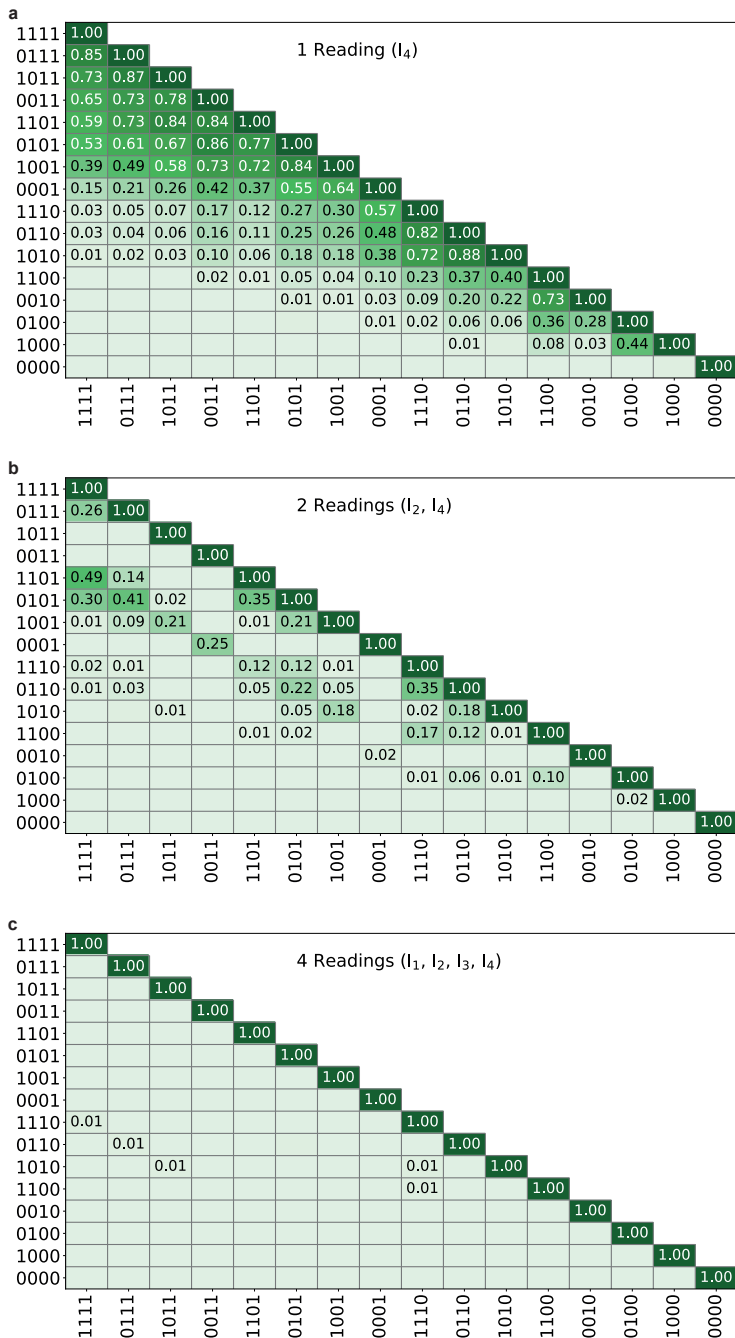


**Figure 5.A.10:** Overlap matrices of the four-bit light input mappings to (a) the current after the fourth bit, (b) the current after the second and the fourth bit, and (c) the currents after all four bits. Overlap coefficients below 0.01 are not plotted for clarity. Significant overlap coefficients are found for similar inputs when mapping to fewer currents.

## 5.B Impact of the $I_4$ currents on classification accuracy

This Section investigates the impact of the obtained currents for 4-bit sequences on the MNIST classification accuracy. We simulate  $I_4$  currents and show the effect of different trends on the MNIST image transformations to explain differences in classification accuracy. The  $I_4$  currents obtained for the light (Figure 5.2c) and voltage inputs (Figure 5.3c) are compared to the generated  $I_4$  currents to explain the differences in performance of the networks in the main text. Finally, we discuss how plotting the  $I_4$  currents for different 4-bit input sequences allows facile estimation of the in-sensor reservoir network performance. These results can be used to find optimal experimental parameters.

In reservoir computing, the reservoir performs a nonlinear transformation of the input,[6] increasing the separability of otherwise convoluted features.[5] In our implementation, the reservoir consists of devices that transform 4-bit voltage and light input sequences into a current. In this context, input sequences are separable if distinct current values are obtained for each sequence. This requires the device to have a volatile memory. Because of its memory, the device outputs a higher  $I_4$  current for a 0011 sequence than it does for a 0001 input. The volatility, on the other hand, causes the output current to depend on the order in which light or voltage pulses are applied in the sequence. It extends the device response beyond an additive, linear response in which inputs with the same number of pulses, such as the 1001 and 0011 sequences, yield the same  $I_4$  current. Due to current decay in our experiments, lower  $I_4$  currents are output if a pulse is applied earlier in the sequence. Consequently, a lower  $I_4$  current is obtained for the 1001 sequence than for the 0011 input. The volatility is thus crucial for separating inputs.

Ideally, the  $I_4$  currents should be as distinct as possible after the transformation. The overlap between  $I_4$  currents is minimized if they follow a linear trend in plots as in Figure 5.2c and 5.3c in the main text. Simulated  $I_4$  currents following a linear trend are given as the gray dotted line in Figure 5.B.1a. The normalized current is calculated as  $I_4(s) = \frac{s}{\Sigma s - 1}$ , where  $I_4$  is the current of the  $s^{th}$  sequence on the x-axis and  $\Sigma s$  is the number of possible sequences (16 sequences for a 4-bit input). The first sequence (0000) is assigned  $s = 0$ . The 4-bit voltage and light sequences in the main text produced  $I_4$  currents that deviate from this linear trend. The voltage inputs (Figure 5.2c) yielded lower  $I_4$  currents for the first half of the sequences. The light inputs (Figure 5.3c), on the other hand, produced  $I_4$  currents above the linear trend over the whole range of sequences. We simulate these responses with polynomial functions.

$I_4$  currents falling below the linear trend are calculated as  $I_4(s) = \left(\frac{s}{\Sigma s - 1}\right)^n$ , shown in blue in Figure 5.B.1a. In the plot,  $n$  is 1.5, 2.0, 3.0, or 4.0, where higher values result in a

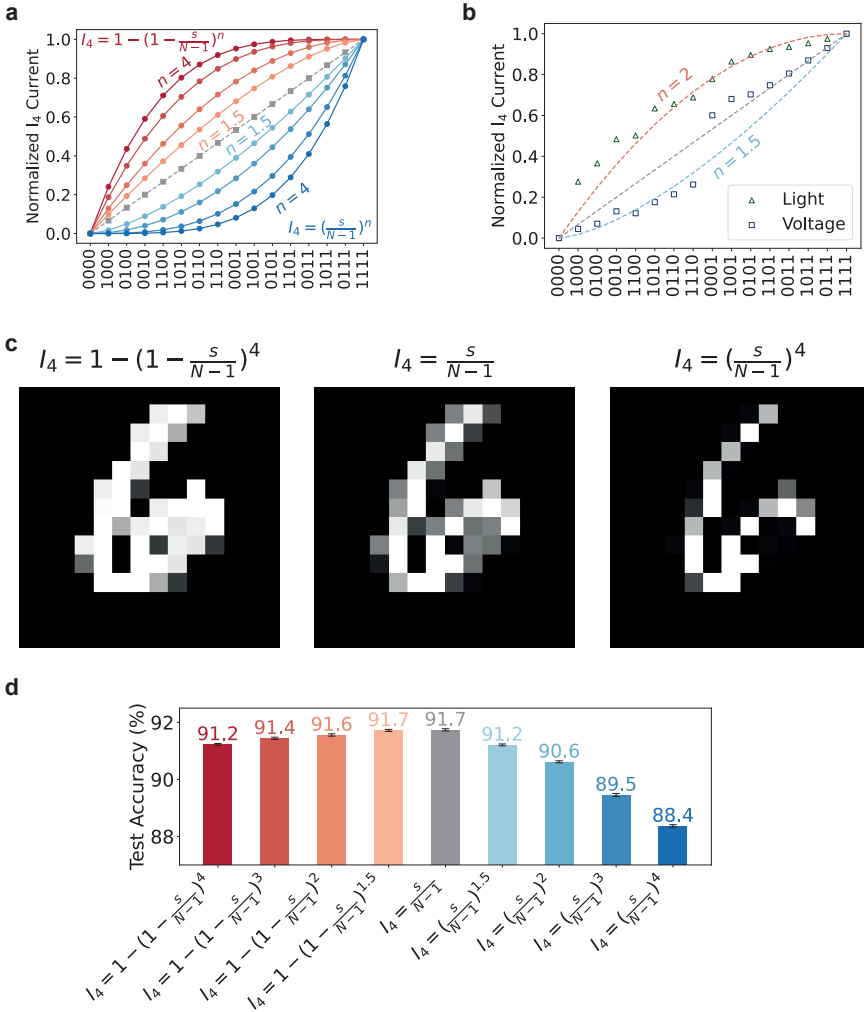


**Figure 5.B.1:** Transformations of the MNIST dataset based on simulated  $I_4$  current following linear and polynomial trends. **(a)** Input sequences with normalized  $I_4$  currents that increase linearly (squares and dotted gray line), or according to polynomial functions  $I_4(s) = 1 - (1 - \frac{s}{\Sigma s-1})^n$  (red circles and lines) and  $I_4(s) = (\frac{s}{\Sigma s-1})^n$  (blue circles and lines), with  $n \in 1.5, 2, 3, 4$ . **(b)** Normalized  $I_4$  currents of the light (green triangles) and voltage (blue squares) inputs compared to the artificial  $I_4$  currents. The light input  $I_4$  currents follow a similar trend to the polynomial  $I_4(s) = 1 - (1 - \frac{s}{\Sigma s-1})^2$ . The  $I_4$  currents of the voltage inputs up to the 1110 sequence resemble those of the function  $I_4(s) = (\frac{s}{\Sigma s-1})^{1.5}$  and become more linear afterwards. **(c)** The same MNIST image as in Figure 5.4a mapped to the  $I_4$  currents calculated based on the  $I_4(s) = (\frac{s}{\Sigma s-1})^4$ ,  $I_4(s) = \frac{s}{\Sigma s-1}$ ,  $I_4(s) = 1 - (1 - \frac{s}{\Sigma s-1})^4$  functions. Mapping to the  $I_4(s) = \frac{s}{\Sigma s-1}$  currents results in a number six with a range of grayscale values. Mapping to currents generated by the polynomial functions yields more extreme grayscale values, with more dark pixels for  $I_4(s) = (\frac{s}{\Sigma s-1})^4$  and more bright pixels for  $I_4(s) = 1 - (1 - \frac{s}{\Sigma s-1})^4$ . **(d)** Classification accuracies of the datasets mapped to the linear and polynomial functions. The highest accuracy of 91.7% is obtained for the linear relation. Minor accuracy penalties are obtained for the concave  $I_4(s) = 1 - (1 - \frac{s}{\Sigma s-1})^n$  functions, while they are more severe for the convex  $I_4(s) = (\frac{s}{\Sigma s-1})^n$  functions.

stronger convex, parabolic shape. These trends compress  $I_4$  currents of earlier sequences on the x-axis (the 0000 end) and stretch out later ones (on the 1111 end). In experimental measurements of the  $I_4$  current, this is due to high volatility, causing a 0000 and 1000 input, for example, to give a similar output. Currents above the linear trend were calculated as  $I_4(s) = 1 - \left(1 - \frac{s}{\Sigma s - 1}\right)^n$  (red curves in Figure 5.B.1a), using the same range of  $n$ -values. These currents follow a concave parabolic curve, with a stronger curvature for higher values of  $n$ . In this case, currents for later sequences on the x-axis are compressed and those of earlier inputs are stretched. In experimental measurements, this response is caused by long retention times, resulting in a saturation of the  $I_4$  current (e.g. a similar  $I_4$  current for 0111 and 1111 sequences).

These polynomial functions were chosen because they stretch and compress the linear response to the same extent, but at opposite ends of the x-axis. The equal magnitude of stretching and compression allows a fair comparison of the two trends.

Figure 5.B.1b illustrates that the measured  $I_4$  currents of the first half of the voltage and all light-inputs are described best by  $I_4(s) = \left(\frac{s}{\Sigma s - 1}\right)^{1.5}$  and  $I_4(s) = 1 - \left(1 - \frac{s}{\Sigma s - 1}\right)^2$ , respectively.

The effects of the deviations from the linearly increasing  $I_4$  currents are visualized in Figure 5.B.1c. The linearly increasing  $I_4$  currents result in a transformation of the MNIST image to an image with a range of grayscale values. Transformations based on convex  $\left(I_4(s) = \left(\frac{s}{\Sigma s - 1}\right)^4\right)$  or concave  $\left(I_4(s) = 1 - \left(1 - \frac{s}{\Sigma s - 1}\right)^4\right)$   $I_4$  currents result in more extreme grayscale values. Convex  $I_4$  currents force intermediate values in the image transformed based on linear  $I_4$  currents closer to 0, resulting in a lossy transformation of the image. The lower right part of the loop of the number six, for example, is no longer visible in the image. Conversely, the image transformed based on concave  $I_4$  currents force otherwise intermediate values closer to 1. This results in saturation in the transformed image, for example in the upper right part of the loop of the number six. At the same time, features that were more difficult to notice, around the curved line of the number for example, are more distinguishable for this transformed image. Both the lossy and saturated transformations are expected to decrease later classification accuracies, as different features become more difficult to distinguish.

Figure 5.B.1d shows the classification accuracies obtained by linear readout layers trained on the transformed datasets. The linearly increasing  $I_4$  currents give the highest accuracy ( $90.6 \pm 0.1\%$ ). The mean accuracies for concave  $I_4$  current transformations decreased only slightly. For  $n = 1.5$ , no statistically significant difference was found compared to the linear  $I_4$  transformation ( $p = 0.252$ ). For higher values of  $n$ , the differences were statistically significant ( $p < 0.001$ ), but modest, with an accuracy of  $91.2 \pm 0.1\%$  for  $n = 4$ .

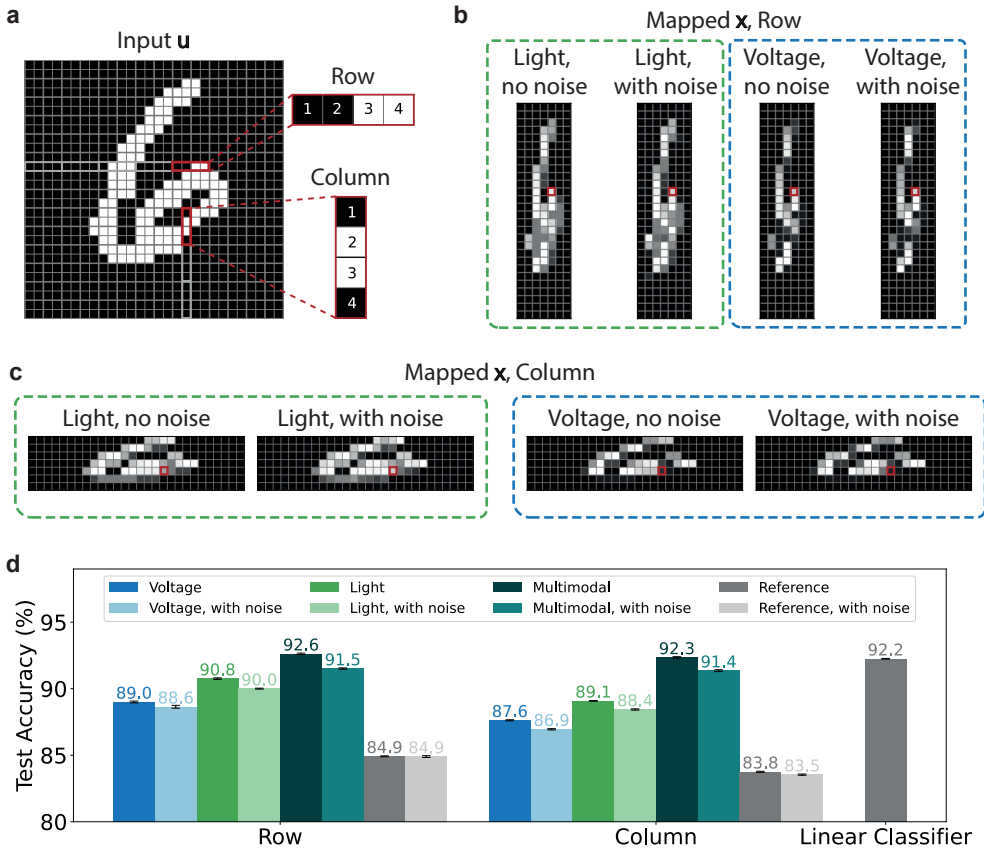
Interestingly, the accuracy penalty was markedly more severe for the convex  $I_4$  currents ( $p < 0.001$  for all differences). The same mean accuracy of  $91.2 \pm 0.1\%$  for the  $n = 4$  concave  $I_4$  currents was reached for  $n = 1.5$  already. The accuracy then decreased further for larger values of  $n$ , down to  $88.4 \pm 0.1\%$  for  $n = 4$ . The accuracies for the convex  $n = 2$  ( $91.6 \pm 0.1\%$ ) and concave  $n = 1.5$  ( $91.2 \pm 0.01\%$ )  $I_4$  transformations are well-matched to those obtained for the voltage ( $91.1 \pm 0.1\%$ ) and light ( $91.6 \pm 0.1\%$ ) inputs in Figure 5.4c. This indicates that the polynomial functions are good approximations for the experimentally measured  $I_4$  currents.

5

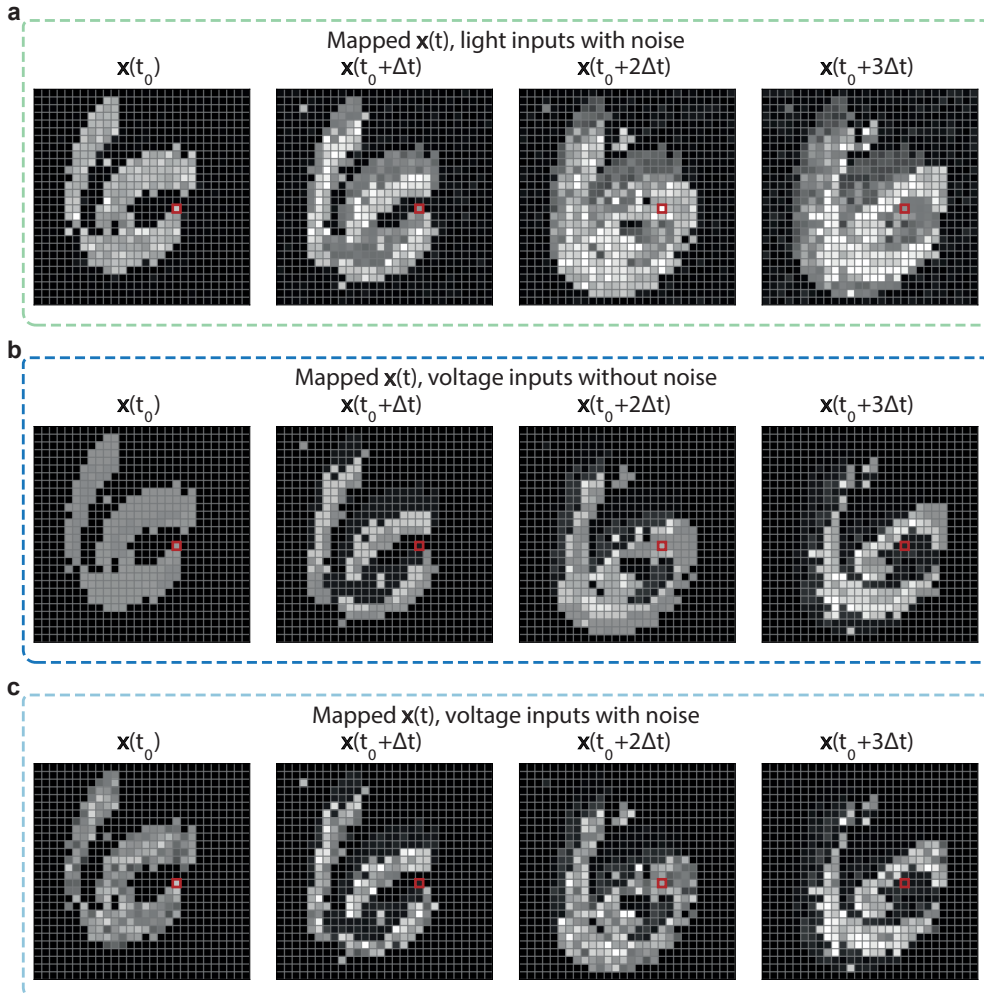
These results suggest that, for MNIST classification, the transformation should ideally give equal separability for all inputs (linear trend), or slightly emphasize the earlier sequences in Figure 5.B.1 where fewer pulses are applied (mildly concave trends). These inputs correspond to patches with few white pixels, which typically constitute the edges of the digits. Our results therefore suggest that these edges should remain distinguishable from the background for optimal classification. Saturation of inputs with more applied pulses, due to transformations with concave  $I_4$  currents, impact the classification accuracy less severely. Contrast between patches with many white pixels therefore seems less important for classification.

Our findings explain the better performance of the light-input networks in Figure 5.4c and 5.5c. Moreover, the simulations are generalizable for MNIST classification with any 4-bit input in-sensor reservoir network. This is particularly valuable when optimizing experimental parameters.  $I_4$  currents, or equivalent outputs, can be measured for the different sequences and plotted as in Figure 5.B.1a. Figure 5.B.1a and c can then function as a simple lookup table to estimate classification accuracy. This removes the need for time-consuming hyperparameter tuning and training of readout layers. Timesteps of the input can be increased (for a more convex  $I_4$  trend) or decreased (for a more concave  $I_4$  trend) to optimize the accuracy of the network. Our results show that, at least for MNIST classification based on 4-bit inputs, experimental parameters should be adjusted to obtain linear or slightly concave  $I_4$  current trends for best results. We note that the timesteps could not be decreased further for our voltage inputs to obtain more concave trends due to limitations of our experimental setup.

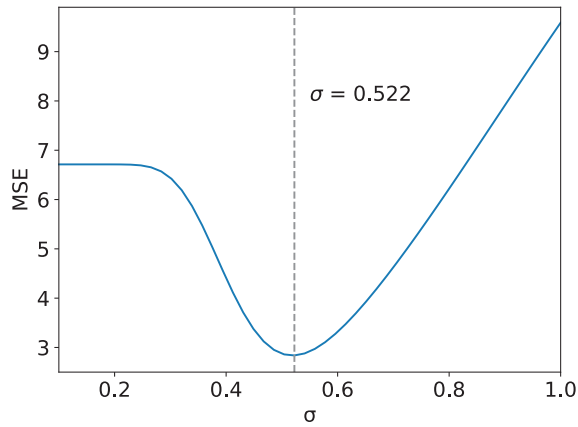
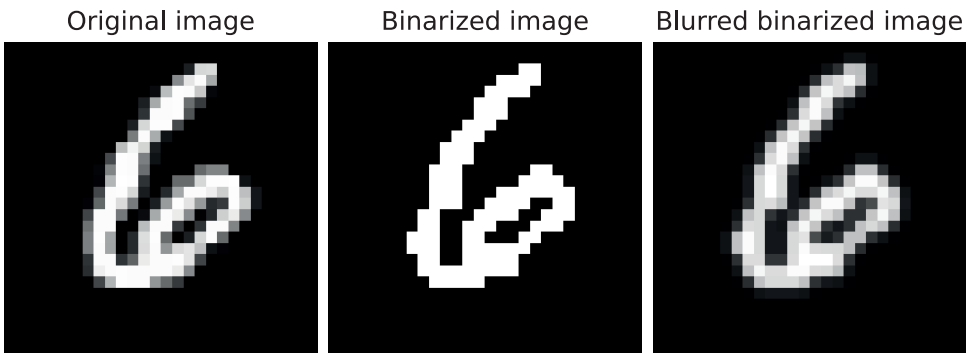
## 5.C Additional transformations



**Figure 5.C.1:** Row and column mapping for MNIST transformation and classification. **(a)** The same sample number six as in Figure 5.4a divided into four-pixel rows or columns. Rows or columns are mapped to the  $I_4$  currents corresponding to their 4-bit sequences. **(b)** The number six transformed by row-mapping. The image retains the same number of pixels vertically (28), but becomes fourfold smaller horizontally (to 7 pixels wide) by the transformation. The pixel outlined in red corresponds to the row outlined in **(a)**. **(c)** The number six transformed by column-mapping. The image retains the same number of pixels horizontally (28), but becomes fourfold smaller vertically (to 7 pixels high) by the transformation. The pixel outlined in red corresponds to the column outlined in **(a)**. **(d)** Mean classification accuracies of the voltage, light, and multimodal networks for datasets transformed by row and column mapping. The accuracies are compared to references, for which each row or column was mapped to the binary value of pixel 4. For the voltage, light, and multimodal networks, noise was included by taking random samples from a normal distribution of the  $I_4$  currents for each sequence. For the reference network, a Gaussian blur with a kernel based on the original MNIST dataset (see Methods for details) was applied to obtain a noisy dataset. The accuracies are compared to a linear classifier trained on the binarized MNIST dataset without any transformations. Each test accuracy was determined from 10 independent runs with different random seeds. Error bars indicate one standard deviation.



**Figure 5.C.2:** (a) Mapping of each pixel of the N-MNIST frames to values drawn from a normal distribution with a mean and standard deviation of the corresponding 4-bit light input data. (b) Mapping to the mean currents obtained for the voltage input measurements. (c) Mapping to random values drawn from a normal distribution with means and standard deviations obtained for the corresponding 4-bit voltage inputs.

**a****b**

**Figure 5.C.3:** Fitting of a Gaussian blurring kernel to the binarized MNIST data. **(a)** Mean squared error (MSE) obtained by comparing Gaussian blurred binarized MNIST images to the original MNIST dataset as a function of the variance ( $\sigma$ ). The variance of the Gaussian blurring kernel with a kernel size of 5 pixels was varied between 0 and 1 to find the lowest MSE value ( $\sigma = 0.522$ ). **(b)** Comparison of an original MNIST image (left) to the binarized image (middle) and the image obtained by applying the Gaussian blurring filter with the optimal variance to the binarized image (right).

# References

1. Mehonic, A. & Kenyon, A. J. Brain-inspired computing needs a master plan. *Nature* **604**, 255–260 (2022).
2. Merolla, P. A. *et al.* A million spiking-neuron integrated circuit with a scalable communication network and interface. *Science* **345**, 668–673 (2014).
3. Zidan, M. A., Strachan, J. P. & Lu, W. D. The future of electronics based on memristive systems. *Nature Electronics* **1**, 22–29 (2018).
4. Zhou, F. & Chai, Y. Near-sensor and in-sensor computing. *Nature Electronics* **3**, 664–671 (2020).
5. Cover, T. M. Geometrical and Statistical Properties of Systems of Linear Inequalities with Applications in Pattern Recognition. *IEEE Transactions on Electronic Computers* **EC-14**, 326–334 (1965).
6. Jaeger, H. & Haas, H. Harnessing Nonlinearity: Predicting Chaotic Systems and Saving Energy in Wireless Communication. *Science* **304**, 78–80 (2004).
7. Appeltant, L., Soriano, M. C., Van Der Sande, G., Danckaert, J., Massar, S., Dambre, J., Schrauwen, B., Mirasso, C. R. & Fischer, I. Information processing using a single dynamical node as complex system. *Nature Communications* **2**, 468 (2011).
8. Davies, M. *et al.* Loihi: A Neuromorphic Manycore Processor with On-Chip Learning. *IEEE Micro* **38**, 82–99 (2018).
9. Midya, R., Wang, Z., Asapu, S., Zhang, X., Rao, M., Song, W., Zhuo, Y., Upadhyay, N., Xia, Q. & Yang, J. J. Reservoir Computing Using Diffusive Memristors. *Advanced Intelligent Systems* **1**, 1900084 (2019).
10. Du, C., Cai, F., Zidan, M. A., Ma, W., Lee, S. H. & Lu, W. D. Reservoir computing using dynamic memristors for temporal information processing. *Nature Communications* **8**, 2204 (2017).
11. Vandoorne, K., Dierckx, W., Schrauwen, B., Verstraeten, D., Baets, R., Bienstman, P. & Campenhout, J. V. Toward optical signal processing using Photonic Reservoir Computing. *Optics Express* **16**, 11182 (2008).
12. Vandoorne, K., Mechet, P., Van Vaerenbergh, T., Fiers, M., Morthier, G., Verstraeten, D., Schrauwen, B., Dambre, J. & Bienstman, P. Experimental demonstration of reservoir computing on a silicon photonics chip. *Nature Communications* **5**, 3541 (2014).

13. Torrejon, J. *et al.* Neuromorphic computing with nanoscale spintronic oscillators. *Nature* **547**, 428–431 (2017).
14. Lin, N., Chen, J., Zhao, R., He, Y., Wong, K., Qiu, Q., Wang, Z. & Yang, J. J. In-memory and in-sensor reservoir computing with memristive devices. *APL Machine Learning* **2**, 010901 (2024).
15. Liu, K., Zhang, T., Dang, B., Bao, L., Xu, L., Cheng, C., Yang, Z., Huang, R. & Yang, Y. An optoelectronic synapse based on  $\alpha$ -In<sub>2</sub>Se<sub>3</sub> with controllable temporal dynamics for multimode and multiscale reservoir computing. *Nature Electronics* **5**, 761–773 (2022).
16. Tress, W., Marinova, N., Moehl, T., Zakeeruddin, S. M., Nazeeruddin, M. K. & Grätzel, M. Understanding the rate-dependent J–V hysteresis, slow time component, and aging in CH<sub>3</sub> NH<sub>3</sub> PbI<sub>3</sub> perovskite solar cells: the role of a compensated electric field. *Energy & Environmental Science* **8**, 995–1004 (2015).
17. Chen, L.-W., Wang, W.-C., Ko, S.-H., Chen, C.-Y., Hsu, C.-T., Chiao, F.-C., Chen, T.-W., Wu, K.-C. & Lin, H.-W. Highly Uniform All-Vacuum-Deposited Inorganic Perovskite Artificial Synapses for Reservoir Computing. *Advanced Intelligent Systems* **3**, 2000196 (2021).
18. Luo, Z., Wang, W., Wu, J., Ma, G., Hou, Y., Yang, C., Wang, X., Zheng, F., Zhao, Z., Zhao, Z., *et al.* Leveraging Dual Resistive Switching in Quasi-2D Perovskite Memristors for Integrated Non-volatile Memory, Synaptic Emulation, and Reservoir Computing. *ACS Applied Materials & Interfaces* **17**, 19879–19891 (2025).
19. Sharma, D., Luqman, A., Ng, S. E., Yantara, N., Xing, X., Tay, Y. B., Basu, A., Chattopadhyay, A. & Mathews, N. Halide perovskite photovoltaics for in-sensor reservoir computing. *Nano Energy* **129**, 109949 (2024).
20. John, R. A. *et al.* Reconfigurable halide perovskite nanocrystal memristors for neuromorphic computing. *Nature Communications* **13**, 2074 (2022).
21. Lin, C. H., Cheng, B., Li, T. Y., Retamal, J. R. D., Wei, T. C., Fu, H. C., Fang, X. & He, J. H. Orthogonal Lithography for Halide Perovskite Optoelectronic Nanodevices. *ACS Nano* **13**, 1168–1176 (2019).
22. Bard, A. J. & Faulkner, L. R. en. *Introduction and Overview of Electrode Processes in Electrochemical methods: fundamentals and applications* 2. edition, 1–43 (Wiley, New York Weinheim, 2001).
23. Zhao, Y.-C., Zhou, W.-K., Zhou, X., Liu, K.-H., Yu, D.-P. & Zhao, Q. Quantification of light-enhanced ionic transport in lead iodide perovskite thin films and its solar cell applications. *Light: Science & Applications* **6**, e16243–e16243 (2016).

24. Inman, H. F. & Bradley Jr, E. L. The overlapping coefficient as a measure of agreement between probability distributions and point estimation of the overlap of two normal densities. *Communications in Statistics-theory and Methods* **18**, 3851–3874 (1989).
25. Bertoluzzi, L., Boyd, C. C., Rolston, N., Xu, J., Prasanna, R., O'Regan, B. C. & McGehee, M. D. Mobile ion concentration measurement and open-access band diagram simulation platform for halide perovskite solar cells. *Joule* **4**, 109–127 (2020).
26. Schaetti, N., Salomon, M. & Couturier, R. *Echo State Networks-Based Reservoir Computing for MNIST Handwritten Digits Recognition in 2016 IEEE Intl Conference on Computational Science and Engineering (CSE) and IEEE Intl Conference on Embedded and Ubiquitous Computing (EUC) and 15th Intl Symposium on Distributed Computing and Applications for Business Engineering (DCABES)* (IEEE, Paris, 2016), 484–491.
27. Lin, N. *et al.* Resistive memory-based zero-shot liquid state machine for multimodal event data learning. *Nature Computational Science* **5**, 37–47 (2025).
28. Jang, Y. H., Kim, W., Kim, J., Woo, K. S., Lee, H. J., Jeon, J. W., Shim, S. K., Han, J. & Hwang, C. S. Time-varying data processing with nonvolatile memristor-based temporal kernel. *Nature Communications* **12**, 5727 (2021).
29. Koh, S.-G., Shima, H., Naitoh, Y., Akinaga, H. & Kinoshita, K. Reservoir computing with dielectric relaxation at an electrode–ionic liquid interface. *Scientific Reports* **12**, 6958 (2022).
30. Yamazaki, Y. & Kinoshita, K. Photonic Physical Reservoir Computing with Tunable Relaxation Time Constant. *Advanced Science* **11**, 2304804 (2024).
31. Orchard, G., Jayawant, A., Cohen, G. K. & Thakor, N. Converting static image datasets to spiking neuromorphic datasets using saccades. *Frontiers in neuroscience* **9**, 437 (2015).
32. Brivio, F., Butler, K. T., Walsh, A. & van Schilfgaarde, M. Relativistic quasiparticle self-consistent electronic structure of hybrid halide perovskite photovoltaic absorbers. *Physical Review B* **89**, 155204 (2014).
33. Caputo, M. *et al.* Electronic structure of MAPbI<sub>3</sub> and MAPbCl<sub>3</sub>: importance of band alignment. *Scientific Reports* **9**, 15159 (2019).
34. Shallue, C. J., Lee, J., Antognini, J., Sohl-Dickstein, J., Frostig, R. & Dahl, G. E. Measuring the Effects of Data Parallelism on Neural Network Training. *Journal of Machine Learning Research* **20**, 1–49 (2019).

## Summary

The capabilities of neural networks have progressed remarkably over recent years, with breakthroughs in areas such as natural language processing, image recognition, and protein folding prediction. However, these advances have come at the cost of rapidly increasing computational demands and, therefore, energy consumption. A major contributor to the energy consumption is the inefficient data movement between separate memory and processing units in classical computers. Compared to contemporary artificial neural networks, biological neural networks, such as the brain, are both highly capable and energy-efficient. Brain-inspired, “neuromorphic” networks aim to mimic these highly efficient biological neural networks in hardware, using electronic devices resembling synapses and neurons. Neuromorphic networks, such as spiking neural networks (SNNs) or reservoirs for reservoir computing (RC), combine memory and processing within the same network. They thereby reduce both energy consumption and latency caused by data movement between separate memory and processing units, as in classical computers. These networks can be integrated efficiently in high densities with memristive devices, i.e. devices with a resistance that can be varied by applying a bias voltage.

Halide perovskites have recently emerged as an attractive semiconductor material class for memristive devices. The soft, partially ionic bonds in these materials support the movement of ionic defects (“mobile ions”) through the crystal lattice with low activation energies. Mobile ions can cause resistance changes through interfacial effects, such as passivation of the halide perovskite-electrode interface or doping of organic layers, as well as by the reversible formation of conductive filaments through the bulk. Owing to the low activation energy of ion migration, halide perovskite artificial synapses can be highly energy-efficient, approaching biological synapses. Properties like the retention time, switching speed, and the number of accessible resistances of halide perovskite artificial synapses are highly tunable by choosing the electrode material, perovskite composition, and by addition of organic layers. Halide perovskites are also excellent light absorbers, allowing implementations that process both electronic and optical inputs.

Nevertheless, halide perovskites face important limitations that prevent their implementation in neuromorphic networks. The ionic nature of the halide perovskite bonds makes these materials highly soluble in polar solvents. This property prevents their microfabrication with conventional procedures, hindering high-density integration in neuromorphic networks. In addition, halide perovskite artificial neurons, a crucial component in SNNs, have remained almost entirely unexplored. Both issues should be addressed to allow the implementation of halide perovskites in efficient neuromorphic networks.

In this thesis, we establish a novel method for the microfabrication of halide perovskite memristive devices. We show how both microscale artificial synapses and neurons can be fabricated with this procedure. Together, these devices could be implemented into all-halide perovskite neuromorphic networks in high densities. Next, we explore microscale optoelectronic synapse implementations that can process both electronic and optical inputs. We simulate a neuromorphic application of these devices in a camera that can learn by an attention mechanism. Next, we simulate multimodal reservoir networks that process both electronic and optical inputs for efficient handwritten digit classification from images and video. Altogether, this work demonstrates a method for the high-density integration of halide perovskite memristive devices into neuromorphic networks. We explore how these networks could leverage halide perovskite devices for efficient neuromorphic computing.

Neuromorphic computing and halide perovskite memristive devices are introduced in **Chapter 1**. We discuss neuromorphic spiking neural networks and reservoir computing networks, and compare them to conventional artificial neural networks implemented on classical computers. We explain how these networks can be implemented efficiently with memristive devices. Next, we introduce halide perovskites. We describe how ionic defects migrate through their crystal lattice and how this migration results in memristive properties of halide perovskite devices. We provide a brief review of halide perovskite artificial synapses, focusing on important device parameters such as the dynamic range of the resistance, switching speed, and retention time. We emphasize the facile tunability of halide perovskite synapses, and discuss how the device response can be tailored by adjusting its composition. Finally, we highlight the limitations of halide perovskite memristive devices for neuromorphic computing. We highlight the absence of demonstrations of artificial neurons, the lack of a scalable microfabrication procedure, and the limited exploration of halide perovskite neuromorphic network implementations.

We demonstrate a scalable microfabrication procedure in **Chapter 2**. We fabricate a scalable back-contacted artificial synapse, consisting of two gold electrodes separated by an  $\text{SiO}_2$  insulating spacer. The halide perovskite layer is spin-coated over the electrodes

in the final step, avoiding its exposure to solvents during the lithography process. We fabricate devices with a footprint of approximately  $6 \mu\text{m}^2$ . The synapse displays resistance changes of up to five orders of magnitude. Multiple resistance states can be programmed by applying successive voltage pulses. The energy consumption of changing the resistance of the device is as low as 640 fJ, owing to the low operating current as a result of the small device size. Compared to artificial synapses of other materials, the synapse presented in this chapter has a large dynamic range and comparatively low energy consumption. The retention time on the order of tens of seconds and the switching speed of tens of milliseconds are similar to those of biological synapses, and complement faster artificial synapses based on other materials.

In **Chapter 3**, we fabricate volatile microscale memristive devices using the newly developed microfabrication procedure, substituting one of the gold electrodes for a silver electrode. Applying a bias voltage to the device causes rapid resistance changes over orders of magnitude, with a retention time below 500 ms. We demonstrate the first on-chip integrated halide perovskite artificial neuron by connecting the memristive device in series with a capacitor. Successive voltage pulses applied to the neuron cause a drastic lowering of the resistance of the memristive device. This resistance switch produces an output voltage spike and rapidly charges the capacitor. After the bias voltage is removed, the memristive device returns to its high-resistance state due to its volatility and the current coming from the discharging capacitor. We demonstrate that the spiking of the neuron is stochastic, following a Poisson behavior. We simulate populations of neurons based on the experimental results. The simulations indicate that the stochasticity allows neuron populations to detect input signals that would remain subthreshold, and therefore undetected, for deterministic neuron populations. The energy consumption per spike is between 20 to 60 pJ in the current implementation, already lower than the 100 pJ of biological neurons. Together with the synapses presented in **Chapter 2**, the neurons could be implemented in energy-efficient all-halide perovskite neuromorphic networks.

Optoelectronic halide perovskite synapses are explored in **Chapter 4**. The synapses are fabricated on the microscale in the back-contacted architecture, but with an insulating  $\text{Al}_2\text{O}_3$  layer separating the two gold electrodes. The  $\text{Al}_2\text{O}_3$  layer covers the entire bottom electrode, preventing the resistance changes measured in **Chapter 2**. Instead, voltage pulses applied to the device cause the accumulation of mobile ions at the perovskite-electrode interface. This induces a transient electric field in the device after the bias voltage is removed. Subsequently illuminating the device results in an output photocurrent with a magnitude and sign that depend on this transient electric field. Illuminating the device while the bias voltage is applied results in stronger modulation of the pho-

to current. We demonstrate a biology-inspired optoelectronic spike-timing-dependent plasticity (STDP) learning rule based on this interplay of the bias light and voltage. Based on the experimental results, we then simulate a neuromorphic camera consisting of an array of optoelectronic synapses. A simple feedback spike allows selective synaptic weight updates by the STDP learning rule. The camera learns to track features of interest through the weight updates, analogous to an attention mechanism. Neuromorphic networks could leverage the attention mechanism for more efficient object detection from visual data.

**Chapter 5** investigates the use of volatile halide perovskite devices in reservoir computing-based multimodal networks. The same microscale optoelectronic devices are used as in **Chapter 4**. Voltage pulses applied to the device induce a volatile ionic current that decays over hundreds of milliseconds. We show that illuminating the device while the voltage is applied results in an increased ionic current. Next, we define four-bit voltage and light input sequences, where each bit corresponds to a timestep during which an input pulse is ("1") or is not ("0") provided. The 4-bit input sequences give separable output ionic currents, with some overlap when considering experimental noise. Reservoir networks are simulated based on the experimental results. The networks consist of simulated arrays of the volatile devices, comprising the reservoir. The arrays transform the MNIST dataset, which is then classified with a linear readout layer. Multimodal networks that combine light and voltage inputs reach high classification accuracies up to  $95.3 \pm 0.1\%$ . Considering the experimentally measured noise introduces a minor accuracy penalty between 0.3 and 1.2 percentage points. We demonstrate, using simulated ionic currents, that relatively long retention times with respect to the input frequency enhance classification accuracy. These simulations can serve as a simple lookup table for estimating MNIST classification accuracies from 4-bit sequence outputs, aiding in the fine-tuning of the input frequency during experimental measurements. Next, we extend handwritten digit classification to video data based on the N-MNIST dataset. The networks achieve high classification accuracies of up to  $89.0 \pm 0.1\%$  for the multimodal network. This constitutes an improvement of 15.8 percentage points compared to a reference network without volatile memory. The networks described in this chapter could be fabricated fully in hardware for neuromorphic devices that efficiently combine sensing and processing.

## Samenvatting

De vaardigheden van neurale netwerken hebben de afgelopen jaren een enorme ontwikkeling doorgemaakt, met doorbraken op gebieden als natuurlijke taalverwerking, beeldherkenning, en het voorspellen van eiwitvouwing. Voor deze vooruitgang is echter een sterke toename van de rekenkracht en daardoor het energieverbruik nodig geweest. De inefficiënte gegevensoverdracht tussen het afzonderlijke geheugen en de verwerkingseenheden in klassieke computers vormt een belangrijke bijdrage aan het energieverbruik. Vergeleken met hedendaagse kunstmatige neurale netwerken zijn biologische neurale netwerken, zoals de hersenen, zowel zeer capabel als energiezuinig. Door de hersenen geïnspireerde "neuromorfische" netwerken proberen deze zeer efficiënte biologische neurale netwerken in hardware na te bootsen, met behulp van elektronische componenten die lijken op synapsen en neuronen. Neuromorfische netwerken, zoals gepulste neurale netwerken of reservoirnetwerken, combineren geheugen en verwerking in hetzelfde netwerk. Ze verminderen daardoor zowel het energieverbruik als de latentie die wordt veroorzaakt door dataverplaatsing tussen het afzonderlijke geheugen en de verwerkingseenheden in klassieke computers. Deze netwerken kunnen efficiënt in hoge dichtheden worden geïntegreerd met memristieve componenten, oftewel componenten met een weerstand die kan worden aangepast door een spanning aan te brengen.

Halideperovskieten zijn recentelijk aangedragen als een aantrekkelijke klasse halfgeleidermaterialen voor memristieve componenten. De zachte, gedeeltelijk ionische bindingen in deze materialen maken het mogelijk voor ionische defecten ("mobiele ionen") om door het kristalrooster te bewegen met lage activeringsenergieën. Mobiele ionen kunnen weerstandsveranderingen veroorzaken door grensvlakeffecten, zoals passivering van het halideperovskiet-elektrode grensvlak, of het doteren van organische lagen. Weerstandsveranderingen kunnen ook veroorzaakt worden door de omkeerbare vorming van geleidende filamenten door de halideperovskiet laag. Dankzij de lage activeringsenergie van ionenmigratie kunnen kunstmatige halideperovskietsynapsen zeer energie-efficiënt zijn, vergelijkbaar met biologische synapsen. Eigenschappen als de re-

tentietijd, schakelsnelheid en het aantal te onderscheiden weerstanden van kunstmatige halideperovskietsynapsen zijn gemakkelijk af te stemmen door het elektrodemateriaal en de perovskietsamenstelling aan te passen en door organische lagen toe te voegen. Halideperovskieten zijn ook uitstekende lichtabsorbeerders, waardoor implementaties mogelijk zijn die zowel elektronische als optische signalen verwerken.

Ondanks deze voordelen kampen halideperovskieten met beperkingen die hun implementatie in neuromorfische netwerken verhinderen. Zo maakt de ionische aard van de halideperovskietbindingen deze materialen gemakkelijk oplosbaar in polaire oplosmiddelen. Hierdoor zijn ze moeilijk te verwerken met conventionele microfabricage methoden, wat hun integratie in neuromorfische netwerken in hoge dichtheden belemmert. Bovendien is er een vrijwel compleet gebrek aan kunstmatige halideperovskietneuronen, een cruciaal onderdeel van gepulste neurale netwerken. Beide beperkingen moeten worden aangepakt om de implementatie van halideperovskieten in efficiënte neuromorfische netwerken mogelijk te maken.

In dit proefschrift ontwikkelen we een nieuwe methode voor de microfabricage van halideperovskiet memristieve componenten. We laten zien hoe zowel kunstmatige synapsen als neuronen op de microschaal gefabriceerd kunnen worden met deze procedure. Samen kunnen deze componenten in hoge dichtheden geïmplementeerd worden in volledig halideperovskiet neuromorfische netwerken. Vervolgens onderzoeken we micrometerschaal opto-elektronische synapsen die zowel elektronische als optische signalen kunnen verwerken. We simuleren een neuromorfische toepassing van deze componenten in een camera die kan leren via een aandachtsmechanisme. Vervolgens simuleren we multimodale reservoirnetwerken die zowel elektronische als optische gegevens verwerken. Deze netwerken kunnen op efficiënte wijze handgeschreven cijfers classificeren van afbeeldingen en video's. Alles tezamen toont dit werk aan hoe halideperovskiet memristieve componenten in hoge dichtheden kunnen worden geïntegreerd in neuromorfische netwerken. We onderzoeken hoe deze netwerken de veelzijdige eigenschappen van de halideperovskiet componenten kunnen gebruiken voor efficiënte neuromorfische toepassingen.

Neuromorfische netwerken en halideperovskiet memristieve componenten worden geïntroduceerd in **Hoofdstuk 1**. We bespreken neuromorfische gepulste neurale netwerken en reservoirnetwerken en vergelijken deze met conventionele kunstmatige neurale netwerken toegepast op klassieke computers. We leggen uit hoe deze netwerken op efficiënte wijze geïmplementeerd kunnen worden met memristieve componenten. Vervolgens introduceren we halideperovskieten. We beschrijven hoe ionische defecten migreren door hun kristalrooster en hoe dit resulteert in memristieve eigenschappen.

We geven een kort overzicht van kunstmatige halideperovskietsynapsen, toegespitst op belangrijke parameters als het dynamische bereik van de weerstand, schakelsnelheid, en retentietijd. We benadrukken hoe de respons van halideperovskite synapsen gemakkelijk aangepast kan worden aan de hand van hun samenstelling. Tot slot bespreken we de huidige limitaties van halideperovskiet memristieve componenten voor neuromorfische doeleinden. We wijzen op het ontbreken van kunstmatige neuronen, het gebrek aan een schaalbare microfabricage procedure, en het beperkte onderzoek naar implementaties van halideperovskiet neuromorfische netwerken.

We demonstreren een schaalbare microfabricage procedure in **Hoofdstuk 2**. We fabriceren een schaalbare kunstmatige achtercontactsynaps die bestaat uit twee gouden elektrodes die worden gescheiden door een isolerende  $\text{SiO}_2$  laag. De halideperovskiet laag wordt pas in de laatste stap over de elektrodes gespincoat, waardoor contact met oplosmiddelen tijdens het lithografieproces wordt voorkomen. We vervaardigen synapsen met een oppervlakte van ongeveer  $6 \mu\text{m}^2$ . De weerstand van de synaps kan gevarieerd worden over vijf ordegroottes. Meerdere weerstandstoestanden kunnen worden geprogrammeerd door opeenvolgende spanningspulsen aan te brengen. De laagst behaalde energieconsumptie van een weerstandsverandering is slechts 640 fJ, dankzij de lage bedrijfsstroom ten gevolge van de kleine afmetingen. Vergeleken met kunstmatige synapsen van andere materialen heeft de synaps die in dit hoofdstuk wordt beschreven een groot dynamisch bereik en een relatief lage energieconsumptie. De retentietijd van tientallen seconden en schakelsnelheid van tientallen milliseconden zijn vergelijkbaar met die van biologische synapsen en complementeren snellere kunstmatige synapsen die gebaseerd zijn op andere materialen.

In **Hoofdstuk 3** vervaardigen we vluchtige memristieve componenten op de microschaal met de nieuwontwikkelde methode van het vorige hoofdstuk, door een gouden elektrode om te wisselen voor een zilveren elektrode. Het aanbrengen van een spanning zorgt voor abrupte weerstandsveranderingen van meerdere ordegroottes, met een retentietijd onder de 500 ms. We demonstreren het eerste op een chip geïntegreerde kunstmatige halideperovskietneuron door de memristieve component in serie te schakelen met een condensator. Opeenvolgende spanningspulsen die worden aangebracht op het neuron veroorzaken een drastische verlaging van de weerstand van de memristieve component. Deze weerstandsverandering brengt een uitgaande spanningspuls voort en zorgt voor een snelle oplading van de condensator. Na het verwijderen van de spanning valt de memristieve component terug in de hoge weerstandstoestand dankzij het vluchtige geheugen en de stroom van de ontladende condensator. We tonen aan dat de neuronpulsen stochastisch zijn, volgens een Poisson proces. We simuleren populaties van neuronen

gebaseerd op de experimentele resultaten. De simulaties tonen aan dat de stochasticiteit het mogelijk maakt voor neuronpopulaties om signalen te detecteren die onder een drempelwaarde liggen, en daardoor onopgemerkt zouden blijven voor deterministische neuronpopulaties. In de huidige implementatie ligt de energieconsumptie per neuronpuls tussen de 20 en 60 pJ, lager dan de 100 pJ van biologische neuronen. Samen met de synapsen omschreven in **Hoofdstuk 2** zouden de neuronen geïmplementeerd kunnen worden in energie-efficiënte neuromorfische netwerken die volledig uit halideperovskiet bestaan.

We onderzoeken opto-elektronische halideperovskiet synapsen in **Hoofdstuk 4**. De synapsen worden vervaardigd op de micrometerschaal met de achtercontactarchitectuur, maar met een isolerende  $\text{Al}_2\text{O}_3$  laag die de twee gouden elektrodes scheidt. De  $\text{Al}_2\text{O}_3$  laag bedekt de onderste elektrode volledig en voorkomt daarmee de weerstandsveranderingen die we maten in **Hoofdstuk 2**. In plaats daarvan veroorzaken aangebrachte spanningspulsen accumulatie van mobiele ionen aan het perovskiet-elektrode grensvlak. Dit wekt een vergankelijk elektrisch veld op in de perovskietlaag. Als de synaps vervolgens belicht wordt, resulteert dit in een fotostroom waarvan de sterkte en polariteit die afhangt van dit vergankelijke elektrisch veld. Belichting van de synaps terwijl de spanning wordt aangebracht versterkt de modulatie van de fotostroom. We demonstreren een opto-elektronische leerregel, afgeleid van biologische synaptische plasticiteit, die gebruik maakt van deze wisselwerking tussen het licht en de spanning. Aan de hand van de experimentele resultaten simuleren we een neuromorfische camera die bestaat uit een reeks van de opto-elektronische synapsen. Aan de hand van de leerregel kan een simpele terugkoppelpuls selectief de synaptische gewichten aanpassen. Op deze manier leert de camera zich te richten op belangrijke kenmerken, vergelijkbaar met een aandachtsmechanisme. Neuromorfische netwerken zouden gebruik kunnen maken van dit mechanisme voor efficiëntere beeldherkenning.

**Hoofdstuk 5** onderzoekt het gebruik van vluchtige halideperovskiet componenten in multimodale reservoirnetwerken. Hiervoor worden dezelfde opto-elektronische componenten als in **Hoofdstuk 4** gebruikt. Spanningspulsen die worden aangebracht veroorzaken een vluchtige ionische stroom die afneemt over een tijdspanne van honderden milliseconden. We laten zien dat belichting tijdens het aanbrenge van de spanning zorgt voor een hogere ionische stroom. Vervolgens definiëren we vier-bits spannings en licht reeksen, waarbij elke bit correspondeert met een tijdstap waarin een puls wel ("1") of niet ("0") wordt aangebracht. De vier-bits reeksen leiden tot verschillende ionische stromen, met enige overlap als de experimentele ruis mee wordt genomen. We simuleren reservoirnetwerken aan de hand van de experimentele resultaten. De netwerken bestaan

uit gesimuleerde reeksen van de vluchtige componenten, die het reservoir vormen. De reeksen transformeren de MNIST-dataset, waarna deze geïnclassificeerd wordt met een lineaire uitleeslaag. Multimodale netwerken die licht en spanningssignalen combineren behalen hoge classificatie nauwkeurigheden tot  $95,3 \pm 0,1\%$ . Als de experimentele ruis mee wordt genomen neemt de nauwkeurigheid af met slechts 0,3 tot 1,2 procentpunten. Aan de hand van gesimuleerde ionische stromen laten we zien dat relatief lange retentietijden ten opzichte van de invoerfrequentie de classificatienauwkeurigheid ten goede komen. Deze simulaties kunnen dienstdoen als simpele referentie om de MNIST-classificatienauwkeurigheid in te schatten aan de hand van de vier-bits reeks metingen. Ze vormen hiermee een hulpmiddel om de invoerfrequentie te optimaliseren tijdens experimentele metingen. Vervolgens breiden we de classificatie van handgeschreven cijfers uit naar video's op basis van de N-MNIST-dataset. De netwerken bereiken hoge classificatienauwkeurigheden tot  $89,0 \pm 0,1\%$  voor de multimodale netwerken. Dit komt overeen met een verbetering van 15,8 procentpunten ten opzichte van een referentienetwerk zonder vluchtig geheugen. De netwerken die worden omschreven in dit hoofdstuk zouden volledig in hardware vervaardigd kunnen worden voor neuromorfische toepassingen die detectie en verwerking op efficiënte wijze combineren.



## Publications

### This thesis is based on the following publications

1. Jeroen J. de Boer & Bruno Ehrler. Scalable Microscale Artificial Synapses of Lead Halide Perovskite with Femtojoule Energy Consumption. *ACS Energy Letters* **9**, 5787–5794 (2024). **(Chapter 2)**

Author contributions: J.J.B. conceived the project and carried out the experimental work. The project was supervised and conceived by B.E. Both authors interpreted the results and wrote the manuscript.

2. Jeroen J. de Boer & Bruno Ehrler. Integrated artificial neurons from metal halide perovskites. *Materials Horizons* **12**, 2701–2708 (2025). **(Chapter 3)**

Author contributions: J.J.B. conceived the project and carried out the experimental work and the simulations. The project was supervised and conceived by B.E. Both authors interpreted the results and wrote the manuscript.

3. Jeroen J. de Boer, Agustin O. Alvarez, Moritz C. Schmidt, Dimitrios Sitaridis & Bruno Ehrler. Microscale optoelectronic synapses with switchable photocurrent from halide perovskite. *In preparation* (2025). **(Chapter 4)**

Author contributions: J.J.B. conceived the project, carried out the experimental work and the attention mechanism simulations, interpreted the results and wrote the manuscript. A.O.A. helped with interpretation of the results and commented on the manuscript. M.C.S. carried out the drift-diffusion simulations and commented on the manuscript. D.S. carried out initial experiments that led to the conception of the project. B.E. conceived and supervised the project, interpreted the results, and wrote and edited the manuscript.

4. Jeroen J. de Boer, Agustin O. Alvarez, Moritz C. Schmidt & Bruno Ehrler. In-sensor computing with halide perovskite-based optoelectronic reservoir networks. *Device* (2025), *in press*. **(Chapter 5)**

Author contributions: J.J.B. conceived the project, carried out the experimental work and the reservoir network training and simulations, interpreted the results and wrote the manuscript.

A.O.A. conceived the project, helped with the experimental work and interpretation of the results, and commented on the manuscript. M.C.S. carried out the drift-diffusion simulations and commented on the manuscript. B.E. conceived and supervised the project, interpreted the results, and wrote and edited the manuscript.

### Other publications by the author

5. Jiaxiong Li, Lijun Chen, Michalis Loizos, [Jeroen J. de Boer](#), Cedric K. Gonzales, Mubashir Mushtaq Ganaie, Mahesh Kumar, Timothy Ng, Nripan Mathews, Bruno Ehrler, Juan Bisquert, Emmanuel Kymakis, Konstantinos Rogdakis, Antonio Guerrero, Maria A. Loi & Jovana V. Milić. Hybrid Halide Perovskite Operation in Resistive Switching Memories, Artificial Synapses, and Neurons for Neuromorphic Computing. *Submitted*.
6. Moritz C. Schmidt, Agustin O. Alvarez, Biruk A. Seid, [Jeroen J. de Boer](#), Felix Lang & Bruno Ehrler. Characterization of Mobile Ions in Perovskite Solar Cells with Capacitance and Current Measurements by Approximating Drift-Diffusion Simulations. *PRX Energy* **4**, 033017 (2025).
7. Sarah C. Gillespie, Jarla Thiesbrummel, Veronique S. Gevaerts, L.J. Geerligs, [Jeroen J. de Boer](#), Gianluca Coletti & Erik C. Garnett. Excitation Intervals Enhance Performance in Perovskite Solar Cells. *ACS Applied Materials & Interfaces* **17**, 59476-59485 (2025).
8. Moritz C. Schmidt, Agustin O. Alvarez, Riccardo Pallotta, Biruk Seid, [Jeroen J. de Boer](#), Jarla Thiesbrummel, Felix Lang, Giulia Grancini & Bruno Ehrler. Quantification of mobile ions in perovskite solar cells with thermally activated ion current measurements. *ACS Energy Letters* (2025), *in press*.
9. Agustin O. Alvarez, [Jeroen J. de Boer](#), Lars Sonneveld, Yorick Bleijji, Esther Alarcón Lladó & Bruno Ehrler. Hysteresis in Perovskite Devices: Understanding the Abrupt Resistive Switching Mechanism. *ACS Energy Letters* **10**, 3983-3992 (2025).
10. Moritz C. Schmidt, Agustin O. Alvarez, [Jeroen J. de Boer](#), Larissa J.M. van de Ven & Bruno Ehrler. Consistent Interpretation of Time- and Frequency-Domain Traces of Ion Migration in Perovskite Semiconductors. *ACS Energy Letters* **9**, 5850-5858 (2024).
11. Maarten L.S. van der Geest, [Jeroen J. de Boer](#), Kevin Murzyn, Peter Jürgens, Bruno Ehrler & Peter M. Kraus. Transient high-harmonic spectroscopy in an inorganic-organic lead halide perovskite. *The Journal of Physical Chemistry Letters* **14**, 10810-10818 (2023).

12. Julia S. van der Burgt, Francesca Scalerandi, Jeroen J. de Boer, Susan A. Rigter & Erik C. Garnett. Perovskite Plasticity: Exploiting Instability for Self-Optimized Performance. *Advanced Functional Materials* **32**, 2203771 (2022).
13. Maarten L.S. Van Der Geest, Lucie McGovern, Stefan van Vliet, Hanya Y. Zwaan, Gianluca Grimaldi, Jeroen J. de Boer, Roland Bliem, Bruno Ehrler & Peter M. Kraus. Extreme-ultraviolet excited scintillation of methylammonium lead bromide perovskites. *The Journal of Physical Chemistry C* **126**, 12554-12562 (2022).
14. Pierre Capiod, Maaike van der Sluijs, Jeroen J. De Boer, Christophe Delerue, Ingmar Swart & Daniel Vanmaekelbergh. Electronic properties of atomically coherent square PbSe nanocrystal superlattice resolved by Scanning Tunneling Spectroscopy. *Nanotechnology* **32**, 325706 (2021).
15. Marianne Lankelma, Jeroen J. de Boer, Marilena Ferbinteanu, André Luis Dantas Ramos, Radu Tanasa, Gadi Rothenberg & Stefania Tanase. A novel one-dimensional chain built of vanadyl ions and pyrazine-2,5-dicarboxylate. *Dalton Transactions* **44**, 11380-11387 (2015).



## Acknowledgements

While this thesis only has my name on the cover, the work it contains would not have been possible without the guidance, help, and support of many people. Besides all (in)direct contributions to the work itself, it is also thanks to these, and a great deal of other people again, that my PhD research has been such a rewarding, educational, and enjoyable experience.

I would like to thank my supervisor **Bruno**, for your supervision throughout my PhD project. I felt a great deal of freedom to explore new research directions and develop my own ideas. At the same time, you were always available for discussions, advice, and feedback whenever it was needed, often with a good sense of humor. I really appreciated this balance of independence and guidance. You always cared for all your master's students, PhD students, and postdocs. I think this is a big reason for the great atmosphere within the Hybrid Solar Cells group, and I am grateful to have been a member of it for the last four years.

I would also like to thank **Wiebke**, my second supervisor. Thank you for your support and supervision, especially at the end of my project. I felt like I could approach you with anything. Thanks for the insightful discussions we had on my work and how it related to neural networks and AI in general throughout my PhD.

Also, thanks to the other LMPV group leaders. Together, you have created a great working environment where critical questions and discussions are encouraged, yet the tone is always kind and respectful. This was crucial in my development as a young researcher, and I suspect for many others as well. **Erik**, thank you for all your input whenever I presented my work. Not only did I enjoy our discussions, but they frequently led to new research ideas and insights. I am glad to have you as a member of my PhD committee. Thank you, **Albert**, for all your foundational work to the LMPV team. You always went out of your way to connect with people both within and outside of AMOLF, which really helped set the open, collaborative atmosphere. **Esther**, I really appreciated the discussions we had on memristive devices. You always managed to be critical of the work, while being

kind towards the person, to me perfectly representing the LMPV spirit.

I would also like to acknowledge **Tae-Youl**, who unfortunately passed away while he was a guest in our research group. I have fond memories of our discussions on halide perovskite memristive devices. I was impressed by your knowledge and creative ideas, and knew you as a kind and dedicated person.

Thank you also to my PhD examining committee, **Wolfgang Tress**, **Beatriz Noheda**, **Maria Loi**, **Jovana Milic**, and, again, **Erik Garnett**, for taking the time to read my thesis. I look forward to our discussions during the defense of my thesis.

I would also like to thank **Susan** and **Julia**, who were the daily supervisors during my master's project at AMOLF, and **Maaïke**, my daily supervisor for my other master's project at Utrecht University. Throughout these projects, you taught me many foundational skills in areas such as project management and planning, experimental design, and scientific writing and presenting, which I happily made use of throughout my own PhD project. I count myself lucky to have had such dedicated supervisors!

As I alluded to before, the great atmosphere in the Hybrid Solar Cells group was a major contributor to my great experience at AMOLF. I thoroughly enjoyed our outings and shared lunches and coffee breaks. I am also grateful for the supportive environment that helped me get through the more frustrating parts of the PhD, such as failed experiments and rejected papers. I was fortunate enough to have shared my entire time at AMOLF with **Imme** and **Moritz**. I remember how we went to our first international in-person conference together in Italy, easily one of my favorites. For the last conference of the PhD, we again went with the three of us, this time to Boston, coming full circle. This was another conference that was easily one of my favorites, in part also because of our trip to New York together afterwards, I must admit. **Imme**, I remember well how you were so welcoming to me when I started my PhD. You had already started your PhD several months before, and were very approachable and knowledgeable already. You really helped me off to a good start. Throughout my PhD, you were one of my most important suppliers of (much-needed) feedback and critical questions, for which many thanks. I am also happy to have gotten to know you outside of work as a kind and caring person. **Moritz**, I am really glad to have had you as my PhD buddy and office mate throughout the entire project. We went through all the happy and frustrating parts of the PhD together. Your kindness and genuine interest helped make the former that much more enjoyable, while your wit and sense of humor helped alleviate the latter. I always enjoyed our talks about our research, but also the unrelated banter. It is hard for me to imagine my PhD without thinking about me crawling out of the clean room after a day-long session to a nearly empty AMOLF, only to find you in our office still hacking away at your simulations or models. Going through

the PhD together has made it that much more rewarding to me.

**Agustin**, you brought so much positivity and humor with you when you joined the group. I really enjoyed our koffie (with a 'k') together. Soon after you joined, we started multiple projects together, which were easily my favorites. I enjoyed our discussions and really valued your view on the research. Thanks also for your advice and insights on finishing the PhD, which really helped me through the final months. I am glad to still be involved in some of your new research projects, albeit from the sidelines now. **Daphne**, you were such a fun and empathetic group member. I really liked our Pirates of the Caribbean discussions, and wish you all the best with the final stretch of your PhD! **Lars**, thanks for all your work as our lab's dedicated spin bot engineer, being the life of many AMOLF borrels and parties, and for your sharp questions whenever I presented my work. **Larissa**, you were my favorite "crazy, hyperactive person" (quoting your own words here) in our group. You always brought so much fun and positivity with you, which I really appreciated. **Jarla**, during your time at AMOLF you made many helpful suggestions to my work, for which thanks. I also really liked learning of all your adventures during your exchanges. **Francesco**, although we only overlapped for a few months, I am grateful for your positive energy and pep-talks during this time. I hope you will get to enjoy your PhD as much as I did mine. Best of luck also to **Athira**. You just started when I finished my PhD. I enjoyed our conversations during the couple of times we spoke. Best of luck with your PhD! **Gianluca**, you are one of the smartest and at the same time kindest and most approachable people I met during my PhD. Thanks for all your input and the many interesting and fun talks. **Maria**, thank you for all your advice at the start of my PhD, the jokes, and for introducing proper (delicious) Columbian food to us. **Lucie**, thanks for all your kindness and for making me feel welcome when I first joined the group. Thank you also for guiding me through the first phase of the PhD. **Loreta** and **Christian**, thank you for welcoming me in the group, and for your help getting started with the PhD. I would like to thank **Marc** for being such a great lab technician and a fun and supportive person. I was always amazed how anyone could come to you with anything and you would have it fixed in a heartbeat. Throughout my PhD, I also supervised four dedicated and motivated master's students, **Oscar**, **Jakub**, **Thomas**, and **Dimitris**. Thank you for all your hard work, and all the lessons you taught me as I supervised you. Also thanks to the many other master's students who worked in the Hybrid Solar Cells group while I was there and made it such a fun experience, **Max**, **Filip**, **Jeong-Ju**, **Fiona**, **Paul**, **Federico**, **Toon**, **Floris**, **Menke**, **David**, **Rens**, and **Georg**, as well as **Cedric** and **Adrian**, who visited AMOLF as guest researchers.

**Sarah**, I still remember very well how we both started as master's students at AMOLF on the same day. I am happy to have shared my entire time at AMOLF with such a fun, lively,

and excellent scientist such as you. I really enjoyed our talks and was always impressed by your work. Thanks also to **Hongyu** and **Harshal**, my office mates during my master's project at AMOLF, for making my initial time there as enjoyable as it was. Thanks also to **Andrea** and **Tom** for all your helpful input on my PhD project when I first started. Thank you **Deba** for all your advice, our many discussions, and for all our fun conversations throughout the years. **Nikolai**, I really enjoyed our talks about machine learning. Thank you for all your suggestions for learning more about it. Thanks also **Daphne A.** for all your advice and our fun talks. Thanks also to the many other people at AMOLF who made it an unforgettable and fun time, **Yorick, Antony, Linde, Daan, Marcel, Fanny, Jerome, Omolara, Elaina, Rohit, Jyoti, Mees, Ethan, Loriane, Francesca, Falco, Fons**, and anyone I might have forgotten.

I would also like to thank professors Sir **Richard Friend, Neil Greenham, Sam Stranks**, and **Akshay Rao** for hosting the wonderful visits to Cambridge during the CAMOLF sessions, and for the many interesting discussions. Thanks to **Changsoon, Gianluca, Juliane, Shabnum**, and **Tianjun** for organizing these sessions.

My thanks also goes out to the support staff at AMOLF. In particular to **Bob, Igor, Arthur, Laura**, and **Dimitry** of the clean room staff, for all your tireless help and expertise, **Bob** of the electronics department for all your help with the delicate setups I used for all my experimental work, and **Mark** and **Niels** from precision manufacturing for dicing the countless wafers I fabricated throughout my PhD.

Verder wil ik graag mijn lieve vrouw **Daniëlle** bedanken, voor al je steun gedurende mijn PhD, en alle jaren daarvoor. Ik houd ontzettend veel van je en ben enorm blij dat je na al mijn gestress het afgelopen jaar nog steeds met me wilde trouwen. Ik kan niet wachten op onze volgende stappen samen! Ik wil ook graag onze vrienden **Miriam** en **Chiron** bedanken voor al jullie hulp bij het organiseren van onze bruiloft terwijl en vlak nadat ik mijn proefschrift afschreef. Zonder jullie onvermoeibare hulp was het ons nooit gelukt om er zo een mooie dag van te maken. Ook bedankt **Kees**, met wie ik mijn eerste (buitenschoolse) wetenschappelijke experimenten uitvoerde. Gelukkig is het er daarna wel wat professioneler aan toegegaan bij het promotieonderzoek. Ook bedankt voor de vele jaren vriendschap die me mede hebben gevormd. Verder wil ik graag mijn broer **Stefan** en **mijn ouders** bedanken voor al jullie steun tijdens mijn promotieonderzoek en nog ver daarvoor. Jullie hebben me geleerd om het leven aan te gaan met nieuwsgierigheid, humor, creativiteit en om het niet te serieus te nemen. Levenslessen die ik ook in mijn onderzoek heb geprobeerd terug te laten komen. Als laatste wil ik graag mijn katten **Flip** en **Nala** bedanken, die me tijdens alle stress rondom het schrijven en afronden van mijn PhD graag op kwamen zoeken om me op hun manier bij te staan en me wat af te leiden.

## About the Author

Jeroen J. de Boer was born in Tiel on 2 September, 1993. He obtained his Bachelor's degree in Chemistry from the joint degree program of the University of Amsterdam and the VU Amsterdam in 2018. He then continued his studies at Utrecht University, where he enrolled in the Nanomaterials Science Master's program. For his master thesis, he worked on the fabrication of two-dimensional superlattices from PbSe quantum dots and their cation exchange to other semiconducting materials. Afterwards, he started a research internship in the group of Erik Garnett at AMOLF. His research project focused on reciprocity-inspired preparation of directional light emitters in mixed-halide perovskite films. After finishing his Master's degree cum laude in 2021, he joined the group of Bruno Ehrler to start a PhD project on energy-efficient halide perovskite neuromorphic devices. The results are presented in this thesis.

